

**CONFORMATIONAL ANALYSIS OF TRICHOTHECENE MYCOTOXINS: A SOLUTION- AND SOLID-
STATE NUCLEAR MAGNETIC RESONANCE (NMR) STUDY**

ROXANNE ANGELA SHANK

B. Sc., University of Lethbridge, 2010

A Thesis

Submitted to the School of Graduate Studies

of the University of Lethbridge

in Partial Fulfillment of the

Requirements for the Degree

MASTER OF SCIENCE

Department of Chemistry and Biochemistry

University of Lethbridge

LETHBRIDGE, ALBERTA, CANADA

© Roxanne Angela Shank, 2014

CONFORMATIONAL ANALYSIS OF TRICHOTHECENE MYCOTOXINS: A SOLUTION- AND SOLID-STATE
NUCLEAR MAGNETIC RESONANCE (NMR) STUDY

ROXANNE ANGELA SHANK

Approved:

* (Print Name)	(Signature)	(Rank)	(Highest Degree)	Date
<hr/> * Dr. Paul Hazendonk	<hr/>	<hr/>	<hr/>	<hr/>
<hr/> * Dr. François Eudes	<hr/>	<hr/>	<hr/>	<hr/>
<hr/> * Dr. Hans-Joachim Wieden	<hr/>	<hr/>	<hr/>	<hr/>
<hr/> * Dr. Marc Roussel	<hr/>	<hr/>	<hr/>	<hr/>
<hr/> * Dr. Roy Golsteyn	<hr/>	<hr/>	<hr/>	<hr/>
<hr/> * External Examiner	<hr/>	<hr/>	<hr/>	<hr/>
<hr/> * Chair, Thesis Examination Committee	<hr/>	<hr/>	<hr/>	<hr/>

To my wonderful son, Ryan, whose ever-present smile has brightened even the darkest of days; and to my parents, Fern and Donna Shank, without whose support none of this would have been possible.

ABSTRACT

Trichothecenes comprise a large family of sesquiterpenoidal mycotoxins that largely effect the production of cereal crops. Recent advances in structural determination through solution- and solid-state NMR provide new avenues to the understanding of the structural dynamics of these toxins.

Refinement of the proton and carbon assignments in deuterated chloroform (CDCl_3) are presented for the type A trichothecene T-2 toxin, and the type B trichothecenes deoxynivalenol (DON), nivalenol (NIV), 3-O-acetyldeoxynivalenol (3-ADON), and 15-O-acetyldeoxynivalenol (15-ADON). The effect of different solvent systems on the type B trichothecenes is investigated, and evidence for structural isomerism of the trichothecenes is presented. The mechanism for the rearrangement between the two isomers is presented.

Solid-state NMR investigations demonstrate multiple configurations for T-2 toxin, and structural isomerism is shown to exist in the solid-state for DON.

Solution- and solid-state NMR data was used to determine the interaction of water with selected trichothecenes, and the water-binding interactions are described.

ACKNOWLEDGEMENTS

This entire experience has been such a season of change for me and my life. It feels as though I have lived many different lives throughout this process, and many different people have come and gone, but all have made an impact on the final product which is presented here. Thus, there are many people that I feel I should thank for their contribution along my journey.

First off, I would like to thank my supervisors. Paul Hazendonk took me on as a research assistant during the second term of my studies at the University of Lethbridge, back in January of 2008. That began my studies in NMR and theoretical chemistry and has led to my interests in quantum mechanics and biophysical chemistry. I have learned much from Paul, and have had a breadth of experience in many different areas of chemistry, from inorganic fluoride chemistry and radiopharmaceuticals, to the study of small organic biologically active molecules. It has been an exercise in patience for me, as the study of NMR and quantum mechanics are not the easiest subjects to comprehend, but they are definitely subjects which hold a lot of interest.

François Eudes, of the Agriculture and Agri-Food Canada (AAFC) Research Center in Lethbridge was also instrumental to my learning process. Through François I came to learn new techniques, such as Dynamic Light Scattering (DLS) and Scanning Electron Microscopy (SEM). Although these techniques were not employed for this study, they would have been part of the original project for my thesis, which was not completed due to issues relating to sample preparation and cost. François also provided me the opportunity to speak at conferences and to colleagues I would have not had the opportunity to encounter otherwise. It has been a great honor to work with him and his team. In particular, the occasion to work with Nora Foroud of AAFC Lethbridge, and Barbara Blackwell of AAFC Ottawa, was a welcome opportunity. Nora's writing ability and thought patterns came as a great asset in the writing of the two publications that came out this work prior to its completion. Barbara's expertise in the field of trichothecenes, and her generous support in the form of trichothecene samples were integral to the work presented here, and her contributions to the writing process were critical to the progression of the papers. The opportunity to present my work to her and her colleagues at AAFC Ottawa was a flattering and delightful experience.

I would also like to thank my NMR group for their continued support in my learning process and presentation techniques. Praveen Chaudhary, Jamie Goettel, Alexey Borisov, Farhad Faghigi, Paul Sidhu, Chuchu Sun, Rudraksh (Rudy) Majumdar and Micheal Opyr are friends and colleagues that have made my experience memorable. I would particularly like to thank Tony Montana for his friendship, mentorship and help, both as a fellow student of Paul's and later as the NMR facility manager. His help with regards to the instrumentation and experimental setup was a crucial contribution to this project, and without his continued support, this work would not have been possible. The group at AAFC Lethbridge also deserves acknowledgement for their support in my process, in particular my office mate and friend Trevor MacMillan, and the lab manager Denise Nielson were a great help to me during my time at AAFC. I would also like to thank Evan Mercier for his contribution to the figure of the proposed interaction of T-2 toxin with the ribosome.

There are many other academic partners who deserve some credit here, Ute Kothe-Wieden, Hans-Joachim Wieden and Steven Mosimann for their help in developing my biochemical skills, and teaching me more about life than they could possibly know. Steve in particular deserves big thanks for the long conversations, patience in my questions regarding X-ray crystallography, and for allowing me to use one of his student offices while writing the first portion of my thesis, and during the long hours of experimental time in the solid-state NMR lab.

Lastly, I would like to thank my friends and family who supported me through this process: my parents for their financial support, and the time that they provided me when they cared for my son; Tobias Hayes, for never giving up the belief that I could do this, and encouraging me to keep going, even when I wanted nothing more than to quit. And finally, to my wonderful son Ryan, for never giving up on me and reminding me that sometimes, you just need to stop what you are doing and have a tickle fight, because laughter is always the very best medicine. There are so many other people who deserve to be thanked here, and to those, you are always in my memories and I wish you all the best in your lives beyond this day. Thank you.

TABLE OF CONTENTS

ABSTRACT	i
ACKNOWLEDGEMENTS	ii
LIST OF TABLES	vi
LIST OF FIGURES	1
1. INTRODUCTION	
1.1. Overview	11
1.2. Trichothecenes	11
1.2.1. Structure-Function Relationship	17
1.2.2. Methods for Determining Structure	22
I. Crystallography	22
II. Nuclear Magnetic Resonance Spectroscopy	26
1.3 Nuclear Magnetic Resonance	
1.3.1 Solution-State NMR	27
I. ¹³ C NMR	27
II. Deuterium Exchange	31
III. Multi-Dimensional Solution-State NMR Experiments	32
i. Heteronuclear Correlation Experiments	33
ii. Homonuclear Correlation Experiments	35
iii. Nuclear Overhauser Effect Spectroscopy (NOESY)	36
1.3.2 Solid-State NMR	39
I. Magic Angle Spinning (MAS)	39
II. Cross-Polarization (CP)	40
III. Multi-Dimensional NMR in the Solid-State	40
i. Incredible Natural Abundance Double	
Quantum Transfer Experiment (INADEQUATE)	40
ii. R-symmetry based CSA recoupling experiment	42
1.3.3 NMR Spectral Parameter Simulations	46
2 Hydrogen-Bonding Interactions of T-2 Toxin	48
2.2 Overview	48
2.3 Introduction	48
2.4 Materials and Methods	50
2.4.1 Solution-State NMR Experiments	50
2.4.2 Simulations	51
2.5 Results	52
2.5.1 Structural Rigidity and Water-Bridging	52
2.5.2 Carbon Spectral Analysis	60
2.6 Discussion	62
2.6.1 Hydrogen-Bonding in Solution	62
2.7 Conclusions	64
3 Structural Analysis of Deoxynivalenol (DON)	66
3.1 Overview	66
3.2 Introduction	66
3.3 Materials and Methods	68
3.3.1 Solution-State NMR Experiments	68
3.3.2 Simulations	70
3.4 Results and Discussion	70
3.4.1 Full Spectral Analysis of Deoxynivalenol in chloroform	70
3.4.2 Characterization of type B trichothecenes	84
3.4.3 Deuterium Exchange and Water-binding in the type B	

	trichothecenes	92
3.5	Conclusions	104
4	Structural Dynamics of Type B trichothecenes due to solvent effects	106
4.1	Overview	106
4.2	Introduction	107
4.3	Solvent Properties and Chemical Structure	110
4.4	Materials and Methods	112
4.4.1	Solution-State NMR Experiments	112
4.4.2	Simulations	114
4.5	Complete Spectral Analysis of Nivalenol in Dimethyl Sulfoxide	114
4.5.1	Results	114
4.5.2	Discussion	124
4.6	Solvent Effects Observed for Deoxynivalenol	134
4.6.1	Results	134
4.6.2	Discussion	141
4.7	Investigation into the effects of Non-Polar CDCl ₃ versus Polar DMSO-d ₆ solvents across the Type B trichothecenes	149
4.7.1	Results	149
4.7.2	Discussion	171
4.8	Conclusions	175
5	Solid-State Structural Analysis of Trichothecene Mycotoxins	177
5.1	Overview	177
5.2	Introduction	177
5.3	Materials and Methods	179
5.3.1	Solid-State NMR Experiments	179
5.4	Results	181
5.4.1	Carbon Spectral Analysis of T-2 Toxin	181
5.4.2	Spectral Analysis of Deoxynivalenol	185
5.4.3	Testing of the INADEQUATE Experiment	190
5.4.4	R-symmetry based CSA recoupling	192
5.5	Discussion	203
5.5.1	Conformations of T-2 Toxin	203
5.5.2	Conformational Dynamics of Deoxynivalenol	208
5.5.3	INADEQUATE	212
5.5.4	Chemical Shielding Tensors for T-2 toxin	212
5.6	Conclusions	215
6	Conclusions and Future Directions	217
6.1	Conclusions	217
6.2	Biological Implications	221
6.3	Future Directions	224
7	References	226

LIST OF TABLES

2.1	¹ H Chemical Shifts for the resonances of the trichothecene core of T-2 Toxin in CDCl ₃ at 300 MHz	54
2.2	¹ H Coupling Constants for the resonances of the trichothecene core of T-2 Toxin in CDCl ₃ at 300 MHz	55
2.3	¹ H chemical Shifts of Side-Chain Groups on T-2 Toxin in CDCl ₃ at 300 MHz	55
2.4	¹ H Coupling Constants of Side-Chain Groups on T-2 Toxin in CDCl ₃ at 300 MHz	56
2.5	Carbon-13 Chemical Shifts and ¹ H- ¹³ C couplings for T-2 Toxin in CDCl ₃ at 75 MHz	61
3.1	Comparison of the experimental and literature data for DON studied in CDCl ₃ at 300 MHz	73
3.2	¹ H- ¹ H Scalar Coupling constants extracted from the 1D and 2D data collected for DON in CDCl ₃ at 300 MHz	74
3.3	Carbon-13 Chemical Shifts and Heteronuclear ¹ H- ¹³ C Couplings observed for DON in CDCl ₃ at 300 MHz	80
3.4	Experimental and Literature ¹ H Chemical Shift data for the type B trichothecenes in CDCl ₃ at 300 MHz	87
3.5	Experimental and Literature Scalar Coupling Constants observed for the type B trichothecenes in CDCl ₃ at 300 MHz	88
3.6	Chemical Shift and Scalar coupling data of the potential degradation products of DON observed upon the addition of two drops of D ₂ O to the DON spectrum in CDCl ₃ at 300 MHz and ambient temperature	99
3.7	Chemical Shift and Scalar coupling data of the potential degradation products of DON observed upon the addition of three drops of D ₂ O to the DON spectrum in CDCl ₃ at 300 MHz and ambient temperature	100
4.1	Chemical Properties of common NMR solvents	111
4.2	Chemical Shift Values and two-dimensional ¹ H Correlations for the major and minor contributors to the NIV spectrum observed in DMSO-d ₆ at 300 MHz	119

4.3	Coupling Constants and Interpretation of the major and minor contributors to the NIV spectrum in DMSO-d ₆ at 300 MHz	120
4.4	Carbon Chemical Shifts and ¹ H- ¹³ C Couplings observed for NIV in DMSO-d ₆ at 75 MHz.	124
4.5	Chemical Shift Data for DON in various solvents at 300 MHz	136
4.6	Scalar Coupling values obtained for DON in various solvents at 300 MHz	137
4.7	Experimental and Literature ¹³ C Chemical Shift data for DON collected in CDCl ₃ , Acetone-d ₆ and DMSO-d ₆	140
4.8	Scalar coupling Values for DON in CDCl ₃ , acetone-d ₆ and DMSO-d ₆ for the 15 _{OH} resonance	148
4.9	Chemical shift data for ¹ H spectra of NIV compared in CDCl ₃ :CD ₃ OD and DMSO-d ₆ at 300 MHz	151
4.10	Scalar coupling data for NIV compared in CDCl ₃ :CD ₃ OD and DMSO-d ₆ at 300 MHz	152
4.11	Chemical Shift comparison for 3-ADON and 15-ADON in CDCl ₃ and DMSO-d ₆ at 300 MHz	154
4.12	¹ H- ¹ H scalar coupling data for 3-ADON and 15-ADON collected in CDCl ₃ and DMSO-d ₆ at 300 MHz	157
4.13	Carbon-13 chemical shifts observed for 3-ADON and 15-ADON in CDCl ₃ and DMSO-d ₆ from the ¹ H- ¹³ C HSQC spectra	161
4.14	Comparison of Chemical Shift Data for the major component of the type B trichothecenes observed in DMSO-d ₆ at 300 MHz	164
4.15	Comparison of the scalar coupling constants observed for the major components of the type B trichothecene obtained in DMSO-d ₆ at 300 MHz	165
4.16	Comparison of the chemical shift data for the minor component observed in the type B trichothecenes observed in DMSO-d ₆ at 300 MHz	166
4.17	Comparison of the scalar coupling constants observed for the minor components of the type B trichothecenes observed in DMSO-d ₆ at 300 MHz	167

4.18	Carbon-13 chemical shift comparison for the type B trichothecenes in DMSO-d ₆	170
5.1	Comparison of the ¹³ C Chemical Shifts for T-2 Toxin in Solution and Solid-state	184
5.2	Carbon Chemical Shift Data for DON in the solid-state, compared with the experimental and literature carbon chemical shifts observed for DON in DMSO-d ₆	188

LIST OF FIGURES

1.1	The chemical structure of the trichothecene core	13
1.2	Three-dimensional stereochemistry of the trichothecene core	14
1.3	The general core structure for the type A, B, C, and D trichothecenes	15
1.4	Pulse schemes for the A) INEPT and B) Refocused INEPT experiments	29
1.5	Pulse scheme for the DEPT experiment	30
1.6	Phase modulation of the methine, methylene and methyl signals of the DEPT experiment	31
1.7	Pulse scheme for the HSQC experiment	34
1.8	Pulse schemes for the A) HMQC and B) HMBC experiments	35
1.9	Pulse scheme for the phase sensitive COSY experiment	36
1.10	Pulse scheme for the NOESY experiment	37
1.11	Pulse scheme for the CP-refocussed INADEQUATE experiment	41
1.12	A general pulse scheme for an R-based symmetry sequence	43
1.13	Spin-space selection (SSS) diagrams for the R-symmetry sequence R18 ₂ ⁵	45
2.1	Structures of type A and B trichothecenes	49
2.2	(A) T-2 toxin ¹ H NMR solution-state spectrum at 300 MHz in CDCl ₃ (B) Deuterium exchange experiment	53
2.3	¹ H- ¹ H COSY spectrum observed for T-2 toxin at 300 MHz in CDCl ₃	56
2.4	¹ H NOESY for T-2 toxin at 300 MHz in CDCl ₃	59
2.5	Proposed chemical structure for T-2 toxin indicating all ¹ H resonances	59
2.6	The solution-state ¹³ C NMR spectrum for T-2 toxin in CDCl ₃ at 75 MHz with ¹ H decoupling	60

2.7	Proposed placement of water in the tetrahydropyranyl pocket of T-2 toxin	63
3.1	Internal hydrogen-bonding network in DON proposed by density functional theory (DFT) analysis	68
3.2	^1H NMR solution-state spectrum for DON at 300 MHz in CDCl_3	72
3.3	The ^1H COSY spectrum for DON at 300 MHz in CDCl_3	76
3.4	The ^1H NOESY spectrum for DON at 300 MHz in CDCl_3	78
3.5	Carbon-13 spectrum for DON in CDCl_3 at 75 MHz	79
3.6	Two-dimensional ^1H - ^{13}C correlation spectra for DON at 300 MHz and 75 MHz respectively, in CDCl_3	81
3.7	Structure for DON depicting the possible formation of an internal hydrogen-bonded network	83
3.8	Relative chemical shift trends of the trichothecene resonances in the ^1H NMR solution-state spectrum in CDCl_3	85
3.9	Stacked plot of the ^1H NMR solution-state spectra for the type B trichothecenes in CDCl_3 at 300 MHz	86
3.10	View down the length of the trichothecene core for DON demonstrating the conformation of the methylene protons for carbon-13 of the epoxide	90
3.11	Comparison of the ^1H spectra collected for DON received from different sources at 300 MHz and ambient temperature	94
3.12	Deuterium exchange experiment for DON in CDCl_3 at 300 MHz	96
3.13	Predicted degradation mechanism of DON upon the addition of D_2O to the sample in CDCl_3 at ambient temperature	101
3.14	^1H NOESY spectrum for DON in CDCl_3 upon the addition of 1 ppm D_2O to the sample.	102
4.1	Three-dimensional stereochemistry of the trichothecene core when (A) the A-ring is in a half-chair and the B-ring in a chair conformation; (B) the A-ring is in a half-chair and the B-ring in a boat conformation	108

4.2	Hemiketal and ether linkages proposed to occur in the type B trichothecenes DON and NIV	109
4.3	Experimental and simulated ^1H spectra for NIV in DMSO- d_6 at 300 MHz depicting the existence of two distinct configurations	116
4.4	The ^1H COSY spectrum for NIV at 300 MHz in DMSO- d_6 depicting ^1H - ^1H correlations for the major and minor contributors to the spectrum	117
4.5	The ^1H NOESY spectrum for NIV at 300 MHz in DMSO- d_6 depicting the through-space ^1H - ^1H correlations for the major and minor contributors to the spectrum	117
4.6	Carbon-13 spectrum for NIV in DMSO- d_6 at 75 MHz observed at ambient temperature	122
4.7	Two-dimensional ^1H - ^{13}C HSQC spectrum for NIV in DMSO- d_6 measured at 300 MHz	123
4.8	Chemical mechanism for the formation of the hemiketal isomer of NIV from the original NIV structure	127
4.9	Three-dimensional structure of the major component of the NIV spectrum observed in DMSO- d_6	129
4.10	Chemical shift comparison for 3-ADON and 15-ADON in CDCl_3 and DMSO- d_6 at 300 MHz observed in DMSO- d_6 depicting the adoption of the boat configuration in the B-ring	131
4.11	^1H NMR spectra observed for DON in CDCl_3 , CD_3OD , acetone- d_6 , DMSO- d_6 and THF- d_8 at 300 MHz	135
4.12	CP ^{13}C spectra for DON in CDCl_3 , acetone- d_6 and DMSO- d_6 at 75 MHz acquired with 4000 scans and a relaxation delay of 2 seconds.	139
4.13	The alignment of acetone- d_6 with respect to the epoxide functionality of DON	143
4.14	Trichothecene core depicting the bonds at C-3 and C-4	144
4.15	Depiction the coupling for the protons on C-4 to the proton H-3 $_{\beta}$	145
4.16	Newmann projections along the H-C-O-H bond for the hydroxyl resonance at C-3 showing the <i>gauche</i> , <i>gauche'</i> and <i>trans</i> coupling orientation for H-3 $_{\beta}$ and H-3 $_{\text{OH}}$	146

4.17	Newmann projections for the rotations observed along the C-15 and O-15 bond in DON	147
4.18	^1H NMR solution-state spectra for NIV compared in CDCl_3 , CD_3OD and DMSO-d_6 at 300 MHz	150
4.19	^1H NMR spectral comparison for 3-ADON in CDCl_3 and DMSO-d_6 at 300 MHz	155
4.20	^1H NMR spectral comparison for 15-ADON in CDCl_3 and DMSO-d_6 at 300 MHz	156
4.21	^1H - ^{13}C HSQC spectra of 3-ADON in A) CDCl_3 and B) DMSO-d_6 at 300 and 75 MHz for ^1H and ^{13}C , respectively	159
4.22	^1H - ^{13}C HSQC spectra of 15-ADON in A) CDCl_3 and B) DMSO-d_6 at 300 and 75 MHz for ^1H and ^{13}C , respectively	160
4.23	Comparison of the ^1H NMR spectra for type B trichothecenes collected in DMSO-d_6 at 300 MHz	163
4.24	Newmann projections along the C-6/C-15 bond in 15-ADON	172
4.25	Structural orientation of the acetyl group at C-15 in 15-ADON predicted to occur in CDCl_3	173
5.1	Carbon-13 spectra of T-2 toxin (A) solution-state spectrum at 75 MHz in CDCl_3 (B) Direct polarization (DP) in the solid-state at 125 MHz and MAS of 25 kHz (C) Cross-Polarization (CP) from ^1H - ^{13}C at 125 MHz and MAS of 25 kHz	182
5.2	Superimposition of the solid-state and solution-state spectra for T-2 toxin	183
5.3	Solid-state ^1H to ^{13}C CP-MAS NMR spectrum of DON at 125 MHz spectrometer frequency and 28 kHz spinning speed	185
5.4	Superimposition of the solution-state ^{13}C simulation spectra for DON in CDCl_3 with the solid-state ^{13}C spectra for DON	186
5.5	Superimposition of the solution-state ^{13}C simulation spectra for DON in DMSO-d_6 with the solid-state ^{13}C spectra for DON	187
5.6	Expected electron density in the (A) major conformation versus the (B) hemiketal conformation for DON, based on the assignment of the NIV structure observed in DMSO-d_6	189
5.7	The CP-refocused INADEQUATE spectrum obtained for $^{13}\text{C}_2$ -glycine	191
5.8	Stacked plot of the spectra obtained for the R10_1^7 CSA recoupling sequence on the test sample for the glucose- $^{13}\text{C}_6$	194
5.9	Spin-space selection (SSS) diagrams for R-symmetry sequence R18_2^5	196

5.10	Stacked plot of the resultant spectra obtained for the R18 ₂ ⁵ CSA recoupling sequence for T-2 toxin	197
5.11	Free induction decay (FID) signals arising from the phase modulation of individual spins to the R18 ₂ ⁵ spectrum for T-2 toxin in the solid-state	199
5.12	Natural powder patterns for the individual signals pulled from the symmetrical powder patterns obtained for (A) the signal C-2 on the C-ring; (B) the signal C-8' on the isovalerate side chain; (C) the signal C-9 in the A-ring	201
5.13	Comparison of solution and solid-state conformations of T-2 toxin	204
5.14	S _N 2 scheme. The angles from which water would have to attack from are shown for both C-12 and C-13	205
5.15	Chemical shielding tensor representation for the carbons (A) C-2 representing a slight biaxiality in the tensor, the tensor is ellipsoid; (B) C-8' represents a chemical shielding tensor which is more cylindrical, and uniaxial, and (C) C-9 is largely biaxial	214
6.1	Model representing the proposed transient interaction of the trichothecene T-2 toxin with W255 of the W-finger of ribosomal protein, RPL3	223

List of Abbreviations

1D – one-dimensional

^1H – proton (Hydrogen atom with no electrons or neutrons)

2D – two-dimensional

^2H – Deuterium (Hydrogen atom with one neutron)

3-ADON – 3-O-acetyldeoxynivalenol

3D – three-dimensional

^{13}C – Carbon-13 (Stable isotope of Carbon containing 6 protons and 7 neutrons)

15-ADON – 15-O-acetyldeoxynivalenol

^{15}N – Nitrogen-15 (Stable isotope of Nitrogen containing 7 protons and 8 neutrons)

60S – The subunit of the ribosome weighing 60 Svedberg units

AAFC – Agriculture and Agri-Food Canada

aa-tRNA – aminoacyl transfer Ribonucleic Acid

acetone- d_6 – deuterated acetone

ATA – Alimentary Toxic Aleukia

A-ring – Cyclohexene ring of the trichothecene core

A-site – the point of entry for aminoacyl-tRNA into the peptidyl transferase center of the ribosome

B-ring – tetrahydropyran ring of the trichothecene core

C-ring – cyclopentyl ring of the trichothecene core

C·m – Coulomb meter (unit of measurement for the dielectric constant)

CDCl₃ – deuterated chloroform

CD₃OD – deuterated methanol

COSY – Correlation Spectroscopy

cP – centipoises (unit of measurement for viscosity)

CP – Cross Polarization

CSA – Chemical Shielding Anisotropy

CW – Continuous Wave

D-glucose-¹³C₆ – glucose which has been isotopically enriched with carbon-13 and deuterium atoms.

D₂O – deuterated water

DAS – Diacetoxyscirpenol

DEPT – Distortionless Enhancement by Polarization Transfer

DFT – Density Functional Theory

DON – deoxynivalenol

DMSO-d₆ – deuterated dimethylsulfoxide

DNA – deoxyribonucleic acid

DP – Direct Polarization

E-site – exit site for protein translation in the ribosome

EXSY – Exchange Spectroscopy

F.graminearum – *Fusarium graminearum*

F. sporotrichiodes – *Fusarium sporotrichiodes*

FHB – Fusarium Head Blight

FID – Free Induction Decay

FT – Fourier Transformation

FT_IR – Fourier Transformed Infrared

Fus-X – Fusarenon-X

Fusarium sp. – *Fusarium* species

g/cm³ – grams per cubic meter (measurement for density)

HDO – water containing a single deuteron

HMBC – Heteronuclear Multiple Bond Corelation

HMQC – Heteronuclear Multiple Quantum Coherence

HSQC – Heteronuclear Single Quantum Coherence

Hz – Hertz (unit of measurement for frequency)

INADEQUATE – Incredible Natural Abundance Double Quantum Transfer

INEPT – Insensitive Nucleu Enhancement by Polarization Transfer

kHz – kilohertz (unit of measurement for frequency)

MAS – Magic Angle Spinning

MHz – megahertz (unit for measuring frequency)

MS – Mass Spectrometry

NEO – neosolaniol

NIV – nivalenol

NMR – Nuclear Magnetic Resonance

NOE – Nuclear Overhauser Effect

NOESY – Nuclear Overhauser Effect Spectroscopy

O-Ac – O-acetyl functional group

O-Isoval – O-isovalerate functional group

P-site – propagation site for protein translation in the ribosome

ppm – parts per million

PTC – peptidyl transferase center (located in the ribosome)

RMSD – Root Mean Squared Deviation

RNA – Ribonucleic Acid

rpl3 – gene encoding the RPL3 protein

RPL3 – Ribosomal Protein L3

S/N – Signal-to-Noise

SBS – Sick Building Syndrome

SCXRD – Single Crystal X-ray Diffraction

SD – Standard Deviation

T₁ – Longitudinal Relaxation

T_{1H} – Longitudinal Relaxation of the Hydrogen Resonance

T₂ – transverse relaxation

THF-d₈ – deuterated Tetrahydrofuran

TMS – Tetramethyl Silane

TPPM – two-pulse phase-modulated decoupling

TRI101 – 3-O-acetyltransferase enzyme

TRI3 – 15-O-acetyltransferase enzyme

Type E –inhibition towards the elongation step of protein translation

Type I –inhibition towards the initiation step of protein translation

Type T – inhibition towards the termination step of protein translation

W255C – notation depicting a mutation at residue 255 from Tryptophan (W) to Cysteine (C)

W-finger – domain protruding from the core of a protein with a Tryptophan (W) residue at the extremity

1. INTRODUCTION

¹Reproduced in part from the manuscript: Shank, R. A., Foroud, N. A., Hazendonk, P., Eudes, F., Blackwell, B.A. (2011) Current and Future Experimental Strategies for Structural Analysis of Trichothecene Mycotoxins – A Prospectus. *Toxins*. **3**(10), 1518-1553.

1.1. Overview

Trichothecene mycotoxins are biologically active, naturally occurring compounds that have detrimental effects on cereal crops throughout the world. On the other hand, these compounds may also serve as powerful antileukemics in the battle against cancer. Without sufficient understanding in regards to the mechanism of action of these compounds, prevention of the infection of crops, or development of cancer treatments, is quite simply a process of trial and error. The rapid evolution of the fungi which produce these toxins has proven to be a stalling point in regards to the prevention of crop loss. Here it is proposed that a careful examination of the structure and dynamics of these compounds may provide some insight into their mechanism of action.

Many different techniques are available to study the structure of various compounds. Nuclear Magnetic Resonance (NMR) is particularly well suited to the structural study of compounds, such as the trichothecenes, which are not suitable for study by single crystal x-ray diffraction (SCXRD). The theory behind the NMR experiment, its instrumentation, and specific pulse sequences are described in detail in section 1.3.

1.2. Trichothecenes¹

The search for biologically active natural products in bacteria, fungi, and higher plants has been a source of major breakthroughs, particularly in medicine. Many small molecules found in nature have provided inspiration to the pharmaceutical industry for the development of new and more effective drugs based on their structures, while others have led to the discovery of toxic compounds that may contribute to life-threatening diseases. The discovery of such toxic molecules becomes important when considering disease prevention. Among the compounds that have been isolated in the past thirty years are a group of fungal toxins (mycotoxins) known as trichothecenes. Trichothecenes are produced by a range of fungi from the order *Hypocreales*, including those of the

genera *Fusarium*, *Myrothecium*, *Verticimonosporium*, *Stachybotrys*, *Trichoderma*, *Trichothecium*, *Cephalosporium*, and *Cylindrocarpon* [29,65,73,141]. Although the majority of trichothecenes contribute to crop disease and mycotoxicoses, they have also been considered as important for use as antibiotics and antileukemics [53,73,75,76]. Therefore, in order to better understand their function, prevent trichothecene-related diseases, or alternatively explore the roles they may play as powerful pharmaceutical agents, it is important to gain insight into the biochemical processes and structure of this important class of compounds.

Trichothecene-producing fungi were originally discovered as contributors to mold in grain products as early as the 1930s and 40s [106]. The *Fusarium* and *Stachybotrys* genera are frequently associated with the infection of crops in temperate climates, such as Europe, Asia and the Americas. *Stachybotrys* is a saprophytic fungus, which is commonly found to infect high-cellulosic crops such as straw and hay, and is the leading cause of stachybotryotoxicosis in livestock [71]. Furthermore, *Stachybotrys* is a toxic black mold commonly found in association with sick building syndrome (SBS), a multitude of illnesses associated with poor air quality in office buildings [9]. The *Fusarium* species are responsible for a wide variety of plant diseases, including Fusarium head blight (FHB), crown rot, red mold and root rot in cereal crops (i.e. barley, wheat, rye, corn, rice, etc.) [44]. These diseases can result in severe yield loss in susceptible crops. In the case of FHB, trichothecenes accumulate in the developing grain of cereal crops. Ingestion of trichothecene-contaminated grain has been linked to emesis, hemorrhaging, abortion and death in animals [121]. In humans, ingestion of trichothecenes is the leading cause of alimentary toxic aleukia (ATA), a condition characterized by vomiting, diarrhea, anemia, dermatitis, gastrointestinal necrosis, which can be lethal, particularly in immuno-suppressed persons [33].

The first trichothecene to be isolated was trichothecin from *Trichothecium roseum*, in 1948 by Freeman and Morrison [48]. Diacetoxyscirpenol (DAS) from *Fusarium equiseti* was preliminarily characterized in 1961 by Brian *et al.* [18], and was later followed by T-2 toxin and nivalenol from *Fusarium sporotrichioides* [106,150]. While these early toxins are acutely toxic, they are not produced in any meaningful concentrations under standard environmental conditions in cereal crops [138]. It

was the discovery of deoxynivalenol (DON) infected wheat in Eastern North America in 1980 [152,160], that truly sparked the research into the *Fusarium* species and led to the discovery of trichothecenes from other genera.

Trichothecenes are a large group of sesquiterpenoid fungal metabolites, that share a common core comprised of a rigid tetracyclic ring system (figure 1.1), and key substitution sites, denoted R1 through R5. The A-ring is typically a cyclohexene with a double bond occurring between C-9 and C-10; the B-ring is tetrahydropyranyl; a cyclopentyl group makes up the C-ring, and an epoxide is also present from C-12/13. The rigidity of this system results in a distinct stereochemistry for the A- and B-rings. The A-ring adopts a half-chair conformation, and the B-ring is most often found in the chair conformation (figure 1.2a) [134,135], although there have been a few odd cases where the B-ring has been shown to adopt a boat conformation (figure 1.2b) [72].

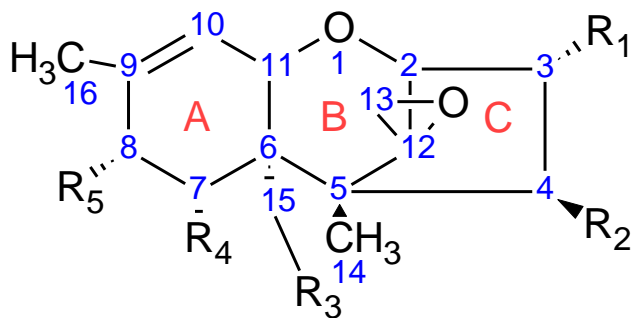


Figure 1. 1: The chemical structure of the trichothecene core depicting the connectivities of the A, B, C and epoxide rings. The substituent groups, listed R1 through R5 are depicted in their stereochemical configuration off the core.

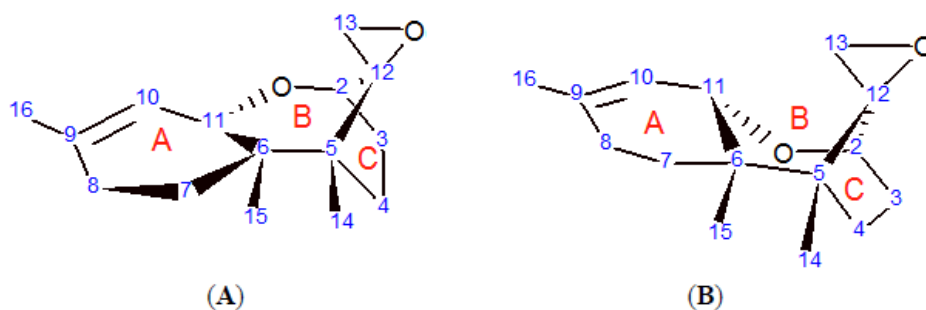


Figure 1. 2: Three-dimensional stereochemistry of the trichothecene core when (A) the A-ring is in a half-chair, and the B-ring in a chair conformation; and (B) the A-ring is a half-chair, and the B-ring in a boat conformation

At present, over 200 trichothecene compounds have been isolated, and they fall into two main classes, simple and macrocyclic. The simple trichothecenes are further divided into three types, A, B and C. Type A trichothecenes are the simplest group, being largely non-substituted, hydroxylated or esterified (figure 1.3a) [44,56,137]. Type B trichothecenes are characterized by a ketone present at R5 (figure 1.3b) [44,56]. Type A and B trichothecenes, such as T-2 toxin and DON, respectively, are often associated with *Fusarium*-infected grain. Type C trichothecenes are less common than the others, and are distinguished by the presence of a second epoxide ring at C-7/8 (figure 1.3c) [149]. A fourth class (Type D), are typically observed to be non-substituted at positions R1, R4 and R5, and are characterized by the presence of a cyclic diester or triester linkage running from C-4 to C-15 (or R2 to R3), comprising a larger macrocycle (figure 1.3d) [68]. It is for this reason that this group is referred to as the macrocyclic trichothecenes. Members of this type include the satratoxins, verrucarins and roridins, such as those produced by the *Stachybotrys* species. It is important to note here that there are many other secondary metabolites produced by the fungus which are commonly found in conjunction with trichothecene toxins. These trichodienoid compounds, including apotrichothecenes, sambucinol and sambucoin derivatives [4,57,172], share the same precursor compound, trichodiene, as the trichothecenes. However, they are composed of different cyclization patterns than those observed for their toxic counterparts. The trichodienoids are believed to

contribute to the toxicity of the trichothecenes through some synergistic mechanism [37,58,96]; however, since they do not possess the C-13 epoxide ring system they will not be covered in detail.

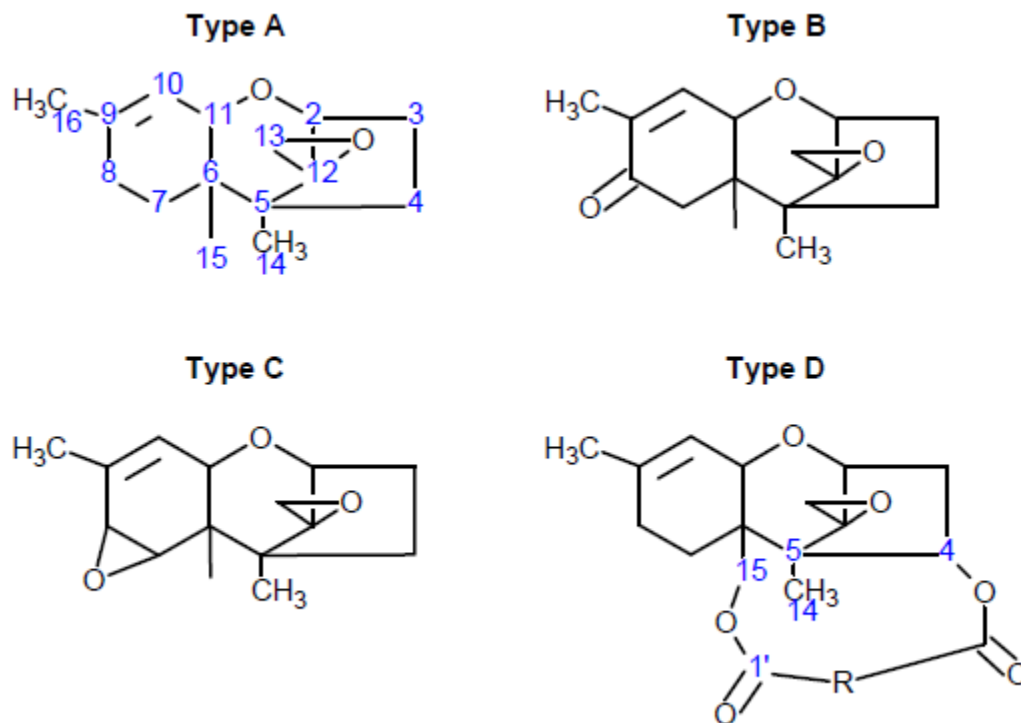


Figure 1. 3: The general core structures for type A, B, C, and D Trichothecenes. The core carbons are numbered for the type A trichothecene structure, as well as the substituent carbons for the macrocyclic type D trichothecene structure.

Trichothecenes have widespread toxicological effects throughout the cell, and have been implicated in membrane destabilization, cytoskeletal collapse, inhibition of ribonucleic acid (RNA) and deoxyribonucleic acid (DNA) synthesis, inhibition of mitochondrial function, and induction of apoptosis [71,127]. However, the most studied effect of the trichothecene toxins has been their involvement in the inhibition of protein synthesis through an interaction with the eukaryotic ribosome. This targeting of the ribosome is similar to the interaction of mainstream antibiotics with prokaryotic ribosomes, and it is for this reason that members of this class of toxins are often referred to as eukaryote specific antibiotics [53,99]. The disruption of eukaryotic ribosomal activity is believed to occur through a binding event of the trichothecene within the peptidyl transferase center

(PTC) of the ribosome [24,30,100,136,142]. Since the epoxide ring is necessary for the disruption of protein synthesis, it is logical to assume that the epoxide ring plays a significant role in the inhibitory mechanism. Typically, epoxide rings are not very stable; thus, the stability of the epoxide ring in the trichothecene structure is rather astounding considering the substantial amount of ring strain imposed on the three-membered cycle [6,38,118].

There has been much interest in the phytotoxic and cytotoxic differences observed among this class of compounds, and particularly the differences observed not only between plants and animals, but also among different species, such as corn and rice [101], or alternatively monkeys and mice [167]. A better understanding of the structural differences leading to the variable toxicity observed among various species could help scientists to develop antifungal and anti-parasitic compounds with little to no toxic effects on the host organism. At this stage, it is important to mention that very few bacterial systems appear to be affected by trichothecene infection; moreover, the few systems that do exhibit trichothecene susceptibility appear to be unrelated. Furthermore, some probiotic strains of *Bacillus* and *Lactobacillus* have been studied for their detoxification potential towards DON [28], a particularly prevalent phytotoxin. These *Bacillus* species have shown enzymatic activity towards the trichothecenes through the opening of the epoxide ring, which results in the detoxification of DON [28]. Regardless, relatively few toxicological effects have been observed for trichothecenes when tested on bacterial systems in comparison to eukaryotic systems, suggesting a certain degree of specificity for eukaryotes. Investigations regarding the cause of this discrimination between prokaryotic and eukaryotic systems are sparse, and it remains to be seen whether the toxicological resistance observed for prokaryotic systems is due to differences in cellular machinery, rapid metabolism, or inefficient membrane translocation.

Investigations focused on the macrocyclic trichothecenes suggest a potential for the targeting of cancer cells, and interest in the use of Type D trichothecenes as antileukemics exists [73,75,76,84]. However, the mechanism of action of the trichothecene compounds, with regard to their toxicological effects, is not well understood. The absolute stereochemistry and structural configuration of these compounds must be analyzed in order to understand the possible interactions. Structural studies

may also help to elucidate the underlying mechanisms for differences in toxicity among these compounds, as well as the determination of the biosynthetic pathway for trichothecene production [36,41,50,51,78,162,165,169].

This work provides information regarding the structure and dynamic nature of these select trichothecenes in order to gain a better understanding of their mechanisms of toxicity for this family of mycotoxins. This chapter will concentrate on a few key papers focused on the structural determination of trichothecenes from the 1980s and early 1990s, as well as the recent resurgence of interest in trichothecenes and the direction in which the new generation of trichothecene research is heading. Furthermore, the methods for determining trichothecene structure and an analysis of how trichothecene structure is related to function and activity will be discussed.

1.2.1. Structure-Function Relationship¹

I. Trichothecene Toxicity¹

The toxicological effects of trichothecenes are still a matter of much interest to researchers in the fields of plant biotechnology, cell biology, food chemistry and biochemistry [44]. The widespread effects of trichothecenes on eukaryotic cells are a somewhat perplexing matter. It is widely accepted that the major mode of action of trichothecene toxicity is the inhibition of protein synthesis due to an interaction with eukaryotic ribosomes [100]. While the exact mechanism of the inhibition of protein synthesis remains unclear, it has been demonstrated that trichothecenes interact with ribosomal protein L3 (RPL3) of the 60S subunit of the ribosome. This protein was first identified as a target in trichothecene-mediated inhibition in a *Saccharomyces cerevisiae* strain possessing resistance to trichodermin [49,54,136]. The observed trichodermin resistance, as well as resistance to other trichothecenes [25], is believed to be linked to a substitution at a key tryptophan residue at position 255 in RPL3. When mutated to cysteine (W255C), the RPL3 protein remains functional, and has little effect on ribosomal activity, and no inhibition due to the presence of trichothecene compounds is observed [109]. A similar substitution (W258C) in a modified rice *rpl3* gene, was demonstrated by Harris and Gleddie to enable DON-tolerance in transgenic tobacco [62].

However, results presented by Mitterbauer *et al.* [109], who expressed a W258C mutated tomato *rpl3* gene in tobacco, seem to suggest that the copy number of the substituted *rpl3* gene may determine the level of resistance observed. The described tryptophan to cysteine substitutions occur in a universally conserved region of the protein known as the tryptophan-finger (W-finger), which has been shown to play a critical role in coordinating the steps involved in protein translation [62,104]. Of particular interest is its role in the movement of aminoacyl-transfer RNA (aa-tRNA) from the A-site to the P-site during the elongation step of protein synthesis. It is for this reason that this moiety is often referred to as the “rocker switch”. All of these studies suggest that trichothecenes may interact with the ribosome in a stereospecific manner, and that hydrogen-bonding may be of critical importance.

Trichothecenes have also been shown to activate the ribotoxic stress response in eukaryotic cells, which ultimately leads to apoptosis [33,105,166]. Other cytotoxic effects of trichothecenes have been observed, including inhibition of nucleic acid synthesis [100], and cell division [173], destabilization of cellular membranes [120], and inhibition of mitochondrial function [21,117,119]. In all cases the exact mechanism of the described toxicity remains a mystery, due to a lack of understanding regarding the properties of these toxins and how they interact with the cell [127]. Without this knowledge it is difficult to determine the genes which must be targeted in order to confer resistance [101]. Furthermore, it is not known whether these are secondary effects of ribosomal toxicity and/or apoptosis, or if there is a direct interaction between trichothecenes and other components of the cell. The stress response produced within the cell as a result of the inhibition of the 60S ribosomal subunit, could result in downstream inhibition of the remaining cellular machinery. In fact, as mentioned in the previous paragraph, when the tryptophan residue of the W-finger is mutated to another functional residue, a reduction or complete suppression of trichothecene toxicity is observed [25,54,109]. Such effects suggest that the widespread cytotoxic effects of trichothecenes are most likely downstream processes resulting from the inhibition of protein synthesis.

Different trichothecenes have been shown to have different levels of toxicity within a species, and these differences can vary among different organisms. For example, while T-2 toxin was shown to be less phytotoxic than DON [106,143], it has been reported to be roughly ten times more toxic in mammals than the latter [106,153]. Similarly, while DON is generally more phytotoxic than nivalenol (NIV) [42,43,106,143,155], the latter has been shown to be more toxic in mammalian systems [108,153,158]. Variations in trichothecene phytotoxicity may explain, in part, the variations in aggressiveness that can be observed among different trichothecene chemotypes of the *Fusarium* species involved in plant disease [107]. For example, reduced virulence of NIV-producing *Fusarium* species has been observed in FHB, compared with DON producers [43]. It has been observed that C-3 acetylation can reduce phytotoxicity of specific trichothecenes in *Arabidopsis*, *Chlamydomonas*, tobacco and rice [1,110,114]; whereas, in wheat seedling germination and coleoptile growth inhibition studies, DON and 3-O-acetyldeoxynivalenol (3-ADON) were generally shown to be equally phytotoxic [35,106]. Thus, it is difficult to predict how a particular toxin will be tolerated from one species to another. Some studies, particularly those performed by Steinmetz in 2009, indicate that the three-dimensional (3D) structure of a given trichothecene does play a part in the overall toxicity of the toxin [148], and may eventually prove to be a helpful predictor of virulence among individual species.

The differences regarding the involvement of trichothecenes in the transmittance of plant infection may be due, in part, to the differential ability of some plants to metabolize these toxins [16,20,34]. Furthermore, differences in phytotoxicity may also be related to structural differences in the PTC. For example, Mitterbauer *et al.* observed several mutations in yeast RPL3 [109], in addition to W255C, that confer trichothecene resistance. He proposed that the differences observed in toxin resistance among species may be linked to different isoforms of RPL3 among these species.

Furthermore, different trichothecenes have been shown to inhibit different stages of protein translation, including inhibition of initiation (Type I inhibitors), elongation (Type E) or termination (Type T) [24,124,142]. The type of inhibition observed is related to the substitution pattern of the

side chains; for example trichothecenes displaying an oxygen functionality at R3 will typically confer Type I inhibition [44].

The differences in toxicity observed between plant and animal systems may be linked to the cellular uptake of these toxins. To date, no cellular receptors for trichothecene uptake have been identified, and the mode of entry into the cell is unknown. However, it is important to note that trichothecenes are amphipathic molecules [34,157], and it may be possible for these molecules to enter the cell through some mode of direct translocation; therefore, the variable lipophilicity of the toxins would also have an effect on access to the cell. Anderson *et al.* have shown that a decrease in toxicity could be observed for compounds containing more than two free hydroxyl groups [2], suggesting that the more hydrophilic compounds have difficulty crossing the hydrophobic portion of the lipid bilayer of the cellular membrane. If trichothecenes are capable of translocation across the cellular membrane, the architectural and biochemical differences between plant and animal systems, such as lipid composition and the presence or absence of a cell wall would have an impact on their cellular uptake. The action of T-2 toxin on cell membrane function in animal cells has been monitored [21], with the presence of phosphatidylcholine as a membrane constituent influencing the action of T-2 [80]. The general structure of many simple trichothecenes resembles that of cholesterol, and it is possible that toxins, such as T-2, are taken up by the cellular membrane as analogues of cholesterol or plant sterols, leading to disruption of cell membranes in animal and plant cell lines respectively [127].

It has been suggested that it may be possible for several trichothecene toxins to act together, in a synergistic fashion, in order to convey virulence [37]. However, in order to understand and predict how multiple toxins might act synergistically with each other, a comprehensive understanding of the mode of action of a single toxin is of vital importance [37]. Several studies have been conducted *in vitro* that suggest that there is indeed an interactive relationship between trichothecenes [37]; however, studies conducted in this field generally produce varied results [33]. Furthermore, there are various trichothecene-related compounds that, although not toxic in their own right, may act as virulence factors in plant and animal pathogenesis [101,129,161].

The first major structure-activity study of a trichothecene was performed in 1969 by Grove and Mortimer following the initial isolation and characterization of DAS [61]. This study was the first to clearly demonstrate that both the epoxide moiety and the structural arrangement of the ring system were essential features in trichothecene toxicity. Since then most structure-function studies of trichothecenes have focused on defining the substitution pattern that bestows the greatest toxicity towards plant and animal systems, as well as which substituent groups convey higher toxicity to cancer cell lines as compared with host cells in an attempt to develop an effective antileukemic compound [75,76].

Differences in trichothecene structure have been studied in order to determine the effects that substituent groups on the backbone may have on animal and plant toxicity. Studies based on natural trichothecenes have attempted to identify the modifications that convey higher or lower toxicity in plant and animal systems [117,158,166]. However, comparative studies of trichothecene toxicity are limited, primarily due to difficulties in obtaining highly purified samples in quantities sufficient for toxicological assays. The fragmentary studies carried out to date have been performed in different laboratories, using unique assay methods and distinct host organisms; therefore, quantitative comparisons regarding trichothecene toxicity remain circumstantial at best [33].

In a study performed by Anderson *et al.* [2], the structure-activity relationships of natural and synthetic trichothecenes were monitored. Forty-eight compounds, derived from modifications of T-2 toxin and neosolaniol,(NEO) were tested against mouse lymphoma cells for antileukemic properties. It was observed that the toxicity is influenced by modifications at C-3, C-4, C-9 and C-10 [2]. By contrast, changes at C-8 result in minimal changes in toxicity, indicating a region of steric tolerance [2].

In order to gain a better understanding of the toxicological properties of trichothecenes and other toxins, it is important to understand the structural dynamics of these compounds and how they might interact with the cellular environment. To this end, more advanced methods must be used for an adequate study of these compounds. Extensive solution and solid-state NMR studies, as well as

NMR crystallography, to determine trichothecene structure and molecular interactions, in conjunction with biochemical assays to determine specific toxicity towards individual components of the cell, are essential methods for determining the mode of action of trichothecenes.

1.2.2. Methods to Study Structure¹

When trichothecin was first isolated by Freeman and Morrison in 1948 [48], the sophisticated techniques used today to study small molecules were not available. The structure of this compound was not described until 1959 when the Freeman group used a form of chemical modification, to determine the toxin core and substituent groups [47]. Although a valid technique, chemical modification is time-consuming and does not provide information regarding the absolute stereochemistry of a compound. Furthermore, any information regarding the flexibility, electronics, or 3D configuration of the molecule is lost. As fungal fermentation procedures became accessible for the isolation of individual variants, and new techniques in structure determination were developed, it became clear that the family of trichothecenes was quite extensive [106]. Although, mass spectrometry (MS) and Fourier-transform infrared (FT-IR) spectroscopy can offer some insight into the chemical structure of organic molecules [64,70,82], they do not provide a complete picture on their own and merely serves as a piece to the puzzle. Since they are not fundamental to the study performed here, they will not be considered further. Of particular interest to the complete structural identification of trichothecenes is the information made available from X-ray crystallography and NMR, which will be dealt with in detail here. Although X-ray crystallography is an important tool to study structure, it is not the main focus of this study. However, a brief description of X-ray crystallography will be presented in section I in order to describe the limitations of the technique with regards to the sample, which restrict the applicability of X-ray based structural analysis, particularly with respect to the A- and B-type trichothecenes. NMR spectroscopy is the method of choice for this study, and will be described in detail in section II.

I. Crystallography¹

X-ray crystallography is a technique that is unrivalled in the structural detail and accuracy it can provide; thus, it remains a highly valued method in virtually all branches of chemistry and biology. However, as with any technical method, limitations on its application exist, and as such it has not been able to truly become a routine characterization method that is readily accessible to all chemists. Recent advances in instrumentation have assuaged some of these restrictions and as a result it is seeing much wider application to inorganic, organic, biological, and some aspects of materials sciences [103,126].

The X-ray diffraction experiment employs high intensity X-ray beams, which are focused on the crystal. The X-ray irradiation is then scattered by the crystal in a number of specific directions. The resultant diffraction pattern is defined by the electron density of the molecule, and corresponds to the regularly spaced arrays of atoms within the crystal [63]. For each orientation of the crystal, with respect to the incident beam, there is a corresponding diffraction pattern. A series of two-dimensional (2D) diffraction patterns are collected over as many orientations as is practicable, and these are combined into a single 3D working structural model representing the electron density within the unit cell of the crystal. This model is compared with chemical information previously collected from other experiments, which is used to refine and optimize the data in order to obtain the structure of best fit. The structural model is composed of a lattice structure, which is determined by the arrangement of smaller building blocks, known as the unit cell. The unit cell may be composed of several molecules, arranged in various configurations [103].

The quality of the diffraction pattern obtained depends greatly upon the quality of the crystal used, as well as the degree to which the electron density is able to scatter the radiation from the X-ray beams [103]. The latter is mainly a question of the number of electrons present around the atomic species in the lattice; hence, in general, the presence of higher atomic weight species produces better data. The former is the more challenging obstacle. Crystals for X-ray diffraction should be as large as possible to give high quality diffraction data; however, they must also be free from defects. Thus, the crystal should have long range order, with no deviation from the regular pattern due to the

molecular structure and unit cell. Consequently, the best quality diffraction data are those which can be obtained from single crystal X-ray diffraction (SCXRD) analysis.

When considering SCXRD we must first understand that many sources of disorder exist, which are inherent to the crystallization process. These include the coexistence of various crystalline forms, or polymorphism [103]; the inclusion of additional species within the crystal, such as solvent; and motion, such as the libration of some portion of the molecule, or in some cases the reorientation of the entire molecule [63]. Often single crystals of sufficient size cannot be obtained, in which case diffraction measurements must be pursued on powders.

Although unit cell dimensions can be obtained from powders, little structural information is obtained since, in the case of powder diffraction, the three-dimensional data must be projected onto a one-dimensional plane in order to properly map the diffraction pattern [63]. Historically speaking, SCXRD has seen extensive use by inorganic chemists, but as the instruments and crystallization methods improved, organic and biological systems were increasingly investigated. The latter two of course suffer from being composed almost entirely of relatively low atomic weight species, which poses more challenges in obtaining crystals of sufficient quality and size. Furthermore, in organic and biological systems the position of hydrogen atoms is often extremely important to relating structure and function, in particular when we consider the possibility of hydrogen bonding. The lack of electron density surrounding hydrogen atoms limits our ability to accurately predict hydrogen positions, and thus can limit in the utility of the technique. With the emergence of high intensity X-ray sources, and very sensitive array detection, SCXRD of biological macromolecules has become largely a matter of making crystals. However, the question still remains as to how the crystal structure relates to the actual biologically active configuration. These are relatively recent advances; as a result SCXRD did not make a large contribution to the early literature in structural studies of natural products such as the trichothecenes. Today's experimental capabilities do offer a tremendous opportunity to expand the structural understanding of these systems, especially regarding the interaction of trichothecenes with biological systems, such as proteins, DNA and RNA [103].

The main contribution of SCXRD to the trichothecene literature has been the determination of the absolute stereochemistry of the side chains in the macrocyclic, type-D systems. However, the discussion of these systems is beyond the scope of the study presented here, which focuses on the type-A and type-B trichothecenes. A brief review of these systems is presented by Shank *et al.* [140] and the reader is directed there for more information.

Type A and B trichothecenes have seen comparatively little attention in terms of X-ray crystallographic analysis, presumably since more stereochemical variation would be expected in the trichothecene backbone as compared with the sidechain of the macrocyclic systems. The structural determination of DON was attempted on several occasions [59,60] however, crystals of sufficient quality could not be obtained. In contrast, suitable crystals for 3-ADON were acquired in 1984 by Greenhalgh *et al.* [59], and a high resolution crystal structure was obtained. It was determined that the absolute configurations of the backbone carbons were essentially identical to those found in verrucarín A by McPhail *et al.* [102], which was determined to adopt the same absolute configuration of the trichothecene core as that described by Savard and Blackwell [135], where the rings of verrucarín A were shown to exist in a half-chair for the A-ring, a chair conformation for the B-ring, and the C-ring exists in an envelope configuration. The unit cell for 3-ADON was shown to be composed of layers of four molecules arranged in tetrameric rings along a 4-fold rotation axis. The centers of the tetramers form channels large enough to include solvent, which accounted for the different crystal forms observed when 3-ADON is recrystallized from different solvents. A significant number of disordered water molecules were shown to be included in the crystals in the aforementioned channels. In a second failed attempt to obtain DON crystals suitable for SCXRD, Greenhalgh and coworkers were able to discern that at least two forms of DON existed, which differed in the degree of water inclusion [60].

In 1990, Gilardi *et al.* performed an SCXRD study on T-2 Toxin [52], and again the stereochemistry of the rings were found to be identical to that of verrucarín A [102]. The unit cell for T-2 toxin contains two distinct molecules differing in the configuration of the isovalerate sidechain. The relatively large thermal-ellipsoid obtained for the atoms in the sidechains as opposed to those in

the core, testify to a significant degree of disorder [52]. Also, hydrogen bonding was observed involving O-1 and O-2, which were shown to donate into the hydroxyl hydrogen at C-7 [52].

X-ray crystallographic analysis can also be applied to trichothecenes complexed with interacting proteins. Garvey *et al.* studied the structure and function of the enzymes trichothecene 3-O-acetyltransferase (TRI101) from *F. graminearum*, and trichothecene 15-O-acetyltransferase (TRI3) from *F. sporotrichioides* [50,51]. These enzymes are directly responsible for the conversion of DON to 3-ADON and 15-ADON, respectively. TRI101 was complexed with acetyl-Coenzyme A (CoA) and DON together, as well as with T-2 toxin and CoA [51], and TRI3 in complex with decalonectrin and DON [50], were studied. Although these studies were focused primarily on the X-ray crystal structure of the protein, information regarding the trichothecene binding site for both TRI101 and TRI3 were unambiguously identified. The determination of the structural dynamics of the trichothecene class of toxins becomes important when considering how such binding interactions occur.

II. Nuclear Magnetic Resonance Spectroscopy

Although X-ray crystallographic analysis is, by and large, the most desirable method for determining structure, not all compounds are amenable to such an analysis. Many members of the class of trichothecene mycotoxins cannot be analyzed by SCXRD, because they do not produce pure crystals, due to factors such as polymorphism, solvent inclusion and molecular libration [63]. As a result, NMR spectroscopy is the principal technique used in the determination of the structure and stereochemistry of trichothecenes, with over 90% of trichothecenes being characterized in this manner. Extensive reviews regarding the characterization of trichothecenes and trichothecene-related compounds were published by the Miller group in the late 1980s [13,55,57,60,86], and by Jarvis *et al.* for the macrocyclic trichothecenes in 1987 [73]. The reader is directed to these works for more information regarding the structural parameters of these compounds.

1.3. Nuclear Magnetic Resonance

NMR spectroscopy is a method for determining the physical properties of a compound, based on the exploitation of the magnetic properties of certain atomic nuclei in a given sample. Discovered simultaneously in 1946 by the independent laboratories of Felix Bloch and Edward Mills Purcell, NMR has become a powerful tool for the determination of chemical structure and dynamics [14,125]. The determination of structure of the majority of organic, biological, as well as numerous inorganic compounds, often begins with a series of NMR experiments. Since its discovery, NMR has undergone a series of advances, including the application of Fourier transformation (FT), the development of multi-dimensional techniques, high-field magnets and polarization transfer techniques, resulting in high-resolution structures rivaling those produced by X-ray crystallography.

An introduction to the physical science and basic principles necessary for the understanding of NMR is available in textbooks such as Levitt or Silverstein [91,144]. The wave function and Hamiltonian are used to describe some of the key differences between solution and solid-state NMR theories, and a more in depth picture is provided in the principles described in the Hamiltonians of NMR series [145].

1.3.1. Solution-State NMR

Solution-state NMR has been widely utilized as an identification tool for the trichothecenes and other natural compounds. It is used here as a tool to probe into the overall three-dimensional structure and dynamics of the trichothecenes. Specifically, addition of information to the literature database for the trichothecenes, including information for the carbon-13 and multi-dimensional NMR experiments, is made. As well as information arising from deuterium exchange experiments.

I. ^{13}C NMR

The inherent receptivity of the ^{13}C nucleus is rather low for two reasons: the low natural abundance of the nucleus in non-isotopically enriched samples; and the moderate gyromagnetic

ratio, γ . It is important to note here that the sensitivity is not precisely related to γ , but rather on the cube, γ^3 , since the signal produced at the coil depends upon several factors, including

- i) The magnetic moment, μ_0 , which is proportional to γ
- ii) The rate of change of flux in the coil, which is dependent of the Larmor frequency of the nucleus, which is proportional to γ
- iii) And finally, the population difference between the spin states, also proportional to γ .

There is also a minor contribution from the noise, which increases with frequency, and is thus also proportional to γ .

Since, ^{13}C nuclei have more electron density than ^1H , the typical spectral width is approximately 220.0 ppm, so the signals are generally better resolved than those of ^1H , and there is relatively little interference from homonuclear coupling in signals collected at natural abundance. Furthermore, as discussed in the previous section, heteronuclear scalar couplings can be removed from the spectrum through broadband decoupling methods. Although, some information is lost in the ^{13}C spectrum due to decoupling, it reduces the complexity of the spectrum significantly, and provides much better signal-to-noise, allowing for the spectrum to be collected in a much shorter time frame.

The ^1H -decoupled ^{13}C spectrum is a simple modification to the single pulse NMR experiment; however, as mentioned there are many modifications to one-dimensional NMR that exist. Among the most common are the INEPT and DEPT experiments, which are described in detail below.

The Insensitive Nuclei Enhancement by Polarization Transfer (INEPT) experiment is a method for transferring strong nuclear magnetization from high receptivity spins to spins with lower receptivity (i.e. ^1H to ^{13}C), for which the pulse sequence is shown in figure 1.4A [91]. Polarization transfer gets past the lower sensitivity issues resulting from a lower gyromagnetic ratio. After polarization transfer has occurred, the magnetization of the lower receptivity spin, ^{13}C , now depends of the γ of ^1H . Furthermore, the relaxation delay, T_1 for the experiment is now dependent on the relaxation of the ^1H spins, and can be set accordingly. Thus, not only is signal enhancement possible,

but the acquisition time for the experiment decreases significantly. However, both in-phase and anti-phase peaks are present in the spectrum. The anti-phase peaks may be brought back into phase by adding a refocusing pulse to the spectrum; thereby, preventing the loss of signal in crowded ^{13}C spectra, see figure 1.4B.

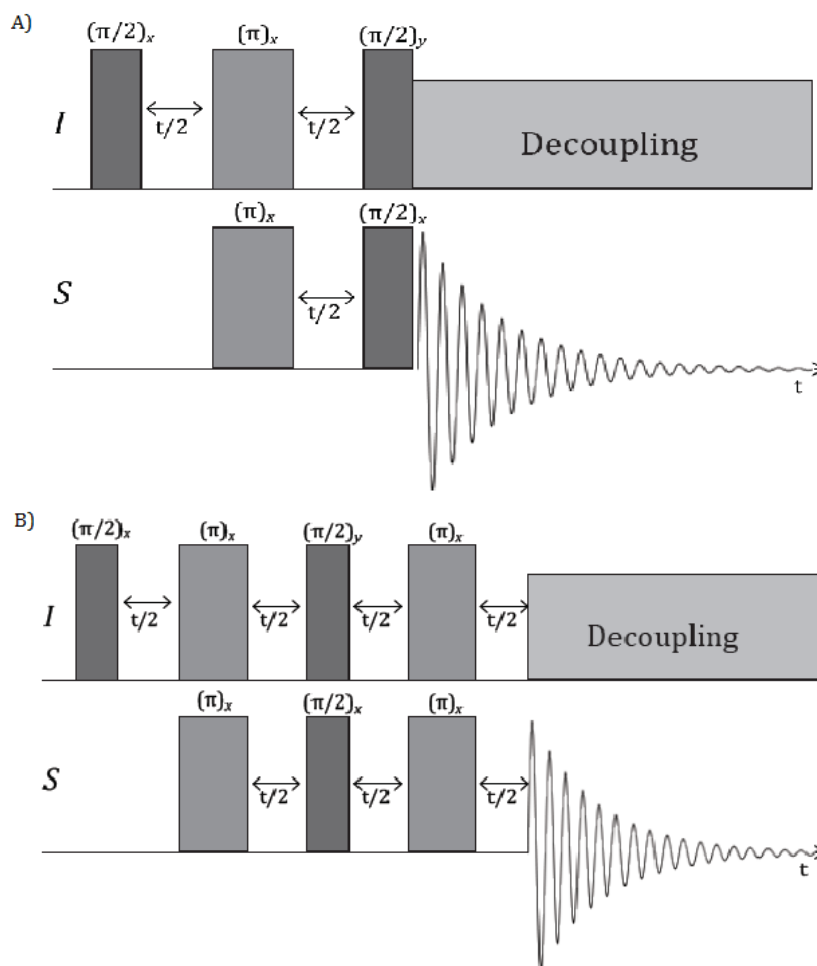


Figure 1. 4: Pulse schemes for the A) INEPT and B) Refocused INEPT experiments. These experiments rely on the transfer of polarization from a higher sensitivity nucleus, such as ^1H , to a lower sensitivity nucleus, such as ^{13}C . The *I* channel represents the former, while *S* the latter. The *I* nucleus is flipped into the transverse plane through the application of a $\pi/2$ -pulse, and then the polarization is transferred through the simultaneous application of a π -pulse on both nuclei. The *I* nucleus is decoupled, and detection occurs on the *S* channel.

The Distortionless Enhancement by Polarization Transfer (DEPT) experiment is a sequence which is closely related to the refocused-INEPT experiment [88]. However, the DEPT experiment works on the generation and manipulation of multiple quantum coherences, rather than single

quantum coherences. The pulse sequence is given in figure 1.5. Since we are working with the concept of polarization transfer over single-bonded systems, quaternary carbons will be absent from the spectrum, as is also the case in the INEPT experiment. As such, these techniques are meant to be utilized in addition to routine ^{13}C spectra, and not in place of it.

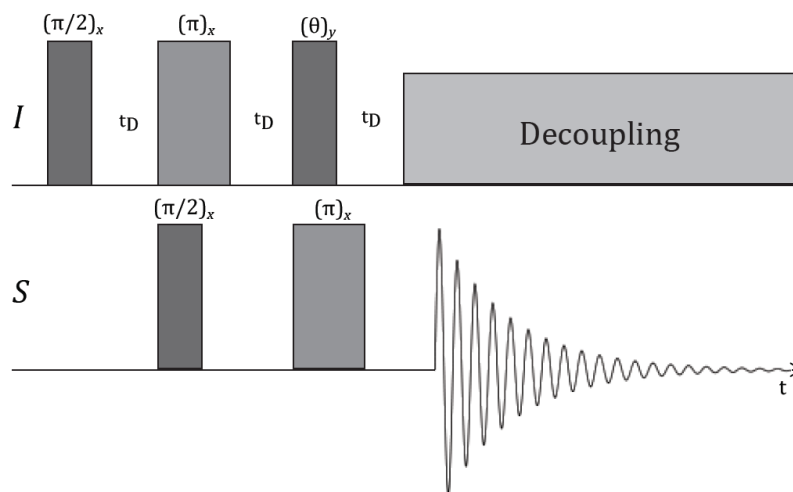


Figure 1. 5: Pulse Scheme for the DEPT experiment. The DEPT experiment also relies on Polarization transfer from a higher sensitivity nucleus, I , to a lower sensitivity nucleus, S . The I nucleus is flipped into the transfer plane by a $\pi/2$ -pulse, and then polarization is transferred through a π -pulse on the I nucleus and simultaneous $\pi/2$ -pulse on the S nucleus. The third pulse in the sequence on the I nucleus is determined by the setting of the angle θ , which is typically set to either $\pi/4$, $\pi/2$, or $3\pi/4$, which produces different effect on the phase of the S signals in the spectrum depending on how many I nuclei are directly attached. The phase modulation behavior is depicted in figure 1.25. Decoupling is applied on the I channel while the signal from the S channel is detected.

The intensity of the signals from methine, methylene and methyl carbons, have differential dependence on the width of the θ pulse, which can be seen in figure 1.6, and it is for this reason that DEPT is usually performed as a sequence of experiments where θ equals $\pi/4$, $\pi/2$ or $3\pi/4$.

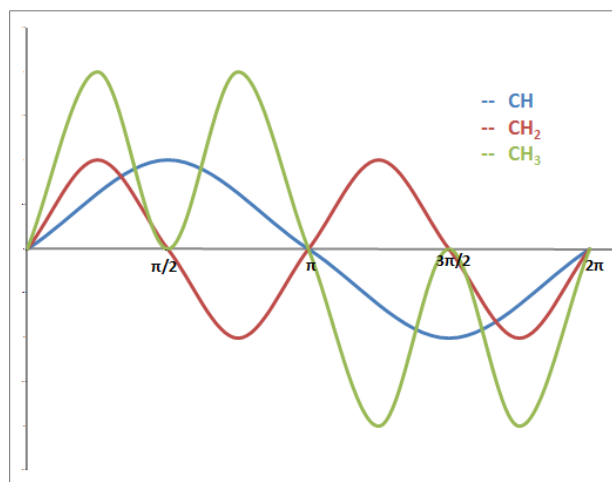


Figure 1. 6: Phase modulation of methine, methylene, and methyl signals under the influence of the DEPT pulse sequence

From figure 1.6, certain interesting properties of the sequence are revealed, and include that

- i) Methine and methylene groups have a maximum intensity when $\theta = \pi/4$, but are null when $\theta = \pi/2$
- ii) Methine intensity is maximal at $\theta = \pi/2$
- iii) Methylene groups are anti-phase when $\theta = 3\pi/4$, but methylys and methines will be in-phase.

II. Deuterium Exchange

The chemical and dynamic exchange processes which may occur in a given sample can broaden the spectral lines, particularly in ^1H NMR spectra. Thus, it may be difficult to extract information from the system without moving to a different NMR solvent, or alternatively by freezing out the process and collecting spectra at a variety of temperatures. However, an advantage of chemical exchange, with regards to ^1H species, is the ability, in most cases, to exchange with water. An easy solution to the problem is the addition of a small amount of D_2O to a sample, resulting in an exchange of the ^1H to a ^2H nucleus. Since the magnetic properties of the ^2H nucleus are vastly different from those of ^1H (i.e. gyromagnetic ratio, quadrupolar), the ^2H nucleus is not observed when ^1H is detected, and the chemically exchangeable signal disappears.

This method is widely used in protein NMR, since it allows the detection of surface exposed amino acid residues, and will provide residue-specific information, particularly in multi-dimensional NMR spectra. For small molecules, such as trichothecenes, deuterium exchange NMR can be used to determine whether a water molecule is bound somewhere on the molecule, or whether it is freely exchanging not only with the molecule in question, but other water molecules which may be free in solution. Furthermore, since the exchange between ^1H and ^2H occurs very rapidly, on the picosecond timescale, it may be possible to determine the rate of exchange between a bound water molecule and the solvent, providing a rough estimate for binding efficiency of the molecule with water.

Deuterium Exchange is a method that can be used in combination with a large number of NMR experiments, and is thus a powerful technique which can assist in structure determination.

III. Multi-Dimensional Solution-State NMR experiments

As multiple-pulse based experiments have preparation, evolution and detection stages, where the final detected spectrum depends primarily on the nature of the preparatory pulse and the length of the evolution time. Those factors that influence the magnetization during the evolution period are quite different from those that influence it during acquisition. In this fashion two very different sets of spectroscopic data can be obtained, and thus, the NMR experiment can be extended to multiple dimensions.

Two-dimensional (2D) NMR techniques use a second FT to convert the time-dependence of the evolution into a second frequency, pulling the familiar one-dimensional spectrum into a second dimension, where it is displayed as a contour plot of intensities. Multi-dimensional NMR experiments require a minimum of two pulses, and as the experiment is repeated, the pulse sequence is varied, either through variation in the pulses themselves, a variation in a particular time period, or both. For a two-dimensional experiment at least one time-period will be varied, for three dimensions, two time periods must be varied, and so on.

Many 2D techniques are similar to their one-dimensional (1D) analogues, and so the same methodology will be used to describe the interactions, where possible.

i. Heteronuclear Correlation Experiments

Heteronuclear Correlation methods provide information about the coupling between individual nuclei of different types (i.e. ^1H to ^{13}C correlations). As described previously, the resultant spectrum is a contour map, and here the contours simultaneously describe the chemical shifts of a proton and the carbon to which it is coupled. Such spectra are commonly used to assign the ^{13}C , or other heteronuclear signals, to a corresponding ^1H .

Heteronuclear Single Quantum Correlation (HSQC) spectroscopy is the 2D equivalent to the INEPT sequence described previously [88]. HSQC uses the single quantum coherence transfer between ^1H and ^{13}C to provide information regarding single bond couplings; thus, only ^{13}C nuclei that are directly bound to a ^1H resonance will display a contour in the spectrum. As in INEPT, the experiment works by developing a magnetization on the stronger nucleus, denoted *I* (typically ^1H), and the transferring the magnetization to the *S* nucleus (typically a heteroatom such as ^{13}C or ^{15}N). The magnetization is then allowed to evolve before it is transferred back to the *I* nucleus for detection. Detection occurs on the *I* nucleus in order to increase the sensitivity of the experiment, and allows for the more receptive nucleus to be finely digitized during FT, which is particularly important when dealing with a crowded ^1H spectrum. This is known as reverse detection. The pulse sequence is described in figure 1.7.

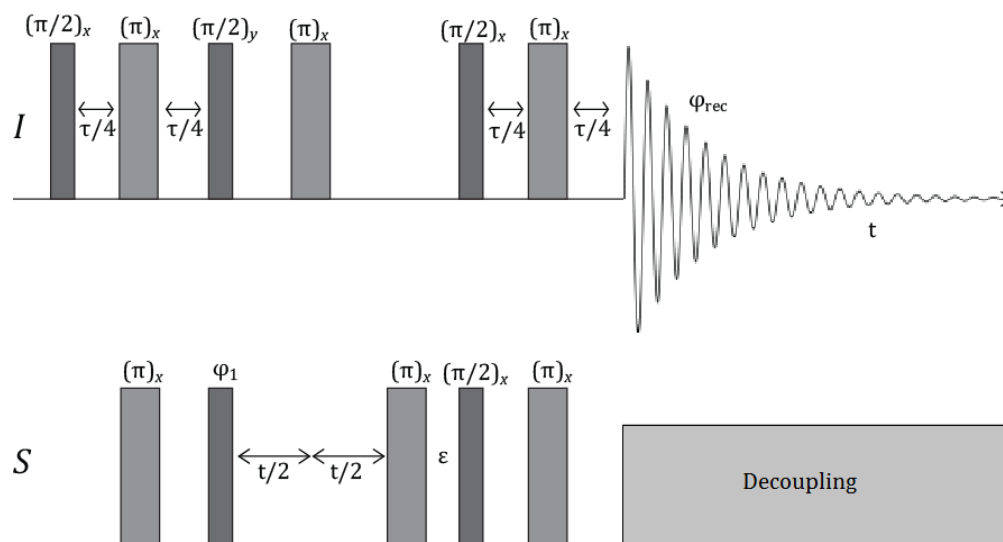


Figure 1. 7: Pulse scheme for the HSQC experiment. The *I* channel represents the nucleus with the higher sensitivity, and is the one on which the signal is detected in order to provide a high resolution spectrum. The *S* channel is typically a species with lower sensitivity, and must be directly bound to the nuclei represented by the *I* channel. Decoupling occurs on the *S* channel in order to reduce the complexity of the spectrum and provide a slight enhancement in the signal due to the effect of the NOE.

A modification on this experiment is the Heteronuclear Multiple Quantum Correlation (HMQC) experiment [88], which contains half the amount of pulses as HSQC, and delivers a virtually identical spectrum; however, it does have a slight reduction in the resolution for the *S* nucleus, and thus tends to find less application. Heteronuclear Multiple-Bond Correlation (HMBC) spectroscopy is similar to the HMQC experiments, but allows for the coupling to be extended over two to four bonds. The defocusing of the longer range coupling in the HSQC and HMQC spectra is governed by the delay time; therefore, by omitting one of the delays in the HMQC experiment, the long range coupling is reintroduced. The pulse sequences for HMQC and HMBC are shown in figure 1.8. Thus, by combining the HSQC and HMBC experiments it is possible to distinguish between ^{13}C nuclei coupled to protons through HSQC, and subsequently assign the quaternary carbons, using HMBC.

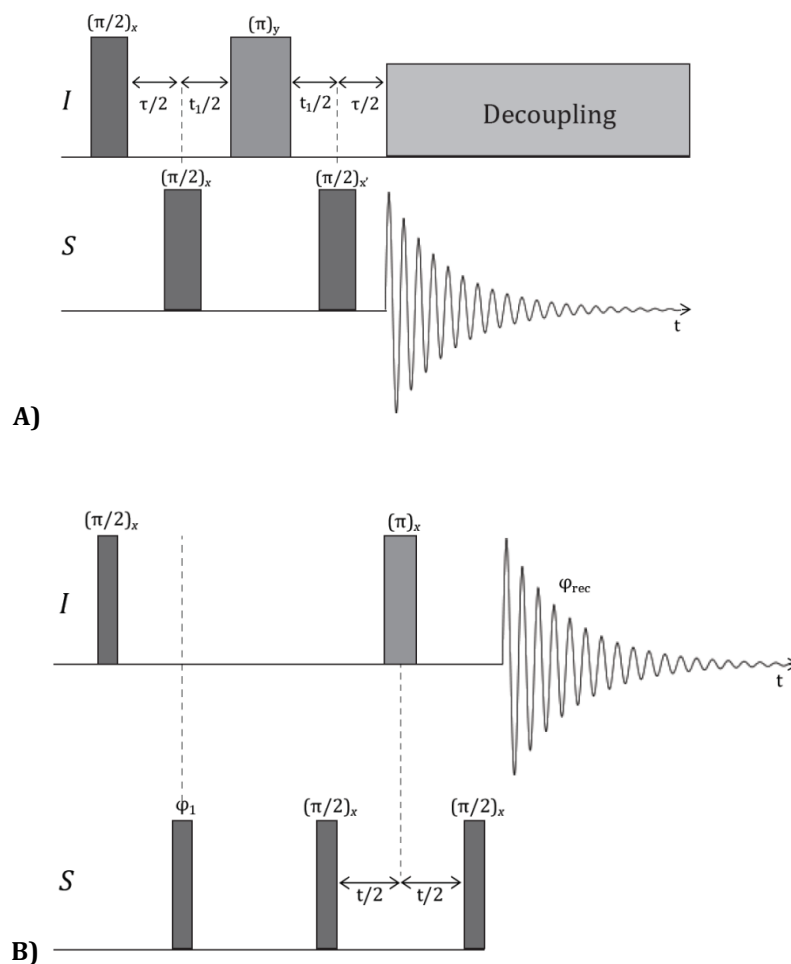


Figure 1. 8: Pulse Scheme for the A) HMQC and B) HMBC experiments. The HMQC experiment provides direct coupling correlations between the I and S nuclei; whereas, the HMBC experiment provides information regarding the coupling of the I and S nuclei over several bonds.

ii. Homonuclear Correlation Experiments

The first 2D NMR experiment was proposed in 1971 by Jean Jeener, and later implemented in 1976 by Richard Ernst, who was awarded the Nobel Prize in Chemistry for his description of the through-bond J-coupling modulated Correlation Spectroscopy (COSY) experiment [88]. COSY is the homonuclear equivalent of the heteronuclear correlation methods mentioned above, having a similar pulse sequence and mechanism of magnetization transfer.

In the standard COSY experiment, the preparation and mixing period are governed by $\pi/2$ -pulses separated by an evolution period, and followed by signal acquisition, the sequence is shown in figure 1.9. Since COSY is a homonuclear technique, the resultant contour plot is symmetrical about a diagonal axis, where the peaks along the diagonal are autocorrelation peaks (the nucleus exchanges with itself), and the off-diagonal peaks are correlations between coupled nuclei. Since the peaks in the spectrum represent nuclei that are coupled through bond, the COSY spectrum allows for a simple method for assigning the peaks corresponding to individual nuclei in a sample, and aids in determination the J-coupling constants for a given spin system.

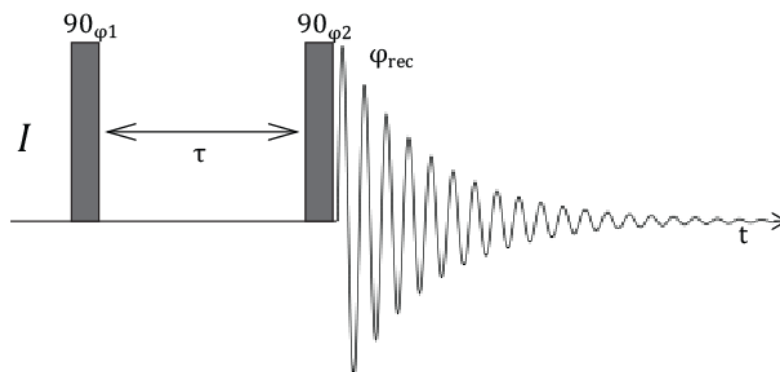


Figure 1. 9: Pulse scheme for the phase sensitive COSY experiment. The relatively simple COSY experiment is a homonuclear coupling method; thus, only a single channel is required to be pulsed on and detected. Only two $\pi/2$ -pulses are used, but have different phases which are cycled through to ensure proper phasing in the final spectrum. The primary, high resolution dimension of the spectrum is collected during the acquisition of the FID. The evolution of the magnetization during the τ time delay is also collected and makes up the second dimension, but has significantly reduced resolution as compared to the primary dimension.

iii. Nuclear Overhauser Enhancement (NOE) Spectroscopies

Through-space correlation methods offer an ability to observe the dipolar couplings between nuclei that are physically close, but may not necessarily be coupled to each other through bonds. Due to the Brownian motion of the solvent, small molecules in the solution state, in general, do not exhibit dipolar couplings. However, nuclei that are significantly proximal to each other (within 5 Å) will cross-relax with each other, and as a result, can transfer polarization to each other. Any

process that induces a change in the polarization of one spin will lead to an NOE in a nearby spin, and as seen previously, this effect is exploited in the ^1H decoupled ^{13}C NMR experiment. However, steady-state NOEs are produced in through-bond coupled systems through the irradiation of one spin and subsequent polarization transfer; whereas, NOEs in through-space systems are transient, and build up over time as a result of cross-relaxation between the spins, reaching a maximum after one T_1 period, and subsequently declining.

In essence, the Nuclear Overhauser Effect Spectroscopy (NOESY) experiment is simply an extension of the COSY experiment [88], the exception being that in the NOESY experiment, transient NOEs are allowed to build up and evolve over time τ , and a final $\pi/2$ pulse is applied to refocus the magnetization prior to detection. The pulse sequence for the NOESY experiment is depicted in figure 1.10.

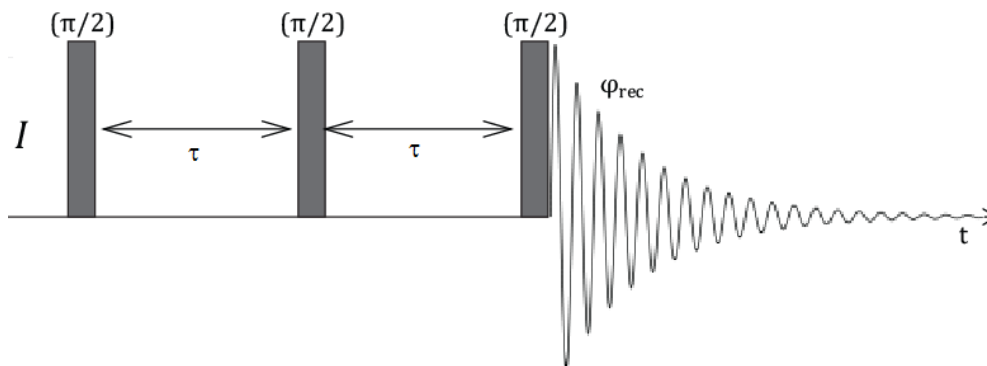


Figure 1. 10: Pulse scheme for the NOESY experiment. Like the COSY experiment, the NOESY experiment is a homonuclear correlation method; thus, only one channel is required for pulsing and detection. The primary dimension is evolved during the FID, and produces a high resolution spectrum. The secondary dimension is collected during the time period τ , and is of lower resolution than the first. Varying the time period τ , allows for different transient NOEs, or through-space couplings, to take precedence in the spectrum.

As with COSY, NOESY is a homonuclear spectroscopy, and both axes in the spectrum are identical; therefore, the spectrum is symmetrical about the diagonal, with peaks appearing on the diagonal being autocorrelation peaks. When the NOESY spectrum is properly phased, the diagonal peaks appear negative due to autocorrelation. NOEs that appear off of the diagonal can appear either positive or negative. For small molecules, positive NOEs denote a first-order correlation, and thus, indicate a coupling interaction between the spins. However, recall that T_1 relaxation is correlated to the correlation time, and consequently, the size of the molecule. As molecular size, or the viscosity of the solvent, increases the T_1 relaxation crosses a zero-point; thus, for larger molecules, NOEs may appear negative despite the nucleus possessing a positive γ . It is also important to note that since the NOESY experiment is merely an extension of COSY, COSY crosspeaks will also appear in the spectrum due to J-coupling; however, these can be effectively removed by introducing small random variations in the τ period.

Exchange Spectroscopy (EXSY) is a specialized form of the NOESY experiment [88] that requires no modifications to the original pulse sequence with the exception of the variation to the time period τ . Crosspeaks in the NOESY spectrum which result from chemical or conformational exchange appear negative, regardless of the sign of the gyromagnetic ratio. Therefore, in order to distinguish between EXSY and NOESY peaks, the experiment must be phase-sensitive. The EXSY experiment is generally much more quantitative, and can be used to determine the rate of exchange of two or more nuclei, through the subsequent collection of numerous NOESY spectra at varying mixing (τ) times.

However, it is important to note that not all negatively phased peaks are true exchange peaks. Often saturation transfer peaks can be mistaken for EXSY peaks, as these may also appear as negative peaks in the spectrum. Saturation transfer occurs when the rate of exchange, k_{ex} , is greater than the longitudinal relaxation rate, T_1 , such that $1/T_1 < k_{ex}$. However, if the rate of exchange is slow compared to the relaxation, such that $1/T_1 > k_{ex}$, then saturation transfer is not possible, and all off-diagonal negatively phased peaks are a result of chemical exchange.

1.3.2. Solid-State NMR

The study of nuclear interactions through NMR spectroscopy provides a wealth of information about the chemical system; however, when several inequivalent sites exist in a solid-state sample, powder patterns may overlap, and the consequent loss of resolution in the spectrum obscures any information that the spectrum may contain. Hence, it is necessary to apply techniques to achieve high-resolution in spectra.

I. Magic-Angle Spinning (MAS)

Magic-Angle Spinning (MAS) is a mechanical technique which is routinely used in solid-state NMR experiments where it is desirable to remove the effects of CSA and heteronuclear dipolar coupling. MAS can also be used to narrow the lines from quadrupolar nuclei, and is increasingly used to remove the effects from homonuclear dipolar coupling. However, for the latter application, the use of extremely high spinning rates is required; therefore, it is not currently routine in the majority of laboratories.

In solution-state NMR, the effects of CSA and dipolar coupling are rarely observed, since the rapid tumbling of molecules in solution results in an averaging of the orientation, θ , for the CSA and dipolar tensors, over all possible values. Thus, the $(3\cos^2\theta - 1)$ dependence of the transition frequencies becomes zero. MAS achieves the same effect for solids.

Let us consider a sample spinning about an axis inclined at an angle, θ_R , to the applied field, with θ describing the orientation of the interaction tensor for the molecules within the sample, which varies with time as the sample rotates. Thus the average for $(3\cos^2\theta - 1)$ is given by,

$$(3\cos^2\theta - 1) = \frac{1}{2}(3\cos^2\theta_R - 1)(3\cos^2\beta - 1) \quad (1.1)$$

The angle β is between the principle z-axis of the interaction tensor and the spinning axis, which is fixed for a given nucleus in a rigid solid; however, θ will take on all possible values in a powder sample and represents the anisotropy. The angle θ_R is set by the experiment. If the angle θ_R is set to 54.74° , then $(3\cos^2\theta - 1) = 0$, and the anisotropy is averaged to zero.

II. Cross-Polarization (CP)

Cross-Polarization (CP) is a commonly employed technique in NMR, which is used to enhance the signal of low natural abundance nuclei. The direct observation of low natural abundance nuclei has two main problems: i) the dilute nature of the spins results in a rather low signal-to-noise ratio, which can make the detection of individual signals rather difficult; ii) the relaxation times for dilute spins tends to be rather long, because the strong homonuclear dipolar coupling which generally contributes to relaxation are absent. When many scans are required to obtain adequate signal-to-noise, long relaxation times result in long experimental times, which is not practical. These problems can be solved by transferring the magnetization from an abundant, high gamma spin (i.e. ^1H) to the low abundance nuclei in a sample.

III. Multi-Dimensional NMR in the Solid-State

Many of the same 2D techniques available for solution-state NMR spectroscopy have solid-state counterparts which are modified in order to provide high resolution spectra. Furthermore, since solid-state NMR spectra contain information regarding CSA, heteronuclear and homonuclear dipolar coupling, and J-anisotropy. In order to understand the information being provided by these interactions, specialized 2D techniques are available. In some cases, multiple conformations can exist simultaneously in the solid-state spectrum, and 2D homonuclear NMR techniques are required to unambiguously assign the signals.

Multi-dimensional NMR experiments in the solid state are often more complex than their solution counterparts. These experiments often involve CP, MAS, and in some cases synchronization of the rf-pulses with the rotation of the sample by MAS.

i. Incredible Natural Abundance Double Quantum Transfer Experiment (INADEQUATE)

The incredible natural abundance double quantum transfer (INADEQUATE) experiment is a well-known solution-state experiment based on the same principles as the INEPT experiment[89],

but extended to a second dimension. The INADEQUATE experiment can thus be used to obtain direct scalar connectivities in the carbon backbone, and has been adapted here for the solid state. The traditional experiment yields signals that are anti-phase, and are not of much use in crowded ^{13}C spectra, or spectra where significant linewidths can result in interference and cancellation of lines within the spectrum [89]. As a result, it is desirable to refocus these anti-phase lineshapes, in order to obtain high-resolution in-phase signals, which can then be interpreted appropriately. The refocused INADEQUATE experiment is simple and robust, with the efficiency of this experiment depending primarily on the refocused line width, which corresponds to the dephasing time [89].

The pulse sequence for the CP-Refocused INADEQUATE experiment is shown in figure 1.11, [89,90]. The ^{13}C magnetization evolves under the isotropic homonuclear scalar coupling Hamiltonian for a period of 2τ , where $\tau = \frac{1}{4J}$. The homonuclear dipolar couplings for ^{13}C - ^{13}C are removed with fast MAS, and a 180° pulse allows for efficient refocusing of the ^{13}C chemical shift. A 90° pulse then converts the magnetization into a double quantum coherence, which is allowed to evolve over a period of t_1 . The anti-phase component is detected during t_2 and is converted back to an in-phase coherence during a second τ - π - τ delay, prior to detection.

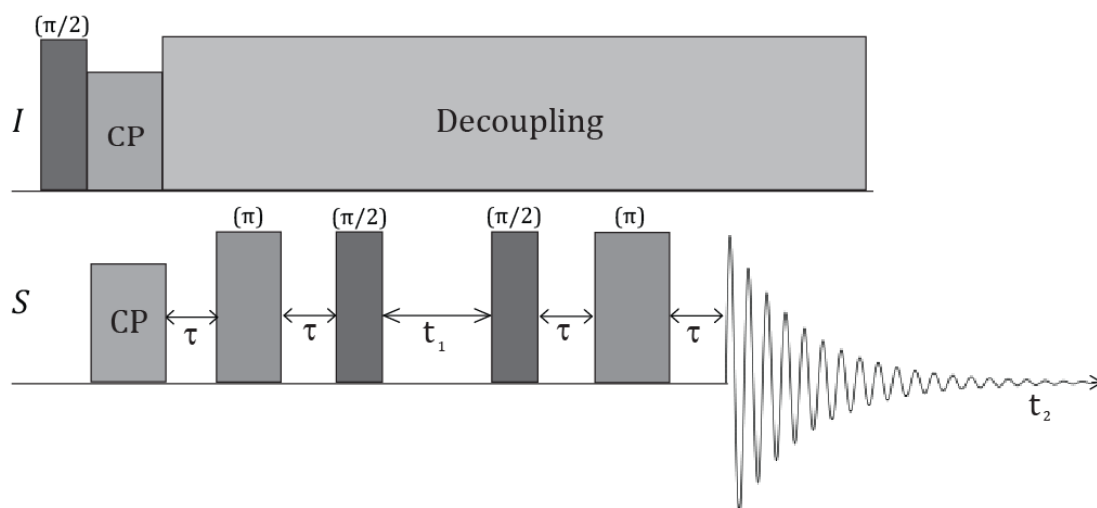


Figure 1. 11: Pulse sequences for the CP-refocused INADEQUATE experiments. t_1 produces the indirect dimension for the two-dimensional spectrum, and t_2 produces the direct dimension.

ii. R-symmetry based CSA Recoupling

Much of modern solid-state NMR is based around the concept of physical manipulation, either through

- i) the rotation of a sample in space. Typically samples are spun at a fixed frequency about some fixed angle; however, some experiments do involve the use of more complex trajectories.
- ii) The rotation of the nuclear spin. Rotation of the nuclear spin polarization is achieved through the application of rf-pulses.

As these two techniques developed, the spatial and spin manipulations were often treated separately, with rotation of the sample by MAS treated as a minor perturbation as compared to the effects resulting from the application of rf-fields.

The term “recoupling” is meant to signify the reintroduction of specific interactions, such as dipolar coupling, or CSA, by counteracting the averaging effects introduced by sample rotation about the magic angle. In order to accomplish such recoupling effects, it is necessary to select an rf amplitude so that the frequency of magic angle rotation is a small integer multiple of the nutation frequency of the nuclei under the rf field; this is a condition known as rotational resonance [92]. Considering the reintroduction of the CSA, the rotational resonance condition is met when the nutation frequency for spin I, ω_{nut}^I is equal to $n\omega_r$, where n is an integer value, and ω_r is the rotation frequency of the sample, or MAS spin rate. Under this condition, the terms in the Chemical Shift Hamiltonian are reintroduced.

The symmetry-based pulse sequences designed by Malcolm Levitt exploit these rotational properties of the nuclear spins through the rotor synchronization of specialized pulse schemes [92]. The *R*-symmetry sequences are simple and robust techniques based on 180° rotational elements. The theory behind this technique is based primarily on the spherical tensor theory, and is rather involved; thus, only a simple explanation is provided here.

The R -sequence is a general format, and describes a class of symmetry-based sequences, which are collectively defined by the symbol RN_n^ν . The integers N , n , and ν , are called the symmetry numbers. A set of selection rules exist for the entire class of R -sequences, which can be used to manipulate the average Hamiltonian, generating decoupling and recoupling properties for the individual nuclear spin interactions [92].

The general scheme for constructing an R -sequence based on the Euler angle symmetries is as follows:

- 1) Select a sequence of rf-pulses that result in the rotation of the nuclear spins through 180° about the x -axis, this is element \mathcal{R} .
- 2) Alter the signs of all rf phases within the element \mathcal{R} . Call this phase-inverted element \mathcal{R}' .
- 3) Select an rf amplitude such that N elements of \mathcal{R} occupy n rotor periods. For R -sequences, N must be even, in order to maintain the symmetry.
- 4) The sequence must consist of $N/2$ elements of $(\mathcal{R}_\varphi \mathcal{R}_{-\varphi})$, where φ is the overall phase shift, and is equal to $\pi\nu/N$ radians.

A simple diagram depicting the principles behind this process is shown in figure 1.12.

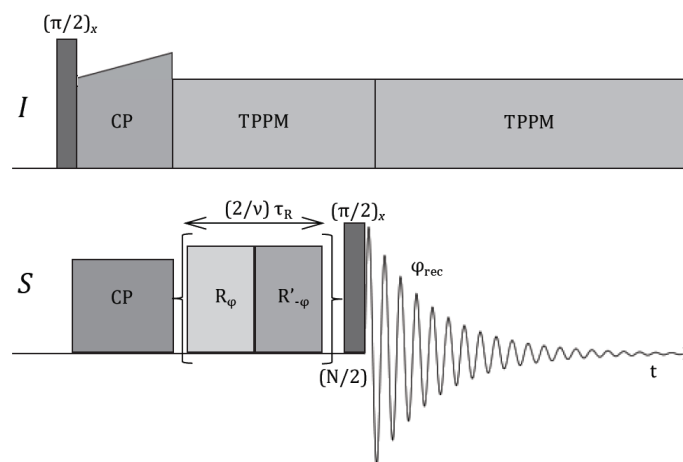


Figure 1. 12: A general pulse scheme for an R -based symmetry sequence. Two-pulse phase-modulated (TPPM) decoupling is suggested for use with this method.

Each of the rotational components of the average Hamiltonian are modulated by the spatial rotations of the sample, as well as the rotations of the spin polarizations induced by the application of rf-pulses. Thus, by synchronizing the modulations, symmetry properties result, leading to some selection rules on the terms in the average Hamiltonian. A Spin Space Selection (SSS) diagram can be constructed for any set of symmetry properties based on the quantum numbers applicable for each of the interactions of the Hamiltonian. Consider the SSS diagram in figure 1.13, which has been constructed for the $R18_2^5$ symmetry sequence.

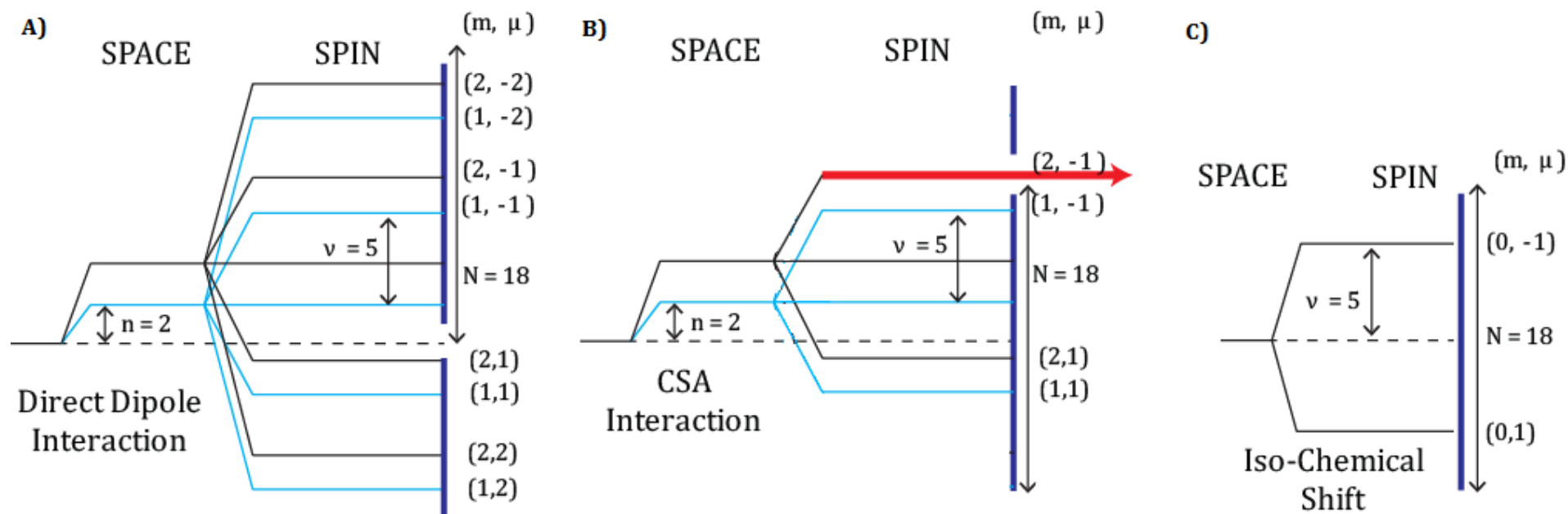


Figure 1.13: Spin-Space Selection (SSS) diagrams for R-symmetry sequence $R18_2^5$. A) The SSS pathway for the dipole-dipole interaction. B) The SSS pathway for the CSA interaction. C) The SSS pathway for the isotropic chemical shift interaction. Only the CSA interaction is allowed under the conditions of the $R18_2^5$ symmetry-sequence.

Thus, it can be said that the $R18_2^5$ symmetry sequence is used to recouple the CSA interactions, and is compensated to first order for the homonuclear dipolar couplings and isotropic chemical shifts.

1.3.3. NMR Spectral Parameter Simulations

Once the NMR experiment has been performed the data must be carefully analyzed in order to pull out the information contained in the spectrum. Simulation of the NMR parameters is a useful technique, where the analyst attempts to reproduce the experimental spectrum by manipulating the values expected for each of the interactions in the Hamiltonian. A variety of computer programs can be used to manipulate the spectra, and greatly simplify the guess work required by allowing simple parameters, such as chemical shift and scalar coupling constants to be entered.

Computer-based NMR prediction and experimental simulation programs are very useful in helping to accurately solve spectra. This study utilizes the programs SpinWorks to gain information about the chemical shift, J-coupling for different individual experiments based on the spin system [97].

SpinWorks is software program developed by Kirk Marat at the University of Manitoba, and is used primarily as an easy to use, basic, offline processing program for one-dimensional and two-dimensional NMR spectra. However, it also serves as a powerful iterative tool for the simulation and analysis of highly complex second-order spectra, which can also be used for dynamic NMR analysis. SpinWorks can also be used to solve some solid-state NMR spectra; however, its strength lies in the simulation of solution-state NMR spectra. SpinWorks works on the basis of assigning each individual transition expected for each nucleus in the spectrum and then works to optimize the spectrum based on the user directed parameters which have been entered.

The input into the program includes the spin system, chemical shifts for each individual resonances, and scalar couplings between the resonances. The user may also choose which parameters are allowed to be varied during the optimization process. Once the user has inputted all of the variables into the program a simulated spectrum is generated. The user then assigns each individual transition in the simulated spectrum to the corresponding signal in the experimental spectrum. The system uses an algorithm to create a representation matrix of the spin system where the eigenvalues of the matrix are the signal frequencies, and the eigenvectors represent the intensity

of the signals. The program has a predetermined cut-off value for the standard deviation of the transitions, and any transitions that lie outside of the cut-off are discounted, while those that meet the parameters of the program are optimized on. The algorithm goes through successive iterations of optimization on the representation matrix, in a manner similar to linear regression, to produce a diagonalized matrix. The result is an optimized simulation of the NMR spectrum. The program also produces an output file that contains the optimized chemical shift and scalar coupling data, with a standard deviation for each individual resonance and coupling interaction, as well as the root-mean-squared deviation (RMSD) for the total spectrum.

2. Hydrogen-Bonding Interaction in T-2 Toxin²

²Reproduced in part from the manuscript: Chaudhary, P., Shank, R. A., Montana, T., Goettel, J. T., Foroud, N. A., Hazendonk, P., Eudes, F. (2011) Hydrogen-bonding interactions in T-2 toxin studied using solution and solid-state NMR. *Toxins*. **3**(10), 1310-1331. All analysis contained in this chapter was performed by the author of this work and rewritten in order to ensure proper authorship.

2.1 Overview

Recall that there are four structural types in the class of trichothecene mycotoxins. Type A and B trichothecenes, produced by members of the *Fusarium* sp. (*Fusarium* species) of fungi, contribute to a large number of crop diseases, and can be passed on to animals and humans if diseased crops are not detected prior to harvesting. Type A trichothecenes tend to be far more toxic to animals and humans than they are towards the plants themselves; whereas, type B trichothecenes are far more phytotoxic.

This chapter deals with the structural analysis of the type A trichothecene T-2 toxin in solution and describes the nature of the hydrogen-bonding interaction of T-2 toxin with water. This portion of the work has been previously published in the journal *Toxins*, and modifications to the original paper have been made in order to ensure appropriate coverage of the work as required for this presentation of the data.

2.2. Introduction

T-2 toxin, shown along with some other significant trichothecenes in figure 2.1, is a type A trichothecene mycotoxin primarily produced by the *Fusarium* sp.. which are associated with the diseases of important food crops. Although instances of T-2 toxin contamination are rare, the seriousness of the infection is animal feed and foodstuffs produced for human consumption cannot be ignored. T-2 toxin has been considered for use as an agent in biological warfare following the observation that bread baked using T-2 toxin contaminated flour in World War II Russia resulted in significant infection and death [106].

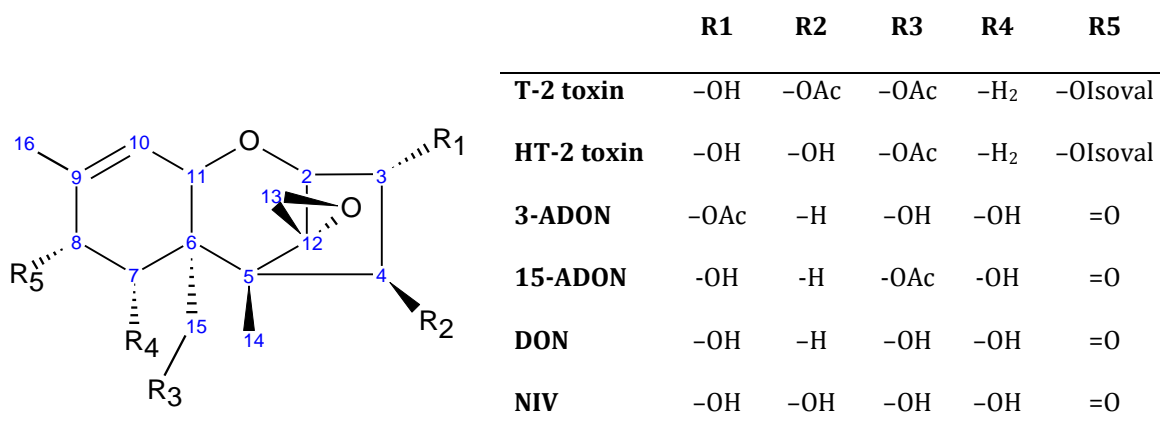


Figure 2. 1: Structures of type A and B trichothecenes. Type A trichothecenes include T-2 toxin, and HT-2 toxin. Type B trichothecenes include nivalenol (NIV), 4-deoxynivalenol (DON), 3,15-*O*-acetyl DON (3,15-ADON). OAc = acetyl function; OIsoval = isovalerate function.

Screening for DON contamination in foodstuffs has become standard practice in the many developed countries. However, no regulations are currently in place for the far more toxic T-2 toxin [156]. While detection of T-2 toxin in grain products is not as commonly observed as DON, an increase in the reports of contamination by T-2 and HT-2 toxin in grain has been observed recently in many European countries [11,39,85,139]. It is thus important to develop a detailed understanding of the toxicity of trichothecenes at the molecular level, which will serve to provide a basis for toxin screening, and may ultimately lead to the development of trichothecene resistant crops.

Detailed insights into the hydrogen bonding and dynamic behavior of this class of molecule will provide a better understanding regarding the mechanisms of inhibition and cytotoxicity of these compounds. Solution NMR structures available in the literature have focused primarily on the spectral identification rather than determining the three-dimensional configuration, structural dynamics, and interactions of these compounds. Thus, an accurate assignment of the T-2 toxin ¹H and ¹³C spectra in solution may provide specific clues regarding the inter- and intra-molecular interactions of this important toxin.

2.3. Materials and Methods

2.3.1. Solution-State NMR Experiments

All the spectra presented here were acquired at ambient temperatures (21-26°C), and were collected on a Bruker Avance 300 spectrometer, outfitted with a 5 mm HX PABBO BB probe. The magnetic field strength of the spectrometer is 7.05 Tesla, which gives rise to a Larmor frequency of 300.131 megaHertz (MHz) for ^1H and 75.468 MHz for ^{13}C nuclei. T-2 toxin (Sigma, CAS 21259-20-1) was dissolved in deuterated chloroform (CDCl_3) with tetramethylsilane (TMS) as an internal reference for both ^{13}C and ^1H nuclei, at a concentration of 1 mg/mL. Trichothecene conformation is highly dependent on the solvent system [31,32,72]; thus, the CDCl_3 was dried over sodium sulfate to prevent contamination of water in the sample. The 1D ^1H spectrum was recorded with 128 transients, using a 90° pulse width of 12.4 μs , and a recycle delay of 1.0 s. The 1D ^{13}C spectrum was recorded with 8464 transients, using a 90° pulse width of 7.6 μs , and a recycle delay of 2.0 s.

The 2D homonuclear magnitude gradient ^1H COSY spectrum was acquired in 256 increments, using a recycle delay of 1.5 s, and covered a spectral width of 1800 Hz (6.0 ppm) in both dimensions. Four transients, having 1024 points, were collected for each increment.

The gradient ^1H NOESY spectrum was acquired in 256 increments, using a recycle delay of 1.0 s and a mixing time of 1.0 s, and covered a spectral width of 1802.45 Hz (6.0 ppm) in both dimensions. Thirty-two transients, having 1024 points, were collected for each increment.

The 2D (^1H - ^{13}C) HSQC heteronuclear correlation spectrum was acquired in 128 increments, using a recycle delay of 2.0 s, and a spectral width covering 4006.41 Hz (13.34 ppm) in the direct dimension and 12500 Hz (165.62 ppm) in the indirect dimension. One-hundred-and-fifty-two transients, having 1024 points, were collected for each increment.

The 2D (^1H - ^{13}C) HMBC spectrum was acquired in 256 increments using a recycle delay of 2.0 s, and a spectral width covering 1951.60 Hz (6.50 ppm) in the direct dimension and 14268 Hz (190.24 ppm) in the indirect dimension. One-hundred transients, having 1024 points, were collected for each increment.

Deuterium exchange experiments were also performed, where deuterated water (D_2O ; Cambridge Isotope Laboratories; CAS 7789-20-0), was added in dropwise fashion between consecutive measurements, over the course of 3 hours. 1D 1H and 2D 1H - 1H NOESY experiments were performed for each drop of D_2O which was added.

2.3.2. Simulations

The SpinWorks software developed at the University of Manitoba was used to simulate the 300 MHz 1H spectra [97]. The free induction decay (FID) for each spectrum was zero-filled four-fold and subjected to Gauss-Lorentz apodization, having a line broadening of 1.00 Hz, and a Gaussian broadening of 0.1. The spectra were simulated in 3 smaller parts, since the software would not allow the spin system as a whole simulated all at once. The isovalerate group, containing the hydrogens 1', 2'A, 2'B, 3', 4' and 5', was simulated as a nine-spin $ABCD_3E_3$ system. Similarly the six-membered A-ring, containing hydrogens, 7 $_{\alpha}$, 7 $_{\beta}$, 8, 16, 10 and 11, was simulated including the sidechain hydrogens 15 $_{AB}$ as a ten-spin $ABCD_3EFGH$ system. The remainder of the core containing hydrogens, 2, 3, 3 $_{OH}$, 4, 14, 13 $_A$ and 13 $_B$, was simulated as a nine-spin $ABCDE_3FG$ spin system. Long range couplings were considered up to 5 bonds, and an inherent line width of 0.3 Hz with Lorentzian line shapes, was used to fit the data. Seventy transitions were assigned in the simulation of the isovalerate group, which had a total root mean squared deviation (RMSD) of less than 0.23 Hz and a largest absolute frequency difference of less than 0.56 Hertz (Hz). Standard deviations (SD) in all the spectral parameters ranged from 0.05-0.10 Hz. In the simulation of the A-ring, 2336 transitions were assigned with RMSD below 0.034 Hz, and a largest absolute difference of 0.08 Hz. SD in all the spectral parameters ranged from 0.03-0.06 Hz. In the simulation of the remaining signals, 1328 transitions were assigned with an RMSD below 0.031 Hz, and a largest absolute difference of 0.09 Hz. SD in all the spectral parameters ranged from 0.003-0.006 Hz.

2.4. Results

2.4.1. Structural Rigidity and Water Bridging

The central core of trichothecene toxins is composed of several fused rings, which impact a considerable amount of rigidity to the structure; however, the tetrahydropyran (B-ring), and cyclopentyl (C-ring) rings may still experience a certain amount of flexibility, particularly in solution. Through-bond coupling constants provide a good indication as to the overall rigidity of a structure.

The solution-state ^1H spectrum (Figure 2.2a) was assigned and simulated to accurately determine chemical shifts and coupling constants. The labeling convention described by Savard and Blackwell was used to maintain standards previously set out in the literature [135]. Coupling constants up to five bonds were considered in regions where significant π -electron density was expected. The corresponding chemical shifts and coupling constants are presented in Tables 2.1-2.4. The close agreement observed between the simulated and experimental spectra strongly supports the accuracy of the assignment. The methine and methylene protons of the isovalerate group are strongly coupled, which is demonstrated by the presence of highly second order features in the spectrum, which are highlighted in the inset of Figure 2.2a. Despite this complication, extraction of coupling constants and chemical shifts that have not previously been reported was possible.

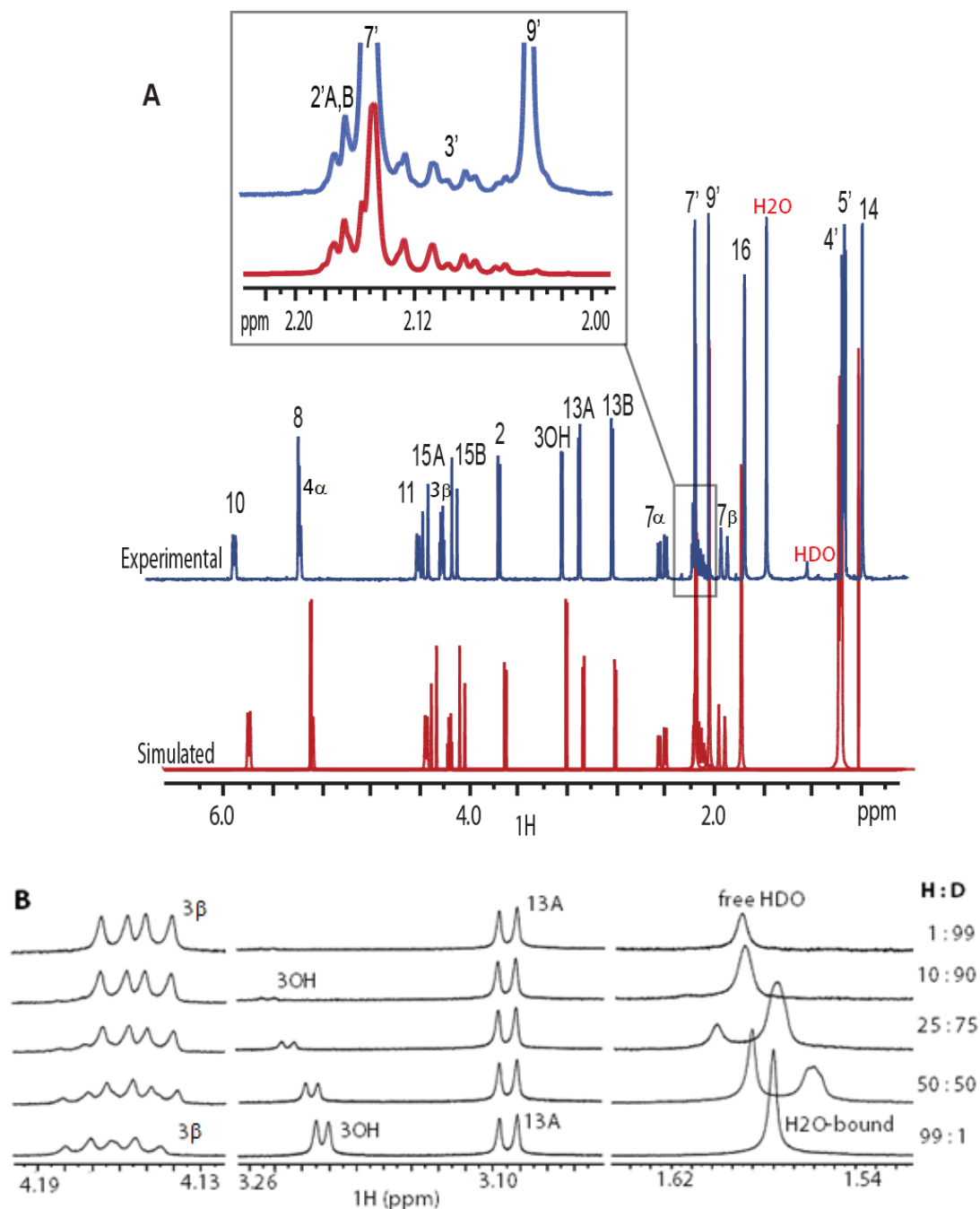


Figure 2. 2 A) T-2 toxin ^1H NMR solution-state spectrum at 300 MHz in CDCl_3 . (B) Deuterium exchange experiment. Regions exhibiting significant changes throughout the incremental addition of D_2O have been expanded to show peak structure. Of particular interest, is the H-3_{OH} and $\text{H}_2\text{O}/\text{HDO}$ regions, which not only demonstrate significant changes in chemical shift, but also exhibit the retention of their sharp peak structure, indicating a slow chemical exchange process. H-3 is less affected in that the only observable changes in the loss of coupling to H-3_{OH} as the latter peak is converted to H-3_{OD}.

Table 2. 1: ¹H chemical shifts for the resonances of the trichothecene core of T-2 toxin in CDCl₃ at 300 MHz

Label	Chemical Shift (ppm)	COSY	NOESY
2	3.681 ¹ ()	3 _β ,3 _{OH} ,14	3 _β ,13 _B
3_β	4.160	2,3 _{OH} ,4 _α	2,3 _{OH} ,4 _α ,H ₂ O
3_{OH}	3.100	2,3 _β	3 _β ,4 _α ,11,H ₂ O
4_α	5.348	3 _β ,9',13 _B ,14	3 _β ,3 _{OH} ,11,14, 15 _{AB} ,9',H ₂ O
7_α	1.886	7 _β ,8,11	7 _β ,8,14
7_β	2.408	7 _α ,8,15 _B	7 _α ,8,13 _A
8	5.298	7 _{αβ} ,10,16	7 _{αβ} ,16,2'
10	5.818	8,11,16	11,16
11	4.355	7 _α ,10,16	3 _{OH} ,4 _α ,10,H ₂ O
13_A	2.809	13 _B ,14	7 _β ,13 _B ,14
13_B	3.046	4 _α ,13 _A ,14	2,13 _A
14	0.817	2,4 _α ,13 _{AB} ,15 _A	4 _α ,7 _α ,13 _A ,15 _A
15_A	4.293	14,15 _B ,7'	4 _α ,15 _B
15_B	4.066	7 _β ,7',15 _A	4 _α ,15 _A
16	1.748	8,10,11	8,10

¹All signals were simulated with an error of ±0.001

Table 2. 2: ^1H coupling constants of the resonances of the trichothecene core of T-2 toxin in CDCl_3 at 300 MHz

Label	Coupling (Hz)	Comment/Assignment
$^3\text{J}_{2,3\beta}$	4.946 (0.005)	2 is gauche to 3_β
$^4\text{J}_{2,3\text{OH}}$	- 0.294 (0.005)	
$^4\text{J}_{2,14}$	- 0.304 (0.004)	
$^3\text{J}_{3\beta,3\text{OH}}$	2.909 (0.005)	3_β is gauche to 3-OH
$^3\text{J}_{3\beta,4\alpha}$	2.885 (0.005)	3_β is gauche to 4_α
$^5\text{J}_{3\beta,13\text{A}}$	0.211 (0.005)	
$^5\text{J}_{4\alpha,13\text{B}}$	0.160 (0.005)	
$^4\text{J}_{3\text{OH},4\alpha}$	- 0.293 (0.005)	
$^4\text{J}_{4\alpha,14}$	- 0.277 (0.003)	
$^2\text{J}_{7\alpha,7\beta}$	-15.015 (0.006)	Geminal coupling typical of sp^3 carbon
$^3\text{J}_{7\alpha,8}$	1.248 (0.006)	7_α nearly perpendicular to 8
$^4\text{J}_{7\alpha,11}$	-1.598(0.006)	W configuration
$^3\text{J}_{7\beta,8}$	5.718 (0.006)	7_β is gauche to 8
$^4\text{J}_{7\beta,15\text{B}}$	-0.446(0.006)	W configuration in one rotational isomer
$^4\text{J}_{8,10}$	-0.979 (0.006)	Typical of H on sp^2 carbon
$^4\text{J}_{8,16}$	-0.700 (0.003)	Indicative of rigidity of ring
$^3\text{J}_{10,11}$	5.892 (0.006)	10 is gauche to 11
$^4\text{J}_{10,16}$	-1.451 (0.003)	Typical of H and CH_3 on sp^2 carbon
$^4\text{J}_{11,15\text{B}}$	-0.588 (0.006)	W configuration in one rotational isomer
$^5\text{J}_{11,16}$	0.739(0.003)	Typical of CH_3 on sp^2 carbon
$^2\text{J}_{13\text{A},13\text{B}}$	3.971 (0.005)	Geminal coupling indicating ring strain
$^2\text{J}_{15\text{A},15\text{B}}$	-12.835 (0.006)	Geminal coupling typical of sp^3 carbon

Table 2. 3: ^1H chemical shifts of side-chain groups on T-2 toxin in CDCl_3 at 300 MHz

Label	Chemical Shift (ppm)
$2'_\text{A}$	2.154(0.0002)
$2'_\text{B}$	2.159(0.0002)
$3'$	2.107(0.0003)
$4'$	0.970(0.0002)
$5'$	0.961(0.0002)
$7'$	2.041(0.0001)
$9'$	2.151(0.0001)

Table 2. 4: ^1H coupling constants of side-chain groups on T-2 toxin in CDCl_3 at 300 MHz

Label	Coupling (Hz)	Comment/Assignment
$^2J_{2'A,2'B}$	-14.03 (0.10)	Typical geminal coupling of sp^3 carbon
$^3J_{2'A,3'}$	7.33 (0.10)	Rotationally averaged
$^3J_{2'B,3'}$	7.56 (0.10)	Rotationally averaged
$^3J_{3',4'}$	6.77 (0.10)	Rotationally averaged
$^3J_{3',5'}$	6.61 (0.10)	Rotationally averaged

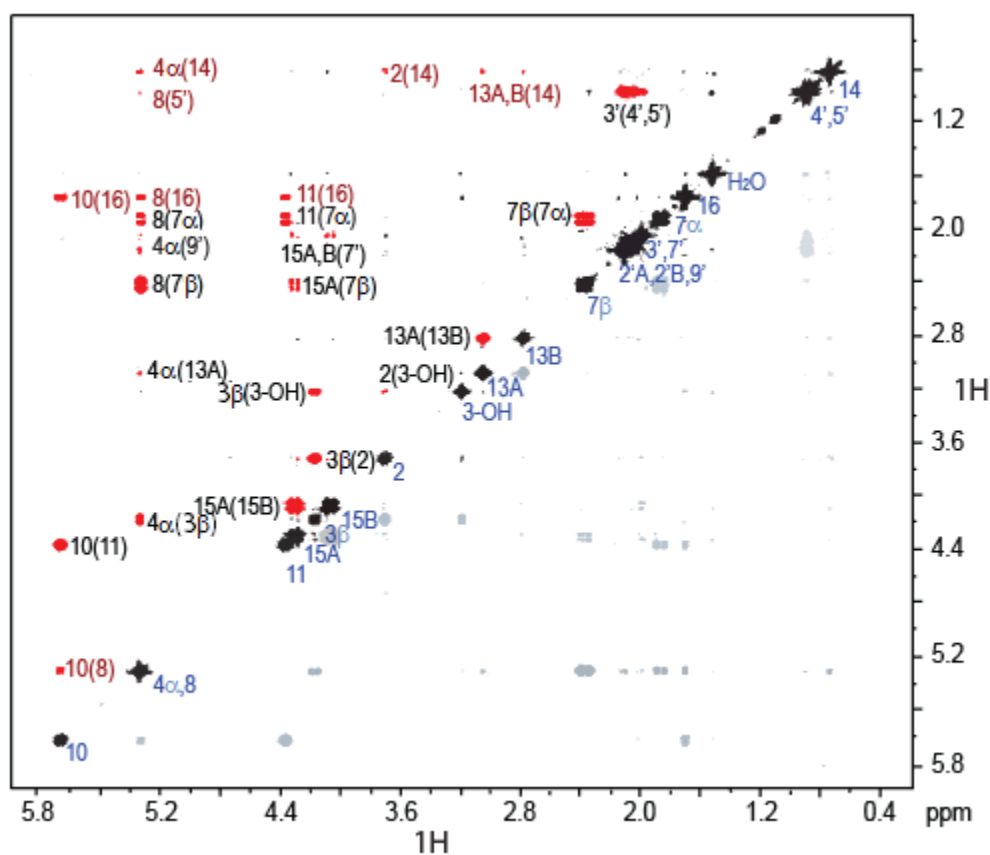


Figure 2. 3: ^1H - ^1H COSY spectrum observed for T-2 toxin at 300 MHz in CDCl_3 . Auto-correlation peaks are shown in black along the diagonal. Correlation peaks appearing off the diagonal are depicted in red. The strong 2- and 3-bond couplings are in black typescript; whereas, the weaker 4- and 5-bond couplings are in red type.

The COSY spectrum (Figure 2.3) supports the assignment of the 1D ^1H spectrum in every aspect, and also indicates some long range connectivities of note. The prominent cross peaks in the COSY spectrum, black typescript, represent primarily two- and three-bond connectivities; whereas, the weaker 4- and 5-bond connectivities are shown in red typescript. These are all listed in tables 2.1 and 2.3. The coupling between H-7 $_{\alpha}$ and H-11 strongly supports that the H-7 $_{\alpha}$ is in an equatorial position. This four-bond coupling has a large value of -1.59 Hz, which indicates a very rigid W-type configuration between these two nuclei. A similar coupling is seen between H-7 $_{\beta}$ and H-15 $_{\text{B}}$, which suggests that H-7 $_{\beta}$ must occupy a position which is axial to the core and H-15 $_{\text{B}}$ points towards C-14 and occupies a space underneath the ring. Therefore, the oxygen of the hydroxyl group on C-15 is *gauche* to both C-7 and C-5. This 4-bond coupling is smaller at -0.45 Hz, suggesting that more than one rotational isomer is likely present in solution, such as one with the oxygen on C-15 being *gauche* to C-7 and *trans* to C-5. Likewise, one may appreciate the 4-bond coupling, which occurs between H-15 $_{\text{B}}$ and H-11 at -0.59 Hz.

The NOESY spectrum (Figure 2.4) provided data which was instrumental in confirming the overall configuration of all the proton resonances, including the methyl resonances of the acetyl side chains, and the specific assignments of the methylene protons (H-7 $_{\alpha\beta}$, H-13 $_{\text{AB}}$ and H-15 $_{\text{AB}}$). Notable cross peaks include those occurring between hydrogens H-7 $_{\beta}$ and H-13 $_{\text{A}}$, H-7 $_{\alpha}$ and H-14, H-2 and H-13 $_{\text{B}}$, H-13 $_{\text{A}}$ and H-14, H-15 $_{\text{A}}$ and H-14, H-15 $_{\text{AB}}$ and H-4 $_{\alpha}$. These fully support the assignments made by Greenhalgh *et al.* [12,55,134,135]. Prominent EXSY crosspeaks were also observed between water and H-3 $_{\text{OH}}$ (Figure 2.4), which indicates the presence of chemical exchange in the sample, which was further confirmed with the deuterium exchange experiment (Figure 2.2b). Furthermore, positive NOESY crosspeaks are observed between the H $_2$ O peak and H-3 $_{\beta}$, H-4 $_{\alpha}$ and H-11, indicating close proximity.

A deuterium exchange experiment was performed to determine whether the water present in the sample was bound to T-2 toxin or whether it is free. Two sharp and rather distinct peaks are observed for H $_2$ O and HDO (Figure 2.2b). The linewidth of the H $_2$ O peak was compared to that of the uncoupled methyl hydrogen on C-14, and is remarkably similar, suggesting that there is no line

broadening in the H₂O peak due to chemical exchange, and that the same correlation time applies to both resonances. Furthermore, despite the decrease in intensity of the H-3_{OH} resonance upon the addition of D₂O, it remains sharp and consistently exhibits coupling behavior to H-3_β, indicating that it is in a slow exchange process with D₂O. Complete exchange of the H-3_{OH} with D₂O occurs over the course of 3 hours.

The 1D ¹H NMR data is consistent with and complements previous NMR findings on T-2 toxin [12,55,134,135]. The chemical shift and coupling constants observed for the hydrogens attached directly to the trichothecene core confirm the previously defined stereochemistry. Additionally, 2D NOESY data made it possible to distinguish between H-13_A and H-13_B, whose geminal coupling indicates severe ring strain, which is to be expected for the three-membered epoxide ring. The vicinal couplings of H-7_α and H-7_β with H-8 confirm that H-7_β is gauche, and that H-7_α is perpendicular to H-8, respectively, confirming the assignments made by Savard and Blackwell [12,55,134,135]. Long range four- and five-bond coupling constants also imply significant conformational rigidity in solution; this is especially true for the coupling observed between H-7_α and H-11. Any long-range couplings to H-10 are primarily the result of efficient π-electron spin propagation due to the nearby conjugated double bond. Also note that the vicinal couplings present for the isovalerate ring, which range from 6.5-7.5 Hz, are consistent with a low barrier to rotation about the C-C bonds, expected within the isovalerate functionality. This is further supported by the near chemical shift equivalence of H-2'_A and H-2'_B. The complete assignment for T-2 toxin is depicted in figure 2.5.

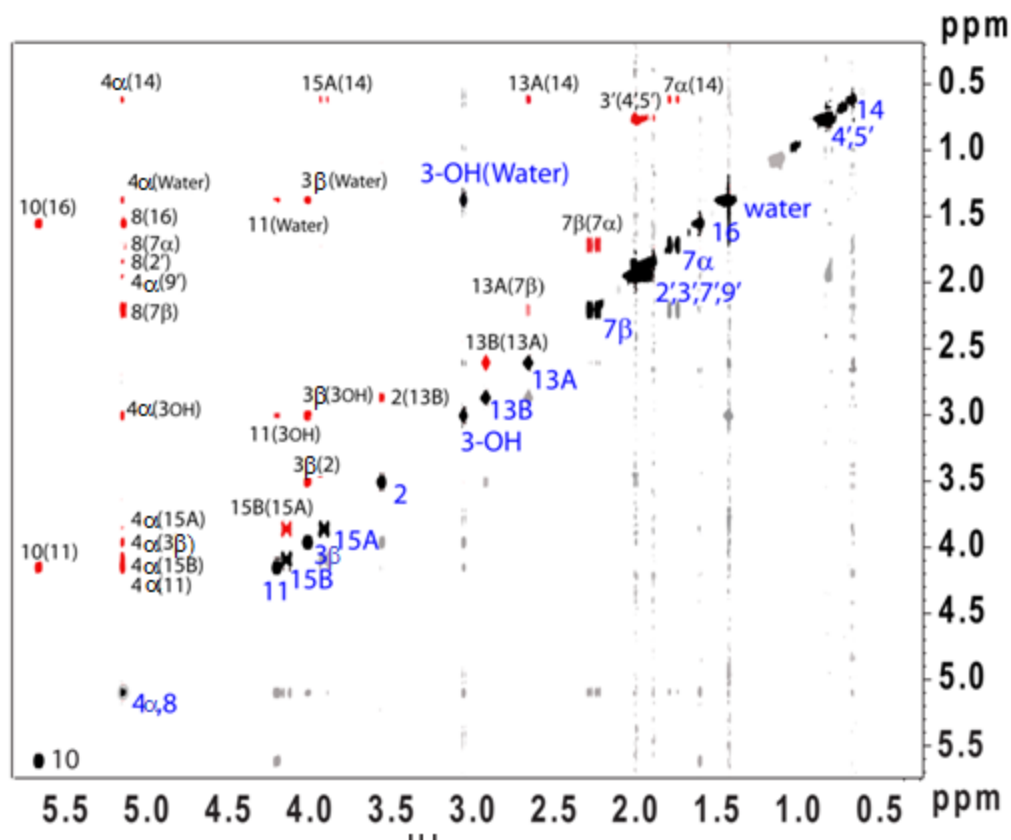


Figure 2. 4: ^1H NOESY for T-2 toxin at 300 MHz in CDCl_3 . Cross-relaxation peaks bearing a positive phase are shown in red. Negatively phased peaks, including the diagonal autocorrelation peaks and exchange (EXSY) peak observed between $\text{H}_2\text{O}(3_{\text{OH}})$ are shown in black, with blue typescript.

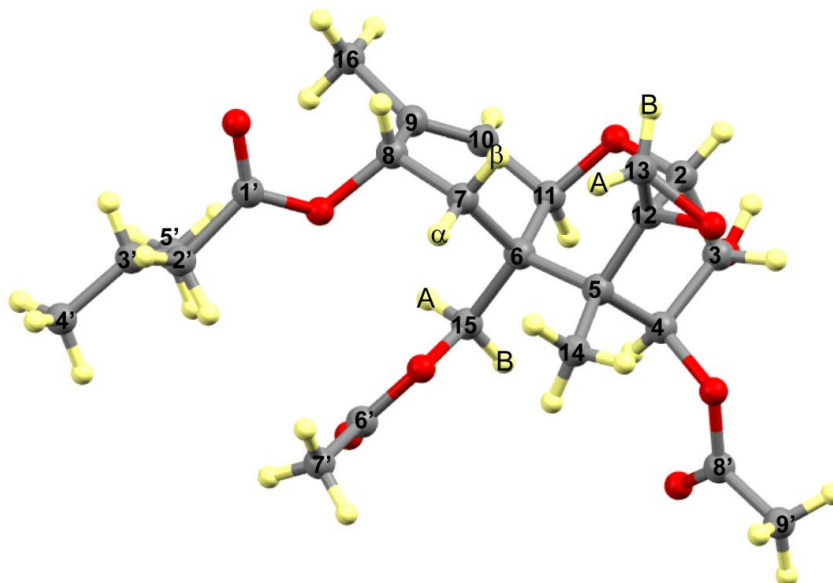


Figure 2. 5: Proposed chemical structure of T-2 toxin indicating all ^1H resonances labelled to show appropriate stereochemistry.

2.4.2. Carbon Spectral Analysis

The 1D ^{13}C spectrum of T-2 toxin in solution is presented in Figure 2.6. The ^{13}C -spectrum was assigned on the basis of chemical shifts and couplings observed in the 2D heteronuclear experiments.

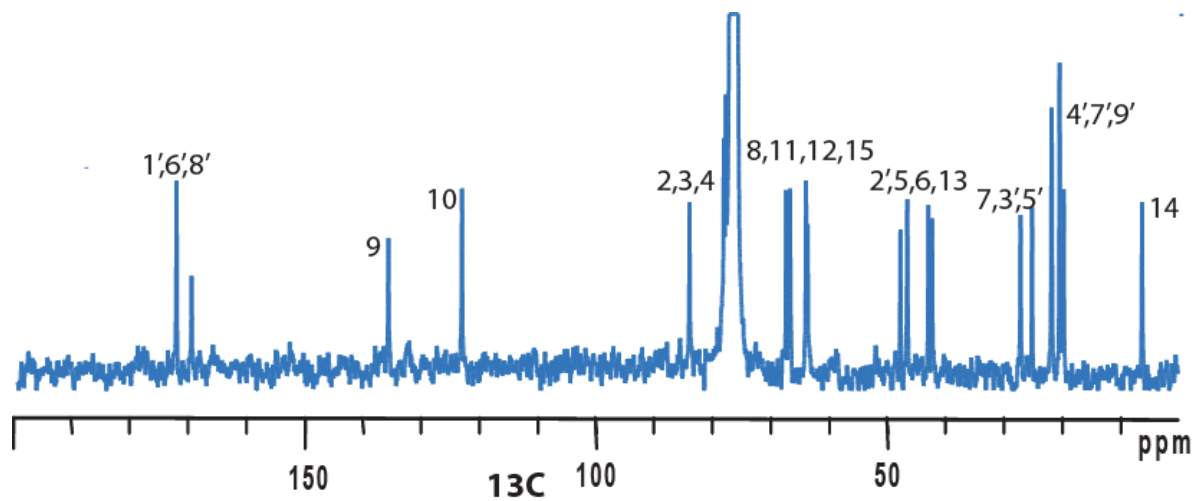


Figure 2. 6: The solution-state ^{13}C NMR spectrum for T-2 toxin in CDCl_3 at 75 MHz with ^1H decoupling

The carbon assignment, along with cross-peaks of note in the HSQC and HMBC spectra are summarized in table 2.5. The heteronuclear correlation methods allow for the unambiguous assignments of all the carbonyl resonances, including those of the carbonyl and methyl carbons of the acetyl side chains, which confirms the assignments previously identified by Savard and Blackwell [134].

Table 2. 5: Carbon-13 chemical shifts and ^1H - ^{13}C couplings for T-2 toxin in CDCl_3 at 75 MHz

Label	Solution (ppm)	HSQC	HMBC
2	78.72	2	$3_{\text{OH}}, 13_{\text{B}}$
3	78.40	3_{β}	4_{α}
4	84.60	4_{α}	2,14
5	48.39		$2, 4_{\alpha}, 14, 15_{\text{AB}}$
6	42.94		$7_{\beta}, 8, 14, 15_{\text{AB}}$
7	27.75	$7_{\alpha\beta}$	15_{B}
8	68.02	8	16
9	136.32		8,11,16
10	123.70	10	11,16
11	67.34	11	$2, 15_{\text{A}}$
12	64.59		$2, 4_{\alpha}, 13_{\text{AB}}, 14$
13	47.21	13_{AB}	
14	6.88	14	
15	64.31	15_{AB}	
16	20.35	16	$7_{\alpha\beta}$
1'	172.73		8
2'	43.58	2'	$4', 5'$
3'	25.78	3'	$2', 4', 5'$
4'	22.37	4'	$3', 5'$
5'	22.45	5'	3'
6'	170.13		7'
7'	21.07	7'	
8'	172.70		15, 9'
9'	21.04	9'	

2.5. Discussion

2.5.1. Hydrogen-Bonding in Solution

Combining the results of the deuterium exchange experiment and the NOESY experiment, some interesting observations arise in regards to the hydrogen-bonding behavior of T-2 toxin. When D_2O is added to a sample, it will rapidly interchange with any free water in the sample, forming HDO. In the case of fast exchange between H_2O and HDO, one would expect to observe a single broad line due to the coupling of the HDO proton to the deuterium nucleus, which confers a fine triplet structure to the peak. The deuterium nucleus shields the proton on the HDO molecule, and shifts the resonance slightly to a lower frequency. However, our observations indicate that the conversion from H_2O to HDO is on a much slower timescale, given by the rather distinct and sharp lines observed for both the H_2O and HDO signals (Figure 2.2b). The coexistence of these peaks in the spectrum suggests that at least a portion of the water in the sample is prevented from freely exchanging with D_2O , indicating that it is likely protected due to a binding interaction with the trichothecene. Furthermore, the linewidth for the $H-3_{OH}$ resonance remains consistent over the course of the exchange experiment. Where $H-3_{OH}$ is undergoing a fast exchange process with water a broad featureless line would be expected. The sharpness of the $H-3_{OH}$ peak, as well as the coupling observed between this proton and $H-3_\beta$, indicate that $H-3_{OH}$ is most likely involved in a hydrogen bonding interaction of some kind. The data suggest that at least some of the H_2O in the sample is bound to T-2 toxin, thereby, preventing the water and $H-3_{OH}$ from exchanging rapidly with D_2O .

The orientation of the bound water, with respect to the molecule, can be determined through analysis of the NOESY spectrum. It is important to note that in spectra where chemical exchange is a factor, second-order artifacts known as saturation transfer peaks cannot be ruled out. Thus, it is necessary to analyze any crosspeaks to water with care in order to determine whether they are true first-order cross-relaxation signals or artifacts due to saturation transfer. Peaks arising from saturation transfer in the analysis of small molecules, such as T-2 toxin, possess the same phase as the diagonal autocorrelation peaks; whereas, molecules with longer correlation times, such as large macromolecules like proteins and nucleic acids, would have saturation transfer peaks that possess the same phase as conventional NOE peaks [112]. Therefore, it is expected that any saturation

transfer peaks in T-2 toxin would appear negative due to the short correlation time of the molecule. Additionally, saturation transfer will not occur if the rate of chemical exchange is on the same order or longer than the rate of longitudinal (T_1) relaxation [26], as the sampling of the experiment would occur prior to exchange, and transfer due to saturation of the signal by chemical exchange would not be possible. If we consider that the rate of chemical exchange observed in the deuterium experiment described above is relatively long, then the observation of saturation transfer peaks for this system is highly unlikely. The observed crosspeaks to water for H-3 $_{\beta}$, H-4 $_{\alpha}$, and H-11 are all positive (Figure 2.4), therefore, they are not due to chemical exchange, and since saturation transfer is not possible in this case, they must arise as a result of cross-relaxation. This suggests that H-3 $_{\beta}$, H-4 $_{\alpha}$, and H-11 are all in close proximity to water. Thus, at least one molecule of water is bound to T-2 toxin, and must lie within the tetrahydropyranyl pocket, which is located on the opposite side of the molecule with respect to the epoxide (Figure 2.7).

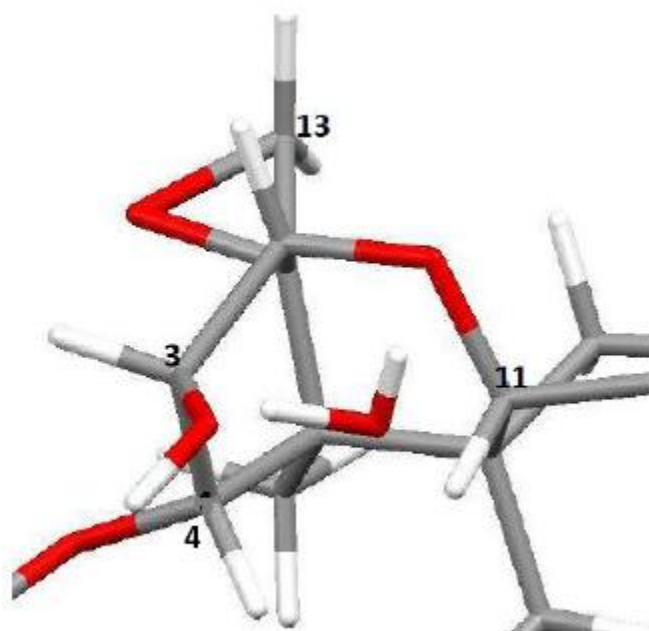


Figure 2. 7: Proposed placement of water in the tetrahydropyranyl pocket of T-2 toxin. estimated placement of the water is based on logical hydrogen-bonding interactions, and EXSY crosspeaks. Cross-relaxation was observed between water and H-3 $_{\beta}$, H-4 $_{\alpha}$ and H-11, indicating close proximity; chemical exchange between water and H-3 $_{OH}$ was also observed.

Evidence of bound water is a very interesting result, as the trichothecenes themselves are known to be insoluble in water; however, it is also accepted that the presence of some water is required in order for the molecules to go into solution. Binding of water within the tetrahydropyranyl pocket may serve as a bridge between the oxygen of the tetrahydropyran ring, and the hydroxyl at C-3, serving to stabilize the molecule, and preventing a significant amount of structural flexibility in this particular ring of the core. It is interesting that this bridging water is found on the opposite side of the trichothecene core from the epoxide ring. The high degree of ring strain in the epoxide ring should ultimately confer a great deal of electrophilic character to C-12; however, throughout all of the literature on the trichothecenes, the consensus remains that this particular epoxide functionality is highly stable, and is subject only to enzymatic degradation [133]. One possible theory is that the bridging water is required in the trichothecene core in order to maintain the unusual stability of the epoxide.

2.6. Conclusions

A complete proton and carbon NMR analysis was performed to verify the stereochemistry of T-2 toxin in solution. This served to confirm and refine the assignment of all the methylene protons, acetyl, methyl and carbonyl resonances previously described in literature. Full simulation of the proton spectrum provided all the spectral parameters to within 0.02-0.06 Hz accuracy, and led to useful structural and dynamic insights for the molecule, which include the rigidity of the ring structure, the conformational flexibility of the side chain, and the ring strain in the epoxide group. Most notably, exchange dynamics were observed between water and H-3_{OH} via EXSY cross peaks, lending support to the existence of a hydrogen bonding interaction between T-2 toxin and water. Additional, cross-relaxation peaks in the NOESY spectrum, observed between water and H-3_β, H-4_α and H-11, indicate that the water is bound within the tetrahydropyranyl pocket present on the side of the ring opposite the epoxide functionality. Deuterium exchange experiments were performed to address whether water was free in solution, or whether it was indeed bound to the toxin. Sharp coupled peaks and slow chemical exchange between H₂O and D₂O, provide strong support that there is at least one water molecule bound to T-2 toxin through a hydrogen bond with the hydroxyl

hydrogen on C-3, which is also observed to be in the slow chemical exchange regime. This hydrogen bond is likely involved in a water-bridging interaction with the molecule and functions to stabilize and rigidify the trichothecene core.

These new insights into the three-dimensional structure of T-2 toxin, as well as the relatively slow exchange with water, provide a basis with which it is possible to begin piecing together the mechanism for toxicity of T-2 toxin, as well for other toxins in the trichothecene subclass.

3. Structural Analysis of the DON family of toxins

3.1 Overview

This chapter deals with the NMR structural analysis of the DON family of mycotoxins in solution, namely DON, nivalenol (NIV) and the acetylated derivatives of DON, 15-O-acetyldeoxynivalenol (15-ADON), and 3-O-acetyldeoxynivalenol (3-ADON), and aims to describe the nature of the hydrogen-bonding interaction for these toxins with water, as previously reviewed for T-2 toxin. All compounds are studied in deuterated chloroform (CDCl_3) at 300 MHz for ^1H and 75 MHz for ^{13}C . The 2D correlation experiments employed here, help to refine the current literature assignments for the type B trichothecenes studied herein. Furthermore, deuterium exchange spectroscopy has been conducted on DON, indicating the presence of bound water, supporting the findings from the previous study of T-2 toxin.

3.2 Introduction

This study was initiated with a view of developing an understanding of the hydrogen-bonding interactions of the type B trichothecenes (i.e. DON, NIV, 15-ADON and 3-ADON), both in internal interactions, and with water, as well as the effects that water has on the 3D conformation of the trichothecenes. This information is essential in gaining insight towards the biochemical interactions that these toxins may undergo with various components in the eukaryotic cell. However, before the biochemical interactions can be understood, it is important to have an advanced understanding of the structure and dynamics of this class of toxins.

The presence of the ketone group at C-8 is the identifying feature for the type B trichothecenes. The type B toxins are structurally simple in terms of the substitution patterns, as they are mostly unsubstituted, hydroxylated, or esterified; therefore, they are expected to exhibit far more dynamics than their type A, C and D type counterparts. Considering DON as the parent compound, the remaining toxins in this class differ from DON at only one of the substitution sites each: NIV is hydroxylated at C-4, 3-ADON is acetylated at C-3, and 15-ADON is acetylated at C-15. The last remaining naturally occurring type B toxin is Fusarenon-X (Fus-X), which resembles NIV with an O-

acetylated group at C-4 [98,115,123]. Fus-X was not included in this study as it is rare in North America, affecting primarily countries in Eastern Europe and Asia [23]. Despite the lack of agricultural concern for Canadian industries, the toxicity of Fus-X towards animal systems is comparable to that of DON [164], and merits future attention on matters regarding its dynamic properties.

Esterification has been shown to dramatically lower the phytotoxicity of DON [1,20,50,51,114,168,170,171]; however, this is not strictly true with respect to animal systems. [37,98,108,113,122,123,148,164]. This difference in toxicity versus phytotoxicity with respect to esterification is somewhat surprising considering the relatively high toxicity of T-2 toxin, which is esterified at three sites; however, it does maintain the overall trend in trichothecene toxicity as related to substitution pattern. The mechanism for the enzymatic esterification of DON has been studied by Garvey *et al.* in an attempt to provide a means of control for the toxin [50,51,114]. Esterification of DON occurs at C-3 or C-15 via the enzymes TRI101, or TRI3, respectively [50,51]. Investigation of the dynamics of the O-acetylated derivatives, 3-ADON and 15-ADON, may provide some insight into how esterification may serve to control the phytotoxicity of DON.

The majority of studies on the type B trichothecenes have focused on structure determination, and as a result there are few dynamic studies available with which comparisons can be made. Density functional theory (DFT) computations were conducted by Nagy *et al.* in 2005 [111], on the internal dynamics of DON, which suggested that the lowest energy configuration contains an internal hydrogen-bonding network. The proposed hydrogen bonding occurs between the C-8 carbonyl oxygen and the C-7 hydroxyl hydrogen, which is linked further to the hydroxyl hydrogen at C-15. This internal network imposes significant rigidity in this compound, as seen in figure 3.1. The energy of this interaction is significantly reduced from all other locally optimal configurations; however, hydrogen-bonding and bridging with water was not taken into account in this study. The literature clearly indicates the need for a small amount of water to render trichothecenes [130-132] soluble in solution in the case of ethanol, methanol and chloroform. This, together with the new evidence presented in chapter 2 for the water binding in T-2 toxin [27],

demonstrates that the hydrogen-bonding, both intra- and inter-molecular, of all the trichothecenes should be carefully considered.

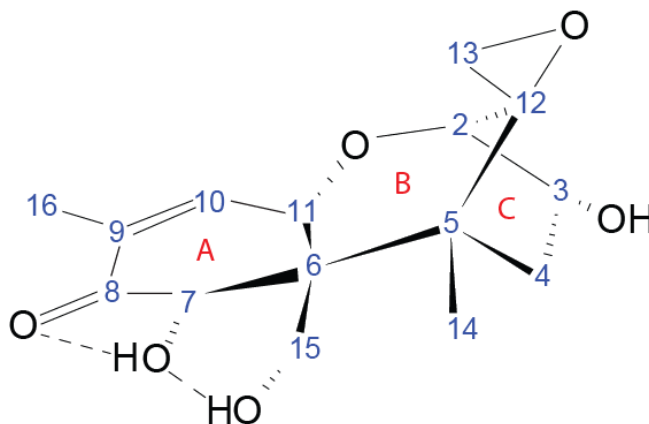


Figure 3. 1: Internal hydrogen-bonding network in DON proposed by density functional theory (DFT) analysis [111], showing the bonds from 15_{OH} to 7_{OH}, and from 7_{OH} to the oxygen of the ketone functionality on C-8. The relative geometry reflects the introduction of the planar bonds due to presence of double bonds in the A-ring.

3.3 Materials and Methods

3.3.1 Solution-State NMR Experiments

All spectra were acquired using a Bruker Avance 300 spectrometer, outfitted with a 5 mm HX PABBO BB probe. The magnetic field strength of the spectrometer is 7.05 Tesla, which gives rise to a Larmor frequency of 300.131 MHz for ^1H and 75.468 MHz for ^{13}C nuclei. All spectra presented here were acquired at ambient temperature (21-26°C). Deoxynivalenol (Sigma, CAS 51481-10-8), Nivalenol (Sigma, CAS 23282-20-4), 15-O-acetyldeoxynivalenol (Sigma, CAS 88337-96-6), and 3-O-acetyldeoxynivalenol (Sigma, CAS 50722-38-8), as well as a second sample of deoxynivalenol acquired from the agriculture and agri-food Canada (AAFC) group in Ottawa were all dissolved in CDCl_3 to a concentration of 1 mg/mL using TMS as an internal reference for both ^{13}C and ^1H nuclei. As previously demonstrated [66,72], trichothecene configuration is highly dependent on solvent, therefore the importance of careful solvent drying of both the toxin and the solvent must be emphasized. The sample of DON acquired from Sigma-Aldrich was placed in a small round-bottom flask and dried by vacuum pumping on the sample for 6 hours under nitrogen gas to remove any

adsorbed water from the sample. CDCl_3 was dried over molecular sieves in order to prevent water contamination in the samples. The 1D ^1H spectrum was recorded as 128 transients, using a 90° pulse width of $12.4\ \mu\text{s}$, and a recycle delay of 1.5 s. The 1D ^{13}C spectrum was recorded as 4000 transients, using a 90° pulse width of $7.6\ \mu\text{s}$, and a recycle delay of 4.0 s.

The homonuclear magnitude gradient ^1H COSY spectrum was acquired in 256 increments over a spectral width of 1800 Hz (12.0 ppm) in both dimensions, using a recycle delay of 1.5 s. 64 transients were collected for each increment, having 4096 points. The direct and indirect dimensions have a digital resolution of 0.88 and 7.03 Hz, respectively.

The gradient ^1H NOESY spectrum was acquired in 256 increments covering a spectral width of 1802.45 Hz (12.0 ppm) in both dimensions, using a recycle delay of 1.5 s and an array of mixing times of 0.5 s, 1.0 s, and 1.5s. 32 transients were collected for each increment, having 4096 points. The direct and indirect dimensions have a digital resolution of 0.88 and 7.03 Hz, respectively.

The ^1H - ^{13}C HSQC spectrum was acquired in 128 increments, using a recycle delay of 2.0 s, and a spectral width of 4006.41 Hz (13.34 ppm) in the direct dimension and 12500 Hz (165.62 ppm) in the indirect dimension. 152 transients were collected for each increment, having 1024 points. The direct and indirect dimensions have a digital resolution of 3.91 and 97.66 Hz, respectively, no zero-filling was employed here.

The ^1H - ^{13}C HMBC spectrum was acquired in 256 increments using a recycle delay of 2.0 s, and a spectral width covering 1951.60 Hz (6.50 ppm) in the direct dimension and 14268 Hz (190.24 ppm) in the indirect dimension. One-hundred transients were collected for each increment, having 1024 points and the FID was zero-filled up to a value of 4096 points. The direct and indirect dimensions have a digital resolution of 0.52 and 56.04 Hz, respectively.

Deuterium exchange experiments were performed at ambient temperature where deuterated water, D_2O (Cambridge Isotope Laboratories; CAS 7789-20-0), was added drop wise to the NMR tube between consecutive NMR measurements, over the course of 3 hours. 1D ^1H and 2D ^1H - ^1H NOESY experiments were performed upon each instance of D_2O addition.

3.3.2 Simulations

The SpinWorks software developed by Marat and colleagues at the University of Manitoba was used to simulate the data obtained for the 300 MHz ^1H spectra [97]. The FIDs were zero-filled to 256k points and were subjected to Gauss-Lorentz apodization with a line broadening between -1.00 to -0.50 Hz, and a Gaussian broadening of 0.33, depending on the signal-to-noise ratio in the data. The spectra were simulated in 2 parts as the whole spin system could not be simulated at once. The subspectrum of the six-membered ring, with hydrogens, H-7_{OH}, H-7 _{β} , H-10, H-11, H-15_A, H-15_B, H-15_{OH}, H-16, and where appropriate, with the those of the 1' methyl, from either the 3-O-acetyl, or 15-O-acetyl, was simulated as either a ten-spin ABCD₃EFGH or 11-spin ABCD₃EFGHI₃ system respectively. Similarly, the subspectrum associated with the remaining hydrogens from the core structure, H-2, H-3, H-3_{OH}, H-4 _{α} , H-14, H-13_A and H-13_A, and H-4 _{β} or, in the case of NIV, H-4_{OH} was simulated as a ten-spin ABCDE₃FGH spin system. Long range connectivities were considered up to 5 bonds, and an inherent line width of 0.3 Hz along with Lorentzian line shapes was used to fit the data. The A ring simulation calculated 2001 transitions which were assigned to within RMS deviation below 0.034 Hz, and a largest absolute difference of 0.08 Hz. Standard deviations (SD) in all the spectral parameters ranged from 0.01-0.04 Hz. In the C ring simulation also the 2216 transitions were assigned with an RMSD below 0.031 Hz, and largest absolute difference of 0.09 Hz. SD in all the spectral parameters range from 0.001-0.009 Hz.

3.4 Results

3.4.1 Full Spectral Assignment of Deoxynivalenol in Chloroform

The substituents of DON's trichothecene core are predominantly small flexible groups (i.e. –OH, and –H); with the exception of the ketal functionality at C-8 which is expected to impose significant rigidity on the system. The core is composed of four fused rings which result in a very rigid structure. The A-ring is expected to be particularly rigid when the ketone functionality is present at C-8, which is conjugated with the double bond between C-9 and C-10. Conjugation locks that side of the molecule in a planar configuration, rather than the half-chair configuration typical for the other trichothecene classes. The ketone at C-8 also offers a strong electron donor at the oxygen,

which is highly favored to undergo hydrogen bonding. It is important to point out that a certain degree of torsional flexibility is expected in the tetrahydropyran (B-) and cyclopentyl (C-) rings, particularly where small substituent groups are present, as is the case with DON. The long range scalar coupling constants between protons on the core structure, seen in the ^1H and ^1H - ^1H COSY spectra are used to gauge the rigidity in this structure.

Although full spectral analysis was performed on all of the samples studied in this section, not all of the spectra and analyses are included in the body of this work. Thus, DON in CDCl_3 is used to exemplify the extent to which data was obtained for each sample presented.

The solution-state ^1H spectrum shown in figure 3.2 was assigned and simulated to determine the chemical shifts and coupling constants of the spin system with a high degree of accuracy. The assignment employs the same labeling convention as determined by Savard and Blackwell [135]. Where significant π -electron density is expected, coupling constants up to five-bonds were considered. The corresponding chemical shift and coupling constants are presented in table 3.1 and 3.2, respectively. The close agreement (on the order of 0.001 Hz in the ^1H chemical shift, and 0.001-0.007 Hz for the coupling) observed between the simulated and experimental data strongly supports the accuracy of the assignment, based on the optimization provided for the SpinWorks program. The inset of figure 3.2 depicts the agreement between the simulated and experimental spectra. The assignment corresponds closely to previously published attempts, serving as a testament to the accuracy of the assignment [111,135]; however, some small discrepancies in the assignment are noted and serve as refinements to the data presented in the literature.

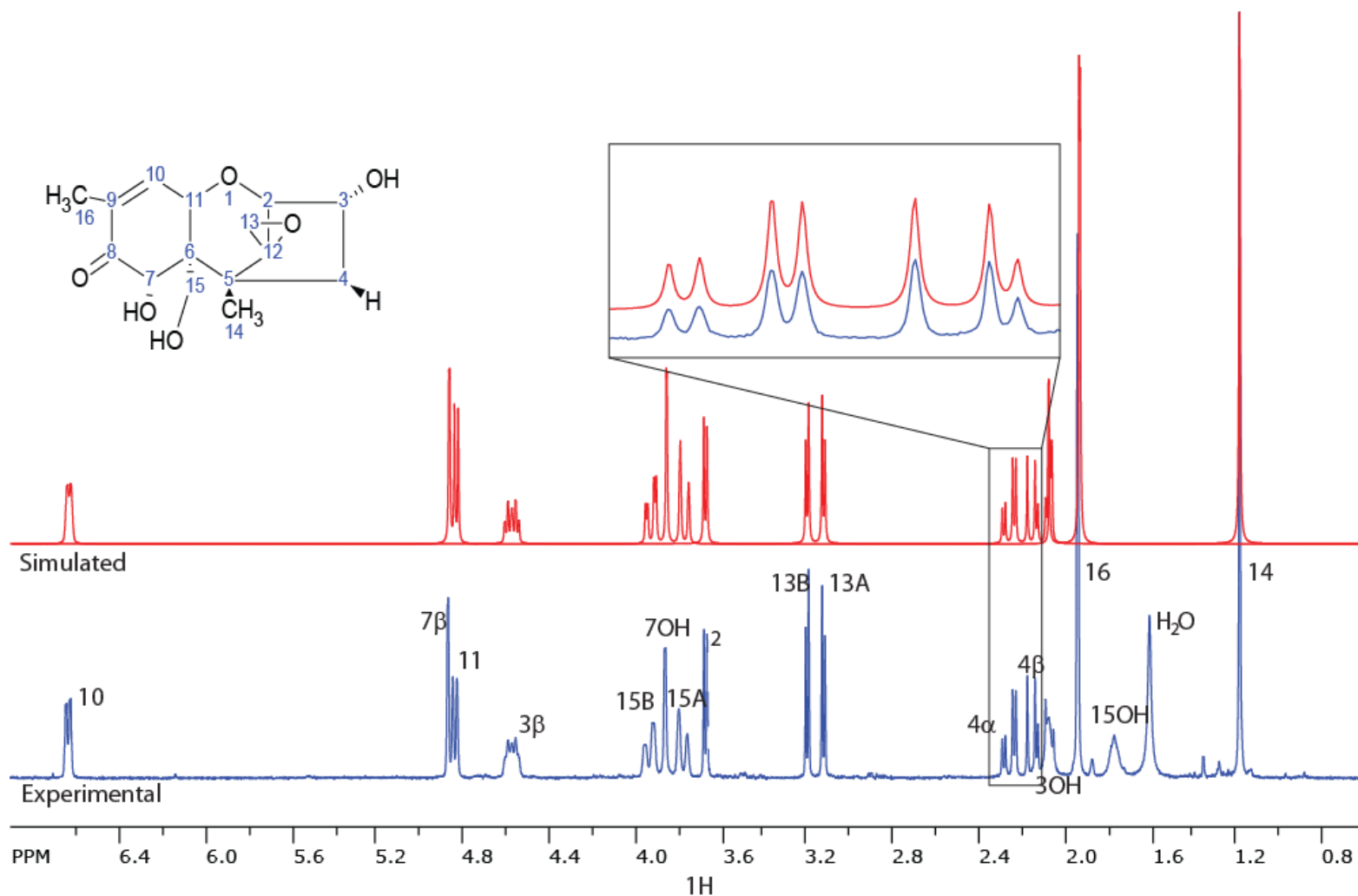


Figure 3. 2: ^1H NMR solution-state spectrum for DON at 300 MHz in CDCl_3 . The experimental spectrum is shown in blue and is labeled according to the convention described by Savard and Blackwell [135], the simulated spectrum is shown in red. An inset depicting the methylene protons of C-4 is provided to show the close agreement between the simulation and the experimental spectra.

Table 3. 1: Comparison of the experimental and literature data for DON studied in CDCl₃ [135]

¹ H label	Exp. Chemical Shift – δ (ppm)	Lit. Chemical Shift –δ (ppm)	COSY	NOESY
2	3.672 ^{1,2}	3.62	3 _β ,14	3 _β
3_β	4.577 ²	4.53	2,4 _α ,4 _β	2,4 _α ,4 _β
3_{OH}	2.067 ²	N/O ³		15 _{OH} , H ₂ O
4_α[*]	2.247	2.21	3 _β ,4 _β	3 _β ,4 _β ,14
4_β[*]	2.129	2.07	3 _β ,4 _α	3 _β ,4 _α ,14
7_β[*]	4.878	4.83	7 _{OH}	7 _{OH}
7_{OH}[*]	3.862	N/O ³	7 _β	7 _β ,14,H ₂ O
10	6.656	6.61	11,16	11,16
11	4.845	4.86	10,16	4 _α ,10,16
13_A[*]	3.120	3.07	13 _B	13 _B
13_B[*]	3.195	3.14	13 _A	13 _A ,14
14	1.174	1.13	2	4 _α ,4 _β ,7 _{OH} ,13 _B ,15 _{AB}
15_A	3.781 ²	3.73	15 _B ,15 _{OH}	14,15 _B ,15 _{OH}
15_B	3.933 ²	3.89	15 _A ,15 _{OH}	14,15 _A ,15 _{OH}
15_{OH}	2.066 ²	N/O ³	15 _{AB}	3 _{OH} ,15 _{AB} ,H ₂ O
16	1.931	1.86	10,11	10

¹ Chemical shifts were simulated within ±0.001 Hz in all cases²Indicates signals which experience line broadening.³Hydroxyl resonance not recorded in the literature.^{*}Denotes that the labeling scheme presented in the literature by Savard and Blackwell is employed in this table and is reviewed in the following two chapters for consistency in the data.

Table 3. 2: ¹H-¹H scalar coupling constants extracted from the 1D and 2D data collected for DON

	J (Hz) – Exp.	J (Hz) – Lit.	Interpretation
³ J _{2,3}	4.643 (± 0.005) ¹	4.5	2 is <i>gauche</i> to 3 _β
³ J _{3,4α} *	4.150 (± 0.005)	4.5	3 _β is <i>gauche</i> to 4 _α
³ J _{3,4β} *	11.013 (± 0.005)	10.7	3 _β is <i>trans</i> to 4 _β
³ J _{3β,3OH}	1.131 (± 0.005)	N/O ²	3 _β is <i>gauche</i> to 3 _{OH}
² J _{4α,4β}	-14.748 (± 0.004)	14.8	Geminal coupling typical of an sp ³ carbon
³ J _{7β,7OH}	1.218 (± 0.003)	2.1	7 _β is <i>gauche</i> to 7 _{OH}
³ J _{10,11}	5.283 (± 0.007)	5.9	10 is <i>gauche</i> to 11
⁵ J _{10,15A}	-1.412 (± 0.007)	N/O ³	Typical coupling for a <i>W</i> -configuration
⁵ J _{10,15B}	-0.948 (± 0.007)	N/O ³	Typical of a rigid conformation
⁴ J _{10,16}	1.519 (± 0.007)	1.5	Typical coupling for an H and CH ₃ on an sp ² Carbon
² J _{13A,13B}	4.268 (± 0.004)	4.3	Geminal coupling indicating significant ring strain. Typical of an epoxide
² J _{15A,15B}	-11.817 (± 0.001)	12	Geminal coupling typical of an sp ³ carbon
³ J _{15A,15OH}	0.965(± 0.007)	N/O ²	15 _A is <i>gauche</i> to 15 _{OH}
³ J _{15B,15OH}	3.065 (± 0.007)	N/O ²	15 _B is <i>gauche</i> to 15 _{OH}

¹Simulations performed with the SpinWorks Operating Program with an RMSD below 0.031 Hz and a standard deviation between 0.01-0.09 Hz.

²Coupling to hydroxyl resonances not recorded in the literature

³Long range coupling not observed in the literature

*The labeling convention presented in the literature by Savard and Blackwell is employed here and will be reviewed in chapter 4.

It is important to note here that, in the previous literature assignment for DON, the hydroxyl protons and their couplings were not observed. Additional water in the sample may result in broadening of the hydroxyl signals due to fast exchange and the stoichiometry of water molecules per toxin, which can make it difficult to observe these signals. Furthermore, protons that are undergoing fast exchange are less likely to experience coupling with the other protons in the spin system since they are in constant motion. By removing the absorbed water, it is possible to effectively remove much of the exchange that occurs with the solvent, which helps to resolve the signals from the exchangeable protons.

The line widths in the ^1H spectrum of DON are relatively large upon comparison with typical solution-state ^1H NMR spectra of small natural products. As a result, the spectrum was simulated using a line width of 1.5 Hz; however, this was not suitable for all the signals, as some required line-broadening up to 3.00 Hz. Line-widths, such as these, may be present for a number of reasons; the first of which is an extremely short apparent transverse relaxation time. Line broadening of this sort is homogeneous, and is expected to affect all of the signals equally. Dynamics occurring between strongly coupled spins also result in line broadening of the participating spins. Long-range couplings can also result in increased apparent line-width and required serious consideration in these rigid systems. The nuclei of the C-ring are isolated from the rest of the molecule as they are connected to quaternary carbons. Only 4-bond and 5-bond coupling from methyl-14 to H-4 and H-3, respectively, would be expected based on the stereochemistry; however, the methyl-14 resonance remains quite sharp, with a width of 0.9 Hz; thus, the apparent line broadening due to long-range coupling can be ruled out.

The line broadening observed in the spectrum appears to be isolated primarily to the spins appearing on the C-ring, which is expected to exhibit a certain degree of flexibility. This may indicate that although the fused ring core is locked primarily in a single conformation, some movement in the C-ring, involving the C-3 and C-4 carbons is still possible. Therefore, signals resulting from the different conformations may be superimposed on each other, contributing to the apparent broadening of these lines. The presence of different conformations in DON will be investigated further in chapter 4.

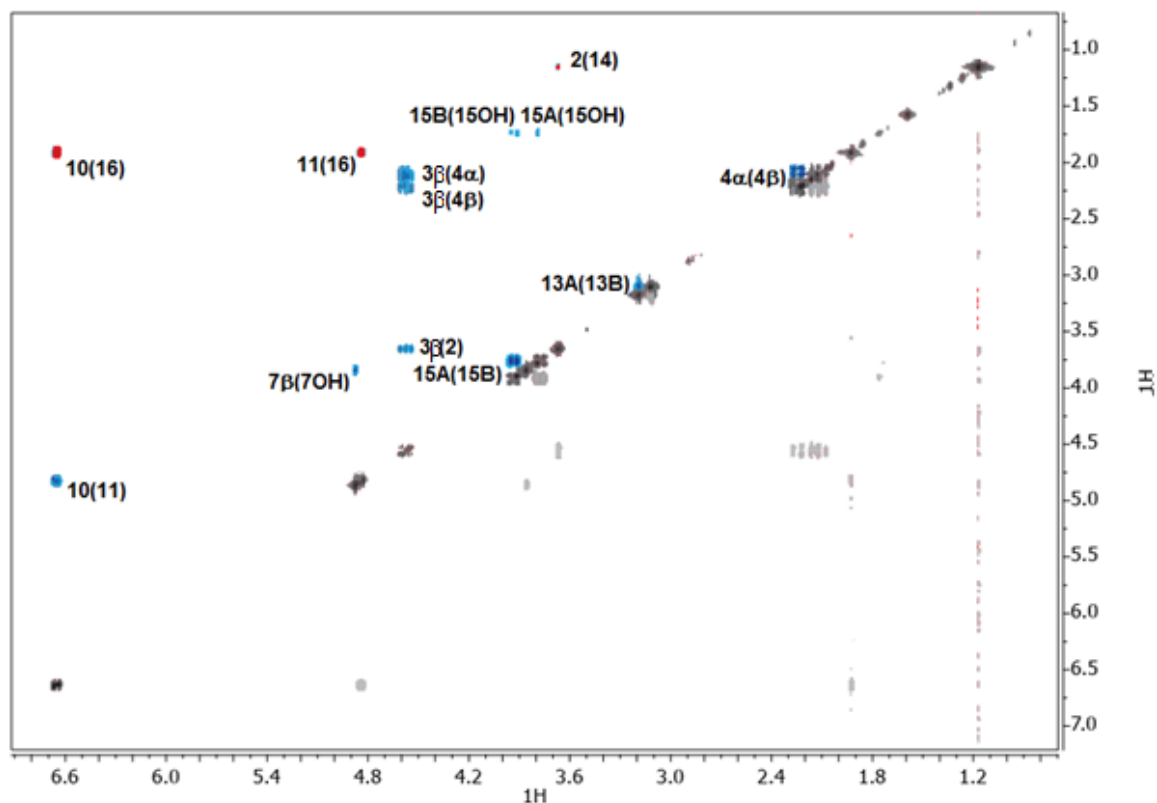


Figure 3. 3: The ^1H COSY spectrum for DON at 300 MHz in CDCl_3 . Strong three-bond couplings are shown in blue; whereas the longer range four- and five-bond couplings are shown in red. Autocorrelation peaks appear in grey.

The ^1H COSY spectrum confirms the assignment of the 1D ^1H spectrum. (figure 3.3) and indicates the presence of some longer range scalar coupling. The prominent cross peaks in the COSY spectrum represent the strong two- and three-bond couplings (blue), listed in table 3.1; and the small four- and five-bond couplings (red), indicate rigidity in parts of the molecule. Autocorrelation peaks appear on the diagonal and are shown in black. The relatively large five-bond coupling values of -1.41 and -0.95 Hz from H-10 to H-15_A and H-15_B, respectively, provide evidence for the rigidity of the A-ring as five-bond couplings are typically not observed due to rotation about the bonding system. Five-bond couplings generally indicate that the bonds are not free to rotate and hence not averaged. Large couplings occurring over 4 or more bonds, such as those between H-10 to H-15_{AB}, indicate that the bonds are locked in place in a manner that forces the C-15 methylene hydrogens to adopt a specific rotational isomer configuration. This rigidity becomes even more apparent when considering

that freely rotating methylene hydrogens should not be participating in long range coupling. Their observation leads to some convincing conclusions. If H-15_{OH} were to be involved in a hydrogen bond, as proposed by Nagy *et al.*, depicted in figure 3.1 [111], then the rotation about the C-6/C-15 axis would be slowed or completely stalled. In this case large long range couplings are suggestive of strong H-bonding imparting significant rigidity in this portion of the molecule. Similar scalar couplings between H-15_A or H-15_B with H-10 are not seen in the COSY spectrum, which may be the result of insufficiently long evolution times. It is important to note that couplings from H-10 to H-15_A and H-15_B are generally not observed for trichothecenes in the literature unless significant rigidity is apparent [79,135]. The COSY spectrum does indicate that a small five-bond coupling occurs between H-2 and methyl-14; however, this is not clearly seen in the 1D ¹H spectrum. Thus, any coupling that does take place is either very small, or if multiple configurations are present only a small population exist in the *trans*-W-configuration between H-2 and methyl-14, this may also serve to explain some of the unusual line broadening behavior observed for H-2.

The NOESY spectrum (figure 3.4) was crucial in determining the overall 3D conformation of DON. Of particular interest are the couplings observed to the methyl protons on C-14. These couplings help determine whether the epoxide proton H-13_B faces methyl-14. Comparing this to the labeling scheme introduced by Blackwell and Savard [135], a discrepancy is noted, as the scheme in the literature has the proton labeled H-13_A facing methyl-14, which is consistent with a similar observation made for T-2 toxin in chapter 2. Thus, the assignment of the H-13 protons of the epoxide appears to have swapped. In order to minimize confusion, the labeling convention in this spectrum will be maintained, which has H-13_A having the lower chemical shift; however, the 3D structure, the labeling must be amended to include these new insights.

Other notable data from the NOESY spectrum include the prevalence of exchange peaks (blue). Exchange with water is observed at the hydroxyl protons, H-3_{OH}, H-7_{OH}, and H-15_{OH}, and between H-3_{OH} and H-15_{OH}. Exchange also appears to be occurring at sites throughout the spectrum where exchange should not occur. This is seen between H-15_{OH} with H-15_A and H-15_B, H-3_β with H-4_α and H-4_β, as well H-10 with H-11. A slice taken through the NOESY spectrum at the location of

exchange between H-15_A and H-15_B, is shown in the inset of figure 3.4. Although these protons are expected to undergo through-space coupling, exchange is not expected, as these are not exchangeable sites. Multiple spectra of different samples of DON were taken in CDCl₃, each with different mixing times. In all cases, EXSY peaks appeared where they were not expected to occur. Thus, it is highly likely that these discrepancies are due to saturation transfer from nearby exchanging protons, signifying that the rate of exchange is much faster than the transverse relaxation time, T₂, of the compound.

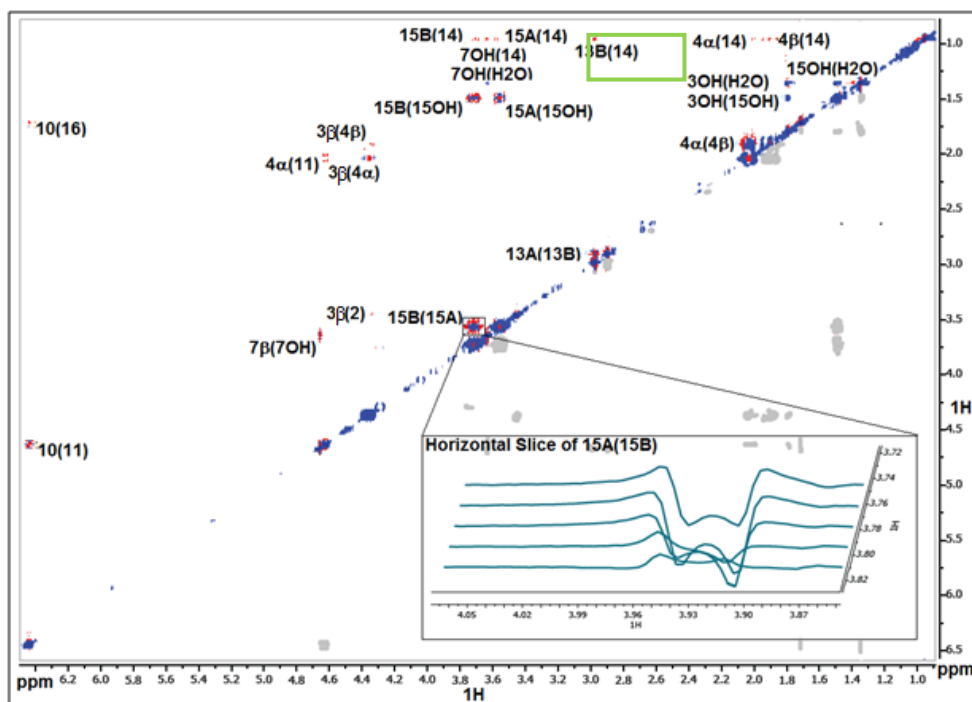


Figure 3. 4: The ¹H NOESY spectrum for DON at 300 MHz in CDCl₃. The positive phase through-space couplings are shown in red, and the negative phase exchange (EXSY) peaks are shown in blue. A horizontal slice through the correlation between 15_A and 15_B is shown in the inset, which clearly depicts that the peak has both positive and negative character.

The 1D and 2D ¹³C spectra help to confirm the assignment, and are depicted in figures 3.5, and 3.6A-B respectively. Of particular importance here is the confirmation of the identity of specific signals (i.e. the identity of H-7_β over that of H-7_{OH}). It is clear from the HSQC that the resonance appearing at 4.878 ppm is unequivocally identified as H-7_β; this is confirmed by the HMBC, which clearly demonstrates the weaker coupling to H-7_{OH}, appearing at 3.862 ppm.

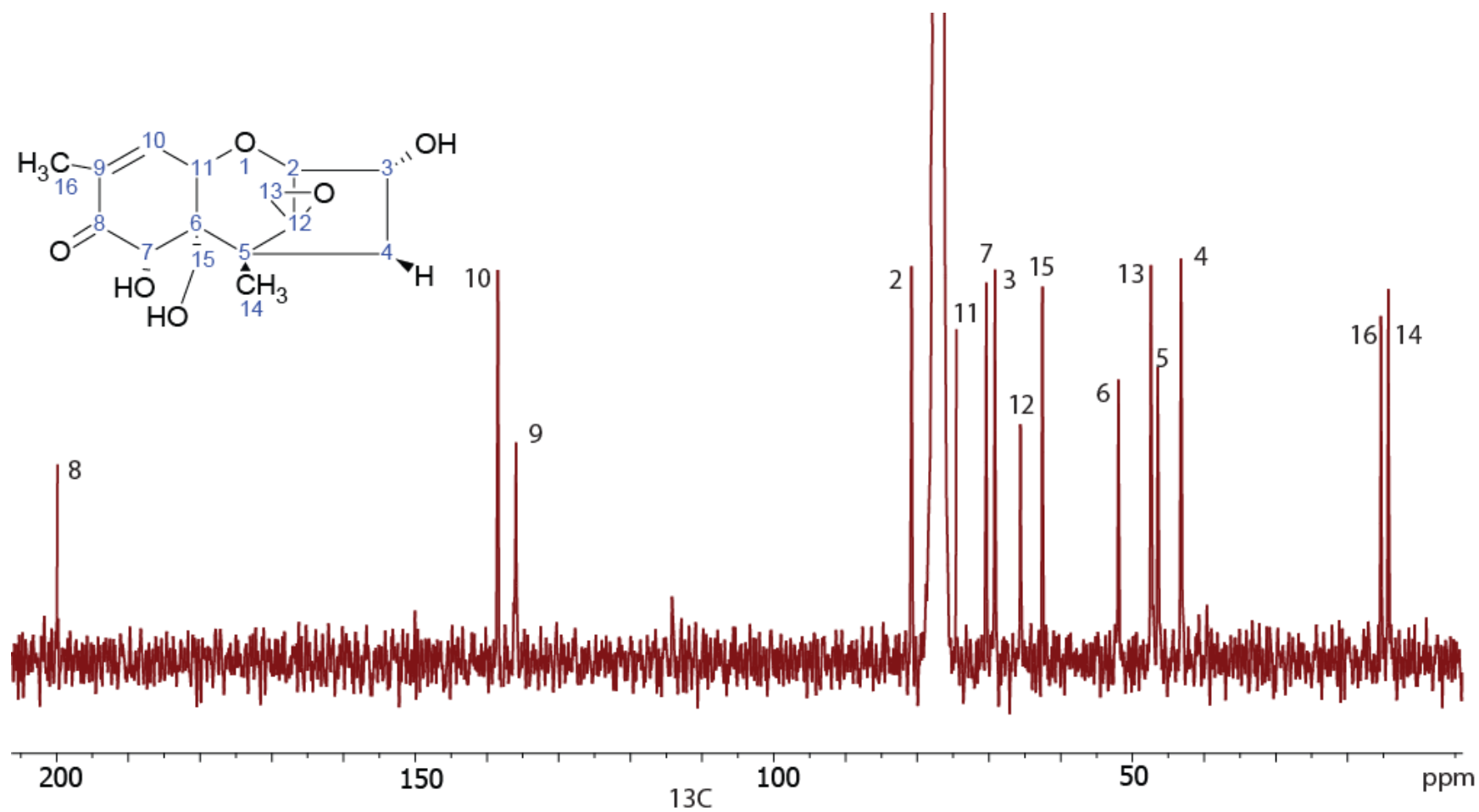


Figure 3. 5: Carbon-13 solution spectrum for DON in CDCl₃ at 75 MHz, all peaks are labeled and correspond to the numbered structure in the inset of the figure

Table 3. 3: Carbon chemical shifts and heteronuclear ^1H - ^{13}C couplings for DON in CDCl_3

^{13}C label	Chemical Shift – δ (ppm)	HSQC	HMBC
2	80.80	2	11
3	69.17	3_β	$2,3_{\text{OH}}, 4_{\alpha\beta}$
4	43.21	$4_\alpha, 4_\beta$	$2,4_\beta, 3_{\text{OH}}$
5	46.46		14
6	51.96		$3_{\text{OH}}, 4_{\alpha\beta}, 7_\beta, 14$
7	70.39	7_β	$7_{\text{OH}}, 14$
8	199.87		
9	135.96		11,16
10	138.46	10	11,16
11	74.53	11	14
12	65.61		$2,4_{\alpha\beta}, 13_{\text{AB}}, 14$
13	47.41	$13_{\text{A}}, 13_{\text{B}}$	
14	14.34	14	
15	62.56	$15_{\text{A}}, 15_{\text{B}}$	
16	15.37	16	11,16

The HSQC and HMBC spectra support the proton spectral assignment through the correlation of the protons to the carbon atoms, and can be used to walk across the carbon skeleton. Correlations for C-8 and C-15 appear to be missing. Carbon-8 is within 3 bonds of the protons on methyl-16, and the hydroxyl proton $\text{H-}7_{\text{OH}}$, and 2 bonds of $\text{H-}7_\beta$; however, C-8 is attached to a highly electronegative oxygen atom which may withdraw much of the electron density surrounding C-8 preventing the transfer of spin polarization between the bonded p-orbitals, consequently preventing the observation of any coupling to nearby protons. Carbon-15 only has one proton within 4 bonds that may be detected by HMBC, the hydroxyl proton 15_{OH} . This resonance appears broadened in the 1D ^1H spectrum, suggesting that it may be undergoing some exchange process with the solvent, eliminating the coupling to C-15 in the HMBC spectrum. Without these correlations, the assignment is incomplete; however, the peaks that are present in the HMBC do support the spectral assignment for DON.

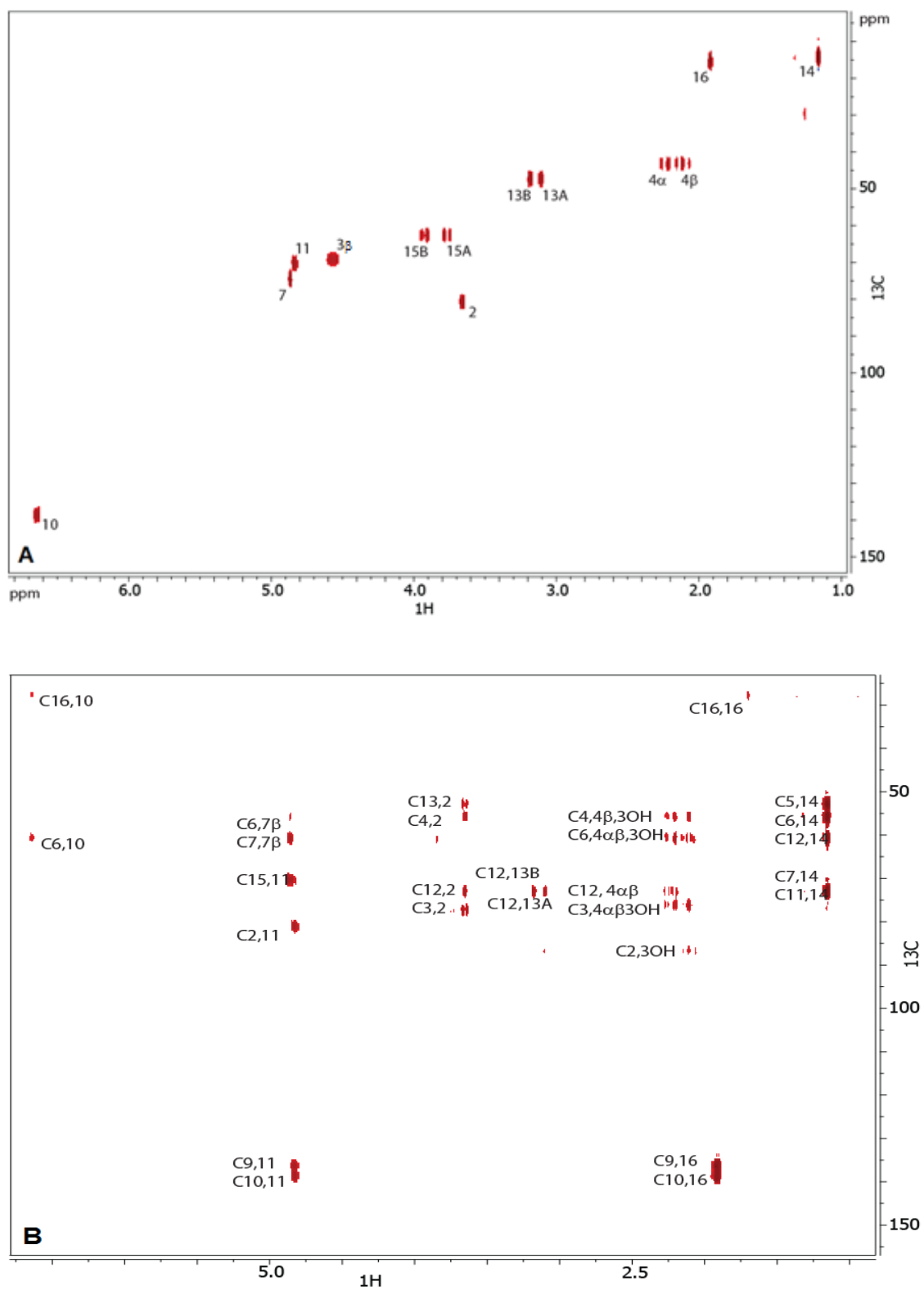


Figure 3. 6: Two-dimensional ^1H - ^{13}C correlation spectra for DON at 300 MHz and 75 MHz, respectively, in CDCl_3 . A) depicts the HSQC spectrum; B) depicts the HMBC spectrum

Interest in regards to the intra- and intermolecular hydrogen bonding interactions for the trichothecenes remains a point of interest for the group and through the careful analysis of these compounds in a water-depleted solvent system, it is possible to begin to analyze these interactions. DFT analysis of DON, performed by Nagy *et al.* suggested that the lowest energy conformation of DON would exhibit an intramolecular hydrogen bonding network [111], shown in figure 3.1. Although no direct evidence for this was obtained, the strong EXSY peaks between H-15_A and H-15_B, depicted in the inset of figure 3.4, suggest that these protons are exchanging with each other. Although this is something which is to be expected for methylene protons next to a chiral carbon, evidence for the exchange between enantiomers is rarely seen, as they are mirror images of each other, and thus, are chemically and magnetically equivalent. However, evidence of exchange between diastereotopic protons is common, as these may experience slightly different environments. In the case of H-15_A and H-15_B, they would become diastereotopic if C-15 were locked in place due to the hydrogen-bonding of H-15_{OH}, or another potential hydrogen bonding interaction. The signal for the proton resonance H-7_{OH} in the ¹H spectrum appears as a rather sharp peak, indicating that exchange with the solvent is not taking place. Were this resonance to undergo only a single hydrogen bond with H-15_{OH}, the signal would likely still appear fairly broad, as is seen for H-15_{OH} itself, which is approximately 2.5 Hz in width; however, H-7_{OH} remains sharp, with a measurable line-width of only 0.4 Hz; therefore, it is possible that a second hydrogen-bond with the carbonyl oxygen at C-8 helps to stabilize any movement of the bond, resulting in the sharp appearance of the H-7_{OH} resonance. This is further supported by the coupling observed between H-7_{OH} and H-7_β. Together, the coupling interactions of H-15_A with H-15_B, and H-7_{OH} with H-7_β, along with the sharp nature of H-7_{OH}, lend support for the lowest energy conformation, described by Nagy and coworkers, for DON [111].

Intermolecular hydrogen-bonding is also an important factor to consider. This appears to indicate that water may be bound to the molecule. Despite having removed much of the water from both the sample, by vacuum-pumping under nitrogen, and the solvent, by drying the chloroform with molecular sieves, there is still a water peak that appears in the proton spectra, as seen in figure 3.2. This water peak is even more apparent in the NOESY spectrum, depicted in figure 3.4, as the water

signals appears to have some through-space coupling interactions, and is observed to exchange with the hydroxyl protons in the compound. This seems to suggest that the interaction with water is not a transient one, but rather results from a more permanent binding event. This binding interaction with water is similar to the interaction previously reported for T-2 toxin, and was described in chapter 2. Exchange was shown to occur at all the hydroxyl sites appearing on the bottom side of the trichothecene core, and at least one water molecule was deemed to bind in the tetrahydropyranyl pocket of T-2 toxin. For DON the tetrahydropyranyl pocket is locked in place by the internal hydrogen bonding network, and water binding in this region may help to further stabilize the interaction, and rigidify the A-ring in DON. Figure 3.7 depicts the overall 3D structure of DON, including the intramolecular hydrogen bonding network, as well as the water bound within the tetrahydropyranyl pocket.

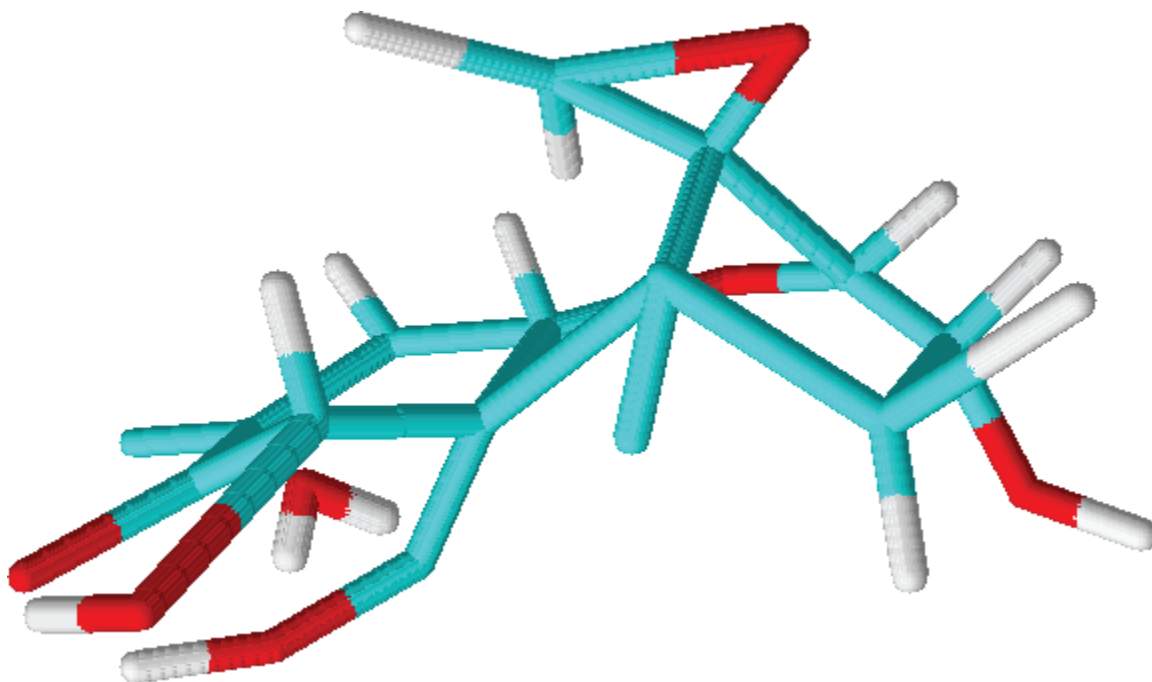


Figure 3. 7: Structure for DON depicting the possible formation of an internal hydrogen-bonded network, due to the proximity of the hydroxyl proton H-15_{OH} to the oxygen of H-7_{OH} and the proximity of the hydroxyl proton H-7_{OH} to the carbonyl oxygen of C-8. A water molecule is also predicted to bind within this region, in the tetrahydropyranyl pocket, and it is depicted here as well.

3.4.2 Characterization of Type B trichothecenes

The remaining trichothecenes comprising the subclass type B, were analyzed in a similar fashion to that described for DON in the previous section. The solution-state ^1H spectra were assigned and simulated to accurately determine the chemical shifts and coupling constants. To understand the rigidity of these compounds in solution, the through-bond scalar coupling was thoroughly examined. Where significant π -electron density was expected, coupling constants up to five-bonds were considered. These assignments follow the labeling conventions previously described by Savard and Blackwell [135]. The corresponding chemical shifts are described in table 3.4, with the coupling constants appearing in table 3.5.

Figure 3.8 provides a stacked plot for the individual toxins dissolved in CDCl_3 (or, in the case of NIV, in a 1:1 mixture of $\text{CDCl}_3:\text{CD}_3\text{OD}$). This figure clearly demonstrates the close agreement of the acetylated derivatives of DON (3-ADON and 15-ADON) with DON itself. The only exceptions are those signals that correspond to, or are coupled with, the acetylated substituents, which are highlighted in the figure. All other resonances in the spectra for 3-ADON and 15-ADON are in close agreement to those described in the spectrum for DON.

The addition of deuterated methanol (CD_3OD) to the NIV sample, in a 1:1 ratio with CDCl_3 , helps the toxin go into solution. NIV is not soluble in either of the neat solvents. Differences in the solvent are likely a major factor contributing to the variations in the chemical shift of the signals for NIV. The general coupling of each of the signals follows the same trend as the other compounds in chloroform; however, the introduction of the second solvent serves to shift some of the signals. The protic nature of the methanol also introduces the potential for chemical exchange with the solvent. Methanol may also interact directly with the molecule, binding to it much like water, inducing some shifts in frequency in the spectrum. Chemical exchange with the solvent will have the largest effect on the hydroxyl protons in the molecule, and this is likely the reason for the simplicity in the coupling of these signals, as well as the large difference in chemical shift, as compared to the other toxins investigated here. The hydroxyl protons for NIV are highlighted in figure 3.9, along with the signal for H-4 α (H-4 $_{\text{OH}}$), which is no longer strongly coupled to H-4 β , due to the hydroxylation at this site, and is

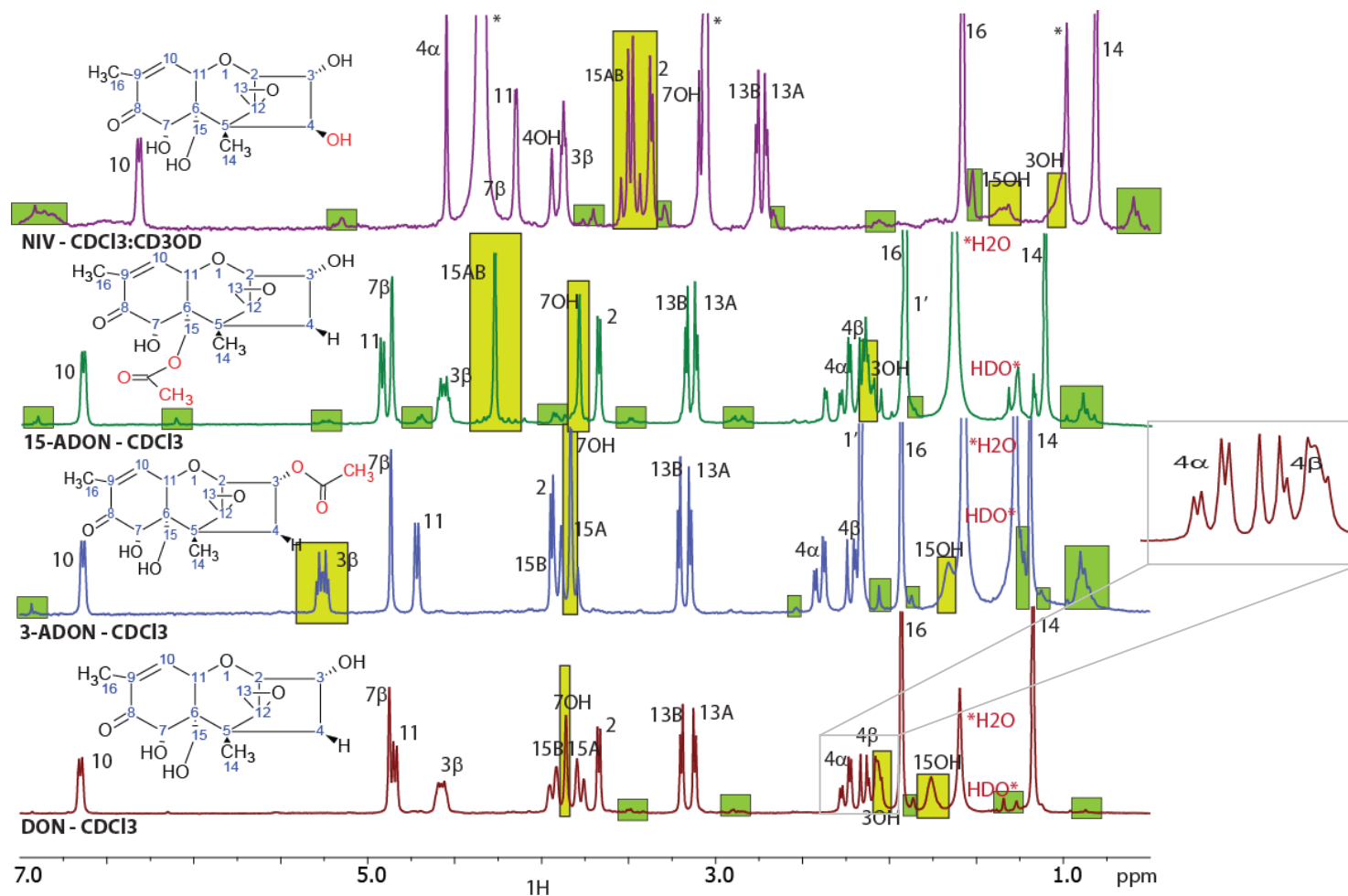


Figure 3. 9: Stacked Plot of the ^1H NMR solution-state spectra for the type B trichothecenes in CDCl_3 at 300 MHz. All spectra are compared to that for DON. The insets depict the structure for each toxin, and deviations in the substituent groups from DON are highlighted in red. Spectral peaks of interest are highlighted in yellow; peaks indicating potential degradation, or alternative configurations are highlighted in green. Solvent peaks are marked with a black asterisk, and the water peaks with a red asterisk. An inset showing the second-order effects on H-4 $\alpha\beta$.

Table 3. 4: Experimental and literature ¹H chemical shift data for the type B trichothecenes in CDCl₃ at 300 MHz

¹ H label	Chemical Shift – δ (ppm) in CDCl ₃							
	DON	DON (lit)	3-ADON	3-ADON (lit)	15-ADON	15-ADON (lit)	*NIV	*NIV (lit)
2	3.672 ¹	3.62	3.939 ¹	3.87	3.679 ¹	3.60	3.366 ¹	3.61 (\pm 0.24)
3_{β}	4.577	4.52	5.258	5.18	4.573	4.50	3.872	4.13 (\pm 0.26)
3_{OH}	2.067	N/O	N/A	N/A	2.143	N/O	0.977	N/O
4_{α}*	2.247	2.20	2.395	2.85	2.262	2.20	4.543	4.41 (\pm 1.3)
4_{β}* or 4_{OH}	2.129	2.07	2.199	2.12	2.145	2.07	3.939	N/O
7_{β}*	4.878	4.83	4.865	4.79	4.873	4.81	4.324	4.80 (\pm 0.36)
7_{OH}	3.862	N/O	3.831	N/O	3.791	N/O	3.157	N/O
10	6.656	6.61	6.635	6.54	6.644	6.58	6.311	6.57 (\pm 0.26)
11	4.845	4.80	4.714	4.66	4.928	4.87	4.329	4.59 (\pm 0.26)
13_B*	3.195	3.15	3.206	3.14	3.178	3.11	2.756	3.01 (\pm 0.25)
13_A*	3.120	3.073	3.144	3.08	3.120	3.06	2.707	2.96 (\pm 0.24)
14	1.174	1.13	1.189	1.12	1.117	1.04	0.807	1.07 (\pm 0.20)
15_B	3.933	3.89	3.912	3.81			3.513	3.72 (\pm 0.21)
15_A	3.783	3.733	3.859	3.75	4.281	4.21	3.459	2.78 (\pm 0.68)
15_{OH}	2.066	N/O	0.985	N/O	N/A	N/A	1.496	N/O
16	1.931	1.86	1.929	1.85	1.927	1.86	1.583	1.83 (\pm 0.25)
1'	N/A	N/A	2.166	N/O	1.917	N/O	N/A	N/A

*NIV was dissolved in a 1:1 ratio of chloroform (CDCl₃): methanol (CD₃OD).

¹All Chemical shifts were simulated to 0.001 Hz accuracy

*Labeling scheme presented in the literature by Savard and Blackwell is employed here and will be evaluated in chapter 4. Previously unreported chemical shifts are highlighted in purple. Large discrepancies between the experimental and literature data are highlighted in peach.

Table 3. 5: Experimental and literature scalar coupling constants observed for the type B trichothecenes in CDCl₃ at 300 MHz

¹ H label	Scalar Coupling Constants – J (Hz) in CDCl ₃							
	DON	DON (lit)	3-ADON	3-ADON (lit)	15-ADON	15-ADON (lit)	NIV	NIV (lit)
³ J _{2,3}	4.643 (± 0.005)	4.5	4.418 (± 0.001)	4.5	4.417 (± 0.001)	4.4	3.572 (± 0.002)	4.7
³ J _{3,4α}	4.150 (± 0.005)	4.5	4.285 (± 0.001)	4.5	4.096 (± 0.001)	4.5	4.891 (± 0.002)	3.4
³ J _{3,4β}	11.013 (± 0.005)	10.9	11.352 (± 0.001)	11.2	11.064 (± 0.001)	10.6	N/A	N/A
³ J _{3,3OH}	1.131 (± 0.005)	N/O	N/A	N/O	N/O	N/O	N/O	N/O
² J _{4α,4β}	-14.748 (± 0.004)	14.8	-15.069 (± 0.001)	15.1	-14.807 (± 0.001)	14.8	N/A	N/A
³ J _{7β, 7OH}	1.218 (± 0.003)	2	1.592 (± 0.001)	2.1	1.438 (± 0.001)	1.9	N/O	N/O
³ J _{10,11}	5.283 (± 0.007)	5.9	5.911 (± 0.001)	5.9	5.769 (± 0.001)	5.8	5.646 (± 0.005)	5.9
⁵ J _{10,15α}	1.412 (± 0.007)	N/O	N/O	N/O	N/O	N/O	N/O	N/O
⁵ J _{10,15β}	0.948 (± 0.007)	N/O	N/O	N/O	N/O	N/O	N/O	N/O
⁴ J _{10,16}	1.519 (± 0.007)	1.5	1.304 (± 0.001)	1.5	1.314 (± 0.001)	1.6	0.483(± 0.002)	1.5
² J _{13α,13β}	4.268 (± 0.004)	4.3	4.247 (± 0.001)	4.3	4.271 (± 0.001)	4.2	4.362 (± 0.002)	4.4
² J _{15α,15β}	-11.817 (± 0.001)	11.7	-11.826 (± 0.001)	11.7	N/O	N/O	-12.022 (± 0.004)	12.1
³ J _{15α,15OH}	0.965 (± 0.007)	N/O	N/O	N/O	N/A	N/O	3.513 (± 0.001)	N/O
³ J _{15β,15OH}	3.059 (± 0.007)	N/O	N/O	N/O	N/A	N/O	3.459 (± 0.001)	N/O
³ J _{11,16}	N/O	N/O	0.739 (± 0.001)	N/O	0.141 (± 0.001)	N/O	0.799 (± 0.001)	N/O

Previously unreported coupling constants are highlighted in purple. Large discrepancies between the experimental and literature data are highlighted in peach.

Close analysis of each of the type B trichothecenes demonstrates that the assignment in the literature for these in CDCl_3 was never completed, either due to a lack of sufficient resolution or the overwhelming presence of water in the solvent system exchanging out the signals from the hydroxyl protons. In order to prevent the interference of water in our samples, the CDCl_3 was dried over molecular sieves prior to sample preparation. Furthermore, the presence of adsorbed water in the sample was of concern, and the powdered DON sample was dried by vacuum-pumping under nitrogen prior to sample preparation. Through the use of water-depleted solvent, chemical shifts and coupling constants not previously reported were observed. Furthermore, the correction of specific assignments in the spectrum was also completed.

For example, the literature data for DON states that H-7_β appears at 4.83 ppm; however, the HSQC (figure 3.6A) connects C-7 to the signal appearing at 3.862 ppm; whereas, the HMBC (figure 3.6B) connects C-7 to the signal at 4.878 ppm in the experimental spectrum. Two-dimensional heteronuclear correlation spectra were not presented in the previously literature and the sharp nature of the H-7_{OH} is rather misleading without having all the information to discern the true identity of this peak. From this study, it is clear that the assignment for H-7_β is incorrect in the current literature, and refinement is required such that H-7_β appears at 3.862 ppm and H-7_{OH} at 4.878 ppm.

For NIV, the majority of the chemical shifts in the experimental data appear to be shifted to a lower frequency as compared to the literature data by roughly 0.2 ppm, this may be due to the removal of water from the CDCl_3 solvent prior to mixing with CD_3OD , or a more precise setting of the reference frequency. However, two shifts in particular appear to deviate dramatically compared to the literature data, H-4_α and H-15_A . The proton H-15_A was confirmed by the coupling observed with H-15_B , and H-4_α by the coupling with H-3 .

The NOESY spectrum for DON also provides information for correction to the 3D structure. A through-space coupling between the signals for protons H-13_B and methyl-14 is observed and is highlighted in figure 3.4. Protons H-13_A and H-13_B are the methylene hydrogens of the epoxide ring.

The 3D geometry of the epoxide places it at the top of the molecule and it aligns with the length of the core, such that it can be used to cut a plane through the molecule. Carbon C-12 is a chiral center, which adopts an *S*-stereochemical configuration, and since the two sides of the plane are not equivalent, see figure 3.10, it is clear that H-13_A and H-13_B are diastereotopic protons. Where one of the methylene protons from the epoxide occupies space on the same side of the molecule as H-2, and the other occupies space on the same side as methyl-14. Previous literature suggests that H-13_A, the lower chemical shift proton, exists on the same side of the molecule as methyl-14 [135]; however, based on the peak from the NOESY spectrum for DON, this is not the case. The coupling in the NOESY correlates the higher chemical shift proton H-13_B to the protons on methyl-14, which suggests that these protons are in close proximity to one another; thus, H-13_B and methyl-14 must be on the same side of the ring, which is demonstrated by the highlighted H-13_A and H-13_B protons in figure 3.10.

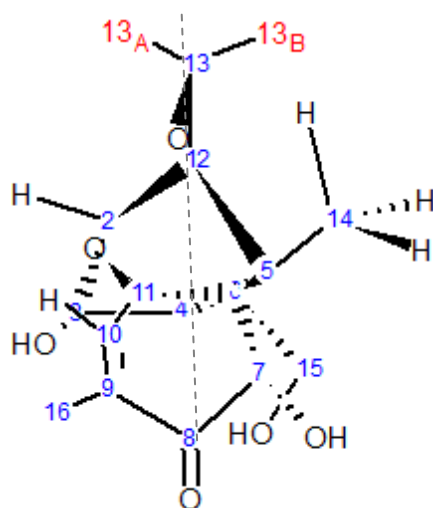


Figure 3. 10: View down the length of the trichothecene core for DON demonstrating the conformation of the methylene protons from carbon-13 of the epoxide, which appear on either side of the core structure. H-13_B is in close proximity to the methyl protons on C-14; whereas, H-13_A is on the opposite side of the ring.

The same labeling error is present for all of the trichothecenes of this sub-class. Thus, the convention for the labeling of the structure at the epoxide methylene protons is reversed, in the case of the type B trichothecenes. This was not the case for T-2 toxin, as seen in chapter 2. It is possible

that this differentiation from the other trichothecene resides with the key structural feature for this sub-class, the ketone functionality at C-8. The presence of the ketone at C-8 offers some interesting features structurally. First of all, the addition of this C=O double bond results in conjugation to the nearby C=C double bond occurring between carbons C-9 and C-10. This is evidenced by the deshielding on H-10, which is shifted to a much higher frequency than what was observed for T-2 toxin in chapter 2, and likewise in the database of literature provided by Savard and Blackwell [135]. The conjugation of the double bonds in the A-ring changes the geometry in this portion of the core structure, and forces a planar bond structure about carbons C-7, C-8, C-9, and C-10. Recall that in chapter 1, the geometry about the A-ring was described as being in a half-chair conformation; however, the planarity about the conjugated portion of the A-ring provides counterevidence for this statement in the case of the type B trichothecenes. The geometry about the A-ring is now primarily planar, with only a slight twist in the bonds from C-7 to C-6 and C-6 to C-11. Due to the fused nature of the rings in the trichothecene core, the increase in ring strain from the A-ring is distributed throughout the entire core structure. Thus, minor structural differences that help in mediating this distribution have likely resulted in the higher frequency H-13 proton appearing on same side of the core as methyl-14, rather than next to the H-2, which is counter to the structure described in the literature for the epoxide protons in the spectrum [135]. Traditional conventions dictate that labeling of the resonances be done according to chemical shift (i.e. the lower chemical shift frequency is given the lower value in the alphabet, such that H_A would have the lower chemical shift). This convention has been maintained, and as a result the labeling of the protons on the structure has been changed accordingly.

In the earlier section on the complete spectral analysis of DON, the existence of an intramolecular hydrogen bonding network was investigated, whereby hydrogen-bonding between H-15_{OH} and H-7_{OH}, as well as H-7_{OH} with the oxygen of the C-8 ketone, was confirmed through the careful analysis of the linewidth of H-7_{OH}, and the couplings between H-15_A with H-15_B, and H-7_{OH} with H-7_β. The same observations are made for all of the toxins. This includes the compound 15-ADON which, due to the presence of an acetyl group at C-15, was expected to disrupt this hydrogen-

bonding network to some extent; however, the signal for H-7_{OH} in 15-ADON remains relatively sharp. Interestingly, the resonance representing the methylene protons H-15_A and H-15_B, appears as a sharp singlet, suggesting that they are chemically and magnetically equivalent, despite the fact that they neighbor a chiral carbon. This may be a result of second-order effects in the spectrum, where the chemical shift difference between the two protons approaches zero, this is described in greater detail in chapter 4.

Lastly, it is important to note that some small peaks appear in all of the samples for the type B trichothecenes which were purchased from Sigma-Aldrich and dissolved in the dried CDCl₃ solvent. The small peaks (highlighted in green in figure 3.7) suggest the coexistence of a secondary configuration, degradation products, or possible impurities. Note that some of these peaks are the same for all of the toxins, where only slight differences in intensity are observed. For example, the multiplet near 0.9 ppm is seen in all of the spectra, but is most intense in 3-ADON, and at baseline level in DON. Another baseline peak appearing in all of the trichothecene spectra near 7.0 ppm, represents a highly deshielded proton and falls within the region of conjugated double bonds, and may represent a second conformation for the proton H-10. As described earlier in this chapter, some of the peaks in the DON spectrum appear to be experiencing some line broadening, which may be due to the presence of multiple conformations. Thus, it is possible that these small baseline peaks are representative of a second conformation for the compounds.

3.4.3 Deuterium exchange and water-binding in the type B trichothecenes

All samples were prepared with CDCl₃ which has been dried over molecular sieves to ensure that any water present was that which was originally bound to the toxin, and not carried by the solvent. DON was obtained from two different sources, and the solid material in each case had a different appearance. The DON from Sigma-Aldrich had a flaky appearance. The material was then packaged and sealed under dry conditions, with estimated purity of the sample being greater than 95%. The sample was originally shipped in a cold box along with dessicant packages. The sample was

further dried under nitrogen by vacuum-pumping on the sample to remove residual water. The second sample was provided by Barbara Blackwell at the Agriculture and Agri-Food Canada (AAFC) Research Center in Ottawa. Sample material was prepared by fermentation of *F. graminearum* inoculated rice cultures, and the toxin was isolated using affinity chromatography. This sample had an estimated purity of greater than 90%. The material obtained from AAFC Ottawa had the appearance of a white powder, and had not been dried under vacuum to remove residual adsorbed water, nor was it tightly sealed. It was shipped in regular packaging, without desiccant, and was analyzed without further drying. Both samples were analyzed in the pre-dried CDCl₃ and the ¹H spectra are compared in figure 3.11.

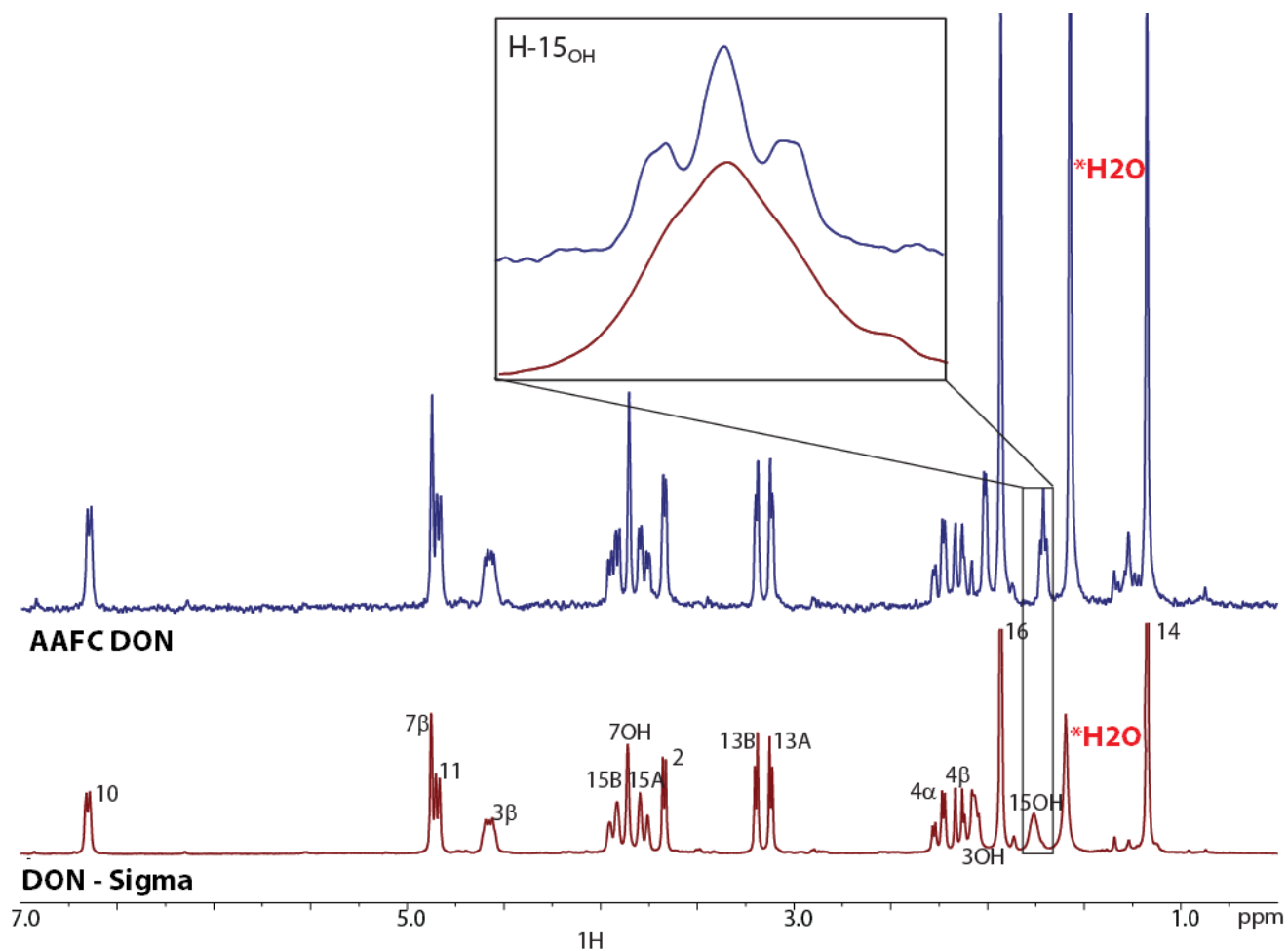


Figure 3. 11: Comparison of the ^1H spectra collected for DON received from different sources at 300 MHz and ambient temperature. The spectrum in blue was recorded for the DON sample obtained from Sigma-Aldrich; the red spectrum was recorded for the sample obtained from AAFC Ottawa. In both cases, the samples were prepared in CDCl_3 which had been dried over molecular sieves to remove absorbed water from the solvent; thus, the water peaks which are highlighted in green are due to water present within the sample itself. Peaks from 15_{OH} and 3_{OH} are sharp and demonstrate a well-defined coupling structure for the AAFC sample, which is demonstrated for 15_{OH} in the inset of the figure.

Despite the fact that more residual water is present in the AAFC Ottawa sample, all of the peaks, and the hydroxyl resonances in particular, appear to be much sharper and without the line broadening observed in the sample prepared from the commercially available Sigma-Aldrich material. Of particular note is the sharp nature and coupling behaviour observed for the H-3_{OH} and H-15_{OH} hydroxyl peaks. The presence of excess water is expected to have the opposite effect, further broadening the signals, due to chemical exchange; however, the linewidths for the hydroxyls are approximately 1.5 Hz, which is now comparable to the linewidths of the other peaks in the spectrum which have a line broadening of 1.0 Hz.

One of the theories for the line broadening in the Sigma-Aldrich sample was the presence of multiple conformations that are coalescing, resulting in broadened signals for H-3_β, H-3_{OH}, H-4_{αβ}, and H-15_{AB}, in particular. It was mentioned by one of our colleagues at AAFC Ottawa that DON has been shown to exist with different water to toxin ratios; however, little direct literature data exists on this matter [59]. If more than one binding site were to exist for water on the DON structure, then we can make the assumption that the binding site described for the tetrahydropyranyl pocket (chapter 2), is an extremely tight water-binding site, allowing for its observation in the dry DON sample from Sigma-Aldrich. The integration ratio for the water in the Sigma-Aldrich sample is approximately 1 molecule of water per 1 molecule of toxin. However, during the synthesis of the toxin, water may be directed to specific sites where it binds less tightly, but also helps to further stabilize the conformation of the toxin. The integration of the water peak in the AAFC spectrum gives a ratio of approximately 7 molecules of water per molecule of DON.

In order to determine whether the water in the Sigma-Aldrich sample is indeed tightly bound, deuterated water (D₂O) was added dropwise to the Sigma-Aldrich sample of DON in CDCl₃, and compared to the original Sigma-Aldrich spectrum collected for DON. ¹H and NOESY spectra were collected for each drop of water added to the sample. Figure 3.12 depicts the results obtained for DON in the presence of a 1 ppm D₂O, as well as in the presence of 2 ppm, 5 ppm and 7 ppm D₂O.

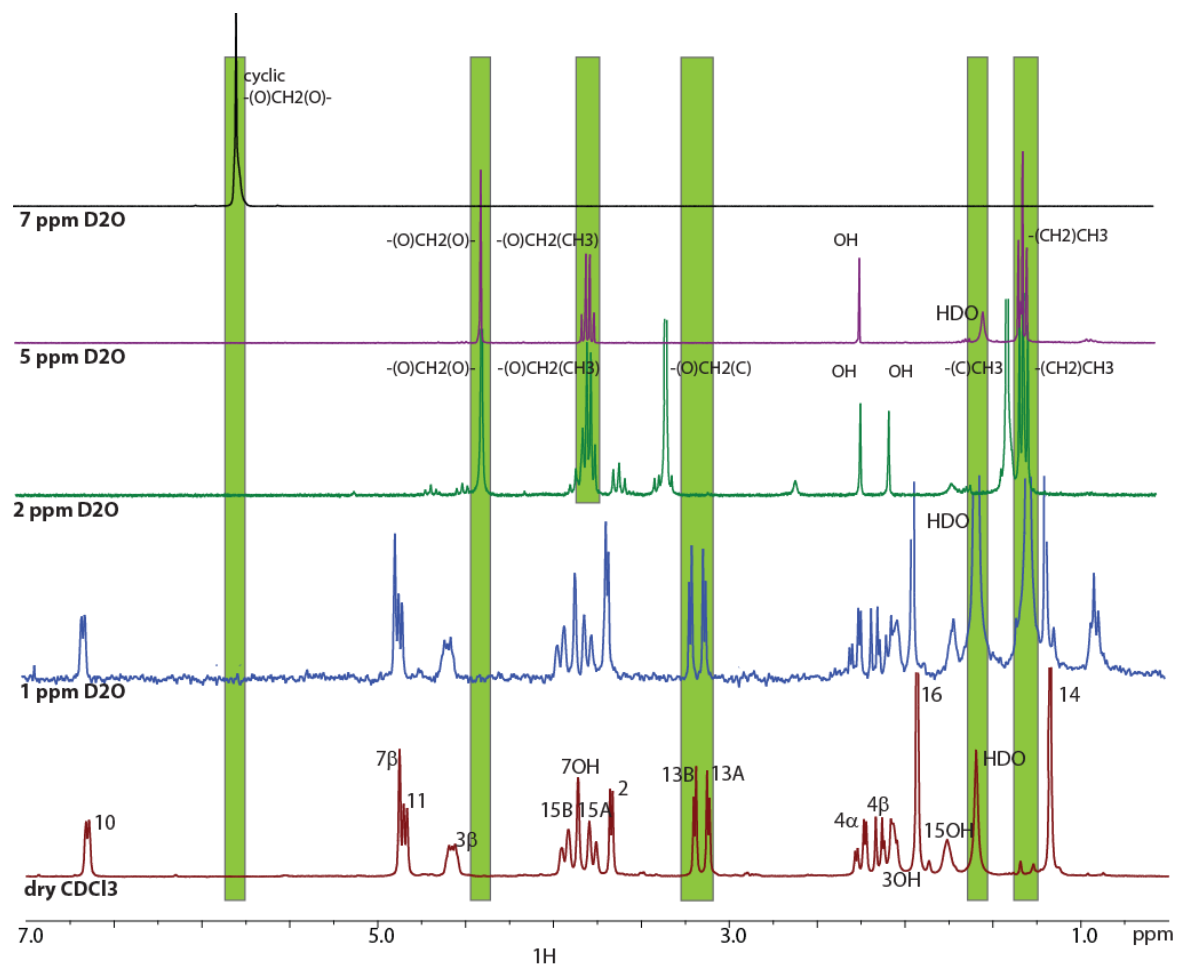


Figure 3. 12: Deuterium exchange experiment for DON in $CDCl_3$ at 300 MHz. Plots are stacked showing the original dry $CDCl_3$ experiment, as well as the spectra for the addition of one through four drops of D_2O . Although all peaks in the spectra observe successive changes, some major peaks of interest are highlighted in the spectrum.

Only a few differences can be seen in the DON spectrum when a 1 ppm D₂O is added to the sample. The linewidth and coupling pattern of all peaks in the sample is preserved. The coupling of the hydroxyl protons to the other resonances within the spectrum is maintained, and is highlighted in figure 3.12. In particular, H-7_{OH} maintains its sharp appearance, and the coupling between H-7_{OH} and H-7_β is preserved. One would expect that if these resonances were exchanging rapidly with the solvent that the hydroxyl signals would have all but disappeared due to exchange with deuterium, and coupling would be interrupted. Minor differences include a slight increase in frequency of the chemical shifts for the epoxide protons (H-13_{AB}) and the two methyl resonances (H-14 and H-16), suggesting further deshielding due to close proximity to an electronegative atom, or alternatively increased ring strain. A slight decrease in frequency is observed for the hydroxyl resonance at C-3, which could indicate that exchange with water is occurring within the sample. The appearance of a low chemical shift triplet at approximately 0.9 ppm in the spectrum is believed to be a second methyl-14 resonance. The splitting of the H-14 signal into two contributions suggests the potential for a second, minutely different configuration, which could arise if two or more trichothecene molecules were to associate with one another as dimers.

When the concentration of D₂O is raised to 2 ppm, the spectrum becomes unrecognizable. One suggestion is that a concentrated impurity is present in the sample, which may have been introduced when the deuterated water was added, and is now obscuring the spectrum due to intensity of the peaks. However, magnification of the vertical scale for the spectrum does not produce any baseline signals for the original toxin; thus, the presence of an impurity is highly unlikely. It is suggested that a degradative process may have occurred in the sample, upon addition of excess D₂O.

Certain features of the spectrum shown in figure 3.12 provide evidence for this type of process. First of all, the epoxide protons H-13_A and H-13_B appear to have been lost when 2 ppm D₂O is present, and do not reappear with the addition of more deuterated water. When a 1 ppm D₂O was added to the sample, the signals for the epoxide protons are shifted slightly to a higher frequency, indicating that they have been further deshielded from the “dry” spectrum. This deshielding may be either a result of some close proximity interaction with the oxygen atom of the water, or an increase

in the ring strain for the 3-membered epoxide ring. In either case, the potential for nucleophilic attack by the water on either the C-12 or C-13 carbons is present. Such an attack would lead to the opening of the epoxide ring, and the methylene protons at C-13 would become enantiomeric, rather than maintain their diastereotopic nature. These methylenes would now be free to rotate and may exhibit chemical and magnetic equivalence in the spectrum, reducing the two signals to a single sharp peak. It is possible to identify the pattern of the major peaks in the spectrum which are listed in table 3.6. Baseline peaks are also observed and are highlighted in blue in the table, suggesting that the degradation process is not yet complete, and that some additional species may exist in the solution.

Another vital element in the spectrum is the loss of the signal for H-10. H-10 is the key feature of the type B trichothecenes, as it has a high chemical shift due to the conjugated double bonds of the C-8 carbonyl and the C-9/C-10 double bond. Loss of this feature indicates loss of conjugation, either through the breaking of the carbonyl bond, or the C-C double bond. Furthermore, the chemical shift for the proton H-3 β is maintained, but the coupling pattern has changed. This particular peak is rather well-resolved, and appears as a doublet of either triplets or quintets. Recall that in the deuterium exchange experiment performed for T-2 toxin (figure 2.2B), the signal for H-3 β changed dramatically, shifting to a much higher frequency, and the loss of coupling between H-3 β and the hydroxyl proton H-3_{OH} simplified the signal to a doublet of triplets as well. Thus, here we see that the water has finally exchanged with the hydroxyl proton for H-3_{OH}. The other signals in the spectrum for the 2 ppm D₂O experiment are indicated in the spectrum in figure 3.12, and described in table 3.6. This leads to the conclusion that an intermediate in the degradation process may have a structure similar to that shown in figure 3.13.

Table 3. 6: Chemical shift and scalar coupling of potential degradation products in the presence of 2 ppm D₂O for the DON spectrum in CDCl₃ taken at 300 MHz and ambient temperature.

Chemical Shift δ (ppm)	J-coupling (Hz)	Integration	Identity
4.63	8.62	0.25	H-3 (Conformation 1)
4.46	8.62	0.25	H-3 (Conformation 2)
4.34	N/A	2	-O-CH ₂ -O
3.80	8.62 (Second-order with 3.56 ppm peak)	0.5	H-15 _A ?
3.73	6.98	2	-O-CH ₂ -CH ₃
3.56	8.62 (Second-order with 3.80 ppm peak)	0.5	H-15 _B ?
3.36	N/A	0.25	
3.29	N/A	2	-O-CH ₂ -C
2.56	N/A	0.25	Broad (-OH)
2.193	N/A	1	-OH
2.02	N/A	1	-OH
1.66	N/A	0.25	Broad (-OH)
1.35	N/A	3	-C-CH ₃
1.26	6.98	3	-CH ₂ -CH ₃

The degradation appears to continue as the 5 ppm and 7 ppm D₂O spectra are recorded. When 5 ppm D₂O is present, the spectrum simplifies further, and only a few signals appear to be present, that of a lone methylene sandwiched between two oxygen atoms (4.34 ppm), and an ethyl group attached to an oxygen (quartet at 3.73 ppm coupled to triplet at 1.25 ppm), as well as a hydroxyl appearing at 1.48 ppm. The peaks observed in the DON spectrum in the presence of 5 ppm D₂O are provided in table 3.7. The baseline peaks which were present in the 2 ppm D₂O spectrum are no longer present, indicating that the degradation process has continued, and nothing remains of the original trichothecene product. The predicted structure for this intermediate is also depicted in figure 3.13, and may be a precursor to diethoxymethane.

Table 3. 7: Chemical shift and scalar coupling of potential degradation product in the presence of 5 ppm D₂O for the DON spectrum in CDCl₃ taken at 300 MHz and ambient temperature.

Chemical Shift δ (ppm)	J-coupling (Hz)	Integration	Identity
4.34	N/A	2	-O-CH ₂ -O
3.73	7.08	2	-O-CH ₂ -CH ₃
1.48	N/A	1	-OH
1.26	N/A	1	HDO
1.25	7.07	3	-CH ₂ -CH ₃

Finally, in the presence of 7 ppm D₂O the spectrum has simplified to only a single peak, appearing at approximately 5.70 ppm. This chemical shift is highly indicative of a simple vinylic proton, and may result from the polymerization and dehydration of the intermediate predicted for the 5 ppm D₂O spectrum. Oxygen species are highly present in the sample, and from the degradation pattern observed for the 2 ppm and 5 ppm D₂O spectra, we can be sufficiently confident that oxygen is incorporated into the final compound. The final compound is predicted from the NMR to be tetrahydrodioxane, which has the appearance in NMR of a singlet at approximately 5.9 ppm. An example of the degradation mechanism, predicted from the chemical shift pattern in the spectra shown in figure 3.12, is depicted in figure 3.13.

Reproduction of this experiment with the collection of two-dimensional homonuclear and heteronuclear spectra, along with the collection of ¹³C spectra and infrared (IR) and mass spectroscopy data will help to confirm the identity of the intermediates in the degradation process and add further weight to these claims.

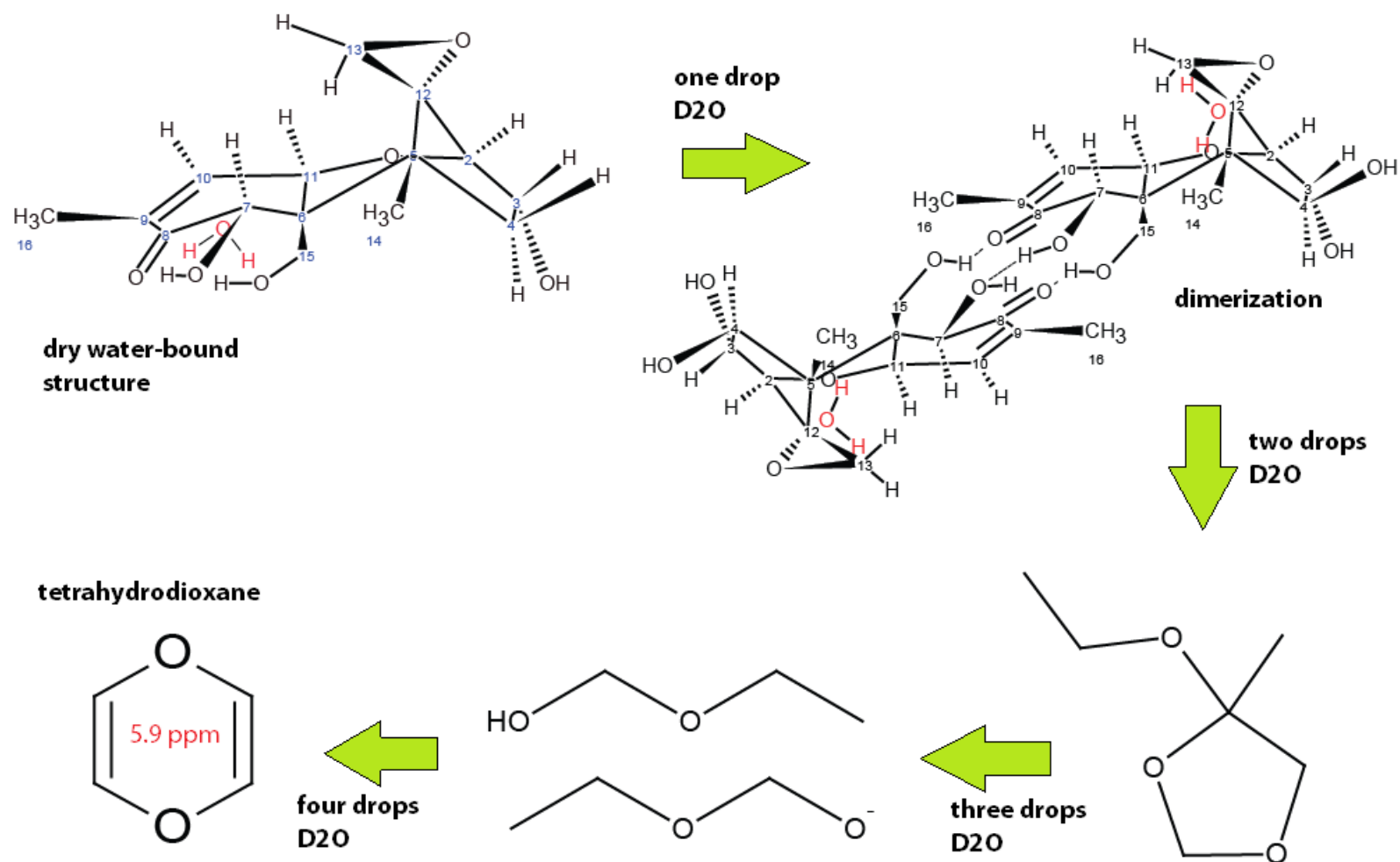


Figure 3. 13: Predicted degradation mechanism of DON upon the addition of D₂O to the sample in CDCl₃ at ambient temperature.

Throughout the literature, the trichothecene core, and particularly the epoxide ring are described as being incredibly stable towards degradative processes involving heat, chemical attack, and time [10,17,28,38,118,133]. Yet the effect of solvent has not been investigated in great detail. It is well understood that water is difficult to remove from samples of the trichothecenes [59,60], and the presence of bound water in the sample of T-2 toxin was described in chapter 2. Water appears to be necessary for structural stability of the toxins, through a bridging interaction in the tetrahydropyranyl pocket, and is evidenced by the sharp lines in the AAFC DON spectrum in CDCl_3 . However, in the case of DON, different water to toxin ratios have been shown to occur, which may indicate that multiple water-binding sites may be present [59]. The different water ratios were discovered during attempts at crystallization of DON from methanol, another polar solvent.

When considering the analysis of the NOESY spectrum (figure 3.14) obtained for the sample where only a 1 ppm D_2O has been added, it becomes apparent that water has been excluded from the DON structure as exchange at the hydroxyl protons is no longer present.

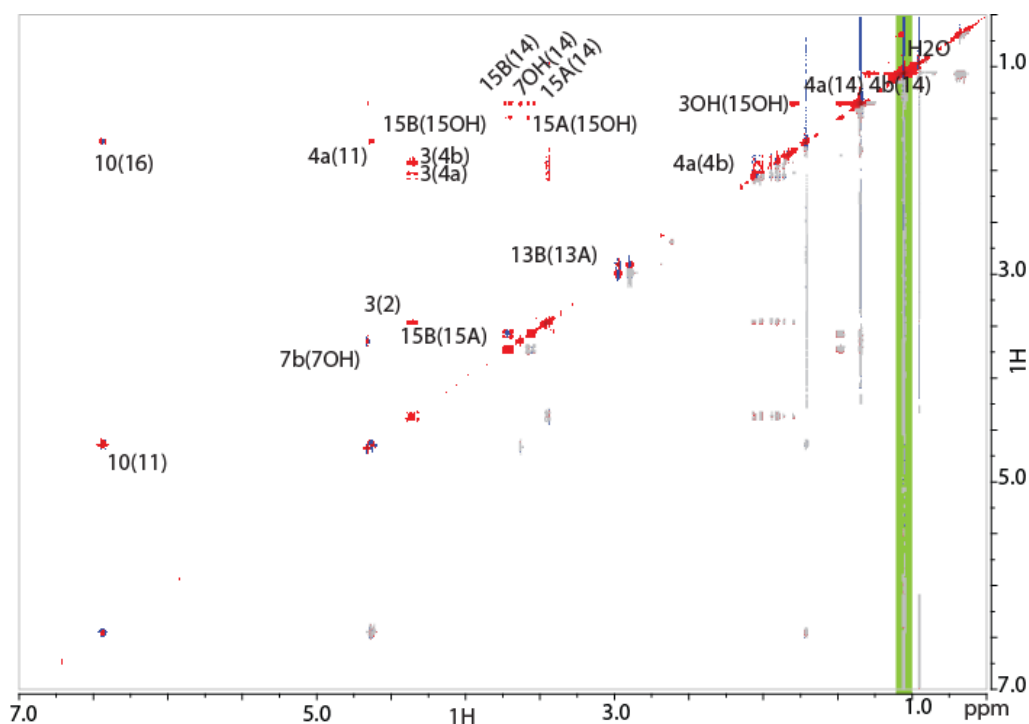


Figure 3. 14: ^1H NOESY spectrum for DON in CDCl_3 upon the addition of 1 ppm D_2O to the sample. The peak for H_2O is highlighted along the vertical.

The NOESY spectrum obtained for the sample where 1 ppm D₂O was added lacks any evidence for exchange with water at any of the hydroxyl sites. The water peak is highlighted in figure 3.14 along the vertical so as to not interfere with any of the other signals. The T₁ noise which is present in the spectrum provides a clear view of the intensity of the water peak. The lack of exchange in this spectrum stands in stark contrast to the spectrum where CDCl₃ had been dried over molecular sieves (figure 3.4), which had indicated that exchange with water was occurring at all the hydroxyl sites. One would expect that the more water is added to the sample, the greater the exchange with water; however, in this case, it appears as though water is being excluded from the tetrahydropyranyl water-binding pocket described previously for T-2 toxin. This may result from an intermolecular hydrogen-bonding interaction between two or more DON molecules, where the hydroxyls in the tetrahydropyranyl pocket are associating with those of another trichothecene molecule, serving to maintain the overall 3D structure of the molecule without requiring the stabilizing effect of the bridging water. Water may then associate with the epoxide oxygen, causing the slight difference in chemical shift noted in the 1D spectrum for the epoxide hydrogens, H-13_{AB}, or alternatively slight bond movement may be required when the two molecules bind together, resulting in an increase in the ring strain about the epoxide. As more water is added to the system, the water molecules may cause significant ring strain on the epoxide, eventually resulting in the opening of the epoxide ring, and a triggering of the degradation process for DON depicted in figure 3.13.

One theory is that as the miscibility limit for chloroform and water is approached, the hydroxyl substituents of DON, which are all present on the tetrahydropyranyl pocket, or bottom, side of the molecule associate with those of another DON molecule, forming a dimer, excluding water from the pocket, and preserving the overall structure of the toxin. Recall, that a low-frequency triplet (at 0.9 ppm) was also introduced into the spectrum when only 1 ppm D₂O is present (figure 3.13), which was suggested to be a second methyl-14 contributor. The splitting of the methyl-14 into two distinct contributions supports the potential dimerization of the trichothecenes shown in figure 3.13.

Then as more water is added, the water may attack the highly strained epoxide ring at either C-12 or C-13 resulting in a ring opening event, which sparks the degradation of the molecules.

3.5. Conclusions

Understanding the mechanism of toxicity of the type B trichothecenes requires the recognition of some of the basic structural properties of the toxins. Development of an accurate three-dimensional model of the compound, including insight into dynamic processes such as hydrogen-bonding, provides fundamental knowledge of how they are able to interact with other molecules within the cell. This study has provided new data regarding the chemical shifts and coupling constants for the hydroxyl residues of the type B trichothecenes, which serve to complete the assignment of all of the compounds studied. New information regarding the overall three-dimensional structure of the type B trichothecenes, including refinement of the structure at the epoxide, corrected assignment for H-7_β and the planar geometry imposed on a portion of the trichothecene core due to the conjugated π -system of the A-ring, and correction to some of the previously reported chemical shifts is provided. Furthermore, an NMR-based investigation into the internal hydrogen-bonding network of DON, previously described through a DFT study conducted by Nagy *et al.* [111], was conducted. This investigation confirms the lowest energy conformation described by Nagy, which is shown to rigidify and ultimately stabilize the molecule.

The presence of bound water in the sample was also investigated, and it was determined that in the presence of a water-depleted system, the type B trichothecenes bind at least one water molecule in the tetrahydropyranyl pocket, which may serve as a water bridge, further stabilizing the trichothecene core, and in water-rich sample the water may add in multiple sites across the molecule providing further stability of the compound, as well as possible protection of the toxin against degradation. However, when excess water is added to the water-depleted sample, exchange with water is lost, and the water appears to be excluded from the structure, potentially through the association of two or more trichothecene molecules. Addition of more water to the sample completely disrupts the spectrum, which provides likely evidence for a degradative process. Thus,

the deuterium exchange studies seem to indicate that as the availability of water increases, the tendency for the molecules to associate increases, and is followed by degradation.

The potential for degradation of trichothecene toxins is a major finding when considering the impact this could have on the agricultural industry. The trichothecenes have been shown to be extremely stable to degradative processes such as time, temperature and chemical degradation [10,17,33,106,133,140], which makes it very difficult to remove the toxins from affected food stores.

4 Structural Dynamics of Type B Trichothecenes Due to Solvent Effects

4.1 Overview

Trichothecenes from all classes have been primarily studied in chloroform. Although a common NMR solvent, deuterated chloroform (CDCl_3) does not exhibit the same features that one would expect to find in the natural biological environment experienced by the trichothecenes. One of the major reasons that CDCl_3 may have been chosen as a solvent for this class of toxins is that it manages to avoid the majority of issues the toxins exhibit in solution, such as aggregation, which seem to arise when studying trichothecenes in pure form. By only studying these toxins in a single solvent, information regarding the dynamic nature of these compounds is often missed. Very few papers in trichothecene literature have taken the dynamics of these compounds into account [45,72,147]. When studied in a variety of solvents, the spectra vary considerably, providing a rationale for the practice of CDCl_3 as the sole solvent of choice. The literature on the conformational effects of solvent on similar organic compounds, such as the ribosome-binding antibiotic virginiamycin M1 [31,32], demonstrate that the solvent can have a large influence on the types of conformations adopted by small amphipathic organic molecules.

Multiple conformations were observed for all of the type B trichothecenes, particularly when observed in aprotic polar solvents. A detailed investigation into the structure of nivalenol (NIV) in deuterated dimethyl sulfoxide (DMSO-d_6) offers evidence of two distinct conformations. Interestingly, one of these conformations provides evidence for the structural rearrangement to a boat configuration in the B-ring for the type B trichothecenes, which was proposed to exist under the influence of certain solvent systems [72]. The rearrangement observed for NIV in DMSO-d_6 , led to each of the type B trichothecenes being compared between CDCl_3 and DMSO-d_6 to determine whether the same structural rearrangements occur in all systems. As deoxynivalenol (DON) is soluble in a wider variety of solvents than the remaining type B trichothecenes, it was investigated in acetone, methanol and tetrahydrofuran, in addition to CDCl_3 and DMSO-d_6 . Evidence for rearrangement of the structure in polar solvents was investigated in detail.

4.2 Introduction

In addition to the toxicological effects of trichothecenes, this class of mycotoxins also constitutes an important group of antibiotics owing to their efficiency in disrupting cellular function. Interest in them continues due to the wide range in toxicity observed between different species, which offers the capability of tailoring them to target specific organisms. This has led to their investigation as potential antifungal agents. Interest remains high regarding their chemical reactivity, especially concerning the mechanism of interaction within various structures in the cellular environment. The chemical reactivity of trichothecenes appears to be diverse due to the large variety of functional groups, available conformations and potential hydrogen bonding interactions they are able to undergo.

Conformational changes of the trichothecenes are largely the result of the stereochemistry observed in the ring systems. The conformational preference is for the B-ring to adopt a chair conformation; however, evidence for rearrangements of this ring to a boat conformation exists [67,72,74,77,79]. Boat configurations have been observed for the macrocyclic trichothecenes; however, suggestions have been made regarding the ability of DON and NIV to undergo such a rearrangement [72]. The structural changes that occur from the chair to the boat configurations are depicted in figure 4.1. The rearrangement to the boat conformation is strongly influenced by the nature of the functional groups on the side chains off the trichothecene core, as well as the hydrogen bonding interactions induced by the solvent. An example of the latter is given by Jarvis *et al.*, for DON [72], where the addition of DMSO-d₆ and acetone-d₆ results in a rearrangement that induces the change from a chair to a boat configuration in the B-ring.

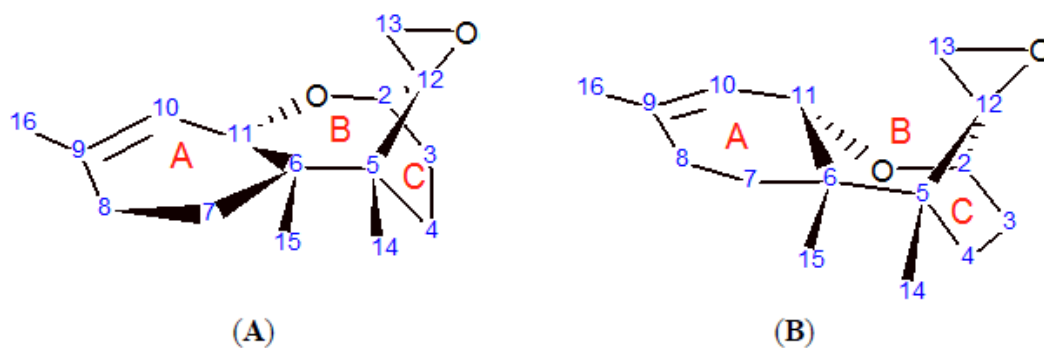


Figure 4. 1: Three-dimensional stereochemistry of the trichothecene core when (A) the A-ring is in a half-chair, and the B-ring in a chair conformation; and (B) the A-ring is a half-chair, and the B-ring in a boat conformation

The majority of NMR studies on trichothecenes have limited the analysis to deuteriochloroform (CDCl_3), as the primary goal was chemical identification, not physical structure and dynamics. Only in the study by Jarvis *et al.* [72] were attempts made to investigate the solution-state configuration of the type B trichothecenes in other solvents, Jarvis investigated NIV and DON in deuterated-acetone (acetone-d_6), methanol (CD_3OD) and dimethyl sulfoxide (DMSO-d_6), and compared the ^{13}C spectra to that observed in CDCl_3 . Jarvis saw preliminary evidence for a second minor configuration in a single crystal X-ray diffraction (SCXRD) study performed for NIV recrystallized from a mixture of methanol and water, and attempted to confirm this structure through the NMR analysis of both DON and NIV in various solvents. He suggested that the second configuration is an isomer resulting from a rearrangement of the ketone at C-8 and hydroxyl at C-15 to a hemiketal linkage between C-8 to C-15 for both DON and NIV. They also proposed another possible linkage, occurring between the C-4 and C-15 hydroxyls in NIV (refer to figure 4.2). Their structural hypothesis is based primarily on the ^{13}C NMR data.

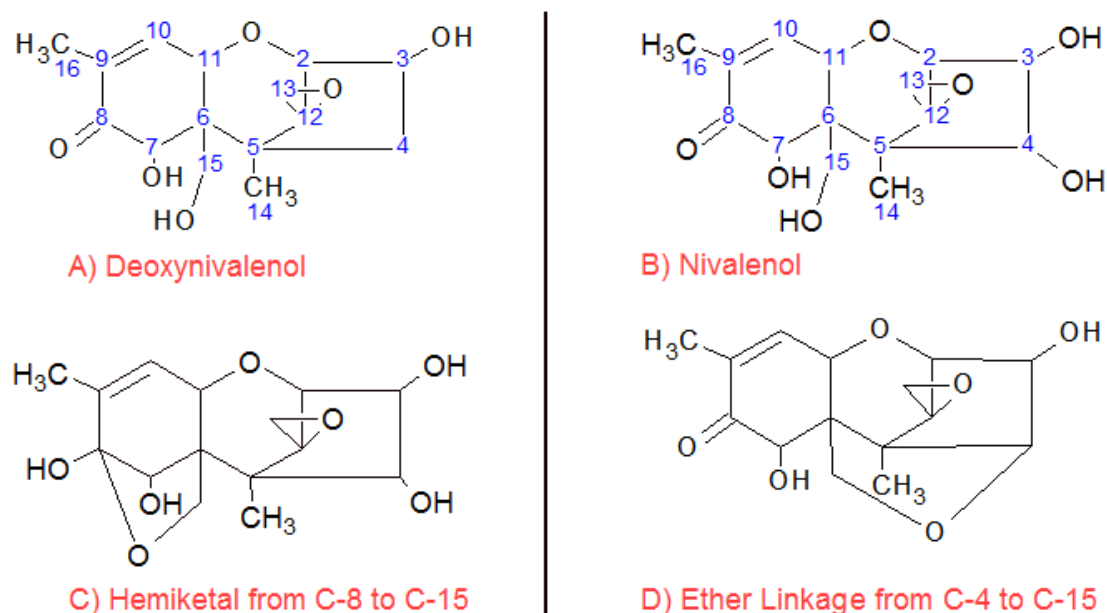


Figure 4. 2: Hemiketal and ether linkages proposed to occur in type B trichothecenes DON and NIV

To the best of our knowledge, these conformational rearrangements in type B trichothecenes have not been investigated further; although, plenty of evidence for similar rearrangements exist for the related macrocycles [67,72,74,77,79]. The key structural feature of the macrocyclic type D trichothecenes is a diester linkage occurring between C-15 and C-4. When the chain from C-4 to C-15 is short the B ring in the trichothecene may experience a significant amount of ring strain, which forces the B-ring to adopt a boat configuration, rather than maintain the typical chair configuration. Jarvis considered the existence of the C-15 to C-4 linkage in the type B trichothecenes based on this prior experience with the macrocycles. The two configurations are not exclusive, and appear to occur simultaneously in dynamic equilibrium [67,69,79].

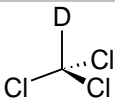
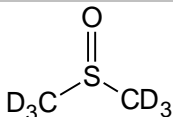
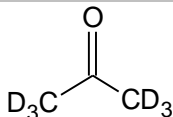
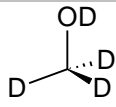
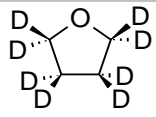
Chloroform is a relatively non-polar aprotic solvent, which is a significant departure from the environment in cellular systems where they are most commonly encountered. Cellular systems comprise primarily an aqueous environment, yet have regions, such as the cellular membrane and certain protein environments, which are hydrophobic in nature. Thus, trichothecene structure and dynamics should be observed in both of these types of environment to garner a better understanding of how these toxins behave in nature. The trichothecenes are particularly amphipathic, which

suggests that they can exist in both hydrophobic and hydrophilic environments, as is the case with other compounds exhibiting similar properties, such as the antibiotic virginiamycin M1. Virginiamycin M1 was shown to exist in different configurations based on the type of environment to which it was subjected [31,32]. Similar observations may be possible for the trichothecenes; however, appropriate solvent conditions must be identified. This study was designed to determine whether different solvent properties induce structural changes in the type B trichothecenes.

4.3 Solvent Properties and Chemical Structure

The physical and chemical properties for the solvents used in this study are listed in table 4.1. Of particular importance are the structure, polarity and protic nature of the solvents, as these will have the greatest influence on the conformations that the compound adopts. For example, the structure of the compound determines whether the solvent interacts with the molecule via hydrogen bonding, or dispersion forces. Protic solvents, such as methanol and water, will exchange protons with any hydrogen-bonding sites on the molecule. Since the NMR solvents are deuterated, exchange with the solvent will significantly reduce the signals for the exchangeable protons on the molecules. Aprotic solvents do not exchange with the molecule and thus are often preferred for compounds containing exchangeable protons.

Table 4. 1: Chemical Properties of Common NMR Solvents

	Chloroform	DMSO	Acetone	Methanol	THF
Chemical Formula	CDCl ₃	(CD ₃) ₂ SO	(CD ₃) ₂ CO	CD ₃ OD	C ₄ D ₈ O
Structure					
Polarity	4.1	7.2	5.1	5.1	4.0
Miscible with water	No	Yes	Yes	Yes	Yes
Protic	No	No	No	Yes	No
Density	1.483 g/cm ³	1.1004 g/cm ³	0.791 g/cm ³	0.7918 g/cm ³	0.8892 g/cm ³
Viscosity	0.786 cP	1.996 cP	0.3075 cP	0.59 cP	0.48 cP
Dielectric Constant	4.81	46.7	21.0	33.0	7.60
Dipole Moment	1.04 C·m	3.96 C·m	2.88 C·m	1.70 C·m	1.75 C·m

Jarvis did study the ¹³C spectra for DON in all of the above solvents, with the exception of THF-d₈ [72]. The choice of adding THF-d₈ to this group of solvents arose from the realization that all of the solvents tested in the Jarvis experiments were all small non-cyclic molecules, and serves to determine whether solvent structure has an impact on trichothecene conformation. Although structurally similar, DMSO-d₆ and acetone-d₆ display slightly different properties as the sulfur group of DMSO-d₆ results in a higher dielectric constant and has a dramatic effect on the polarity of the solvent. Methanol, being the only protic solvent among the group was expected to exhibit rather unique properties in comparison to the others, as it is intrinsically capable of chemical exchange with the hydroxyl resonances resulting in the replacement of the hydroxyl proton with a deuterium atom, reducing the intensity of the hydroxyl signals. Deutero-chloroform, being neither protic, nor particularly polar, was also expected to have unique properties among the group, as it does not contribute anything towards the molecule except the ability to go into solution. THF-d₈ exhibits a very different structure than the rest of the solvent molecules, as it is cyclic, aprotic and relatively non-polar.

Jarvis estimated, from the ^{13}C spectrum, that the rearrangement of the type B compounds to the hemiketal isomer occurs up to 11% of the time in the solvents that were used [72]. In chapter 3 it was suggested that when dissolved in CDCl_3 , each of the trichothecenes adopt only a single observable conformation, which greatly simplifies the analysis, permitting rapid identification, which was the primary concern of early studies on the trichothecenes. However, with the observation of multiple configurations and dynamics between them, how can one be certain that the accepted structure is correct in natural environments?

One of the most prevalent theories regarding the spectrum of chemical reactivity observed for the entire class of trichothecene toxins is the potential of these molecules to undergo intramolecular rearrangements [67,69,79], as well as both intra- and intermolecular hydrogen bonding [27,140]. In order to gain further insight into the rearrangement and hydrogen-bonding possibilities, the type B trichothecenes were observed in a variety of solvents to determine the influence of solvent interactions on the toxins.

4.4 Materials and Methods

4.4.1 Solution-State NMR Experiments

All spectra were acquired at ambient temperatures ranging from 21-26°C on a Bruker Avance 300 spectrometer, outfitted with a 5 mm HX PABBO BB probe. The spectrometer operates at a Larmor frequency of 300.131 MHz for ^1H and 75.468 MHz for ^{13}C . Deoxynivalenol (Sigma, CAS 51481-10-8), Nivalenol (Sigma, CAS 23282-20-4), 15-O-acetyldeoxynivalenol (SIGMA, CAS 88337-96-6), and 3-O-acetyldeoxynivalenol (Sigma, CAS 50722-38-8) were vacuum-pumped under nitrogen (N_2) gas to remove residual water and/or ethanol from the sample. The toxins were then dissolved in deuterated dimethyl sulfoxide (DMSO-d_6) (Cambridge Isotope Labs, 2206-27-1) to a concentration of 1 mg/mL, and compared to the deuterated chloroform (CDCl_3) spectra previously described in Chapter 3. Samples of DON were also dissolved in 1 mg/mL deuterated acetone ($(\text{CD}_3)_2\text{CO}$ acetone- d_6) (Cambridge Isotope Lab, CAS 666-52-4), 1 mg/mL deuterated methanol (CD_3OD) (Sigma, CAS 811-98-3), and 1 mg/mL deuterated Tetrahydrofuran (THF-d_8) (Sigma, CAS 1693-74-9). The CDCl_3 ,

and acetone- d_6 were dried over molecular sieves in order to prevent water contamination; whereas, the DMSO- d_6 , CD_3OD , and THF- d_8 were obtained from individually sealed ampoules and were used without further drying. The 1D 1H spectra were recorded with a 90° pulse width of 12.4 μs , a recycle delay of 1.5 s, and 128 transients. The 1D INEPT ^{13}C spectra were recorded with a 90° pulse width of 7.6 μs , a recycle delay of 4.0 s, and 8464 transients.

The 2D homonuclear 1H COSY spectra were acquired in 256 increments covering a spectral width of 1800 Hz (12.0 ppm) in both dimensions, using a recycle delay of 1.5 s, which is estimated to be approximately five times the T_1 relaxation rate for 1H in solution. Four transients were collected for each increment, having 4096 points. The direct and indirect dimensions have a digital resolution of 0.88 and 7.03 Hz, respectively, the direct dimension was zero filled to 128,000 complex points and no line broadening was used.

The 1H NOESY spectra were acquired in 256 increments covering a spectral width of 1802.45 Hz (12.0 ppm) in both dimensions, using a recycle delay of 1.5 s. An array of mixing times, including 0.5 s, 1.0 s, and 1.5s, was used to ensure that all through-space signals were allowed sufficient time to build up prior to signal decay. Thirty-two transients were collected for each increment, having 4096 points. The direct and indirect dimensions have a digital resolution of 0.88 and 7.03 Hz, respectively. The spectra were processed using the phase sensitive States method [87], and were zero-filled to 128,000 complex points.

The 2D (1H - ^{13}C) HSQC heteronuclear correlation spectra were acquired in 128 increments, using a recycle delay of 2.0 s, and a spectral width covering 4006.41 Hz (13.34 ppm) in the direct dimension and 12500 Hz (165.62 ppm) in the indirect dimension. One-hundred-and-fifty-two transients were collected for each increment, having 1024 points to ensure that sufficient signal-to-noise was achieved in each of the spectra. The direct and indirect dimensions have a digital resolution of 3.91 and 97.66 Hz, respectively.

The 2D (1H - ^{13}C) HMBC spectra were acquired in 256 increments using a recycle delay of 2.0 s, and a spectral width covering 1951.60 Hz (6.50 ppm) in the direct dimension and 14268 Hz (190.24 ppm) in the indirect dimension. One-hundred transients were collected for each increment,

having 1024 points and were zero-filled up to a value of 4096 points. The direct and indirect dimensions have a digital resolution of 0.52 and 56.04 Hz, respectively.

4.4.2 Simulations

The SpinWorks software developed by Kirk Marat at the University of Manitoba was used to simulate the 300 MHz ^1H spectra [97]. The ^1H FIDs were zero-filled four-fold and subjected to Gauss-Lorentz apodization with a line broadening between -0.3 to -0.90 Hz, and a Gaussian multiplication of 0.10 to 0.33, depending on the signal-to-noise level. All ^1H spectra were simulated as two separate spin systems as the whole spin system could not be simulated at once due to memory allocation limits in the program. The six-membered ring, containing hydrogens H-7_{OH}, H-7 _{β} , H-10, H-11, H-15_A, H-15_B, H-15_{OH}, methyl-16, and, where applicable, the 1' methyl from either the 3-O-acetyl, or 15-O-acetyl group, was a ten-spin ABCD₃EFGH or 11-spin ABCD₃EFGHI₃ system. Similarly, the five-membered ring containing the hydrogens, H-2, H-3 _{β} , H-3_{OH}, H-4 _{α} , H-14, H-13_A and H-13_B, including the H-4 _{β} , or in the case of NIV H-4_{OH}, hydrogen, was simulated as a ten-spin ABCDE₃FGH spin system. Long range couplings were considered up to 5 bonds, and an inherent line width of 0.3 Hz was used along with the assumption of Lorentzian line shapes. In the simulation of the A ring for NIV a total of 2001 transitions (of a total possible maximum of 3200 transitions) were assigned with an average RMS deviation below 0.034 Hz and a largest absolute difference of 0.08 Hz. Standard deviations in all the spectral parameters ranged from 0.03-0.06 Hz. In the C ring simulation for NIV the 2334 transitions were assigned (of a total possible maximum of 3200 transitions) with an RMS deviation below 0.031 Hz, and largest absolute difference of 0.09 Hz. Standard deviations for all of the spectra range from 0.001-0.006 Hz.

4.5 Complete Spectral Analysis of Nivalenol in Dimethyl Sulfoxide

4.5.1 Results

The complete analysis of NIV in DMSO- d_6 was performed at 300 MHz for ^1H and 75 MHz for ^{13}C . Two distinct conformations are present in different populations. The presence of the second

conformation is obvious in the 1D ^1H spectrum, shown in figure 4.3 composing 20% of the total signal. The 4:1 ratio provides a basis on which signals from each conformation can be distinguished, and are henceforth referred to as the major and minor contributors to the spectrum.

The agreement between the simulated spectrum for each of the individual subspectra and the experimental spectrum is remarkably close, lending confidence to the accuracy of the assignments.

The minor peaks are sufficiently strong, such that the scalar and through-space coupling can be readily discerned from the cross-peaks in the COSY and NOESY spectra respectively, which are shown in figures 4.4 and 4.5. The cross-peaks in the COSY and NOESY spectra are colored blue for the major peaks and red for the minor peaks, corresponding to the colors used in the simulations described in figure 4.3. Exchange peaks in the NOESY spectrum are indicated in orange and green for the major and minor peaks, respectively. The COSY spectrum for NIV in DMSO-d_6 does support the assignment of both the major and minor configurations appearing in the one-dimensional ^1H spectrum.

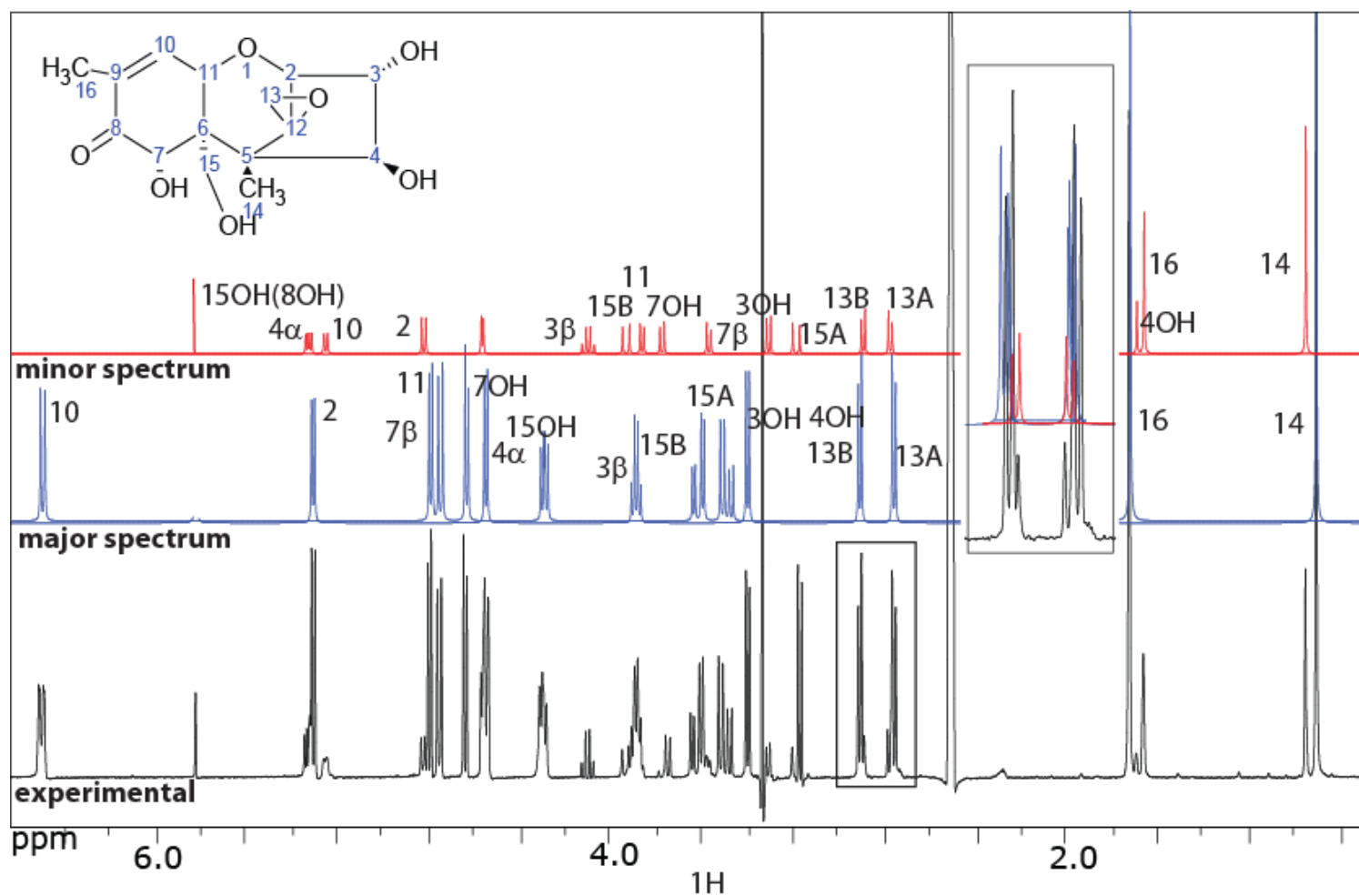


Figure 4. 3: Experimental and simulated ^1H spectra for NIV in DMSO-d_6 at 300 MHz depicting the existence of two distinct configurations. The experimental spectrum is shown in black, and the major and minor spectral simulations are depicted in blue and red respectively. The inset shows the combination of the major and minor simulations and the accuracy of the fit that their superposition has to the experimental spectrum for the protons 13_A and 13_B.

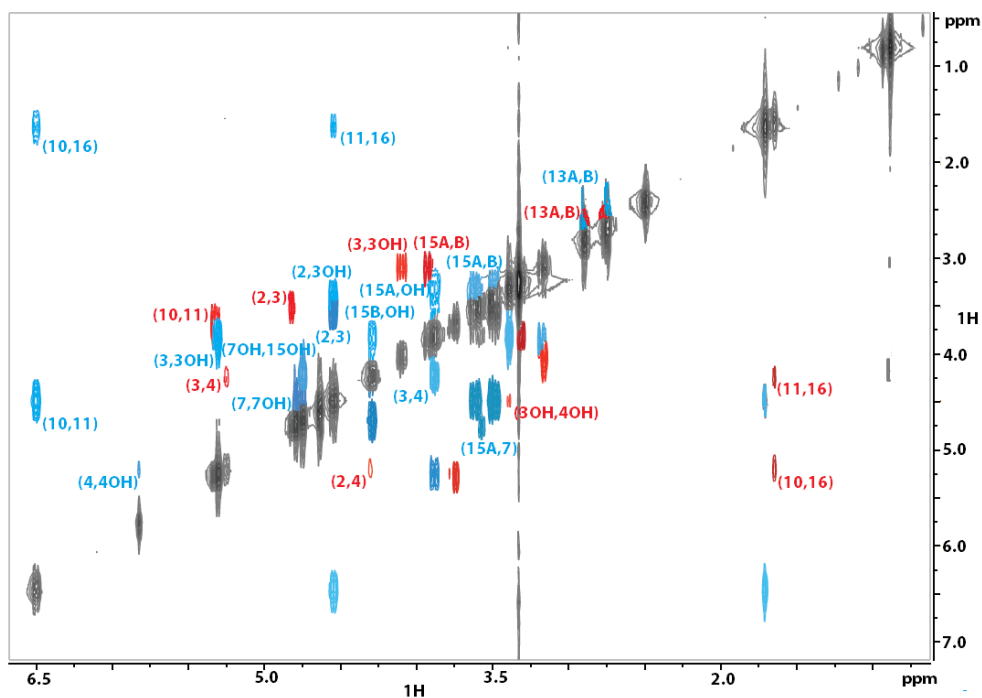


Figure 4. 4: The ^1H COSY spectrum for NIV at 300 MHz in DMSO-d_6 depicting ^1H - ^1H correlations for the major (blue) and minor (red) contributors to the spectrum.

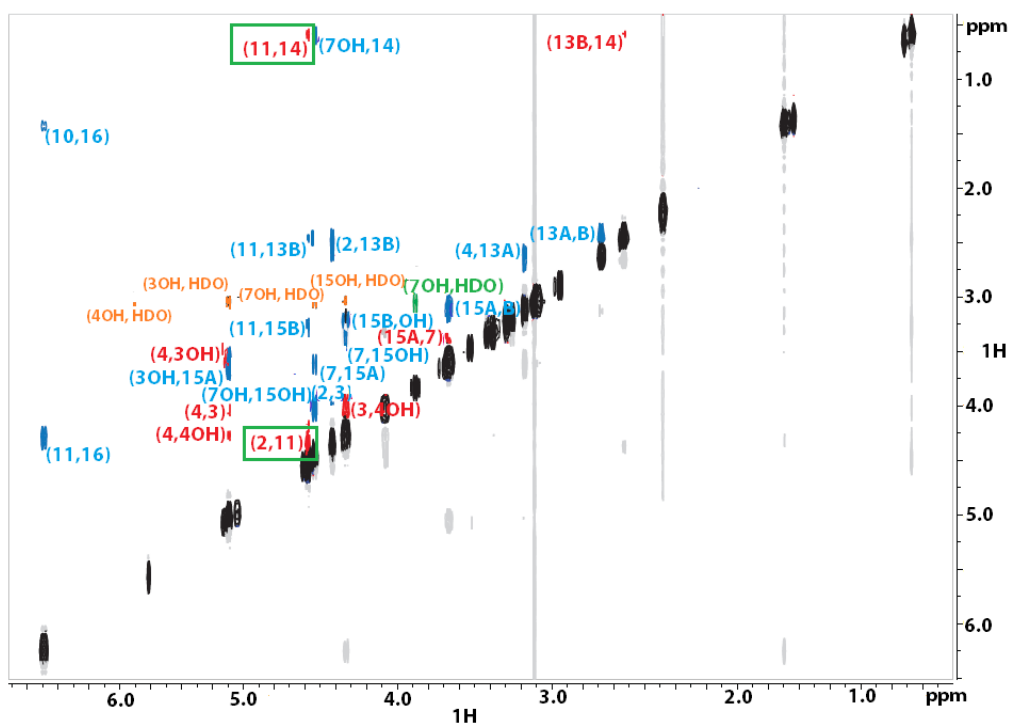


Figure 4. 5: The ^1H NOESY spectrum for NIV at 300 MHz in DMSO-d_6 depicting the through-space ^1H - ^1H correlations for the major (blue) contributor with exchange peaks (EXSY) in orange, and the minor (red) contributor with EXSY peaks in green. Minor crosspeaks that suggest significant changes to the three-dimensional geometry of the trichothecene core are highlighted with green boxes.

Evidence supporting the assignments of the major and minor components is also provided in the NOESY spectrum, where crosspeaks indicate through-space coupling. Exchange peaks are present for the major spectrum, and indicate that water exchange occurs with all hydroxyl substituents in the major configuration of NIV. The core structural configuration determined for the major contributor to the NIV spectrum supports the ^1H assignment described by Savard and Blackwell [135]. Only one exchange peak with water is observed for the minor set of peaks, that of the H-7_{OH} hydroxyl proton, indicating that exchange is present only at this site in the minor structure.

Other important peaks observed for the minor contributor appearing in the NOESY spectra are those which occur between H-2 and H-11, as well as H-11 and the methyl hydrogens present on C-14, which are highlighted by the green boxes in figure 4.5. The chemical shift and 2D ^1H correlations are given in table 4.2, while the scalar coupling values are presented in table 4.3 for both the major and minor configurations.

Not all of the crosspeaks expected were observed in the COSY and NOESY spectra, in particular many of the NOESY crosspeaks for the minor spectrum appear to be missing, see footnotes for Table 4.2. A significant amount of overlap in the crosspeak signals is seen, especially in the 3-5 ppm range where many of these signals are obscured by the stronger peaks from the major conformation. For example, the NOESY crosspeak between the minor 13_A and 13_B appears to be missing; however, the crosspeak belonging to the major 13_A(13_B) would overlap with the minor crosspeak and effectively drown it out. Despite this complication, the COSY and NOESY assignments presented in Table 4.2 correspond well with the one-dimensional NMR spectra for NIV.

Table 4. 2: Chemical shift values and two-dimensional ¹H correlations for the major and minor contributors to the NIV spectra observed in DMSO-d₆

Label	Chemical Shift - major	COSY	NOESY	Chemical Shift - Minor	COSY	NOESY
2	5.312 ¹	3 _β ,3 _{OH}	3,13 _A	4.827 ²	3 _β ,4 _α	11
3_β	3.889	2,3 _{OH} ,4 _α	2	4.103	2,3 _{OH} ,4 _α	4,4 _{OH}
3_{OH}	3.398	2,3 _β	15 _B ,HDO	3.308	3 _β ,4 _{OH}	3 _{OH}
4_α	4.556	3 _β ,4 _{OH}	13 _B	5.336	2,3	3 _β ,3 _{OH} ,4 _{OH}
4_{OH}	3.168	4 _α	HDO	1.699	3 _{OH}	3 _β ,4 _α
7_β	4.800	7 _{OH} ,15 _B	15 _{OH}	3.572	N/O ¹	
7_{OH}	4.642	7 _β ,15 _{OH}	14,15 _{OH} ,HDO	3.777	N/O ²	HDO
10	6.509	11,16	11,16	5.259	11,16	N/O ⁴
11	4.757	10,16	10,13 _A , 15 _A	3.866	10,16	2,14
13_B	2.903	13 _A	4 _α ,13 _A	2.891	13 _A	N/O ²
13_A	2.754	13 _B	2,11,13 _B	2.773	13 _B	14
14	0.893	N/O ³	7 _{OH} ,	0.942	N/O ³	11
15_B	3.619	7 _β ,15 _A ,15 _{OH}	3 _{OH} ,7 _{OH} ,15 _A , 15 _{OH}	3.936	15 _A	7 _β
15_A	3.499	15 _B ,15 _{OH}	11,15 _B ,15 _{OH}	3.187	15 _B	N/O ²
15_{OH}(8)	4.299	7 _{OH} ,15 _{AB}	7 _β ,7 _{OH} ,15 _A ,HDO	5.830	N/O ⁴	N/O ⁴
16	1.719	10,16	10	1.654	10,11	N/O ⁴

¹All Chemical Shifts were simulated within 0.001 Hz, ²N/O due to overlap, ³N/O due to long range, ⁴N/O due to changes in the structural configuration.

Table 4. 3: Coupling constants and interpretation of the major and minor contributors to the NIV spectrum in DMSO-d₆ at 300 MHz.

	J (Hz) Major	Interpretation	J (Hz) Minor	Interpretation
³ J _{2,3}	4.147 (±0.001)	2 is <i>gauche</i> to 3	5.362 (±0.001)	2 is <i>gauche</i> to 3
³ J _{3,4}	4.147 (±0.001)	3 is <i>gauche</i> to 4	5.654 (±0.001)	3 is <i>gauche</i> to 4
³ J _{3,3OH}	4.401 (±0.001)	3 is <i>gauche</i> to 3 _{OH}	5.413 (±0.001)	3 is <i>gauche</i> to 3 _{OH}
³ J _{4,4OH}	5.360 (±0.001)	4 is <i>gauche</i> to 4 _{OH}	2.987 (±0.001)	4 is <i>gauche</i> to 4 _{OH}
⁵ J _{3OH,4OH}	0.623 (±0.001)	Long Range coupling mediated by the electrons on the oxygen atoms	N/O	No coupling
³ J _{7,7OH}	4.359 (±0.001)	7 is <i>gauche</i> to 7 _{OH}	5.569 (±0.001)	7 is <i>gauche</i> to 7 _{OH}
³ J _{10,11}	5.815 (±0.001)	10 is <i>gauche</i> to 11	4.783 (±0.001)	10 is <i>gauche</i> to 11
⁴ J _{10,16}	0.281 (±0.001)	Typical of H and CH ₃ <i>cis</i> -across a double bond	0.503 (±0.001)	Typical of H and CH ₃ <i>cis</i> -across a double bond
² J _{13AB}	4.501 (±0.001)	Typical for germinal on sp ³ under ring strain	4.853 (±0.001)	Typical for germinal on sp ³ under ring strain
² J _{15AB}	-11.641 (±0.001)	Typical germinal on sp ³ carbon	-9.052 (±0.001)	Typical germinal on sp ³ carbon
³ J _{15B,15OH}	3.976 (±0.001)	15 _B is <i>gauche</i> to 15 _{OH}	N/O	No coupling
³ J _{15A,15OH}	5.545 (±0.001)	15 _A is <i>gauche</i> to 15 _{OH}	N/O	No coupling

Carbon Spectral identification for NIV in DMSO-d₆

Further evidence for a second configuration is provided by the solution-state ¹³C NMR, appearing in figure 4.6. Recall, that the signals from the minor spectrum represent approximately 20% of the total product in solution. Since ¹³C NMR is plagued by low natural abundance and a moderate gyromagnetic (γ) ratio, the signal intensity for the major signals is expected to be low; therefore, observation of the minor peaks in the spectrum is opportune. The intensity of these signals is quite low, even when significant line broadening is used to increase the signal to noise. Some of the signals from the minor component are visible just above the noise level. These are indicated with red and blue asterisks in figure 4.6. Of particular importance are the minor peaks appearing at 104.67

ppm and 123.82 ppm, indicated with the red asterisks. Jarvis, identified two signals in the ^{13}C spectrum of DON in DMSO-d_6 appearing at 104 ppm and 121 ppm, these were assigned to the hemiketal counterparts of C-8 and C-10 respectively, and indicate the formation of the hemiketal linkage between C-8 and C-15. Even though no literature examples for the ^{13}C spectrum of NIV are available, a comparison between DON and NIV can be drawn, as these two compounds differ only by the substitution at C-4, which does not significantly affect the chemical shifts for the C-8 or C-15 signals.

Several other minor peaks are present in the spectrum and are highlighted by the blue asterisks. These have been assigned to the signals of the A-ring as seen in Table 4.4.

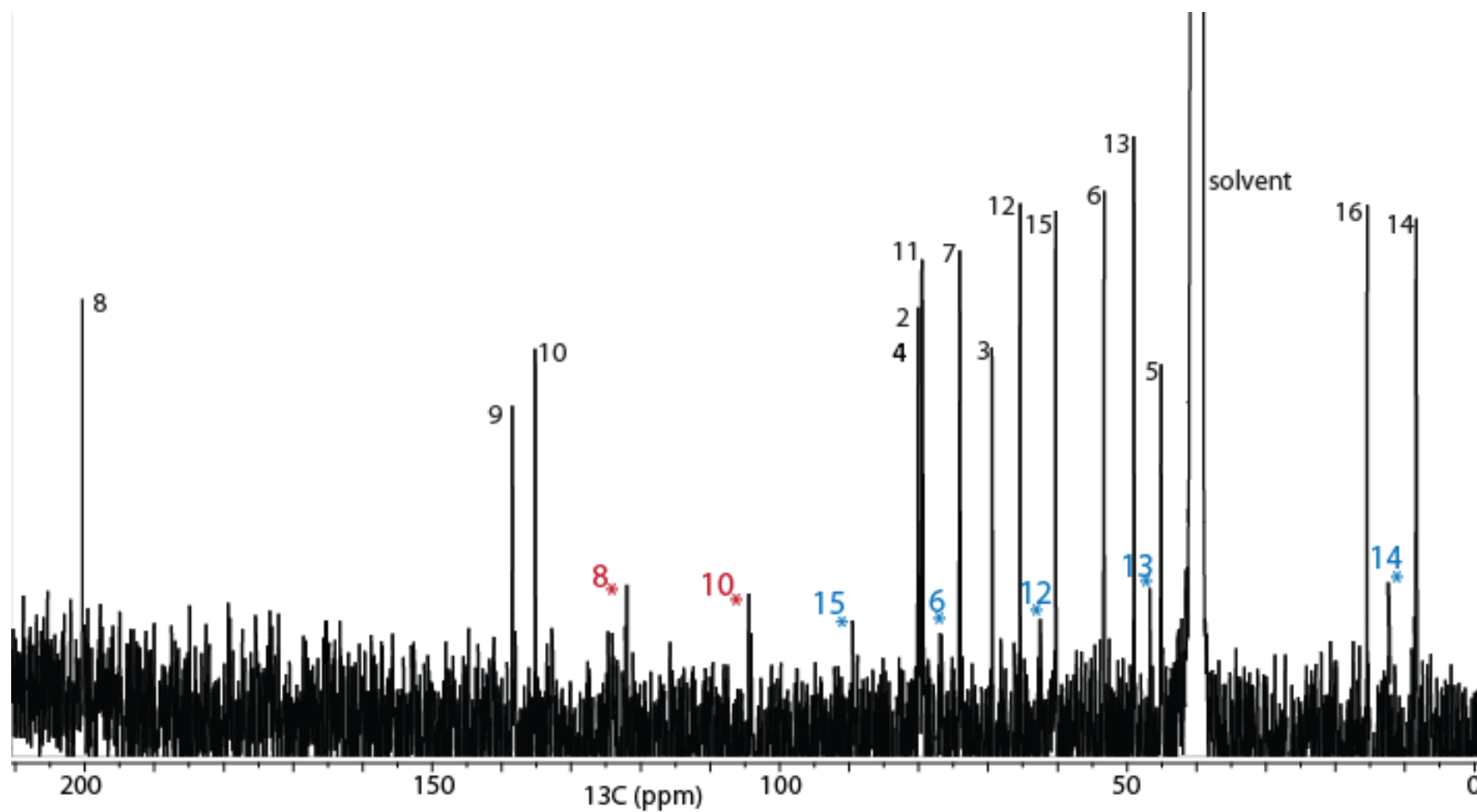


Figure 4. 6: Carbon-13 spectrum for NIV in DMSO- d_6 at 75 MHz, observed at ambient temperature. Major signals are labeled with their appropriate assignment corresponding to the structure in the inset. Minor peaks are labeled with asterisks.

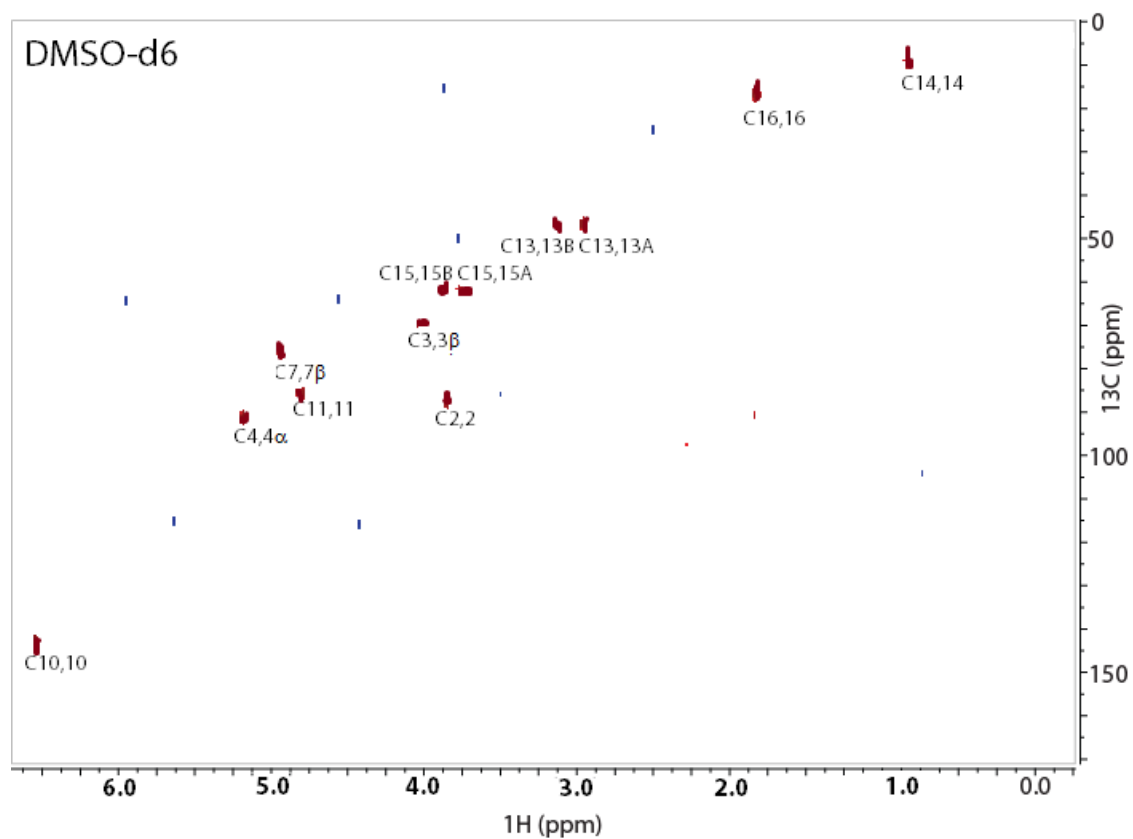


Figure 4. 7: Two-dimensional ^1H - ^{13}C HSQC spectrum for NIV in DMSO- d_6 measured at 300 MHz. Only the peaks for the major spectrum are clearly discerned. The peaks for the minor contributor appear to be lost in the noise.

Table 4. 4: Carbon chemical shifts and couplings observed for NIV in DMSO-d₆ at 75 MHz

¹³ C label	Chemical Shift – δ (ppm)	HSQC	Chemical Shift – δ (ppm)
	major	Major	Minor
2	79.11	H-2	
3	69.02	H-3 β	
4	79.69	H-4 α	
5	48.66		
6	56.05		76.19
7	73.66	H-7 β	
8	199.89		103.71
9	134.73		
10	141.76	H-10	113.87
11	78.98	H-11	
12	64.93		61.89
13	52.88	H-13 _A ,H-13 _B	46.60
14	7.94	H-14	11.97
15	59.78	H-15 _A ,H-15 _B	88.61
16	15.03	H-16	

4.5.2 Discussion

The solubility of trichothecenes in many solvent systems is of concern, with respect to spectral resolution and the propensity to form aggregates in solution. NIV is no exception, and in fact, is even less soluble than the majority of the toxins. NIV is only sparingly soluble in CDCl₃, and aggregates in solution; however, a 1:1 mixture of CDCl₃ and deuterio-methanol (CDCl₃) does make a suitable solvent. Previous reports describe the ¹³C NMR structure of NIV in acetone-d₆ and DMSO-d₆ [72]; however, the chemical shift assignments are far from complete. Attempts were also made to obtain the structure of NIV in pure methanol; however, as with CDCl₃, its poor solubility resulted in significantly distorted spectra due to the aggregation of the compound in solution.

Prior work by Jarvis *et al.* describes a second configuration of NIV and DON in solvents other than CDCl₃ [72]. The evidence provided for this alternative structure was limited to the ¹³C spectra

for DON and a structure generated by single crystal X-ray diffraction (SCXRD) study of a modified version of the macrocyclic trichothecene verrucarín. Verrucarín was prepared in such a way as to mimic the hemiketal isomer hypothesized for the type B trichothecenes. The hypothesis regarding the hemiketal structure is based primarily on the presence of two previously unobserved signals appearing in the ^{13}C spectrum for DON and NIV when dissolved in deuterated DMSO and acetone. Jarvis suggested that these signals represent up to 11% of the spectrum, with approximately one tenth of the sample adopting this second configuration in DMSO-d_6 . To the best of our knowledge, no further investigations into the veracity of this claim have been made. Thus, gaining knowledge regarding whether structural rearrangements occur in the type B trichothecenes is important for the elucidation of their interactions.

The original paper presented by Jarvis indicated that the structural rearrangements occur more readily in NIV than in DON [72]; however, no experimental parameters were given that could be matched to replicate the ^{13}C experiment performed by Jarvis, and it was rather surprising in this study to find that two distinct and well-resolved sets of peaks were observed in the ^1H spectrum for NIV when collected in DMSO-d_6 with no significant overlap occurring between signals of the two configurations. The intensities of the minor set of peaks appear in a ratio of roughly one quarter of the intensity of the other set, which greatly simplifies the assignment of the peaks.

The presence of signals from two conformations in the spectrum of NIV (figure 4.3), indicates that the rate of exchange is slow compared to the timescale determined by the chemical shift differences between the major and minor signals. As no significant line broadening is observed in the signals of the minor components in DMSO-d_6 , the rate of exchange must be much slower than the T_1 relaxation time for the experiment. Furthermore, no evidence for exchange is seen in the NOESY spectrum, owing to the lack of exchange crosspeaks.

The minor contributor to the NIV spectrum dissolved in DMSO-d_6 exhibits some major differences in both the chemical shift and coupling constants for individual signals. For example, H_{10} appears at a chemical shift of 6.5 ppm with a coupling to H_{11} of 5.8 Hz in the major contribution, but

has a chemical shift of 5.3 ppm with a 4.8 Hz coupling to H₁₁ for the minor. In the case of the methylene protons on C-15, H_{15B} experiences an increase in frequency; whereas, H_{15A} experiences a decrease in frequency, and the coupling between them changes from -11.6 Hz to -9.1 Hz, this is likely due to an increase in the ring strain of the system, which is consistent with theory of a hemiketal isomer. Both H_{15A} and H_{15B} experience coupling to the hydroxyl proton H_{15OH} for the major configuration; however, this coupling is not observed for the minor configuration. It is important to note that every signal in the spectrum is affected by the structural change, as a corresponding signal exists for each of the protons in the minor configuration appearing at a distinct chemical shift from its major counterpart, although some of the signals appear to be less affected than others. For example, the methylene protons on the epoxide carbon C-13 do not experience a significant deviation in chemical shift, and in fact are overlapping slightly with the signals from their major counterpart, and the coupling between them is remarkably similar for the two configurations, indicating that this part of the molecule is not affected significantly by the structural change.

A thorough analysis of each of the configurations of NIV was performed in order to determine the nature of the bonding arrangement, and the three-dimensional structure of each conformation. A particularly important difference between the two contributors to the spectrum for NIV is the large deviation in chemical shift observed for H₁₀. The high chemical shift of 6.5 ppm for the H₁₀ resonance in the major configuration is a result of conjugation for the double bond between C-9 and C-10, and the carbonyl at C-8, and serves as a characteristic peak for the type B trichothecenes. The chemical shift trend described by Savard and Blackwell for the type A trichothecenes, suggests that H-10 is typically located between 5.4-5.8 ppm [135]. The chemical shift for H₁₀ in NIV is 5.3 ppm for the minor contribution, suggesting that H₁₀ is attached to an sp² carbon, and the ethene bond remains intact; however, the conjugation to the C-8 carbonyl has been lost.

Jarvis proposed two different mechanisms for the rearrangements observed in the type B trichothecenes, the first requires the formation of a bond between C-8 and C-15, which would require that the double bond of the carbonyl be broken, and a loss of the hydroxyl at C-15 to occur. The second mechanism, described by Jarvis [72], is the result of a dehydration reaction between the

hydroxyls present at C-4 and C-15. The loss of conjugation observed by the change in chemical shift for the H₁₀ resonance lends support to the first mechanism, which is further supported by the H_{4OH} signal appearing at 4.6 ppm with a 3.0 Hz coupling to H_{4α} in the minor spectrum of NIV in DMSO-d₆, with corresponding signals for this coupling appearing in the COSY and NOESY spectra.

The conversion from a ketone to a hemiketal would also result in a loss of the hydroxyl resonance at C-15, and the loss of the double bond to C-8 would require a hydrogen transfer to this carbon resulting in sp³-hybridization, and a new hydroxyl resonance at C-8. This mechanism is depicted in figure 4.8

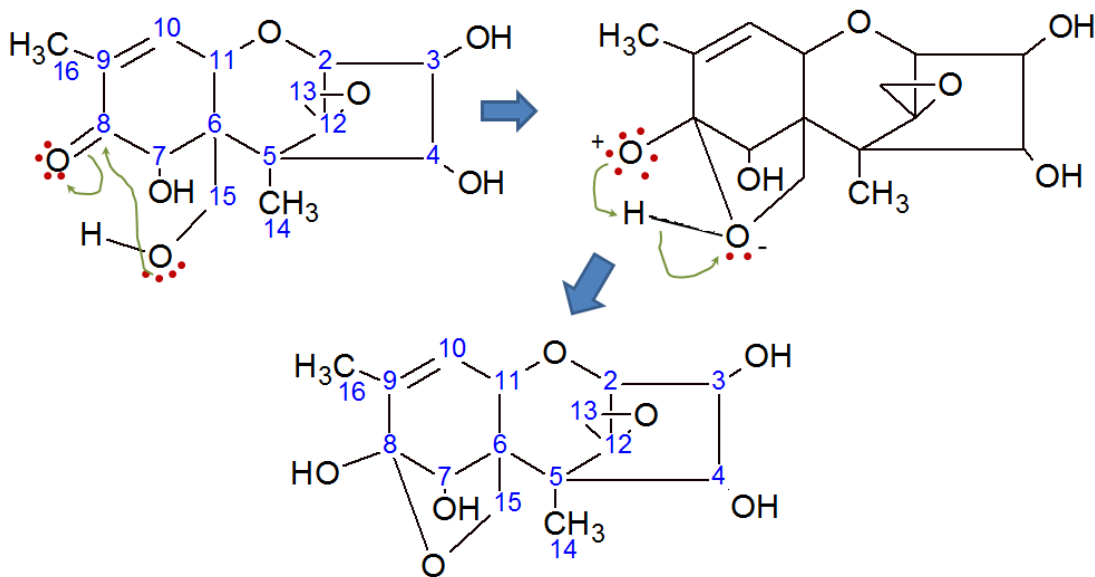


Figure 4. 8: Chemical mechanism for the formation of the hemiketal isomer of NIV from the original NIV structure

For the minor configuration, a loss in the coupling of H-15_A and H-15_B to H-15_{OH} is observed in the ¹H, COSY and NOESY spectra, and is indicated in Table 4.3. Exchange with water is not observed for the minor component at H-15_{OH} in the NOESY spectrum. Thus, it is possible that the peak in Table 4.2 attributed to H-15_{OH} in the minor component, appearing at 5.8 ppm, is actually the signal for the H-8_{OH} resonance for the hemiketal isomer.

Some of the more compelling evidence for the minor configuration of NIV is seen in the NOESY spectrum. No evidence for exchange between the two conformations of NIV is seen in the NOESY spectrum. The peaks representing the minor configuration and those for the major configuration are relatively well resolved from each other. Furthermore, the contours in the NOESY spectrum (see figure 4.5) are negative for the majority of the crosspeaks, with the exception of some of the hydroxyl residues, indicating chemical exchange with water. If exchange were to occur between the two configurations, positive contours would be observed throughout the spectrum. For example, a crosspeak representing the interaction of H-10 for the major configuration and H-10 for the minor configuration would be present, and would be opposite in phase to a crosspeak representing an interaction between H-10 and H-11 occurring solely on the major configuration.

In the case of the major configuration for NIV positive NOESY crosspeaks, indicating exchange with water, occur at all hydroxyl sites, supporting the three-dimensional configuration originally proposed by Savard and Blackwell [135]. A major discrepancy with the previously accepted spectral assignment is encountered, which involves the assignments for the methylene protons of C-13 on the epoxide ring. In this work the DMSO- d_6 NOESY spectrum, indicates that H-13_A is in close proximity to the protons on methyl-14; whereas, H-13_B is close to the proton on C-2 as indicated by the associated crosspeaks. This is opposite to that in the proposed assignment by Savard and Blackwell; thus, these two protons were initially assigned incorrectly. This is consistent with the observations regarding the labeling scheme for the epoxide protons described in Chapter 3.

Recall that the vicinal coupling constants are mediated through the p-orbital overlap; thus, the dihedral (or torsion) angles, defined by the bond geometry, can be obtained from the vicinal coupling constants via the Karplus equation. Based on the torsion angles obtained from vicinal couplings in the ^1H spectrum for the major and minor contributions for NIV in DMSO- d_6 (Table 4.3), in addition to the spatial proximity information from the NOESY spectra, the structures appearing in figures 4.9 and 4.10, for the major and minor structures of NIV respectively, are proposed.

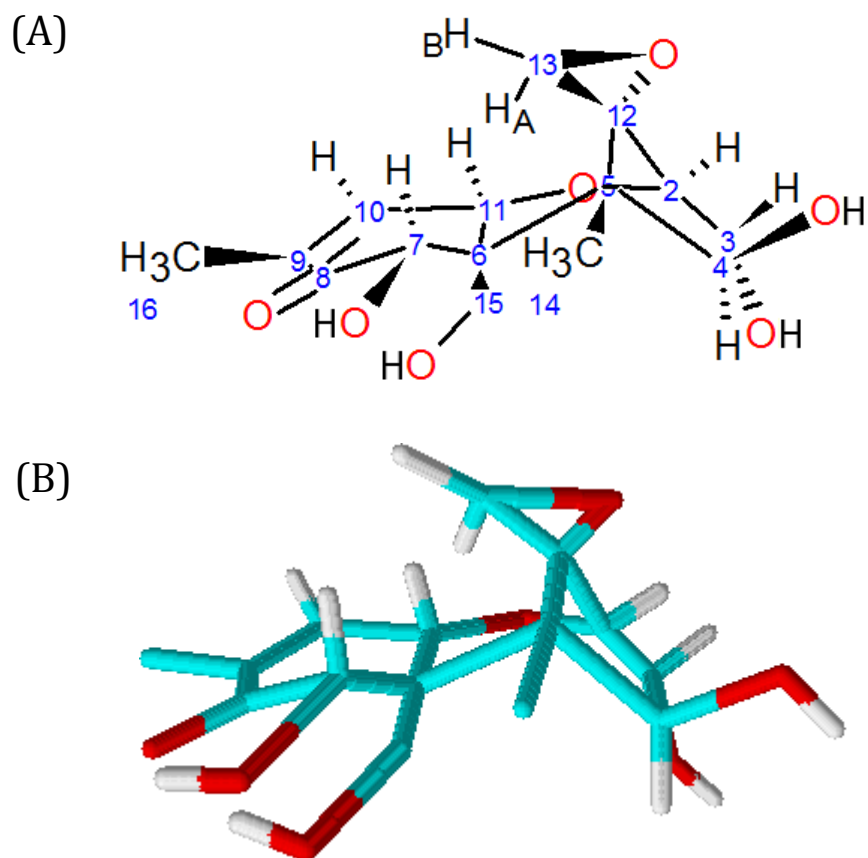


Figure 4. 9: Three-dimensional structure of the major component of the NIV spectrum observed in DMSO- d_6 . The configuration for the major contributor to the spectrum is in close agreement with the core structure described in chapter 2 for T-2 toxin, as well as that observed for DON in chloroform. (A) Chemical structure formula included for reference, (B) Stick structure showing 3D geometry and torsion angles.

The peaks corresponding to the minor contributor in the NOESY spectrum tell a different story. Only one exchange peak with water is observed for the minor component at H-7_{OH}, and numerous peaks are present in the spectrum which would not be expected if the minor structure of NIV were to adopt the same configuration as that observed for the core trichothecene structure described by Savard and Blackwell [135]. For example, if the B-ring were to exist in the chair configuration, which is characteristic of the trichothecene core, then H-2 and H-11 would be on opposite planes of the central ring, with H-2 occupying space on the bottom side of the ring, and H-11 occupying space on the top side of the ring closest to the epoxide functionality. Thus, it would not be possible for the two spins to couple through-space; however, this interaction is clearly observed in

the NOESY spectrum for the minor configuration, and is highlighted in figure 4.5 by the green boxes. The correlation observed between H-11 and the methyl protons on C-14 is also highlighted in figure 4.5 for the same reason. These two groups are located on opposite planes in the major configuration; however, the through-space coupling between them indicates that they must be in close proximity for the minor configuration. Therefore, H-2, H-11 and methyl-14 are all in axial positions on the B-ring, which would only be possible if the B-ring were to adopt a boat configuration. Thus, the NOESY spectrum was crucial in determining the overall three-dimensional structure of the minor contributor to the NIV spectrum. The minor conformation is depicted in figure 4.10.

According to the study performed by Jarvis *et al.* the minor hemiketal configuration adopted by the trichothecenes should result in a structural change in the B-ring to a stable boat conformation induced by the added ring strain placed on the B-ring when the additional ring is formed between C-8 and C-15 [72]. The observation of crosspeaks due to dipolar interactions mediated through cross-relaxation between protons H-11 and H-2, and H-11 and methyl-14 in the NOESY spectrum, and the 3D structure proposed in figure 4.10, lend support to the structure hypothesized by Jarvis.

Dynamic chemical exchange with water is also observed in the NOESY spectrum. Both of the configurations appear to be exchanging with residual water in the sample. For the major contributor, exchange with water occurs at all four of the hydroxyl groups; whereas, in the case of the minor contributor, the only hydroxyl group which appears to be undergoing exchange with water is that present at C-7. This indicates that there must be something tying up the other hydroxyl moieties, thereby preventing exchange with water. From figure 4.10, it is clear that H-7_{OH} is on the bottom side of the trichothecene, and sits in the newly formed hemiketal pocket. Hydroxyls H-3_{OH} and H-4_{OH} are present on the C-ring of the NIV molecule and removed from the H-7_{OH} proton, and lie in close proximity to the tetrahydropyranyl pocket. If the only water in the sample is directly bound to NIV, then only the hydroxyls that are directly interacting with the water will exhibit exchange in the spectrum. Thus, it is possible that a bound water molecule has been released from the tetrahydropyranyl pocket in the minor structure, and now occupies the space in the hemiketal pocket, with no other water molecules are interacting with the NIV molecule in its minor

configuration. Further investigations into the water dynamics of the system should be focused primarily on this mechanism; however, care must be taken to add the water in sub-stoichiometric amounts, so as not to saturate the NIV molecules with water; thus, leading to the loss of signal from the minor components in DMSO- d_6 . A more concentrated sample of NIV in DMSO- d_6 is recommended for future deuterium exchange studies.

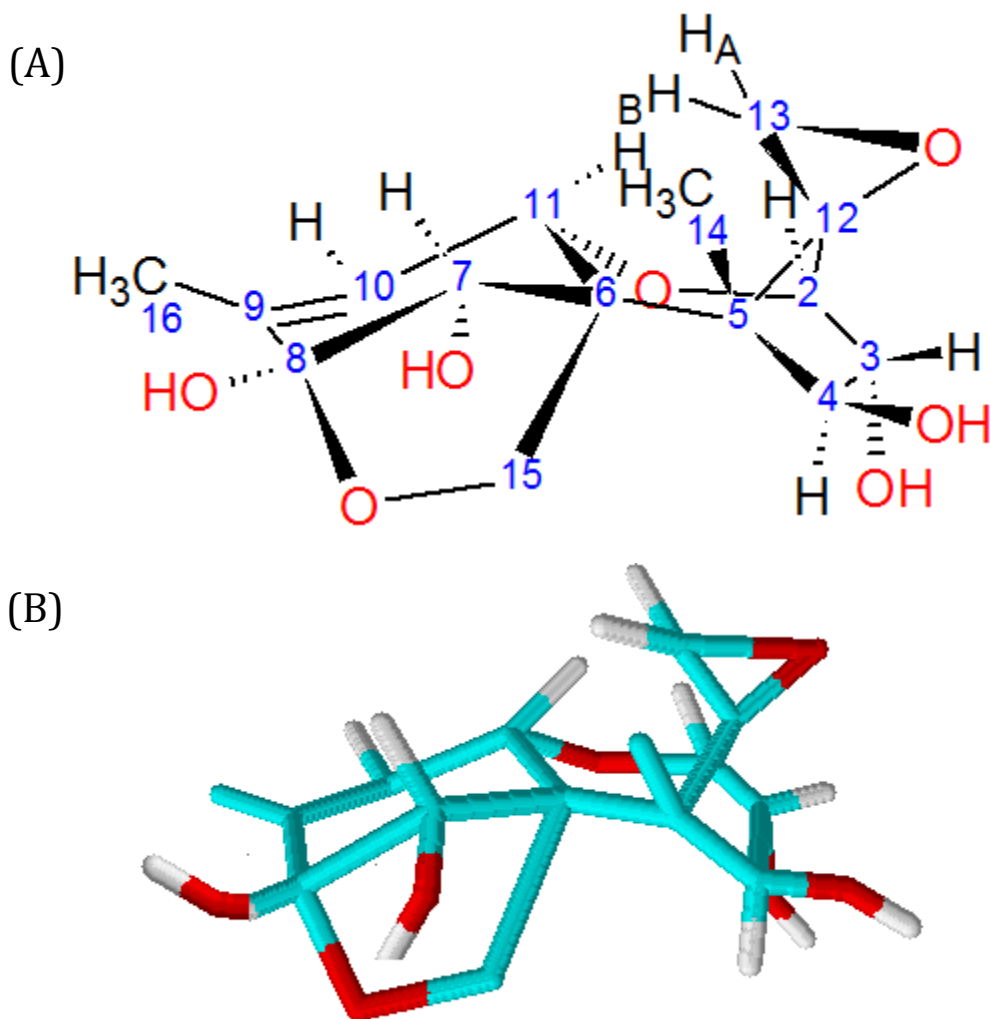


Figure 4. 10: Three-dimensional structure for the minor component of the NIV spectrum observed in DMSO- d_6 depicting the adoption of a boat configuration in the B-ring. (A) Chemical Structure formula included for reference, (B) Stick structure showing 3D geometry and torsion angles.

Analysis of the Carbon-13 spectrum for NIV in DMSO-d₆

The presence of a minor contribution to the spectrum is observed in all of the spectra collected for NIV in DMSO-d₆, including the ¹³C spectrum. In addition to the new evidence presented here for the minor contribution as described by the 1D and 2D ¹H spectra, the ¹³C spectrum confirms the presence of the peaks observed by Jarvis *et al.* (red asterisks, figure 4.6) [72], for the hemiketal isomer, and also indicates the presence of additional peaks (blue asterisks figure 4.6) which may also be attributed to the hemiketal structure shown in figure 4.10.

The peaks appearing at 103.71 ppm and 113.87 ppm in the CP ¹³C spectrum for NIV in DMSO-d₆ correspond well with the minor C-8 and C-10 peaks described by Jarvis *et al.* for the ¹³C DEPT spectrum acquired for DON in DMSO-d₆ [72]. In the major component C-8 appears at 199.89 ppm due to the double bond with the oxygen of the C-8 carbonyl. However, in the hemiketal structure, the double bond character is lost, and C-8 is now sp³-hybridized. The oxygen at C-8 now forms part of the hemiketal with C-15; thus, the chemical shift remains significantly deshielded due to the direct attachment of the oxygen.

In the major configuration C-10 is involved in an ethene bond with C-9 that is conjugated with the carbonyl at C-8. However, in the minor configuration, the carbonyl is no longer present, and the conjugation is lost. The change in conjugation results in a slightly lower chemical shift frequency for C-10.

Five other peaks are observed in the CP ¹³C spectrum for NIV in DMSO-d₆, and are attributed to carbon resonances in the A-ring for NIV. Carbon C-6, which is at the hinge point for the A-ring, B-ring, as well as the newly formed hemiketal ring, is predicted to observe a rather large increase in chemical shift, from 56.05 ppm in the major configuration to 76.19 ppm in the minor configuration due to the large increase in the ring strain applied to this carbon. Carbon C-15 is also predicted to experience a large change in chemical shift, increasing from 59.78 ppm in the major configuration to 88.61 ppm in the minor configuration. For C-15, the change from the hydroxyl substituent, H-15_{OH}, to

the hemiketal substitution, is not expected to have a significant effect on the chemical shift simply due to the chemical structure; however, the change in the three-dimensional geometry, and added ring strain observed for C-15 may produce the large increase in chemical shift. Carbon C-15 is now locked into place, and is in close proximity to the oxygen atom of the hydroxyl substituent at C-7, which will produce significant electron withdrawing effects, serving to further deshield C-15. Furthermore, an increase in the chemical shift of C-15 serves to support the hypothesis that water-binding in the hemiketal configuration occurs within the newly formed hemiketal pocket, which was suggested due to the exchange peak with water observed for H-7_{OH} in the NOESY spectrum (figure 4.5).

Carbons C-12, C-13 and C-14 also experience slight changes in chemical shift, 3 to 8 ppm, due to the change in the three-dimensional geometry of the trichothecene core. The largest difference among these is the decrease in chemical shift of C-13, which shifts from 52.88 ppm in the major configuration to 46.60 ppm in the minor. No significant changes were observed for protons H-13_A and H-13_B for the minor configuration of NIV; therefore, the geometry of the epoxide is not significantly affected; however, the proximity of C-13 to an electron withdrawing group, such as that present at O-1 in the trichothecene core, could result in the decrease in chemical shift. Thus, the change in chemical shift of C-13 supports the change in geometry of the B-ring from a chair to a boat configuration.

Overall, the information gathered for the minor contribution of NIV as acquired in DMSO-d₆, indicates that NIV undergoes a rearrangement from the accepted C-8 ketone type B trichothecene structure, to the less well documented hemiketal structure. Furthermore, it also provides direct evidence for a boat conformation adopted by the B-ring. Evidence also exists for a change in the water-binding between the major and minor configurations, where the major configuration showed the presence of at least one water molecule binding within the tetrahydropyranyl pocket, and the minor configuration appears to support the binding of water within the newly formed hemiketal pocket, but not within the tetrahydropyranyl pocket.

4.6 Solvent Effects Observed for DON

4.6.1 Results

Previous work by Jarvis *et al.* suggests that like NIV, DON also exists in a second minor conformation [72]. Jarvis collected the ^{13}C DEPT spectra of DON in several solvent systems to probe the effects of solvent on the trichothecene structure. The physical and chemical properties of the solvents of interest in this study are listed in table 4.1.

The spectra of DON prepared for the chosen solvents are shown in figure 4.11, with chemical shift and coupling constants tabulated in Tables 4.5 and 4.6, respectively.

Many of the ^1H chemical shifts for DON in CDCl_3 , CD_3OD and THF-d_8 are in remarkably close agreement, deviating only where significant interactions with the solvent are to be expected; such as areas that are more susceptible to the different properties of the solvent due to hydrogen-bonding, chemical exchange, or solvent polarity (i.e. the hydroxyl protons). The physical effects of the solvent are also reflected by the water signal. The chemical shift of the water is incredibly sensitive to the surrounding environment. It is affected by solvent polarity, hydrogen bonding, temperature, pH and ionic strength; the same is true of the chemical shift of the hydroxyl protons. In the case of CD_3OD , none of the hydroxyl hydrogens are seen due to exchange with this aprotic solvent, and the water peak is in fact attributed to HDO, due to exchange with the solvent. The hydroxyl residues are observed in THF, but are shifted with respect to those in CDCl_3 , most likely due to the effects of the different polarities of the solvents.

The chemical shifts of the protons on C-4, 4_α and 4_β , in the chloroform spectrum experience a difference in frequency of 0.1 ppm; however, in the case of all other solvents, the difference in frequency is much larger, approximately 0.5 ppm

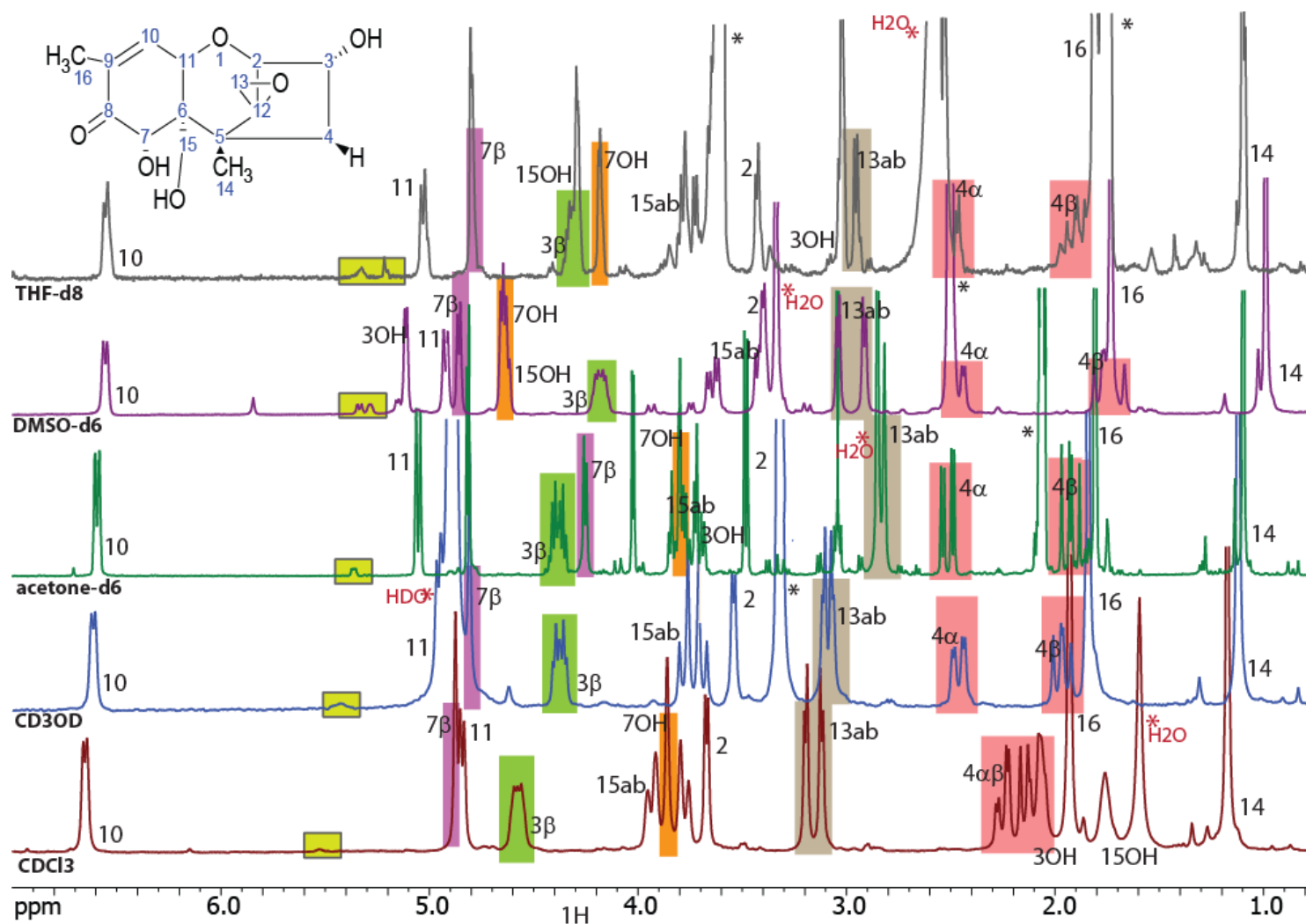


Figure 4. 11: ^1H NMR spectra observed for DON in CDCl_3 , methanol (CD_3OD), acetone- d_6 , DMSO- d_6 , and THF- d_8 at 300 MHz. Peaks of interest in the spectrum are highlighted. Solvent peaks are denoted with a black asterisk; whereas, the water peaks are denoted by a red asterisk.

Table 4. 5: Chemical shift data for DON in various solvent systems at 300 MHz

¹ H label	Chemical Shift – δ (ppm)				
	CDCl ₃	CD ₃ OD	(CD ₃) ₂ CO	DMSO-d ₆	THF-d ₈
2	3.672 ¹	3.545 ¹	3.484 ¹	3.401	3.39 ²
3_β	4.577	4.378	4.386	4.180	4.28
3_{OH}	2.067	N/O ³	4.256	5.114	3.02
4_α	2.247	2.464	2.515	2.463	2.45
4_β	2.129	1.970	1.928	1.771	1.89
7_β	4.878	4.811	4.257	4.859	4.76
7_{OH}	3.862	N/O ³	3.803	4.654	4.15
10	6.656	6.615	6.597	6.555	6.51
11	4.845	4.959	5.055	4.923	4.99
13_A	3.120	3.111	4.818	3.041	2.99
13_B	3.195	3.072	4.026	2.916	2.92
14	1.174	1.124	1.097	0.991	1.06
15_A	3.781	3.697	3.825	3.641	3.79
15_B	3.933	3.779	3.709	3.412	3.69
15_{OH}	2.066	N/O ³	3.753	4.632	4.29
16	1.931	1.846	1.809	1.734	1.78

¹Chemical shifts were simulated to an accuracy of 0.001 Hz²Chemical shifts were simulated to an accuracy of 0.02 Hz³Chemical shifts for the hydroxyl resonances are not observed in CD₃OD due to exchange with the solvent.

Table 4. 6: Scalar coupling values obtained for DON in various solvent systems at 300 MHz

J	Scalar Coupling Constants – J (Hz)				
	CDCl ₃	CD ₃ OD	(CD ₃) ₂ CO	DMSO-d ₆	THF-d ₈
³ J _{2,3}	4.643 (± 0.005) ¹	4.479 (± 0.015) ¹	4.367 (± 0.02) ¹	4.182 (± 0.013) ¹	4.161 ²
³ J _{3,4α}	4.150 (± 0.005)	4.355 (± 0.014)	4.360 (± 0.02)	4.024 (± 0.014)	4.161
³ J _{3,4β}	11.013 (± 0.005)	11.101 (± 0.014)	11.151 (± 0.02)	11.312 (± 0.014)	9.708
³ J _{3,3OH}	1.131 (± 0.004)	N/O ³	4.222 (± 0.02)	3.853 (± 0.013)	N/O ⁵
² J _{4α,4β}	-14.748 (± 0.004)	-14.498 (± 0.015)	-14.457 (± 0.02)	-14.391 (± 0.014)	-14.423
³ J _{7β, 7OH}	1.213 (± 0.003)	N/O ³	2.630 (± 0.2)	4.226 (± 0.012)	2.774
³ J _{10,11}	5.283 (± 0.007)	5.583 (± 0.007)	6.100 (± 0.1)	5.918 (± 0.004)	N/O
⁵ J _{10,15α}	1.412 (± 0.007)	N/O ⁴	N/O ⁴	N/O ⁴	N/O ⁴
⁵ J _{10,15β}	0.948 (± 0.007)	N/O ⁴	N/O ⁴	N/O ⁴	N/O ⁴
⁴ J _{10,16}	1.519 (± 0.007)	N/O ⁴	0.490 (± 0.3)	0.936 (± 0.005)	N/O ⁴
² J _{13a,13b}	4.268 (± 0.004)	4.181 (± 0.015)	3.031 (± 0.2)	4.395 (± 0.004)	4.577
² J _{15a,15b}	-11.817 (± 0.007)	-12.075 (± 0.007)	-9.581 (± 0.2)	-11.673 (± 0.005)	-11.993
³ J _{15a 15OH}	0.965 (± 0.007)	N/O ³	4.356 (± 0.2)	4.783 (± 0.005)	N/O ⁵
³ J _{15b,15OH}	3.095 (± 0.007)	N/O ³	6.342 (± 0.2)	5.087 (± 0.005)	N/O ⁵

¹Simulations performed with SpinWorks 3.0 computer software. ²Spectrum could not be simulated due to lack of sufficient resolution. ³Hydroxyl resonances could not be observed in CD₃OD due to chemical exchange. ⁴Long Range coupling not observed. ⁵Coupling not measured due to lack of sufficient resolution.

The coupling constants observed for DON in CDCl_3 and DMSO-d_6 are in remarkably close agreement, only exhibiting significant differences for coupling that involve the hydroxyl resonances. CD_3OD and THF-d_8 also follow the same trends, but lack information regarding coupling in the hydroxyls and in such long range couplings as H-10 to H-15_{AB} and H-16. In the protic solvent CD_3OD , couplings to the hydroxyls are lost, due to deuterium exchange; thus, the couplings between the hydroxyl resonances to neighbouring protons cannot be obtained. The long range 4- and 5-bond couplings in the A-ring of the DON molecule are also lost. Of note are the long range couplings observed between H-10 to H-15_A and H-15_B, as well as the coupling of H-10 to the methyl-16 resonances, which are absent from the CD_3OD spectrum. The long range couplings on the A-ring are also missing in the spectrum in THF-d_8 . The signal-to-noise in the THF-d_8 spectrum is low, due to poor solubility, and was insufficient to allow for optimization of the simulations, which may have resulted in errors in the spectral assignment. For example, H-10 appears as a rather broad peak, indicating small line splitting; however, individual couplings could not be discerned. As a result, couplings involving H-10 to H-11, H-10 to H-15_A and H-15_B, as well as H-10 to H-16 were not obtained with the usual high degree of accuracy. Notable differences are observed among the ^1H chemical shifts in the presence of acetone- d_6 . In particular, the epoxide resonances appear at higher frequency (4.0 and 4.8 ppm) in acetone- d_6 when compared to CDCl_3 (3.1 and 3.2 ppm) and the other solvents.

Scalar couplings to the hydroxyl protons of DON in acetone- d_6 and DMSO-d_6 appear to be much larger than those observed in CDCl_3 . For example, the couplings between H-15_{OH} and H-15_A and H-15_B are 0.97 and 3.10 Hz, respectively in CDCl_3 , but appear to be 4.36 and 6.34 Hz in acetone- d_6 , and 4.78 and 5.09 Hz in DMSO-d_6 . The internal hydrogen bonding network in DON is not disrupted, as the signals indicating this interaction (the narrow line-width, and well-defined couplings of H-7_{OH}) remain sharp; however, the differences in couplings observed involving the protons on C-15, suggest that a different geometry is adopted in these solvents.

The same changes in coupling occurs for H-3_β and the hydroxyl H-3_{OH} proton. In CDCl_3 the couplings are rather small, on the order of 1.1 Hz; however, in acetone- d_6 and DMSO-d_6 the coupling

is much larger, approximately 4.2 and 3.9 Hz, respectively. The hydroxyl couplings are not observed in CD₃OD due to chemical exchange with the solvent, and in THF-d₈ due a lack in sufficient resolution.

Solvent Effects on the Carbon Spectra for DON

Although ¹³C NMR was performed for DON in all of the solvents listed in table 4.1, only those in CDCl₃, acetone-d₆, and DMSO-d₆ were acquired with sufficient signal-to-noise to allow for spectral analysis, and are depicted in figure 4.11. The ¹³C spectra for DON in CD₃OD and THF-d₈ were also acquired with the same experimental time and number of scans as the other solvents; however, the signal for the solvent is overwhelming in these spectra, such that even when linear prediction and line broadening methods are applied [144], the sample signals are lost in the noise. The chemical shift information for the spectra shown in figure 4.12 is tabulated in table 4.7, and are compared with the shifts previously reported by Jarvis *et al.* [72].

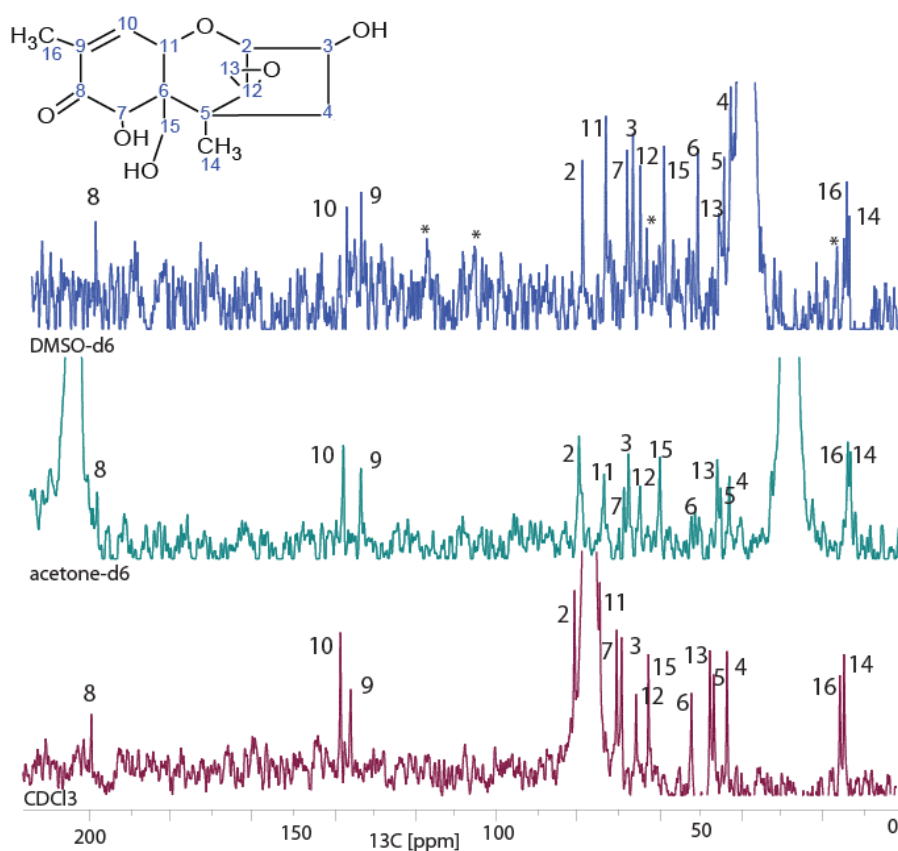


Figure 4. 12: CP ¹³C spectra for DON in CDCl₃, acetone-d₆ and DMSO-d₆ at 75 MHz, acquired with 4000 scans and a relaxation delay of 2 seconds. Peaks detected for the minor contribution to the spectrum are highlighted in the spectrum for DMSO-d₆ with black asterisks.

Table 4. 7: Experimental and literature ^{13}C chemical shift data for DON collected in CDCl_3 , acetone- d_6 and $\text{DMSO}-\text{d}_6$

CDCl_3			Acetone- d_6		$\text{DMSO}-\text{d}_6$	
Carbon	Literature ¹	Experimental	Literature ¹	Experimental	Literature ¹	Experimental
2	80.6	80.80	81.6	80.84	80.2	80.62
3	68.6	69.17	69.3	68.60	67.8	68.17
4	43.0	43.21	44.4	43.64	43.7	44.12
5	47.2	46.46	46.5	45.79	45.4	45.75
6	52.1	51.96	53.0	52.20	51.8	52.18 (64.77)
7	70.2	70.39	70.6	69.71	69.3	69.61
8	202.3	199.87	200.7 (104.7)	199.83	200.0 (104)	200.58 (100.64)
9	135.7	135.96	135.6	134.68	134.8	135.18
10	138.5	138.4	139.7 (122.0)	138.99	138.2 (121)	138.71 (119.10)
11	74.4	74.53	75.4	74.57	74.5	74.84
12	65.6	65.61	66.5	65.66	66.0	66.31
13	46.0	47.41	47.5	46.66	46.7	47.11
14	13.9	14.34	14.5	13.71	14.5	14.84
15	61.4	62.56	61.5	60.80	60.1	60.47
16	14.9	15.37	15.2	14.41	15.1	15.46 (16.20)

¹All literature data obtained from Jarvis *et al.* [72]. *Comparison of NIV ^1H Spectra in $\text{DMSO}-\text{d}_6$ and CDCl_3*

4.6.2 Discussion

The structure of DON appears frequently in the literature; however, in the majority of cases the NMR structure has been studied strictly in CDCl_3 . In the paper describing the structural rearrangement to a hemiketal observed by Jarvis [72], the ^{13}C NMR was also obtained in deuterated acetone, methanol and DMSO. However, with only a ^{13}C spectrum to work from, the evidence for the hemiketal remains limited. In this study, the 1D and 2D ^1H NMR, as well as the ^{13}C spectra, were collected in deuterated chloroform, acetone, methanol, DMSO and THF, and were compared to determine whether the structure proposed by Jarvis *et al.* could be observed.

From the stacked plot of the spectra in figure 4.8, it is clear that only when DON is dissolved in CDCl_3 does the compound adopt a single structural conformation. In all other cases at least a small percentage of the compound is rearranged in the hemiketal form. In the past, high resolution spectra such as those reported in this study were not always possible, and with only a single contribution appearing in the CDCl_3 spectrum, this may have resulted in CDCl_3 being the solvent of choice. However, with the second conformation appearing across the various solvents, it begs the question as to whether the structure observed for the trichothecenes when dissolved in CDCl_3 , is the only true structure, or whether the rearrangement to the hemiketal form should be given more consideration.

As was observed for NIV, the possibility for rearrangement is largely influenced by the conformation of the ring system. A large undertaking to determine the key structural features of trichothecene toxins, as described by ^1H NMR, was performed in the late 1980s by Marc Savard and Barbara Blackwell [135]. They proposed that the B-ring preferentially adopts a chair conformation, with the epoxide ring in an axial position, and the methyl at carbon-14 sitting equatorial to the ring. However, not long after the Savard and Blackwell description of trichothecene structure was released, Jarvis and colleagues described a structural rearrangement of some type B trichothecenes, where the B-ring was shown to adopt a boat configuration, in which the methyl adopts an axial position on the ring, with the epoxide adopting an equatorial position [72]. The arrangement of the B-ring, which is central in the trichothecene core, influences the overall structural conformation of

the toxin. The preference for the B-ring to adopt either a chair or boat configuration is strongly influenced by the covalent bonding and hydrogen bonding interactions induced by its immediate environment (i.e. solvent system).

With the difficulties in obtaining crystals of sufficient quality to perform SCXRD [59], and the well documented capability of DON to form intramolecular hydrogen bonds [111], it seems only natural that DON may exist in more than one stable conformation. Thus, in an attempt to tease out the information regarding other possible conformations of DON, the compound was dissolved in several solvents (DMSO- d_6 , acetone- d_6 , methanol- d_4 , and tetrahydrofuran (THF- d_4)), see table 4.1 for a description of the physical and chemical properties, and compared to the original structure in $CDCl_3$, which is described in detail in chapter 3.

The most notable differences observed for DON dissolved in different solvents occur in the chemical shifts observed in the presence of $(CD_3)_2CO$ (acetone- d_6); see table 4.5. In acetone- d_6 , the epoxide resonances appear at a much higher frequency (4.0 and 4.8 ppm) as compared to those in $CDCl_3$ (3.1 and 3.2 ppm). The carbon atom of the carbonyl functionality in acetone- d_6 acts as a strong electrophilic center, and the oxygen a strong nucleophile. Interaction with the highly strained carbon atoms (C-12 and C-13) of the epoxide is possible, where the oxygen atom would interact primarily with C-13, as C-12 is sterically obscured. The proximity of the oxygen to the epoxide hydrogens would serve to further deshield these centers and a higher chemical shift frequency would be observed. The positioning of the solvent with respect to the epoxide ring is depicted in figure 4.19. The interaction of the solvent with the trichothecene molecule results in the delocalization of the electrons within the π -bonded system of acetone- d_6 , which results in a local magnetic field about the carbonyl, as shown in figure 4.20. Areas along the axis of the π -bond would experience a stronger deshielding effect, resulting in a higher frequency in their chemical shift; whereas those electrons located in areas adjacent to the π -bond would experience a shielding effect, resulting in a much lower chemical shift frequency. Note that H-7 $_{\beta}$ also experiences a significant deviation in chemical shift from 4.8 ppm in $CDCl_3$ to 4.3 ppm in acetone- d_6 . This serves to confirm the orientation of the solvent molecule shown in figure 4.13, as H-7 $_{\beta}$ is located in the region where shielding would occur, and a

decrease in frequency is expected. H-11 is pointing into the page in this instance, and thus would likely be out of range of the shielding effects of the solvent.

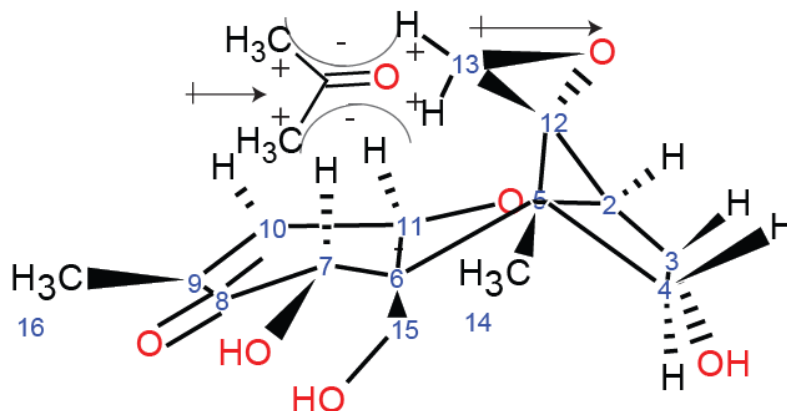


Figure 4. 13: The alignment of acetone- d_6 with respect to the epoxide functionality of DON. The double bond character of the carbonyl functionality of acetone results in areas that cause an increase in the deshielding, and subsequently the frequency, of the atoms located in those regions, these are denoted by the positive signs. As well as areas where increased shielding and a subsequent decrease in frequency are observed, denoted by the negative signs.

Upon introduction of the protic CD_3OD solvent, coupling to the hydroxyls is lost, as they are not observed in the spectrum due to chemical exchange. Thus, the couplings between the hydroxyl resonances to their nearby neighbours cannot be measured. A loss of the long-range 4- and 5-bond couplings on the A-ring of the DON molecule is also noted. The couplings between H-10 to H-15_A and H-15_B, as well as the coupling of H-10 to the methyl-16 resonances are not observed in the CD_3OD spectrum. The loss of coupling between H-10 to the protons on C-15 suggest that a disruption in the internal hydrogen bonding network, described for DON in chapter 3, has occurred; possibly due to the exchange of the 1H atom of the C-15 hydroxyl to the heavier 2H atom, or alternatively through the introduction of a new hydrogen bond with the solvent. It is important to note that the CD_3OD spectrum is not as well resolved as the $CDCl_3$ spectrum, which may reduce the ability to observe the longer range couplings. The rigidity of the A-ring has been disrupted to some extent, allowing the molecule to relax and the longer-range couplings to effectively disappear. The loss of rigidity of the A-ring would also result in the loss of observable coupling between H-10 and the methyl-16 resonances.

Solvent effects on the C-ring

Across the solvents, one area where a rather notable difference is seen are the chemical shifts in the C-ring. The difference between the shifts in CDCl₃ is approximately 0.1 ppm; whereas, in all the other solvents, the difference is approximately 0.5 ppm.

The C-ring is a rigid ring system, and the C-3/C-4 bond is locked without significant movement. As such, H-4_α is *cis* to H-3_{OH} and *trans* to H-3_β; H-4_β is *cis* to H-3_β and *trans* to H-3_{OH}. Based on the *cis*-substituent effect of rigid ring systems described by Williamson for a similar system [163], the proton which is *trans* to the hydroxyl, H-4_β in this case, would experience the higher chemical shift to that which is *cis* to the hydroxyl, H-4_α, due to the electron withdrawing effects of the oxygen. H-4_α is further shielded by the electron of the hydroxyl oxygen due to the neighboring group effect. The orientation is shown in figure 4.14, and is simplified by the use of a plane drawn along the C-ring.

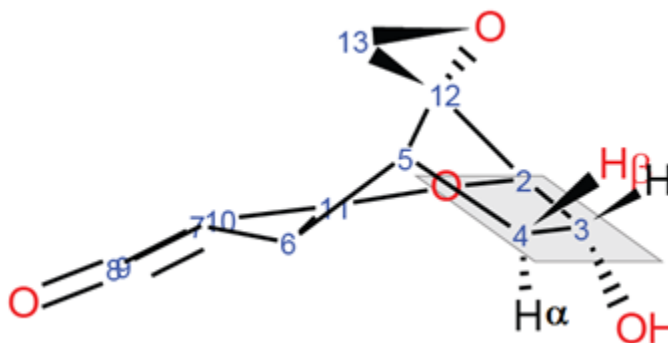


Figure 4. 14: Trichothecene core depicting the bonds at C-3 and C-4. The plane of the C-ring is shown in grey. H-4 α and H-3OH are present in the same plane across the ring and are *cis* to each other. H-4 β , shown in red is present on opposite side of the plane from H-3OH; thus, they are *trans* to each other.

This effect does not support the assignment which was adopted from the labeling in the literature by Savard and Blackwell [135]. Upon closer inspection, the coupling constants from H-3 β and H-4 β which is approximately 11.0 to 11.3 Hz, and from H-3 β to H-4 α , approximately 4.0 to 4.3 Hz, do not support the Savard and Blackwell assignment either. Typical *trans* coupling constants have values of approximately 10-14 Hz; whereas, *cis* coupling tends to be on the order of 3-5 Hz. Therefore, the coupling of 11 Hz suggests a *trans* coupling, and a coupling of 4 Hz supports a *cis*

coupling. Thus, the assignment should be revised and the labeling scheme for H-4 α and H-4 β needs to be swapped.

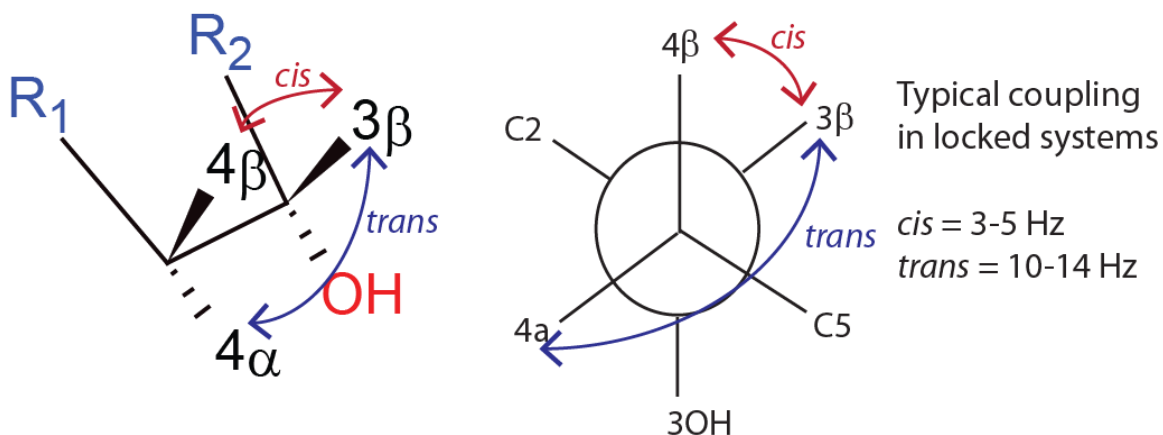


Figure 4. 15: Depiction of the coupling for the protons on C-4 to the proton H-3 β , along with the Newmann projection for this interaction which looks down the bond from C-3 to C-4. The coupling observed for H-3 β to H-4 β should be typical of a *cis* coupling which is on the order of 3-5 Hz; whereas the coupling from H-3 β to H-4 α should be typical of a *trans* coupling, 10-14 Hz.

Vicinal coupling observed for the hydroxyl resonances in DON

It was observed that in the non-polar solvent chloroform, CDCl₃, the coupling constants involving hydroxyl protons were all very small, on the order of 0.9 to 1.2 Hz. However, as the solvent was changed to a more polar system such as acetone-d₆ or DMSO-d₆, the vicinal coupling constants involving hydroxyl protons became much larger. Investigation into this phenomenon produced information regarding the Karplus relationship for J_{HCOH} couplings, which were described in detail in a paper by Fraser *et al.* [46]. The paper describes the Karplus equation for J_{HCOH} couplings, and also indicates that the polarity of the solvent used seems to have an effect on the sampling of the rotational isomers in solution. The Karplus equation for J_{HCCH}, equation 4.1, differs slightly from that which Fraser calculated for J_{HCOH}, equation 4.2.

$$^3J_{HCC H} = 13.0 \cos^2 \varphi + (-1.5) \cos \varphi + (-0.3) \text{ Hz} \quad (4.1)$$

$$^3J_{HCO H} = 10.4 \cos^2 \varphi + (-1.5) \cos \varphi + 0.2 \text{ Hz} \quad (4.2)$$

Using the equation for $^3J_{HCO H}$ it is possible to estimate what the couplings for the *trans* (180°), *gauche* (60°), and *gauche'* (300°) rotations about these hydroxyl bonds will evaluate to.

$$J_g = 10.4 (0.5)^2 - 1.5(0.5) + 0.2 = 2.05 \text{ Hz}$$

$$J_{g'} = 10.4 (0.5)^2 - 1.5(0.5) + 0.2 = 2.05 \text{ Hz} \quad (4.3)$$

$$J_t = 10.4 (-1)^2 - 1.5(-1) + 0.2 = 12.1 \text{ Hz}$$

$$J_{\text{avg}} = (J_g + J_{g'} + J_t)/3 = (2.05 + 2.05 + 12.1)/3 = 5.4 \text{ Hz}$$

This information provides a means with which to describe the orientation of the hydroxyl bonds in solution.

For example, the change in coupling observed for $^3J_{3,3OH}$ from non-polar CDCl_3 to the polar acetone- d_6 and DMSO- d_6 solvents appears to indicate that a change in configuration about the bond has occurred. In CDCl_3 the vicinal coupling $^3J_{3,3OH}$ is approximately 1.1 Hz; whereas, in acetone- d_6 and DMSO- d_6 the coupling changes to 4.2 and 3.9 Hz respectively.

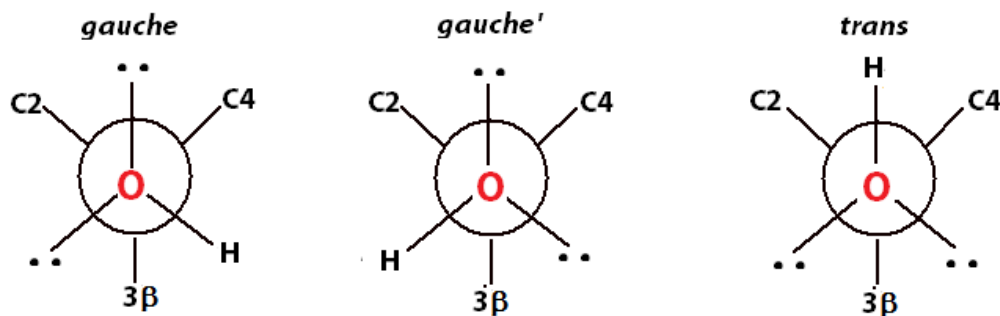


Figure 4. 16: Newmann projections along the H-C-O-H bond for the hydroxyl resonance at C-3 showing the *gauche*, *gauche'* and *trans* coupling orientation for H- 3_β to H- 3_{OH} .

The coupling constant observed for ${}^3J_{3,3OH}$ in $CDCl_3$ suggests that the bond orientation preferentially rotates between the *gauche* and *gauche'* configurations, barely spending any time at all in the *trans* orientation. However, in the polar solvent systems, acetone- d_6 and DMSO- d_6 the 4.2 and 3.8 Hz coupling suggest that the rotational isomers are sampled more evenly, as the coupling is much closer to the average value of 5.4 Hz; however, a slight preference for the *gauche* and *gauche'* configurations does exist.

Similarly, the couplings observed for the hydroxyl at C-7 appears to follow the same trend as that described for the hydroxyl at C-3. In $CDCl_3$, ${}^3J_{7,7OH}$ has a value of 1.2 Hz, but when measured in acetone- d_6 and THF- d_8 the coupling increases to 2.6 and 2.8 Hz, respectively, suggesting that the orientation is preferentially *gauche* and *gauche'*, with only a slight increase in *trans* sampling for the more polar solvents. Even in DMSO- d_6 , the value for ${}^3J_{7,7OH}$ only increases to 4.2 Hz, indicating that the *gauche* orientations are still preferentially sampled in solution.

The final region of the molecule where the H-C-O-H bond angles are present are along the C-15 bond to C-15_{OH}. If the bond angles are different in non-polar versus polar solvents, then some explanation regarding the absence of hemiketal isomers in non-polar solvent systems may be available. The hemiketal isomer appears to be present in all of the solvent systems in which DON was dissolved, with the exception of $CDCl_3$. Based on the data recorded here the hemiketal isomer appears to only occupy up to 20% of the population in the sample.

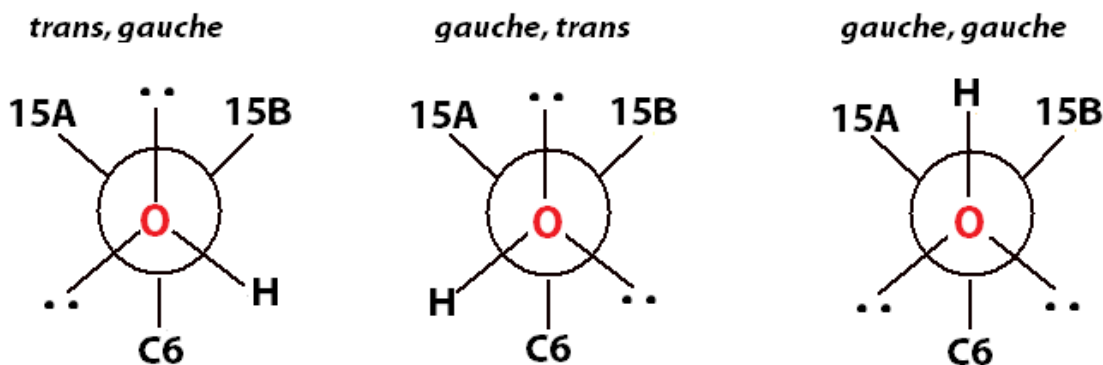


Figure 4. 17: Newmann projections for the rotations observed along the C-15 to O-15 bond in DON. The labeling scheme refers to the coupling of 15_A(15_{OH}), 15_B(15_{OH}), such that the term *trans, gauche* refers to 15_A being *trans* to 15_{OH}, and 15_B being *gauche* to 15_{OH}

Table 4. 8: Scalar coupling values for DON in CDCl₃, acetone-d₆, and DMSO-d₆

Solvent	CDCl ₃	Acetone-d ₆	DMSO-d ₆
³ J _{15A,15OH}	0.965	4.356	4.783
³ J _{15B,15OH}	3.095	6.342	5.087
Interpretation	Coupling pattern suggests that the protons preferentially sample a <i>gauche, gauche</i> configuration	Coupling pattern suggests that the protons sample all rotations, but have a slight bias towards a <i>gauche, trans</i> configuration.	Coupling pattern suggests that the protons sample all rotations, but have a slight bias towards a <i>gauche, gauche</i> configuration.

In terms of the three-dimensional configuration for DON, it is clear a *gauche, gauche* configuration along the C-15 to O-15 bond will not promote the proper geometry for bond formation between the carbonyl at C-8 and the hydroxyl at C-15, which must take place in order for the hemiketal configuration to form. However, sampling of the *trans* configuration along this bond in DON, places the C-15 hydroxyl in the proper geometry to promote interaction with the C-8 carbonyl. Without the proper orientation and the appropriate energy within the system, the reaction which produces the hemiketal bond cannot take place.

Therefore, in polar solvent systems the conditions for hemiketal formation are present to a greater extent than in non-polar solvent systems. Surprisingly, evidence for the hemiketal isomer exists in THF-d₈, which according to table 4.1, is relatively non-polar with a polarity index of only 4.0; whereas, CDCl₃ has a polarity index of 4.1. However, the dielectric constant for THF-d₈ is greater than CDCl₃, at 7.60 versus 4.81, and the actual dipole moment of THF-d₈ (1.75) is also much larger than that of CDCl₃ (1.04) both of which also has an effect on the relative polarity of the solvent. Thus, THF is considered to be a borderline polar aprotic solvent, for all intents and purposes and may serve to influence the orientation about the hydroxyl bonds, while CDCl₃ is a non-polar aprotic solvent, and does not serve to align the molecule in the proper orientation for hemiketal formation.

The hemiketal isomer is present in different proportions in different solvent systems, which suggests that the two conformations exist in equilibrium with each other. The polarity of the solvent appears to have a large effect of the equilibrium between the two isomers. However, the equilibrium does not

appear to be directly proportional to the polarity of the solvent, which suggests that other factors may play a significant role in the equilibrium between the isomers of the type B trichothecenes.

4.7 Investigation into the effects of non-polar CDCl_3 versus polar DMSO-d_6 solvents across the Type B trichothecenes

4.7.1 Results

The differences in the spectra and overall conformation observed among the non-polar and polar solvents for the type B trichothecene DON, led to the investigation of the other type B trichothecenes NIV, 3-ADON and 15-ADON in both the non-polar solvent CDCl_3 and the polar solvent DMSO-d_6 .

DMSO-d_6 was chosen among the polar solvents since DON spectra it was shown to adopt a larger percentage of the secondary hemiketal isomer in this solvent. Furthermore, the type B trichothecenes displayed sufficient solubility in DMSO-d_6 , in particular, NIV was insoluble in all other solvents presented including CDCl_3 . The relatively high solubility of the trichothecenes in DMSO-d_6 also produces spectra with greater signal-to-noise ratio and spectral resolution.

As mentioned, NIV was unfortunately not soluble in the non-polar CDCl_3 alone, and had to be analyzed in a mixture of CDCl_3 and CD_3OD , which results in a much more polar solvent overall. In fact, evidence exists for the secondary minor hemiketal conformation for NIV in the $\text{CDCl}_3:\text{CD}_3\text{OD}$ spectrum, which is highlighted in figure 4.18 by the presence of the characteristic H-8_{OH} peak at approximately 5.3 ppm.

Figure 4.18 contains the ^1H spectra of NIV in $\text{CDCl}_3:\text{CD}_3\text{OD}$ and DMSO-d_6 . Both spectra were analyzed separately and presented earlier. The chemical shift and coupling constant data is retabulated in tables 4.9 and 4.10, respectively, for ease of comparison.

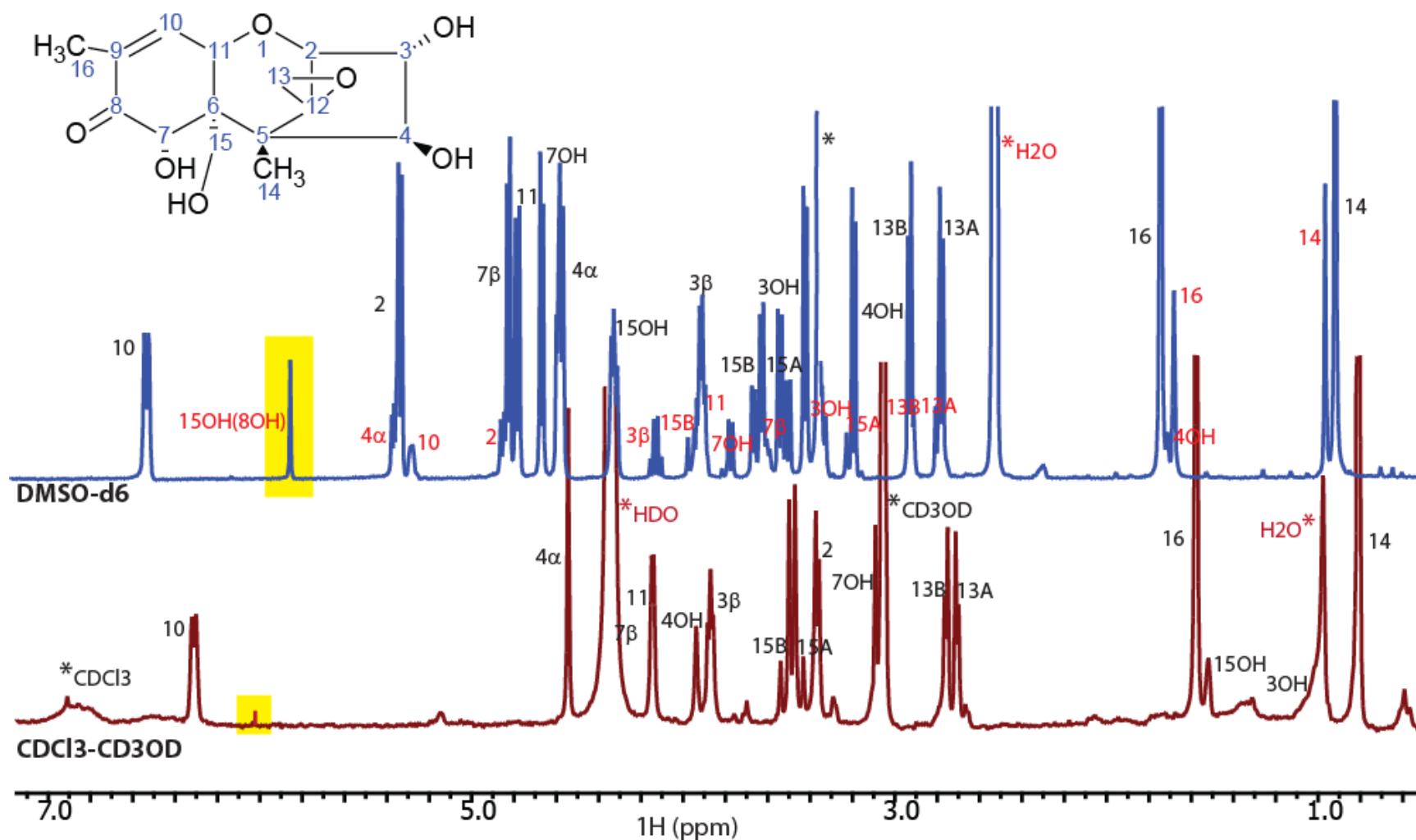


Figure 4. 18: ^1H NMR solution-state spectra for NIV compared in $\text{CDCl}_3\text{:CD}_3\text{OD}$ and DMSO-d_6 at 300 MHz. The major contributors to the spectra are labeled with black typescript; whereas, the minor contributor to the DMSO-d_6 spectrum for NIV is labeled with red type. The major spectrum conforms to the numbered structure depicted in the inset of the figure. The characteristic peak for the hemiketal configuration is highlighted in the spectra by yellow boxes.

Table 4. 9: Chemical shift data for the ^1H spectra of NIV in $\text{CDCl}_3:\text{CD}_3\text{OD}$ and $\text{DMSO}-d_6$ at 300 MHz

^1H label	Chemical Shift – δ (ppm)		
	$\text{CDCl}_3:\text{CD}_3\text{OD}$	$\text{DMSO}-d_6$ (Major)	$\text{DMSO}-d_6$ (minor)
2	3.366 ¹	5.312 ¹	4.827 ¹
3$_{\beta}$	3.872	3.889	4.103
3$_{\text{OH}}$	0.977	3.398	3.308
4$_{\alpha}$	4.543	4.556	5.336
4$_{\text{OH}}$	3.939	3.168	1.699
7$_{\beta}$	4.324	4.800	3.572
7$_{\text{OH}}$	3.157	4.642	3.777
10	6.311	6.509	5.259
11	4.329	4.757	3.866
13$_{\text{B}}$	2.756	2.903	2.891
13$_{\text{A}}$	2.707	2.754	2.773
14	0.807	0.893	0.942
15$_{\text{B}}$	3.513	3.619	3.936
15$_{\text{A}}$	3.459	3.499	3.187
15$_{\text{OH}}$(8$_{\text{OH}}$)	1.496	4.299	5.830
16	1.583	1.719	1.654

¹All spectra in Figure 4.15 were simulated to an accuracy of 0.001 Hz

Table 4. 10: Scalar $^1\text{H}\{^1\text{H}\}$ coupling data for NIV compared in $\text{CDCl}_3:\text{CD}_3\text{OD}$ and DMSO-d_6 at 300 MHz

^1H label	Scalar Coupling Constants – J (Hz)		
	$\text{CDCl}_3:\text{CD}_3\text{OD}$	DMSO-d_6 (Major)	DMSO-d_6 (minor)
$^3\text{J}_{2,3}$	$3.572 (\pm 0.002)^1$	$4.147 (\pm 0.001)^1$	$5.362 (\pm 0.001)^1$
$^3\text{J}_{3,4}$	$4.891 (\pm 0.002)$	$4.147 (\pm 0.001)$	$5.654 (\pm 0.001)$
$^3\text{J}_{3,3\text{OH}}$	N/O ²	$4.401 (\pm 0.001)$	$5.413 (\pm 0.001)$
$^2\text{J}_{4\alpha,4\text{OH}}$	N/O ²	$5.360 (\pm 0.001)$	$2.987 (\pm 0.001)$
$^5\text{J}_{3\text{OH},4\text{OH}}$	N/O ⁴	$0.623 (\pm 0.001)$	N/O ⁴
$^3\text{J}_{7\beta, 7\text{OH}}$	N/O ²	$4.359 (\pm 0.001)$	$5.569 (\pm 0.001)$
$^3\text{J}_{10,11}$	$5.646 (\pm 0.005)$	$5.815 (\pm 0.001)$	$4.783 (\pm 0.001)$
$^4\text{J}_{10,16}$	$0.483 (\pm 0.002)$	$0.281 (\pm 0.001)$	$0.503 (\pm 0.001)$
$^2\text{J}_{13\alpha,13\beta}$	$4.362 (\pm 0.002)$	$4.507 (\pm 0.001)$	$4.852 (\pm 0.001)$
$^5\text{J}_{11,16}$	$0.799 (\pm 0.001)$	N/O ⁴	N/O ⁴
$^2\text{J}_{15\alpha,15\beta}$	$-12.022 (\pm 0.004)$	$-11.641 (\pm 0.001)$	$9.052 (\pm 0.001)$
$^3\text{J}_{15\alpha 15\text{OH}}$	$3.513 (\pm 0.001)$	$3.976 (\pm 0.001)$	N/O ³
$^3\text{J}_{15\beta,15\text{OH}}$	$3.459 (\pm 0.001)$	$5.545 (\pm 0.001)$	N/O ³

¹All spectra were simulated with the SpinWorks program with an average RMSD below 0.034 Hz and a standard deviation between 0.03 and 0.06 Hz

²These hydroxyl couplings were not observed in the $\text{CDCl}_3:\text{CD}_3\text{OD}$ spectrum due to chemical exchange

³Couplings not observed due to structural changes, and loss of the 15_{OH} signal.

⁴Long range couplings not observed.

In terms of the ^1H spectrum for the major component of NIV observed in DMSO-d_6 and the $\text{CDCl}_3:\text{CD}_3\text{OD}$ mixture, the chemical shifts differ slightly from each other, which can readily be attributed to differences in the dielectric constants and polarity of the solvents, suggesting that their configurations are essentially the same. The most significant changes in the ^1H chemical shifts between the two solvent systems occur in the hydroxyl resonances of H-3_{OH} , H-4_{OH} , H-7_{OH} and H-15_{OH} , which can be attributed to the differences in the solvent polarity [15,95,116,151]. For example, H-3_{OH} has a chemical shift of 0.977 ppm in $\text{CDCl}_3:\text{CD}_3\text{OD}$ and a chemical shift of 4.551 ppm in DMSO-d_6 . The hydroxyl resonances of NIV undergo rapid exchange with methanol; thus, any couplings to them are lost in the $\text{CDCl}_3:\text{CD}_3\text{OD}$ mixture. Interestingly, the couplings between H-15_A and H-15_B to H-15_{OH} are preserved in the mixed solvent, indicating that H-15_{OH} may be involved in hydrogen bonding, preventing exchange. These couplings change in different proportions, such that the coupling $^3\text{J}_{15\text{A},15\text{OH}}$ is approximately 3.5 Hz in $\text{CDCl}_3:\text{CD}_3\text{OD}$ and 4.0 Hz in DMSO-d_6 ; whereas, $^3\text{J}_{15\text{B},15\text{OH}}$ is 3.5 Hz in $\text{CDCl}_3:\text{CD}_3\text{OD}$ and 5.5 Hz in DMSO-d_6 . These couplings suggest that in $\text{CDCl}_3:\text{CD}_3\text{OD}$ the bonds preferentially adopt a *gauche, gauche* configuration, but in DMSO-d_6 all configurations are sampled nearly equally. The chemical shift and coupling constants of the minor component of NIV observed in DMSO-d_6 bear little resemblance to those of the major component and the spectrum observed in the $\text{CD}_3\text{OD}:\text{CDCl}_3$ mixture. These differences will be revisited in the following discussion.

The chemical shift for H-4_α also deviates greatly between the DMSO-d_6 and $\text{CD}_3\text{OD}:\text{CDCl}_2$ spectra. This may also be attributed to the variation in hydrogen bonding behavior amongst the solvents. H-4_α lies in close proximity to both H-3_{OH} and H-4_{OH} . Orientation of the hydroxyls may affect the chemical shift of H-4_α as we saw with DON.

The carbon chemical shifts for NIV in $\text{CD}_3\text{OD}:\text{CDCl}_3$ could not be obtained by direct observation of the carbon-13 spectrum, and upon close analysis of the HSQC $^1\text{H-}^{13}\text{C}$ spectrum, it was determined that the signals present do not correspond to any available internal reference. Thus, only the carbon chemical shifts for NIV in DMSO-d_6 are available, and the comparison between the carbon data for NIV cannot be made.

Comparison of 3-ADON and 15-ADON Spectra in DMSO-d₆ and CDCl₃

The ¹H spectra shown in figures 4.19 and 4.20 allow comparisons to be drawn between the structures of 3-ADON and 15-ADON in CDCl₃ and DMSO-d₆, respectively. The data for these are combined in Tables 4.11 and 4.12, which contain the chemical shifts and coupling constants, respectively.

Table 4. 11: ¹H chemical shift comparison for 3-ADON and 15-ADON in CDCl₃ and DMSO-d₆ at 300 MHz ¹All

¹ H label	3-ADON Chemical Shift – δ (ppm)		15-ADON Chemical Shift – δ (ppm)	
	CDCl ₃	DMSO-d ₆	CDCl ₃	DMSO-d ₆
2	3.939 ¹	3.777 ¹	3.679 ¹	3.444 ¹
3_β	5.258	4.949	4.573	4.224
3_{OH}	N/A	N/A	2.143	5.289
4_α	2.395	2.806	2.262	2.140
4_β	2.199	1.908	2.145	1.888
7_β	4.865	5.041	4.873	4.723
7_{OH}	3.831	4.639	3.791	5.254
10	6.635	6.617	6.644	6.597
11	4.714	4.788	4.928	4.847
13_B	3.206	3.148	3.178	3.090
13_A	3.144	2.983	3.120	2.935
14	1.189	1.043	1.117	0.973
15_B	3.912	3.786	4.281	4.259
15_A	3.859	3.499		4.078
15_{OH}	1.789	0.971	N/A	N/A
16	1.929	1.739	1.927	1.765
1'	2.166	2.098	1.917	1.843

chemical shifts were simulated to with 0.001 Hz accuracy

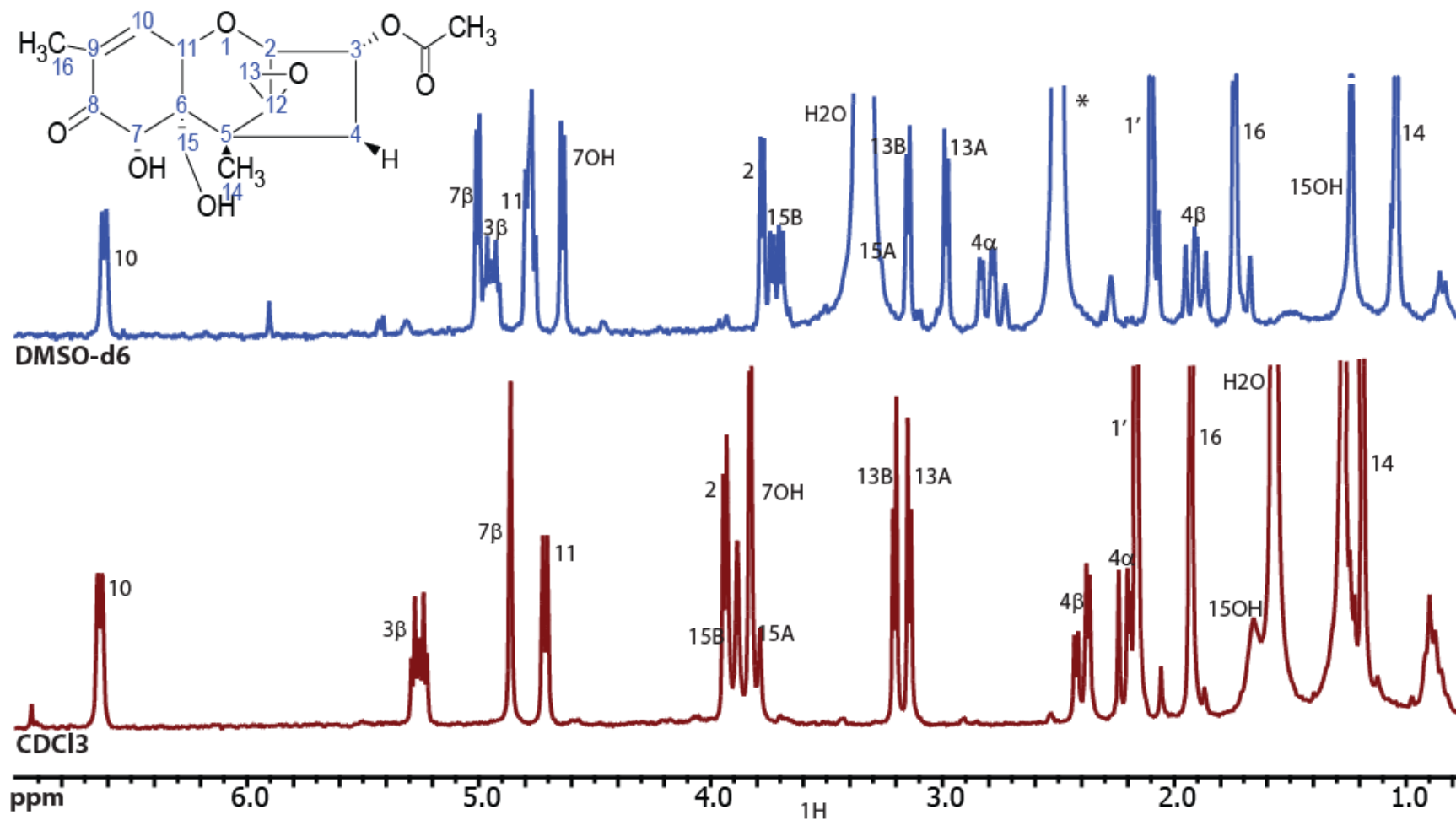


Figure 4. 19: ^1H NMR spectral comparison for 3-ADON in CDCl_3 and DMSO-d_6 at 300 MHz. The labels for the signals in the spectra correspond to the numbered structure depicted in the inset of the figure.

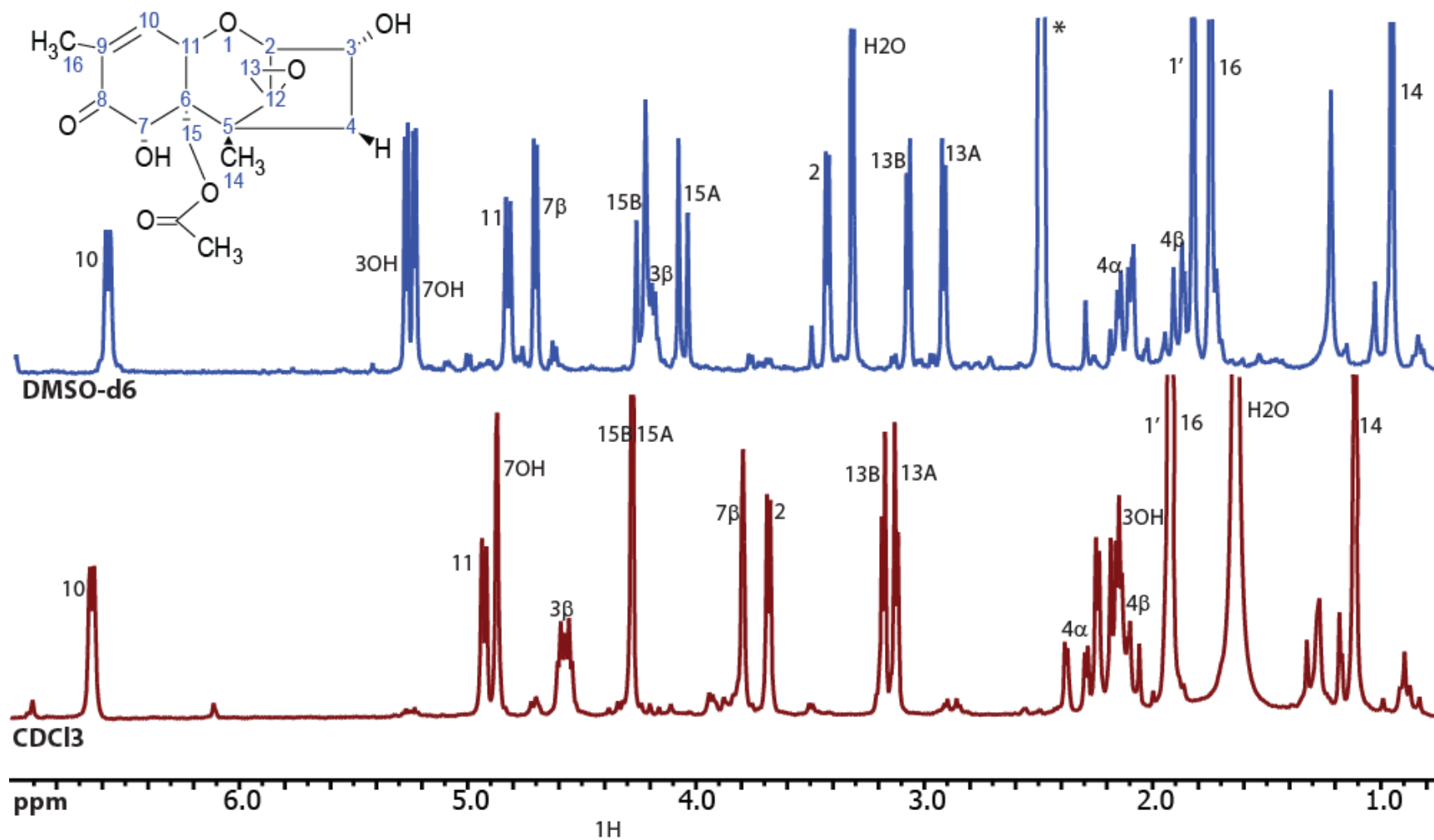


Figure 4. 20: ^1H NMR spectral comparison for 15-ADON in CDCl_3 and DMSO-d_6 at 300 MHz. The labels for the signals in the spectra correspond to the numbered structure depicted in the inset of the figure.

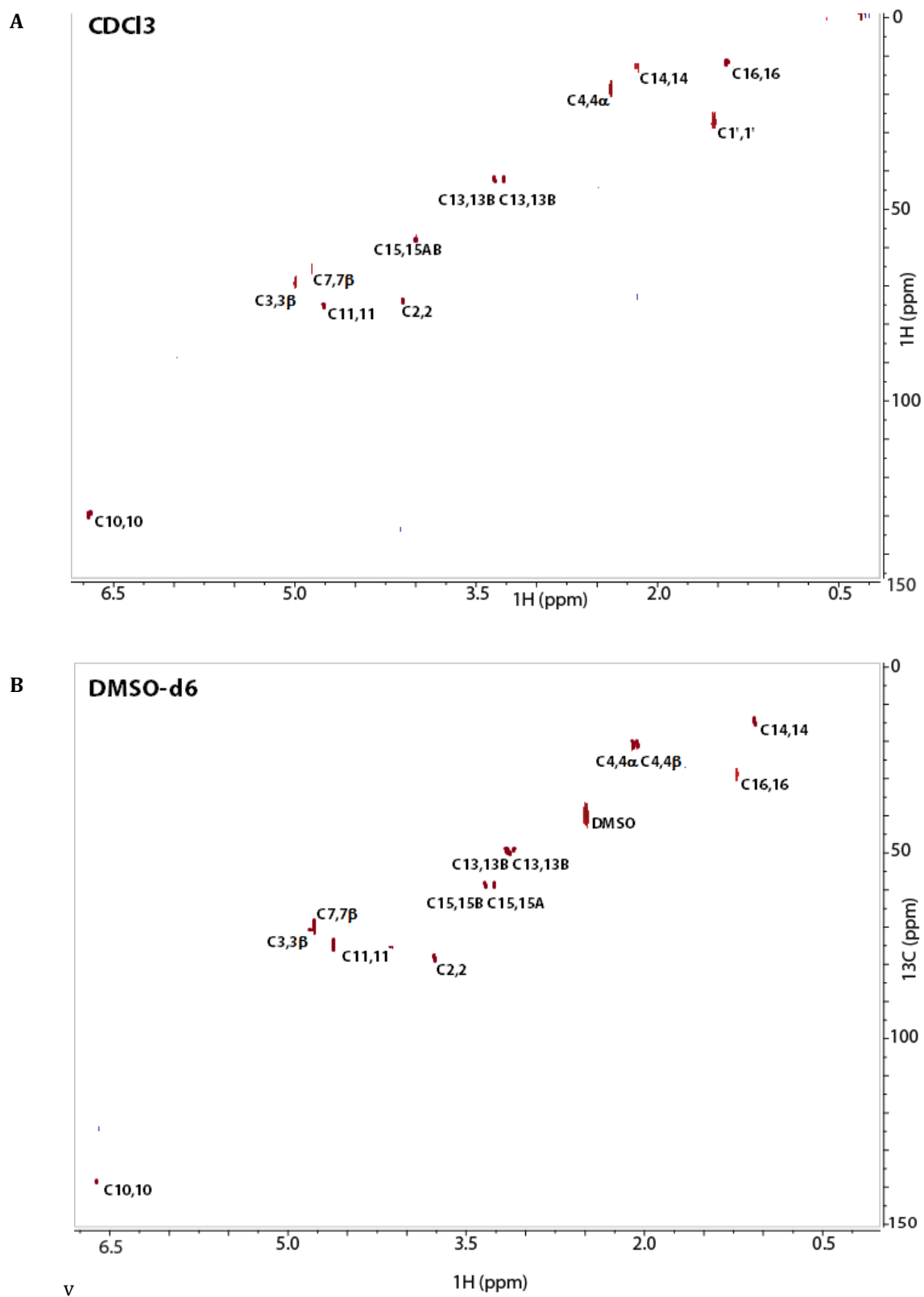
Table 4. 12: $^1\text{H}\{^1\text{H}\}$ scalar coupling data for 3-ADON and 15-ADON collected in CDCl_3 and DMSO-d_6 at 300 MHz

^1H label	3-ADON Scalar Coupling – J (Hz)		15-ADON Scalar Coupling – J (Hz)	
	CDCl_3	DMSO-d_6	CDCl_3	DMSO-d_6
$^3\text{J}_{2,3}$	4.418 (± 0.001)	4.401 (± 0.001)	4.417 (± 0.001)	4.394 (± 0.001)
$^3\text{J}_{3,4\alpha}$	4.285 (± 0.001)	4.257 (± 0.001)	4.096 (± 0.001)	4.411 (± 0.001)
$^3\text{J}_{3,4\beta}$	11.352 (± 0.001)	11.394 (± 0.001)	11.064 (± 0.001)	11.239 (± 0.001)
$^3\text{J}_{3,3\text{OH}}$	N/A	N/A	N/O	4.185 (± 0.001)
$^2\text{J}_{4\alpha,4\beta}$	-15.069 (± 0.001)	-15.070 (± 0.001)	-14.807 (± 0.001)	-14.533 (± 0.001)
$^3\text{J}_{7\beta, 7\text{OH}}$	1.592 (± 0.001)	4.515 (± 0.001)	1.438 (± 0.001)	4.285 (± 0.001)
$^3\text{J}_{10,11}$	5.911 (± 0.001)	5.197 (± 0.001)	5.769 (± 0.001)	3.729 (± 0.001)
$^4\text{J}_{10,16}$	1.304 (± 0.001)	1.191 (± 0.001)	1.314 (± 0.001)	1.073 (± 0.001)
$^2\text{J}_{13\text{A},13\text{B}}$	4.247 (± 0.001)	4.384 (± 0.001)	4.271 (± 0.001)	4.342 (± 0.001)
$^2\text{J}_{15\text{A},15\text{B}}$	-11.826 (± 0.001)	-11.702 (± 0.001)	N/O	-11.957 (± 0.001)
$^3\text{J}_{15\text{A}, 15\text{OH}}$	N/O	5.041 (± 0.001)	N/A	N/A
$^3\text{J}_{15\text{B}, 15\text{OH}}$	N/O	4.893 (± 0.001)	N/A	N/A
$^3\text{J}_{11,16}$	0.739 (± 0.001)	0.451 (± 0.001)	0.141 (± 0.001)	0.799 (± 0.001)

No significant deviations are observed in the ^1H chemical shifts for 3-ADON between the CDCl_3 and DMSO-d_6 . Once again the only true deviations appear amongst the hydroxyl protons, which can be attributed to the differences in polarity between the two solvents. In the case of 15-ADON, a couple of interesting observations can be made. First of all, the chemical shift of H-7_β varies from 3.8 ppm in CDCl_3 to 4.7 ppm in DMSO-d_6 . This rather large deviation may be associated with a change in configuration at C-15. Note that the methylene protons H-15_A and H-15_B appear to be equivalent giving rise to a broad singlet in the CDCl_3 spectrum; whereas they are not equivalent in DMSO-d_6 and exhibit a strongly coupled AB quartet. These methylene signals are not chemically equivalent owing to the chirality of C-6; therefore, in CDCl_3 these signals have coalesced into a single broad peak, on the order of 1.73 Hz, and any associated coupling information is lost due to rapid interchange. In DMSO-d_6

d_6 , these signals are well resolved. They are no longer magnetically equivalent and their geminal coupling can be readily obtained. The high polarity of DMSO- d_6 likely plays an important role in altering the geometry of the 15-O-acetyl group and will be elaborated on in the discussion. Other notable changes are seen in the coupling of H-10 to H-11, which is 5.77 Hz in $CDCl_3$ and 3.73 Hz in DMSO- d_6 , suggesting a conformational change in the A-ring.

The carbon-13 spectra were not sufficiently resolved to provide direct information regarding the carbon chemical shifts. The two-dimensional heteronuclear HSQC spectra on the other hand, were very well resolved, and many of the carbon chemical shifts are available.



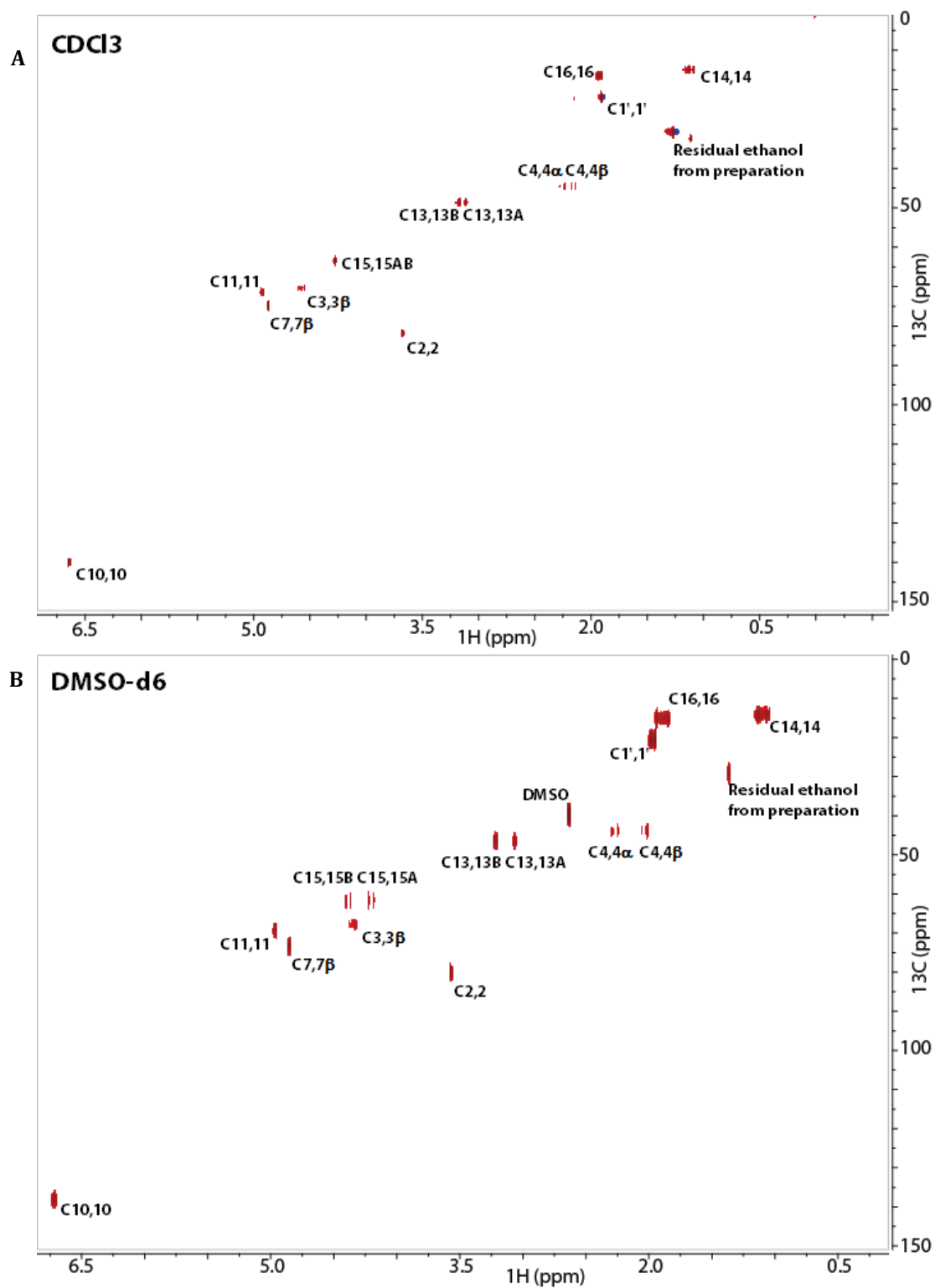


Figure 4. 22: ^1H - ^{13}C HSQC spectra of 15-ADON in A) CDCl_3 and B) DMSO-d_6 at 300 and 75 MHz for ^1H and ^{13}C respectively.

Table 4. 13: Carbon-13 chemical shift data of 3-ADON and 15-ADON in CDCl₃ and DMSO-d₆ from ¹H-¹³C HSQC.

¹³ C label	3-ADON Chemical Shift – δ (ppm)		15-ADON Chemical Shift – δ (ppm)	
	CDCl ₃	DMSO-d ₆	CDCl ₃	DMSO-d ₆
2	79.47	79.09	81.94	80.61
3	75.54	70.86	68.60	67.78
4	20.64	21.56	43.08	43.77
5	N/O	N/O	N/O	N/O
6	N/O	N/O	N/O	N/O
7	70.10	69.79	73.66	73.29
8	N/O	N/O	N/O	N/O
9	N/O	N/O	N/O	N/O
10	137.81	139.24	138.37	138.50
11	79.19	74.89	69.85	69.87
12	N/O	N/O	N/O	N/O
13	47.18	52.09	46.89	46.36
14	13.77	14.66	13.26	14.26
15	62.37	59.49	61.80	61.78
16	14.91	28.76	15.57	15.52
1'	30.09	29.62	21.37	21.10

Comparisons between the type B trichothecenes in DMSO-d₆

As all the type B trichothecenes were studied in DMSO-d₆, a stacked plot of the ¹H spectra of these compounds is provided in figure 4.23 for ease of comparison. The data corresponding to the major components of the spectra of the type B trichothecenes in DMSO-d₆ are provided in Tables 4.14 and 4.15. It is clear from these spectra that each contains signals from minor components. The ¹H chemical shift and scalar coupling data obtained for the minor components for each of DON, 3-ADON, and NIV have been tabulated in Tables 4.16 and 4.17.

When making comparisons between the major contributors for the type B trichothecenes dissolved in DMSO-d₆, depicted in figure 4.23, it appears that the same general trend in the chemical shifts and coupling constants described by Savard and Blackwell for the compounds in CDCl₃ is observed [135]. These trends were addressed in chapter 3, and are depicted in figure 3.8 on page 85. The data for this family of compounds in CDCl₃ is offered in Tables 3.4 and 3.5 for the chemical shift and coupling constants, respectively on pages 87 and 88. The comparison of each of the compounds dissolved in both CDCl₃ and DMSO-d₆ were given individually earlier in this chapter.

Some minor deviations in the ¹H chemical shifts are observed in the ¹H spectra across the family of DON toxins in DMSO-d₆; however, they are limited to specific parts of the molecule. For instance, H-3_β is typically found between 3.8 and 4.2 ppm; however, for 3-ADON, it is 4.95 ppm, where the 3-OH group is substituted by an -O-acetyl group which exhibits a stronger electron withdrawing effect of H-3_β as the hydroxyl substituent. However, the shifts and coupling between all the protons in the core of the trichothecene compounds are in close agreement, indicating that the overall 3D structure for the major components is preserved across the series.

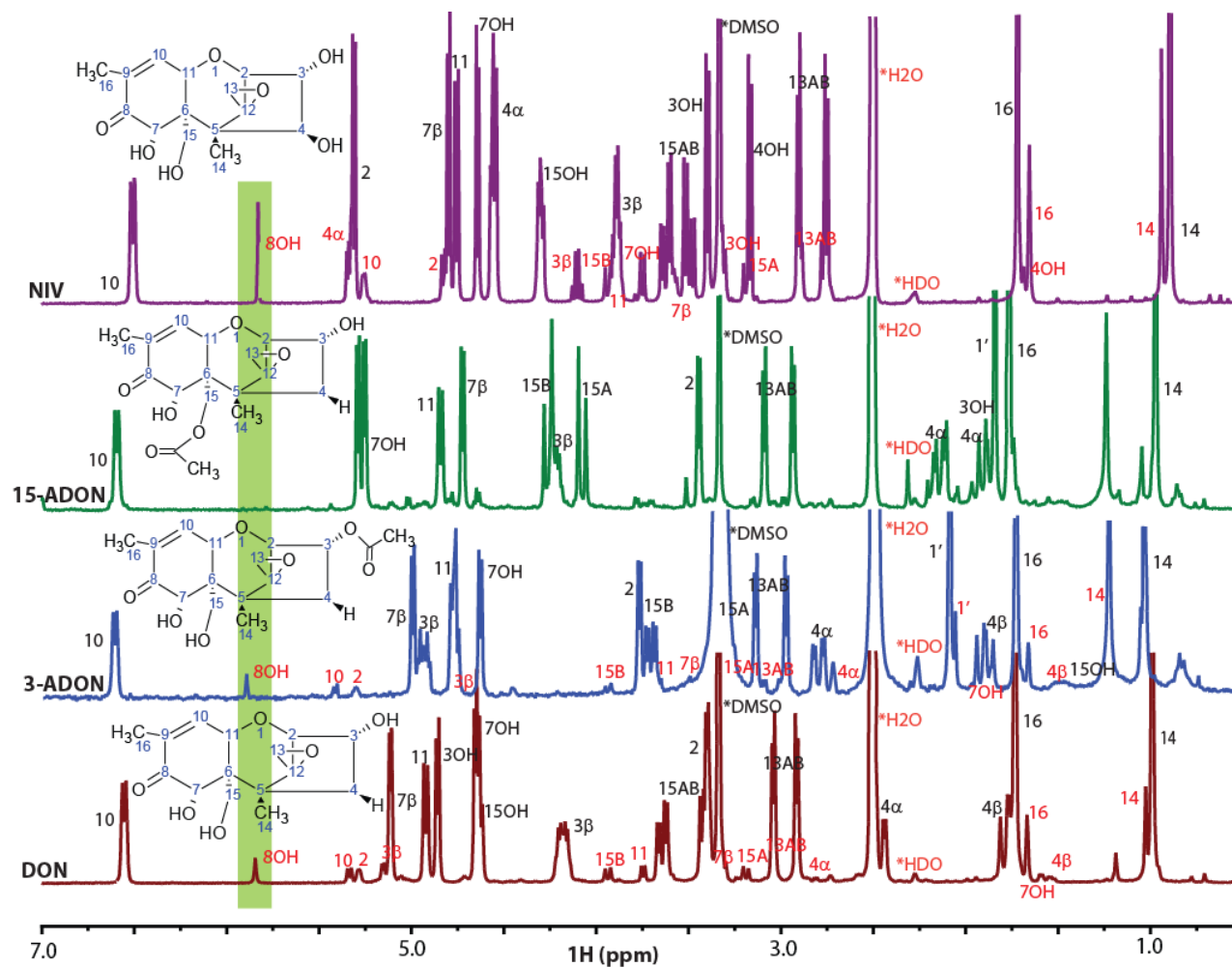


Figure 4. 23: Comparison of the ^1H NMR spectra for type B trichothecenes collected in $\text{DMSO}-d_6$ at 300 MHz. Major peaks are labeled in black and correspond to the numbered figure in the inset. Minor peaks are labeled in red, and correspond to the hemiketal rearranged conformation for each of the components with the exception of 15-ADON for which the rearrangement is not possible.

Table 4. 14: Comparison of the ¹H chemical shifts for the major component of the type B trichothecenes observed in DMSO-d₆ at 300 MHz

¹ H label	Chemical Shift – δ (ppm) in DMSO-d ₆			
	DON	3-ADON	15-ADON	NIV
2	3.401 ¹	3.777 ¹	3.444 ¹	5.312 ¹
3_β	4.180	4.949	4.224	3.889
3_{OH}	5.114	N/A	5.289	3.398
4_α	2.463	2.806	2.140	4.556
4_β	1.771	1.908	1.888	N/A
4_{OH}	N/A	N/A	N/A	3.168
7_β	4.859	5.041	4.723	4.800
7_{OH}	4.654	4.639	5.254	4.642
10	6.555	6.617	6.597	6.509
11	4.923	4.788	4.847	4.757
13_B	3.041	3.148	3.090	2.903
13_A	2.916	2.983	2.935	2.754
14	0.991	1.043	0.973	0.893
15_B	3.641	3.786	4.259	3.619
15_A	3.412	3.499	4.078	3.499
15_{OH}	4.632	0.971	N/A	4.299
16	1.734	1.739	1.765	1.719
1'	N/A	2.098	1.843	N/A

¹All spectra were simulated to an accuracy of 0.001 Hz and were referenced with respect to DMSO-d₆

Table 4. 15: Comparison of the ^1H scalar coupling constants for the major components of the type B trichothecenes obtained in DMSO- d_6 at 300 MHz

^1H label	Scalar Coupling Constant – J (Hz) in DMSO- d_6			
	DON	3-ADON	15-ADON	NIV
$^3J_{2,3}$	4.182 (\pm 0.013)	4.401 (\pm 0.001)	4.394 (\pm 0.001)	4.147 (\pm 0.001)
$^3J_{3,4\alpha}$	4.024 (\pm 0.014)	4.257 (\pm 0.001)	4.411 (\pm 0.001)	4.147(\pm 0.001)
$^3J_{3,4\beta}$	11.312 (\pm 0.014)	11.394 (\pm 0.001)	11.239 (\pm 0.001)	N/A
$^3J_{3,3\text{OH}}$	3.853 (\pm 0.013)	N/A	4.185 (\pm 0.001)	4.401 (\pm 0.001)
$^2J_{4\alpha,4\beta}$	-14.391 (\pm 0.014)	-15.070 (\pm 0.001)	-14.533 (\pm 0.001)	N/A
$^2J_{4\alpha,4\text{OH}}$	N/A	N/A	N/A	5.360 (\pm 0.001)
$^5J_{3\text{OH},4\text{OH}}$	N/A	N/A	N/A	0.623 (\pm 0.001)
$^3J_{7\beta, 7\text{OH}}$	4.226 (\pm 0.012)	4.515 (\pm 0.001)	4.285 (\pm 0.001)	4.359 (\pm 0.03)
$^3J_{10,11}$	5.918 (\pm 0.004)	5.197 (\pm 0.001)	3.729 (\pm 0.001)	5.815 (\pm 0.02)
$^4J_{10,16}$	0.936 (\pm 0.005)	1.191 (\pm 0.001)	1.073 (\pm 0.001)	0.281 (\pm 0.03)
$^2J_{13\alpha,13\beta}$	4.395 (\pm 0.004)	4.384 (\pm 0.001)	4.342 (\pm 0.001)	4.507(\pm 0.001)
$^2J_{15\alpha,15\beta}$	-11.673 (\pm 0.005)	-11.702 (\pm 0.001)	-11.957 (\pm 0.001)	-11.641 (\pm 0.03)
$^3J_{15\alpha 15\text{OH}}$	4.783 (\pm 0.005)	5.041 (\pm 0.001)	N/A	3.976 (\pm 0.03)
$^3J_{15\beta,15\text{OH}}$	5.087 (\pm 0.005)	4.893 (\pm 0.001)	N/A	5.545 (\pm 0.03)
$^3J_{11,16}$	N/O	0.451 (\pm 0.001)	0.799 (\pm 0.001)	N/O

Table 4. 16: Comparison between the chemical shifts for the minor component of the type B trichothecenes observed in DMSO-d₆ at 300 MHz

¹ H label	Chemical Shift – δ (ppm) in DMSO-d ₆		
	DON	3-ADON	NIV
2	5.34 ¹	5.42 ¹	4.827 ²
3_β	5.05	4.78	4.103
3_{OH}	1.57	N/A	3.308
4_α	2.83	3.71	5.334
4_β	2.12	1.57	N/A
4_{OH}	N/A	N/A	1.699
7_β	3.24	3.29	3.572
7_{OH}	1.59	1.87	3.777
8_{OH}	5.85	5.90	5.830
10	5.28	5.31	5.259
11	3.74	3.75	3.866
13_B	3.35	3.10	2.891
13_A	3.07	3.02	2.773
14	1.19	1.07	0.942
15_B	3.94	3.95	3.936
15_A	3.19	3.28	3.187
16	1.67	1.67	1.654
1'	N/A	2.07	N/A

¹The spectra were simulated to an accuracy of 0.01 Hz

²The spectra were simulated to an accuracy of 0.001 Hz

Table 4. 17: Comparison between the $^1\text{H}\{^1\text{H}\}$ scalar coupling constants observed for the minor components of the type B trichothecenes obtained in DMSO- d_6 at 300 MHz

^1H label	Scalar Coupling Constant - J (Hz) in DMSO- d_6		
	DON	3-ADON	NIV
$^3\text{J}_{2,3}$	5.77	4.73	5.362 (± 0.001)
$^3\text{J}_{3,4\alpha}$	4.57	4.37	5.654(± 0.001)
$^3\text{J}_{3,4\beta}$	4.54	4.57	N/A
$^3\text{J}_{3,3\text{OH}}$	N/O	N/A	5.413 (± 0.001)
$^2\text{J}_{4\alpha,4\beta}$	-11.84	-9.60	N/A
$^2\text{J}_{4\alpha,4\text{OH}}$	N/A	N/A	2.987 (± 0.001)
$^3\text{J}_{7\beta, 7\text{OH}}$	4.55	4.56	5.569 (± 0.03)
$^3\text{J}_{10,11}$	3.84	4.18	4.783 (± 0.02)
$^4\text{J}_{10,16}$	1.10	1.20	0.503 (± 0.03)
$^2\text{J}_{13\text{a},13\text{b}}$	4.80	4.72	4.852(± 0.001)
$^2\text{J}_{15\text{a},15\text{b}}$	-8.397	-8.79	-9.052 (± 0.03)
$^3\text{J}_{15\text{a } 8\text{OH}}$	N/O	N/O	N/O
$^3\text{J}_{15\text{b},8\text{OH}}$	N/O	N/O	N/O
$^3\text{J}_{11,16}$	0.7	0.6	N/O

Minor contributors to the ^1H spectra are present for all of the type B trichothecenes in DMSO-d_6 . The ^1H chemical shifts and coupling constants of the minor contribution of DON, 3-ADON and NIV are all in close agreement with only small deviations for the nuclei in the trichothecene core, rarely exceeding 0.3 ppm (table 4.16). Only the protons of the C-ring appear to have significant changes in chemical shift and couplings across the series of compounds, which reflect variations in the substituents on C-3 and C-4. Thus, based on such close agreement of the data for the minor contributions of DON, NIV, and 3-ADON, it is clear that these compounds adopt a similar structure in their minor form, and that this structure is stable in solution, as no chemical exchange is observed.

Of particular interest are the large differences between the minor and major contributions of each compound. The chemical shifts are tabulated in table 4.14 and 4.16, and labeled in figure 4.23 in black and red, for the major and minor spectra, respectively. It is apparent that the majority of the signals from the minor components deviate significantly from those of the associated major components; however, there is no clear trend with respect to magnitude and direction comparing DON to 3-ADON to NIV. More specifically, the trend in H-15_B is to move to higher frequency from 3.6 ppm to 3.9 ppm; whereas H-15_A moves to a lower frequency, from 3.4 ppm to 3.2 ppm; H-7_β covers a range in frequency of 4.7 to 5.0 ppm in the major spectra to 3.2-3.5 ppm in the minor spectra. The vinylic proton, H-10 , also exhibits a large shift from approximately 6.5 ppm to 5.3 ppm. This deviation in chemical shift is of particular importance, as the signal for H-10 is a key feature of the type B trichothecenes. The chemical shift of H-10 is diagnostic of the presence of a conjugated double bond between the carbonyl at C-8 and the double bond at C-9/10. The reduction in shift to 5.3 ppm in the minor spectrum indicates a loss of conjugation to the carbonyl at C-8.

The chemical shift of the epoxide protons of the type B trichothecenes, H-13_A and H-13_B , remain in the same range in the spectra of the minor component as in the major component. The scalar couplings also remain consistent across the type B trichothecenes between the major and minor components.

Lastly, a characteristic peak unique to the ^1H spectra of the minor components of the B-type trichothecene spectra is identified near 5.8 ppm, as highlighted in figure 4.23. This peak was originally attributed to H-15_{OH} ; however, this relatively sharp singlet does not appear to have vicinal couplings to either of the H-15_A and H-15_B resonances. Thus, a rearrangement must have occurred, resulting in a hemiketal linkage between the carbonyl at C-8 and the hydroxyl at C-15, with the concomitant loss of the hydroxyl at C-15. The new resonance appears as a new hydroxyl proton, attached to C-8, which would be diagnostic of such a rearrangement.

With regards to 15-ADON, signals from the minor components are present in the spectrum, but are far too numerous to result from a single contributor. Furthermore, the characteristic peak at H-8 is not present. An explanation of the minor peaks for 15-ADON will be offered in the succeeding discussion.

The carbon-13 spectra obtained for all of the type B trichothecenes in DMSO-d_6

A complete carbon-13 chemical shift analysis for DON and NIV was possible in DMSO-d_6 ; however, for 3-ADON and 15-ADON the carbon chemical shifts were obtained indirectly via $^1\text{H-}^{13}\text{C}$ correlations using HSQC. The carbon chemical shifts for the type B trichothecenes studied are tabulated together in Table 4.18 for direct comparison.

Table 4. 18: Carbon chemical shift comparison for the type B trichothecenes in DMSO-d₆ at 75 MHz

¹³ C label	DON	3-ADON	15-ADON	NIV
2	80.62	79.09	80.61	79.11
3	68.17	70.86	67.78	69.02
4	44.12	21.56	43.77	79.60
5	45.75	N/O	N/O	48.66
6	52.18	N/O	N/O	56.05
7	67.61	69.79	73.29	73.66
8	200.58	N/O	N/O	199.89
9	135.18	N/O	N/O	134.73
10	138.71	139.24	138.50	141.76
11	74.84	74.89	69.87	78.98
12	66.31	N/O	N/O	64.93
13	47.11	52.09	46.36	52.88
14	14.84	14.66	14.26	7.94
15	60.47	59.49	61.78	59.78
16	15.46	28.76	15.52	15.03
1'	N/A	29.62	21.10	N/A

4.7. Discussion

The differences observed in the chemical shifts of NIV, DON, 3-ADON or 15-ADON between the CDCl_3 spectrum and the major contributor of the DMSO-d_6 spectrum are easily attributed to the differences in polarity and hydrogen-bonding potential between the two solvents. Any major changes in chemical shift are observed primarily among the hydroxyl hydrogens, which are far more susceptible to such differences in the properties of the solvent. Similar observations can be made for the coupling constants, as the only significant deviations between the two spectra are the couplings of the hydroxyl hydrogens to nearby neighbours. In general, the chemical shift and coupling constant data for the minor components of the type B trichothecenes bear little resemblance to those observed for the major components. The overall 3D structure for the major components of the type B trichothecenes are all in close agreement with each other, as are those of the minor components for NIV, DON and 3-ADON.

In the case of 15-ADON (figure 4.14), a couple of interesting observations can be made. First of all, a rather large deviation in the chemical shift of H-7_β (from 3.8 ppm in CDCl_3 to 4.7 ppm in DMSO-d_6), is observed, which may be linked to a change in structure at C-15. Note that the methylene protons H-15_A and H-15_B appear as a broad singlet in the CDCl_3 spectrum (see figure 4.14), which is attributable to a near chemical shift equivalence. This gives rise to second-order effects in the spectrum, resulting in the loss of any scalar coupling information between the resonances. However, methylene protons on a carbon which is next to a chiral center rarely experience chemical shift equivalence.

In order to explain this phenomenon, it is necessary to look at the interactions of the surrounding chemical and electronic environment. When looking at the bonds using a Newmann projection, the differences which give rise to the chirality in C-6 are not immediately obvious, nor are the reasons for chemical equivalence. For this it is necessary to move outward to the next level of bonding, which is displayed in figure 4.24.

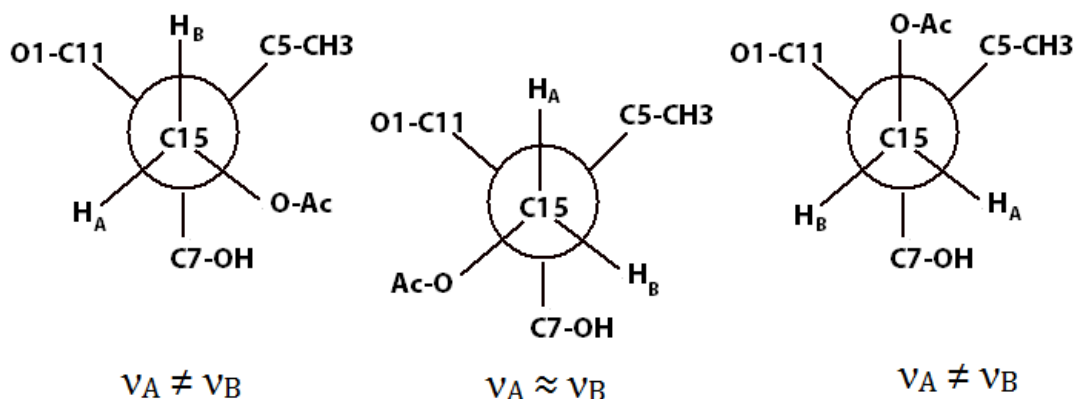


Figure 4. 24: Newmann projections along the C-6/C-15 bond in 15-ADON. The second level of bonding off C-6 was required to provide insight into the chemical equivalence observed between H-15_A and H-15_B in CDCl₃. Only when the O-acetyl group is positioned *gauche* to C7, and *gauche'* to C-11 will the chemical shift of H-15_A approximate that of H-15_B.

The carbon C-6 is a quaternary carbon which is directly bound to C-15, C-5, C-7, and C-11. Looking along the C-6/C-15 bond we must move to the second level of bonding to determine the nature of the chemical equivalence observed for H-15_A and H-15_B in CDCl₃. The carbon C-5 is also a quaternary carbon which is bound to methyl-14 which serves as a discriminating factor. Carbons C-7 and C-11 are both tertiary carbons. C-7 is directly bound to a hydroxyl group; whereas, C-11 forms part of the tetrahydropyran ring, and is directly bound to oxygen O-1. Thus, C-7 and C-11 can be described as having near chemical and magnetic equivalence; whereas, C-5 poses as the significantly different substituent. In order for H-15_A and H-15_B to experience near chemical shift equivalence, they must both be in an orientation which is *gauche* to C-5. Only this specific rotational isomer allows for the near chemical and magnetic equivalence in H-15_A and H-15_B; thus, this bond must be locked in place, since free rotation about the bond would result in the sampling of the other two rotational isomers and the observation of coupling between the two protons. The carbonyl of the O-acetyl group of C-15 acts as a strong acceptor, and in this configuration is in close proximity to H-7_{OH} which may act as a donor for hydrogen bonding, in order to lock the O-acetyl group in place.

Were the oxygen of the O-acetyl carbonyl at C-15 to form a hydrogen bond with H-7_{OH} this would bring the carbonyl resonance in close proximity to H-7_β, which would serve to shield this

resonance due to the neighboring group effect, and decrease the chemical shift frequency. This arrangement further supports the locking of the C-6/C-15 bond in place. The proposed structure in the CDCl_3 solvent is depicted in figure 4.25.

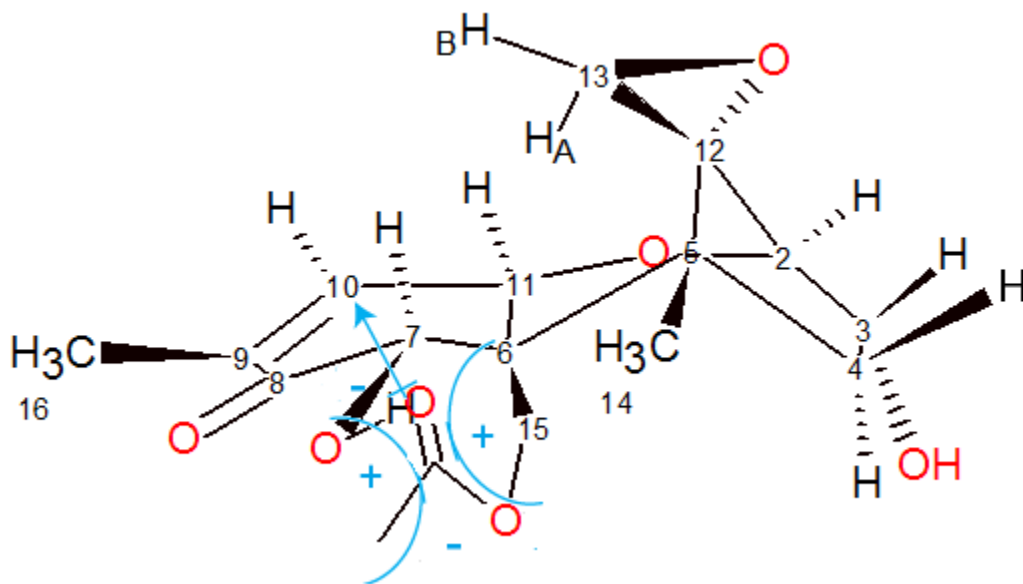


Figure 4. 25: Structural orientation of the acetyl group at C-15 in 15-ADON predicted to occur in CDCl_3 . The double bond character of the carbonyl functionality of the acetyl group at C-15 results in areas that cause an increase in the shielding, and a subsequent decrease in the frequency of the chemical shift. These regions are denoted by the negative signs. Where deshielding due to electron withdrawing effects may be observed, an increase in the chemical shift frequency results, denoted by the positive signs.

In the presence of DMSO-d_6 , the H-15_{AB} signals are better resolved and the doublet structure has returned, indicating that they are no longer magnetically equivalent. The coupling between them has been reintroduced, which appears to indicate that this bond is now free to rotate in solution.

The coupling between H-10 and H-11 has also changed significantly in the spectrum of 15-ADON dissolved in DMSO-d_6 . The coupling of 5.77 Hz seen in CDCl_3 , is similar to the coupling observed for the other compounds throughout the study; however, in DMSO-d_6 the coupling between H-10 and H-11 for 15-ADON is reduced to 3.73 Hz, suggesting that a slight change in the geometry of the A-ring may have occurred. This may be a reflection of the loss of the hydrogen bond formed

between the acetyl group on C-15 with the H-7_{OH} hydroxyl in the non-polar solvent, shown in figure 4.23, lending further support to this slight rearrangement.

A certain percentage of the compounds are observed to be in a secondary conformation when dissolved in DMSO-d₆ (figure 4.18), which for DON, NIV, and 3-ADON appear to correspond with the hemiketal isomer. The exception in DMSO-d₆ is 15-ADON, which is not expected to be capable of existing in the hemiketal form due to the acetylation of C-15 in this variation of DON. The spectrum for 15-ADON in DMSO-d₆ does contain minor contributors, which appear to each contribute approximately 5% to the total spectrum; however, there are far too many small signals in the baseline for only a single contribution. By simple observation of the pattern of peaks for the minor contributors, it is clear that the contributions made to the 15-ADON spectrum are significantly different than those for the other 3 toxins studied here. Recall that for NIV, the conformation involves the formation of a hemiketal from C-8 to C-15, and this arrangement is evidenced by the presence of a characteristic peak appearing around 5.8 ppm. The lack of the characteristic H-8_{OH} peak in the spectrum for 15-ADON, as observed in DMSO-d₆, does not support the rearrangement to the hemiketal isomer for this sample. This particular conformation cannot be adopted by 15-ADON as the O-acetyl substituent present at C-15 would prevent the formation of a hemiketal at this location. Furthermore, 15-ADON did not go into solution in DMSO-d₆ as readily as the other compounds, and a round of evaporation and solvent addition was required before a suitable spectrum was obtained. Therefore, it is possible that these minor contributions are in fact peaks depicting degradation of the compound.

Considering that minor spectra were also observed in the baseline for DON in the deuterated solvents acetone and THF, as seen figure 4.8, it would be interesting to observe whether the other type B trichothecenes also demonstrate these same structural conformations in these solvents, as well as whether the minor conformations for DON in these solvents are similar to those observed for DON in DMSO-d₆.

Carbon-13 chemical shift data across the type B trichothecenes

The carbon-13 spectra were obtained for all of the compounds in CDCl₃ and DMSO-d₆, as well as acetone-d₆, CD₃OD and THF-d₈ in DON. However, not all of the carbon spectra were amenable to direct carbon chemical shift analysis. Indirect carbon chemical shifts were obtained for 3-ADON and 15-ADON in CDCl₃. The carbon chemical shifts appear to be in close agreement across the majority of the signals. For example, across all the spectra, the signal for H-2 does not deviate to any great extent, from 79.09 ppm for 3-ADON in DMSO to 81.94 in 15-ADON in CDCl₃.

Nivalenol appears to have some of the largest deviations across the group of trichothecenes. The carbon nucleus C-10 in DON and its derivatives tends to appear around 138 ppm; however for NIV it appears at 148 ppm in DMSO-d₆. Carbons C-9, C-11 and C-14 also experience somewhat significant deviations in chemical shift from the other compounds. This is not easily explained based on the inductive and field based effects of the substituent at C-4, as the carbon nuclei which experience the deviations are on the other side of the molecule. This particular piece of information came at a much later phase of the project, and should be followed up with in future studies.

Lastly, within the carbon chemical shift data a slight difference in the chemical shift between the spectrum obtained in the non-polar CDCl₃ solvent, versus the polar DMSO-d₆ solvent is observed for the C-15 signal. In the DON derivatives C-15 appears at approximately 62 ppm in CDCl₃ versus 60 ppm in DMSO-d₆, as well as for DON in acetone-d₆.

Peaks for the minor component, observed in DMSO-d₆ are present in the DON and NIV spectra. These peaks have been assigned to signals from the A-ring, which would likely experience the greatest chemical and magnetic changes due to the loss of the carbonyl double bond. The minor peaks are not observed in the two-dimensional HSQC spectra.

4.8 Conclusions

The hemiketal rearrangement proposed by Jarvis *et al.* [72], which was said to occur in DON and NIV, involving a linkage from C-8 to C-15 was confirmed, and the 3D structure of this stable isomer was determined from novel data presented in the 1D and 2D ¹H NMR spectra, and

supplemented with new evidence described in the ^{13}C NMR spectrum. Jarvis also proposed a second potential rearrangement mechanism involving a linkage between C-4 and C-15; however, no evidence for this conformation was observed. The hemiketal isomer was also determined to exist not only in other toxins classified as type B trichothecenes (i.e. 3-ADON), but also in various solvent systems, with CDCl_3 being the only solvent, from those measured where a minor conformation attributable to the hemiketal isomer was not observed.

The bond angles for hydroxyl substituents in rigid ring systems are different in polar and non-polar solvents. In non-polar solvents, such as CDCl_3 , the H-C-O-H bonds preferentially adopt a configuration which appears to rotate between *gauche* and *gauche'*, but in polar solvents, the rotation samples more of the *trans* configuration. This change in the bond rotation at sites where hydroxyl groups exist serves as an important tool in the description of the mechanism for the formation of the hemiketal isomer. In polar environments the hydroxyl group at C-15 adopts a slight preference towards the *trans* configuration, which places the hydroxyl functionality in close proximity to the carbonyl bond at C-8, thus providing the optimal geometry for the formation of the hemiketal and a potential first step in the mechanism of formation.

The protons H-4 $_{\alpha}$ and H-4 $_{\beta}$ were misassigned in previous works [135], and must be revisited to correct for the *cis* and *trans* effects in rigid ring systems, such as that observed for the trichothecenes.

This novel information regarding the structure of the type B trichothecenes raises new questions, such as whether similar isomers occur in the other trichothecene classes in polar solvents, and to what extent; what are the kinetics of the dynamics of this isomerism process; and, what factors other than the solvent may affect the dynamics of this process. Finally, it raises the question as to how important the hemiketal isomer may be with regards to the toxicity of the trichothecenes on biological systems.

5. Solid-State Structural Analysis of Trichothecene Mycotoxins

5.1. Overview

The low solubility for trichothecene toxins in the majority of solvents, both aqueous and organic, poses a rather unique challenge in the determination of their three-dimensional (3D) structure, as well as the structural dynamics that are possible. Studying these compounds through the technique of solid-state nuclear magnetic resonance (NMR) may provide some insight for the determination of the relative 3D structure of this interesting class of compounds.

Solid-state NMR experiments were performed on T-2 toxin and deoxynivalenol (DON) in an attempt to gain some understanding regarding their overall three-dimensional structure, and potential interactions with water. Multiple conformations were found to exist for both of these compounds and information was gathered regarding their amenability towards further investigations in the area of NMR crystallography.

In this section the attempts to setup the NMR crystallographic techniques of the Incredible Natural Abundance Double Quantum Transfer Experiment (INADEQUATE) and an R-symmetry based Chemical Shift Anisotropy (CSA) experiment are described. The pitfalls that were encountered with the INADEQUATE experiment are explained, and the initial success of the R-symmetry sequence on the T-2 toxin sample is addressed.

5.2. Introduction

The trichothecene class of toxins is highly insoluble in the majority of solvent systems available for analysis, the most important of which is water itself. The behavior of the toxin in aqueous systems is important for the determination of the toxicological mechanism of the trichothecene class of mycotoxins at the cellular level. Yet, it is difficult to predict the behavior of the molecules in cellular systems, as the trichothecenes exhibit extremely low solubility in water. This proves to be a major roadblock towards the study of the trichothecenes in the solution state.

Studying the structure of the trichothecenes in the solid state and comparing this to the results for solution NMR, and other structural methods such as SCXRD where available, may help to

confirm the overall three-dimensional structure of the toxins in nature, as well as the interactions of these toxins with water.

In previous literature, it was determined that the unit cell for crystallized T-2 toxin consists of two molecules of T-2 toxin in slightly different orientations [52]. Solid-state carbon-13 experiments were used to confirm the presence of two distinct conformers of T-2 toxin in the solid state and an attempt was made to unequivocally distinguish the signals appearing in the spectrum for each of these, using NMR crystallographic methods.

Two specialized NMR experiments were used to investigate the solid-state structure of T-2 toxin, and extract information from the carbon-13 spectra which is inaccessible using standard NMR techniques. The solid-state INADEQUATE experiment was conducted in an attempt to obtain information regarding the scalar connectivities of the carbon nuclei in T-2 toxin in order to distinguish between the signals in the solid-state spectrum [89,90].

An R-symmetry based CSA recoupling experiment was also utilized to pull out information regarding the chemical shielding tensors in the T-2 spectrum. The chemical shielding tensors provide information regarding the local electronic environment of the nucleus, and can be used along with any SCXRD data to distinguish between the two conformers of T-2 toxin in the solid state.

Solid-state carbon-13 NMR investigations were also performed on DON, which was used as a model toxin for the type B trichothecenes. The carbon-13 spectrum was used to determine the structure in the solid state, as well as investigate the presence of the hemiketal conformation which was observed in polar solvent systems in chapter 4. The intramolecular interactions with water were also investigated.

5.3. Materials and Methods

5.3.1. Solid-State NMR Experiments

All spectra were acquired at ambient temperature (21.5° C) using a Varian Inova 500 spectrometer, outfitted with either a 2.5 mm or 2.0 mm four channel HFXV Varian T3 probe. The spectrometer operates at 11.7 Tesla, with a Larmor frequency of 500.13 MHz for ^1H and 125 MHz for ^{13}C nuclei. Samples for T-2 toxin were used as received from the Sigma-Aldrich Chemical Company (SIGMA, CAS 21259-20-1). This highly crystalline sample exhibited typical needle-like crystals. The microcrystalline powder (11 mg) was loaded into a zirconium oxide rotor with a diameter of 2.5 mm for the solid-state CP and DP experiments. The material was later repacked into a 2.0 mm rotor with a sample volume of 10 μL for the CSA recoupling experiments. The ^1H 90° pulse was calibrated at 2.0 μs for the CP and DP experiments, and 1.8 μs for the R-symmetry experiment.

Samples of DON were used as received from Barbara Blackwell at Agriculture and Agri-Food Canada, Ottawa. The fine powder sample was loaded into a 2.0 mm zirconium oxide rotor with a sample volume of 10 μL . The ^1H 90° pulse was calibrated at 1.8 μs .

Setup samples of D-glucose- $^{13}\text{C}_6$ (Sigma, CAS 110187-42-3) and glycine-1,2- $^{13}\text{C}_2$ (Cambridge Isotope Labs, CAS 67836-01-5) were used for the INADEQUATE and CSA recoupling sequence. The glucose sample was ground with a mortar and pestle prior to loading in the NMR rotor; whereas the glycine sample was a fine microcrystalline powder, and was used as received. The samples were loaded into a 2.5 mm zirconium oxide rotor with a sample volume of 11 μL for the INADEQUATE experiment. The glucose sample was also used for the CSA recoupling sequence and was loaded into a 2.0 mm zirconium oxide rotor with a sample volume of 10 μL . The ^1H 90° pulse was calibrated at 2.0 μs for the INADEQUATE experiment and 1.8 μs for the CSA recoupling sequence.

A magic angle spinning (MAS) rate of 22.0 kHz was used for the T-2 samples, 18.0 kHz for the INADEQUATE experiments, and 28.0 kHz for the DON samples. A total of 4096 points were acquired over 40.96 ms using a spectral width of 100 kHz. Two-pulse phase modulation (TPPM) ^1H decoupling was calibrated with a phase angle of 13° and a 165° pulse length of 5.4 μs , resulting in a ^1H -decoupling field strength of 120 kHz for all ^{13}C spectra [8,40]. The direct polarization (DP) ^{13}C spectrum was acquired with a total of 4096 transients, using a recycle delay of 15 s for T-2 toxin,

and a total of 8196. The 5 second recycle delay for DON was determined by arraying the relaxation delay, d_1 . The cross polarization (CP) ^{13}C spectra were acquired with a total of 14000 transients, and a recycle delay of 5 s for T-2 toxin, and 4780 transients with a recycle delay of 15 s for DON. The recycle delay for the CP experiment is based on $T_{1\text{H}}$, as the polarization transfer occurs from ^1H to ^{13}C . As with the DP experiment, the recycle delay for the CP experiment was determined using a saturation recovery experiment. Cross-polarization was achieved using the adiabatic passage method with a contact time of 1.5 ms, and a curved sweep width covering 10 kHz [83]. The DP and CP ^{13}C spectra were processed using linear prediction up to 64 thousand points for T-2 toxin, and 256 thousand points for DON.

The CP refocused INADEQUATE ^{13}C spectrum was acquired as 32 increments with 2000 data points in 64 scans. An array of recycle delays was performed, from which a recycle delay of 20 s was chosen for glucose- $^{13}\text{C}_6$, and 4 s for the glycine-1,2- $^{13}\text{C}_2$. Ramped cross polarization from ^1H to ^{13}C was used to help enhance the signal, and Continuous Wave (CW) ^1H decoupling was used to prevent interference in the signal from heteronuclear coupling of the ^1H nuclei. The delay between pulses, τ , is equal to $1/4J$, where J is the average one-bond homonuclear coupling value observed for ^{13}C nuclei, which typically ranges between 20 and 30 Hz. In order to provide the largest possible homonuclear recoupling, the delay for τ was set to 6.5 ms. The experiment was also attempted without refocusing of the antiphase signal for glycine, the tau delay for this experiment were modified to 7.6 ms.

A separated local field experiment with CSA recoupling was implemented employing the R-symmetry based sequences. For the D-glucose- $^{13}\text{C}_6$ sample the $R10_1^7$ experiment was employed, and was collected with a total of 20 transients acquired for each of the 129 increments, covering 0 to 128 cycles of the R sequence, using a recycle delay of 15 s. The recycle delay was determined by saturation recovery methods. The delay, τ , was set to 8.3 μs for all R-symmetry sequences employed. The $R18_2^5$ sequence was employed for the T-2 toxin sample, and was acquired with a total of 2800 transients and 33 increments, covering 0 to 32 cycles of the R sequence, using a recycle delay of 5 s. An MAS rate of 27.777 kHz was used for the D-glucose- $^{13}\text{C}_6$ sample, and 22.222 kHz for the T-2 toxin

sample. MAS was used in an attempt to reduce dipolar coupling among the nuclei [3,93]. The CP method was achieved using the adiabatic pulse method with a contact time of 1.5 ms [83].

5.4 Results

5.4.1 Carbon Spectral Analysis of T-2 Toxin²

²This section is reproduced in part from the manuscript: Chaudhary, P., Shank, R. A., Montana, T., Goettel, J. T., Foroud, N. A., Hazendonk, P., Eudes, F. (2011) Hydrogen-bonding interactions in T-2 toxin studied using solution and solid-state NMR. *Toxins*. **3**(10), 1310-1331. The section has been rewritten to reflect the contributions made by the author of the thesis.

The solid-state magic angle spinning (MAS) spectra, obtained either through the direct polarization on ¹³C (figure 5.1B), or the cross polarization to the ¹³C nuclei from nearby ¹H nuclei (figure 5.1C), were collected in approximately the same experiment time as in the solution state (figure 5.1A). While the signal-to-noise ratio (S/N) of the DP spectrum is comparable to that of the solution-state spectrum, the S/N is much higher in the CP spectrum compared to either the solution or the DP spectra. It is remarkable that, although the resolution in the solution-state spectrum is expectedly better, the differences in line-width of the solid- and solution-state spectra are as small as 4 Hz (as can be observed in figure 5.2). This exceptional resolution in the solid-state spectra was made possible by the fast spinning (22 kHz), the high power multiple pulse decoupling, as well as the microcrystallinity of the sample. Under less favorable conditions, line-widths of hundreds of Hz are not unusual. The most apparent observation in the solid-state is the twinning of all the carbon resonances, when compared with the solution data (figure 5.2). This is consistent with the findings of the X-ray study of T-2 toxin by Gilardi *et al.* [52], which describes the presence of two molecules in the unit cell, which differ primarily in the conformation of the isovalerate side-chain, and placement of the water molecules.

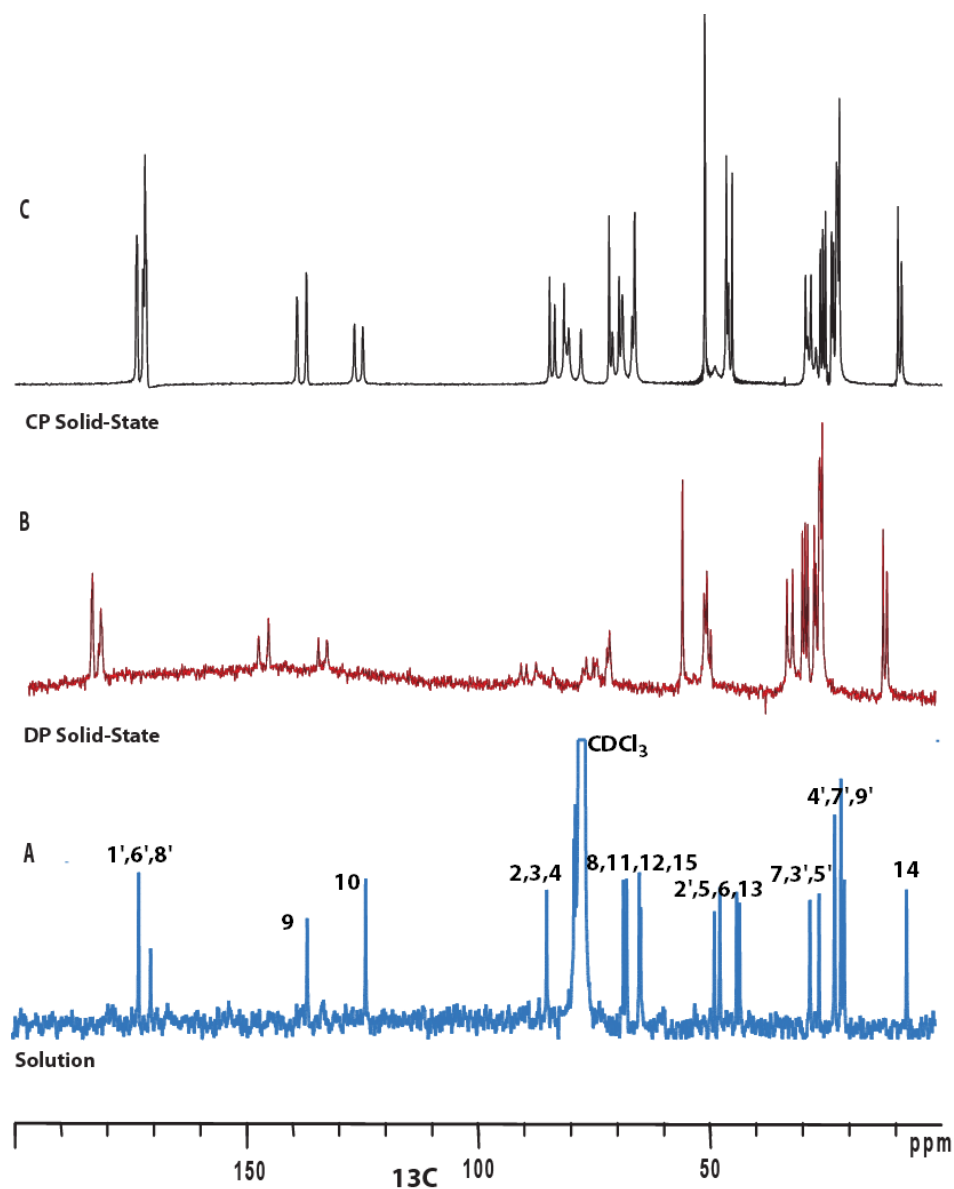


Figure 5. 1: Carbon-13 spectra of T-2 toxin (A) Solution-state spectrum at 75 MHz in CDCl_3 , (B) Direct-polarization (DP) in the solid-state at 125 MHz and MAS of 25 kHz, (C) Cross-polarization (CP) from ^1H - ^{13}C at 125 MHz and MAS of 25 kHz.

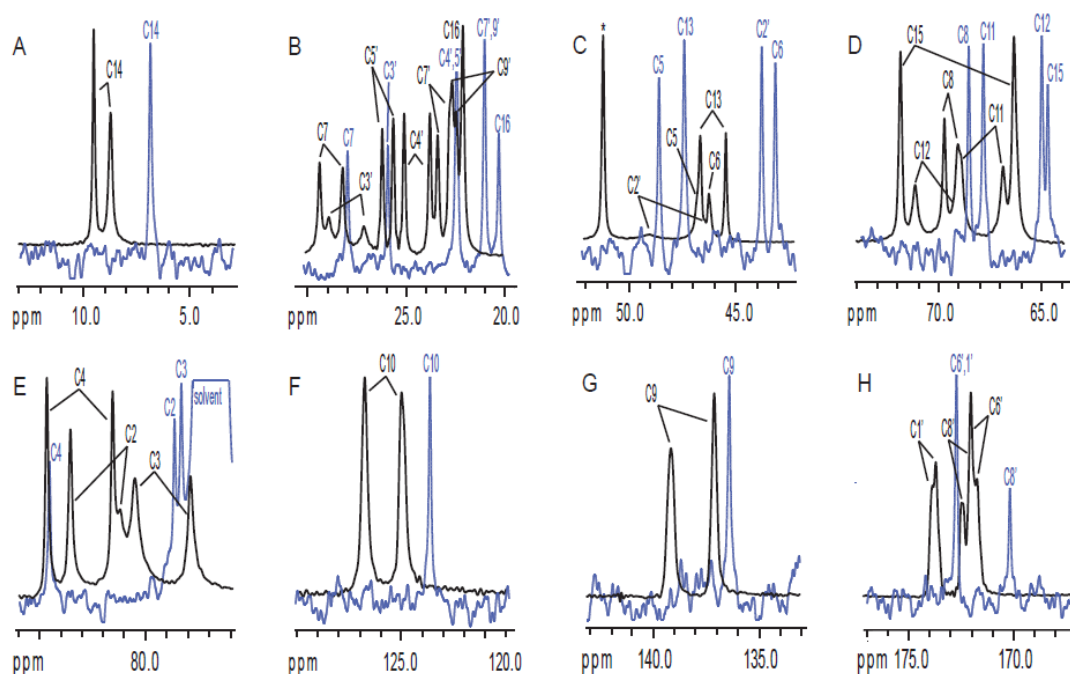


Figure 5. 2: Superimposition of the solid state (black) and solution state (blue) spectra for T-2 toxin, displaying the twinning observed in the solid-state signals, indicating that two distinct conformations for T-2 toxin are present in the unit cell. (A) methyl carbons, (B-C) methylene carbons, (D-G) methine, π -bonded, and quaternary carbons, (H) carbonyl carbons, respectively.

No simple correspondence exists between the carbon chemical shifts in solution to those of the solids (i.e. no fixed difference in frequency), which suggests that they have significant differences in their conformations and in their immediate chemical environment. These differences in the carbon chemical shifts were reconciled through the analysis of close contacts observed in the X-ray structure from Gilardi *et al.* which are described in the paper by Chaudhary *et al.* (2011) [27,52], and were used to assign the chemical shifts appearing in Table 5.1. This allowed for the development of the three chemical structures depicted in figure 5.13 of the discussion, and discussed further in that section. At this stage, no distinction can be made to describe which of the signals belong to each of the two molecule, as no carbon-carbon correlation information is available. Experiments which are able to correlate the carbon signals in the spectrum exist; however, this is rather difficult due to the low sensitivity of the natural abundance carbon signal, as well as the long T_1 relaxation of carbon. Attempts were made to access this information through the implementation and use of the ^{13}C INADEQUATE [89,90] experiment and the R-symmetry based CSA recoupling experiment [19,92], which are described later in this chapter.

Table 5. 1. Comparison of the ^{13}C chemical shifts for T-2 toxin in solution and solid state

Label	Solution (ppm)	HSQC	HMBC	Solid 1 (ppm)	Solid 2 (ppm)
2	78.72	2	$3_{\text{OH}}, 13_{\text{B}}$	81.25 (2.83) ¹	83.59 (4.83)
3	78.40	3	4	77.94 (-0.46)	80.57 (2.17)
4	84.60	4	2,14	81.60 (-3.00)	84.70 (0.10)
5	48.39		2,4,14,15 _{AB}	46.80 (-1.60)	46.80 (-1.60)
6	42.94		$7_{\text{B}}, 8, 14, 15_{\text{AB}}$	46.10 (3.16)	46.10 (3.16)
7	27.75	$7_{\alpha\beta}$	15_{B}	28.32 (0.57)	29.49 (1.74)
8	68.02	8	16	69.07 (1.05)	69.73 (1.71)
9	136.32		8,11,16	137.15 (0.83)	139.20 (2.92)
10	123.70	10	11,16	125.03 (1.33)	126.82 (3.12)
11	67.34	11	2,15 _A	69.45 (2.11)	71.15 (3.89)
12	64.59		2,4,13 _{AB} ,14	66.36 (1.77)	71.86 (7.37)
13	47.21	13_{AB}		45.33 (-1.88)	46.56 (-0.77)
14	6.88	14		9.51 (2.63)	8.73 (1.85)
15	64.31	15_{AB}		66.85 (2.54)	68.90 (4.59)
16	20.35	16	$7_{\alpha\beta}$	22.19 (1.84)	22.19 (1.84)
1'	172.73		8	173.71 (0.98)	173.9 (1.17)
2'	43.58	2'	4',5'	49.00 (5.42)	51.30 (8.72)
3'	25.78	3'	2',4',5'	27.22 (1.44)	29.02 (3.24)
4'	22.37	4'	3',5'	23.87 (1.50)	25.18 (2.81)
5'	22.45	5'	3'	25.73 (3.28)	26.29 (5.56)
6'	170.13		7'	171.74 (1.61)	172.00 (1.87)
7'	21.07	7'		22.53 (1.46)	22.76 (1.69)
8'	172.70		15, 9'	172.00 (-0.70)	172.44 (-0.26)
9'	21.04	9'		22.76 (1.72)	23.47 (2.43)

¹Values in parentheses represent the chemical shift deviation from the solution-state chemical shift. Positive values are shifts to higher frequency; whereas, negative values are shifts to lower frequency.

5.4.2. Conformational Dynamics of Deoxynivalenol in the Solid State

In order to determine whether multiple conformations exist regardless of solvent effects for DON and its derivatives, a solid-state NMR analysis of purified DON was conducted with a sample of DON obtained from a colleague at the Agriculture and Agri-Food Canada Research center in Ottawa, Barbara Blackwell. Cross-polarization was employed. Although the spectrum of DON was not as well resolved as that obtained for T-2 toxin, shown in figure 5.1, the signal-to-noise ratio remains quite high, as is shown in figure 5.3.

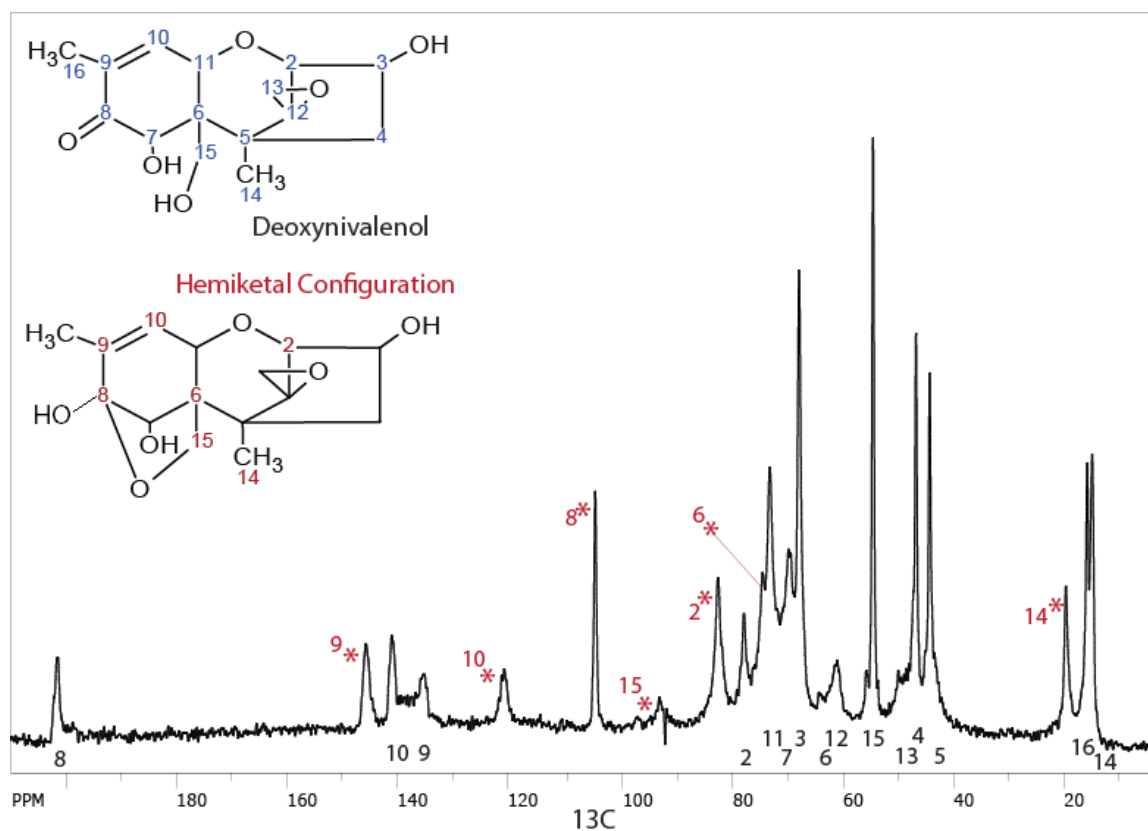


Figure 5. 3: Solid-state ^1H to ^{13}C CP-MAS NMR spectrum of DON at 125 MHz spectrometer frequency and 28 kHz spinning speed. Signals labeled in black correspond to the deoxynivalenol (DON) structure described by Blackwell and Savard [135]. Signals denoted with a red asterisk (*) are attributed to the “extra” signals for the second conformation in the solid-state, which is believed to correspond to the hemiketal conformation described in Chapter 4. The carbons labeled in red for the hemiketal conformation are those believed to be present with significant intensity in the solid-state spectrum.

The chemical shift values for the solid-state carbon spectrum of DON correspond well to those of the solution-state spectrum; however, there appear to be 7 “extra” peaks in the spectrum, which are not attributed to the literature structure of DON. These were assigned to resonances of the A- and B-rings, which would experience the majority of conformational rearrangement in the event of the hemiketal formation described by Jarvis *et al* [72]. Although it is not possible to accurately estimate the percentage of DON which would have experienced this shift to the hemiketal form from the CP- ^{13}C spectrum, it is interesting to note that some of the “extra” peaks are of similar height to those which have been assigned to the major spectrum. Significant shoulders are also present on some of the peaks; for example, the shoulder on C-8 and in between C-9 and C-10 are the most obvious in the ^{13}C spectrum.

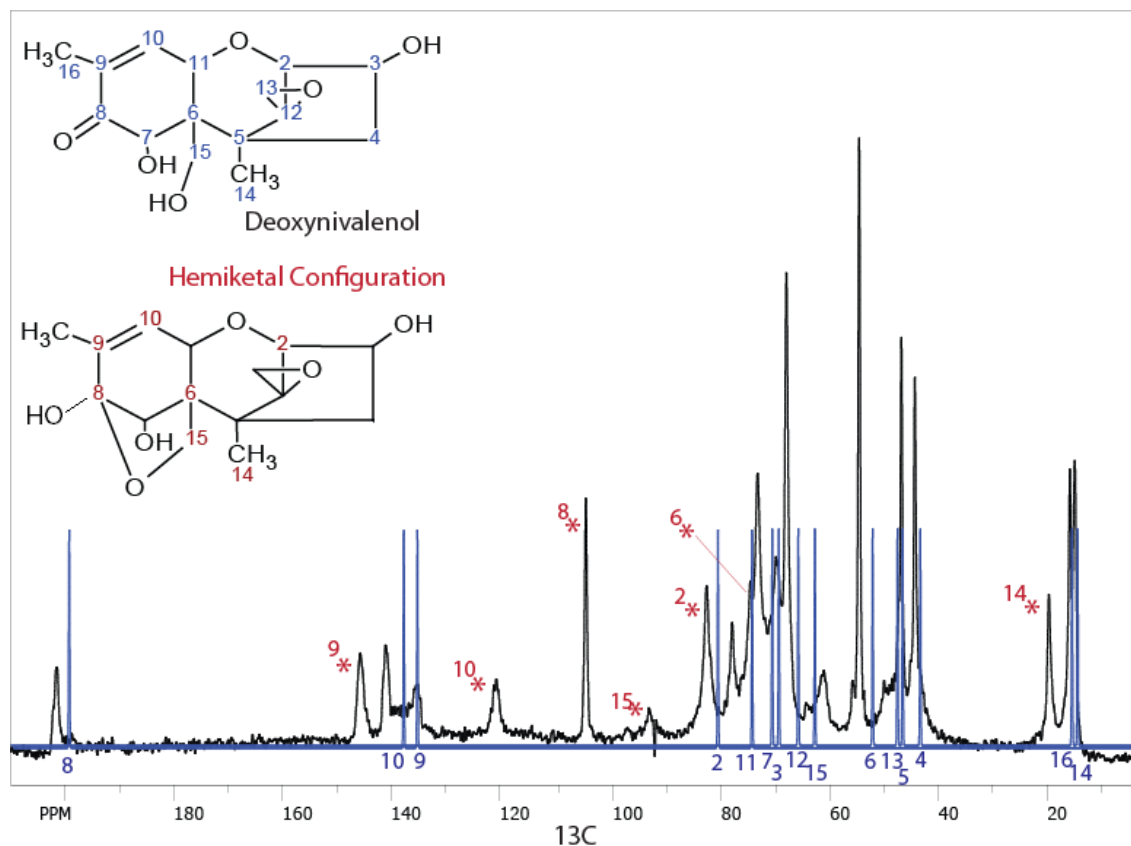


Figure 5. 4: Superimposition of the solution-state ^{13}C simulation spectra for DON in CDCl_3 , shown in blue, with the solid-state ^{13}C spectra for DON, shown in black. Peaks representing the hemiketal conformation for DON in the solid-state are denoted with the red asterisks.

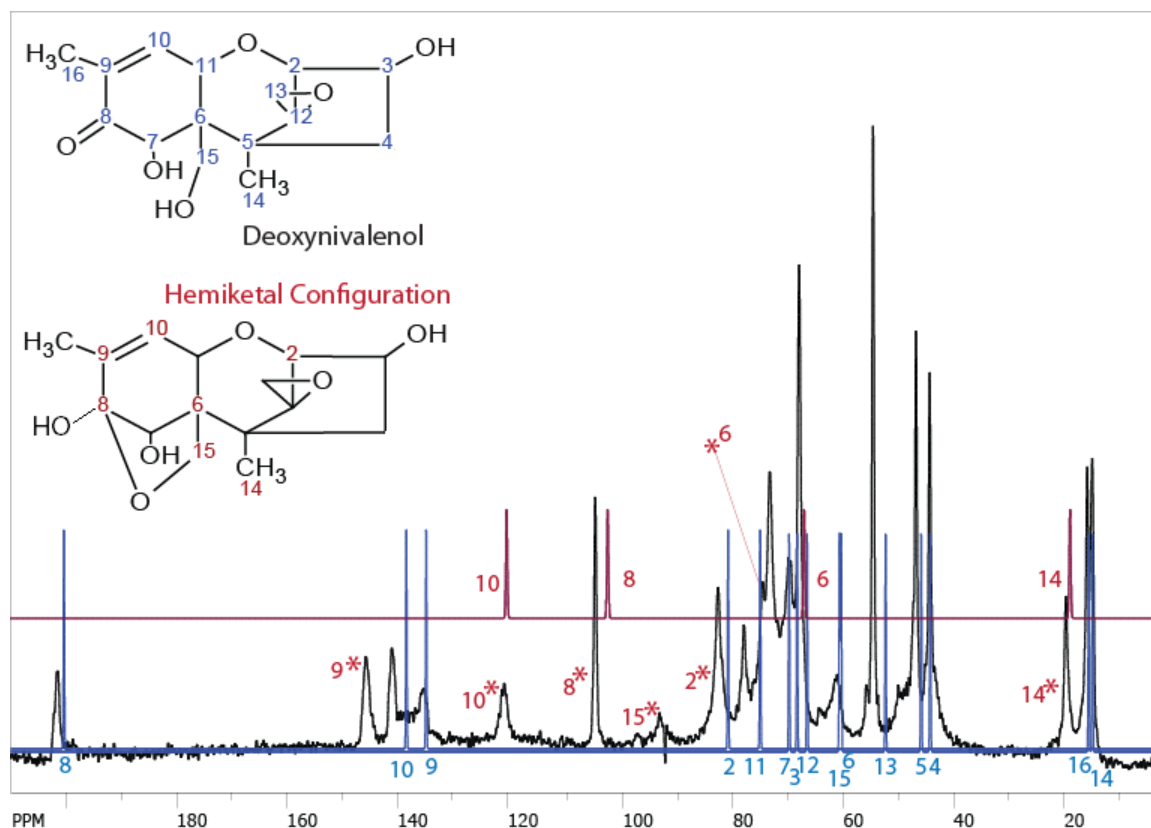


Figure 5. 5: Superimposition of the solution-state ^{13}C simulation spectra for DON in DMSO-d_6 , shown in blue for the major conformation and red for the minor hemiketal conformation, with the solid-state ^{13}C spectra for DON, shown in black. Peaks representing the hemiketal conformation for DON in the solid-state are denoted with the red asterisks.

Beginning with the prior analysis provided by Jarvis *et al.* for the hemiketal functionality[72], the extra peaks were assigned as listed in table 5.2. The changes expected to occur in the overall π -electron density at each carbon location were taken into account, and are depicted in figure 5.6. The electron density is assumed from the atoms present in the structure. Oxygen functionalities are more electronegative, thus neighboring nuclei tend to have less density, and are deshielded by the electrons, resulting in an increase in chemical shift. Nuclei that are not in close proximity to an oxygen atom will be relatively shielded by the nearby electrons, and the chemical shift will decrease.

Table 5. 2: Carbon chemical shift data for DON in the solid state, compared with the experimental and literature carbon chemical shifts observed for DON in CDCl₃ and DMSO-d₆

Carbon	Chemical Shift – δ (ppm)	Exp. in CDCl₃ (ppm)	Lit for DMSO-d₆ (ppm)	Exp in DMSO-d₆ (ppm)
2	82.42 (93.04)	80.80	80.2	80.62
3	67.78	69.17	67.8	68.17
4	44.22	43.21	43.7	44.12
5	46.69	46.46	45.4	45.75
6	65.4 (73.08)	51.96	51.8	52.18 (64.77)
7	69.33	70.39	69.3	69.61
8	201.74 (104.61)	199.87	200.0 (104)	200.58 (100.64)
9	135.65 (146.05)	135.96	134.8	135.18
10	141.33 (121.12)	138.46	138.2 (121)	138.71 (119.10)
11	74.41	74.53	74.5	74.84
12	64.16	65.61	66	66.31
13	49.58	47.41	46.7	47.11
14	14.87 (19.62)	14.34	14.5	14.84
15	60.91 (97.04)	62.56	60.1	60.47
16	15.77	15.37	15.1	15.46 (16.20)

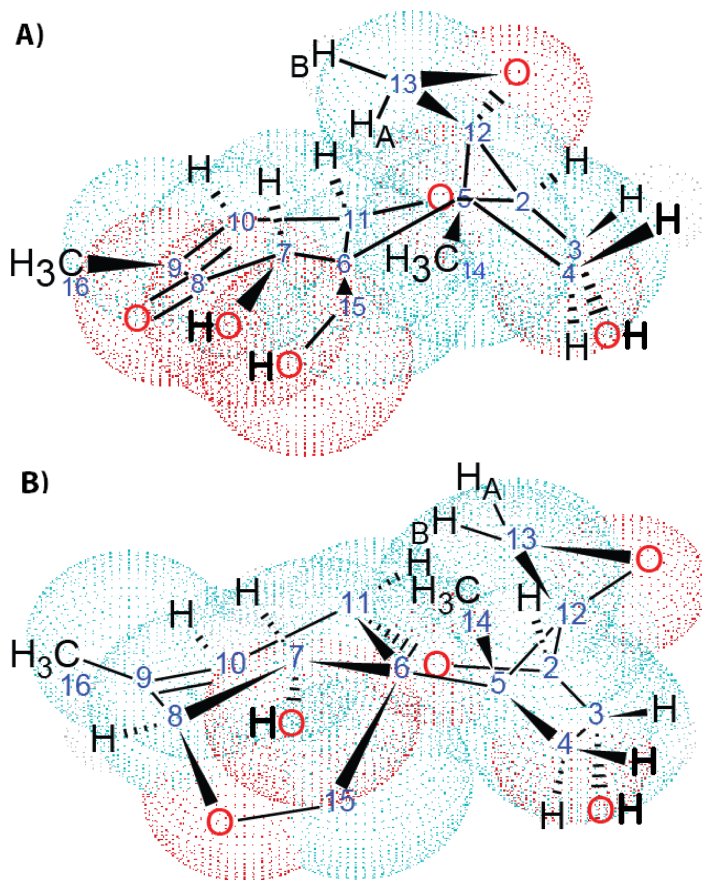


Figure 5. 6: Expected electron density in the (A) major conformation versus the (B) hemiketal conformation for DON, based on the assignment of the NIV structure observed in DMSO- d_6 . Areas shown in red are expected to experience higher electron density, due to the proximity to oxygen atoms; whereas, areas in light green are less electron rich.

Certain observations can be made regarding the electron density depicted in the diagrams in figure 5.6. The most notable differences in the electron density of the two structures appear in the A-ring of the molecule. In the major conformation, significant electron density is noted along the bonds for C-6, C-7, C-8, C-9 and C-10 due largely to the conjugated π -system and the orientation of the hydroxyl oxygens which are involved in the intramolecular hydrogen bonding network from H-15_{OH} and H-7_{OH} to the carbonyl oxygen at C-8, which was described by Nagy *et al.* and confirmed in chapter 3 [111]. This electron dense region is not present in the hemiketal conformation, although some areas of high electron density still persist due to the presence of the oxygen atoms in the structure. This change in the electron density surrounding the A-ring further supports the assignment of the

extra peaks that are present in the carbon-13 spectrum for DON to carbons which are located on the A-ring.

The linewidths observed for the signals in the DON spectrum are between 65 to 170 Hz, which are significantly broader than the 4 Hz linewidths obtained for T-2 toxin in the solid state. The average linewidth of ^1H -decoupled solid-state ^{13}C signals tends to be on the order of 30-60 Hz, and is strongly indicative of the bulk environment within the sample [7]. The rather large linewidths in the DON spectrum likely result from a combination of strong homonuclear dipolar coupling between the carbon nuclei that has not been spun out at the MAS speed utilized for this experiment, and inhomogeneous line broadening due to the presence of multiple conformations in the sample. It is clear from the extra signals in the spectrum obtained for the >95% chemically pure DON sample, that at least two distinct chemical environments are present for DON. Several of the DON signals, such as C-8, and C-9 and/or C-10, appear to have significant shoulders, which are not present on other peaks within the spectrum; thus, improper shimming of the magnetic field can be ruled out. These shoulders may be attributed to another, slightly different chemical environment than that of the major conformation.

5.4.3. Testing of the INADEQUATE experiment

The CP refocused INADEQUATE experiment (Figure 1. 11) was attempted on the isotopically enriched glucose- $^{13}\text{C}_6$ sample. An array of recycle delays was performed to identify an appropriate delay time for the CP spectrum. The recycle delays were determined to be more than 20 s long based on the saturation recovery experiment. When the CP spectrum was obtained for the glucose- $^{13}\text{C}_6$, it appeared to be severely line broadened due to the presence of multiple conformations for the glucose- $^{13}\text{C}_6$ molecule in the sample, which are further broadened by the presence of homonuclear dipolar couplings on the order of 2-4 kHz. The CP refocused INADEQUATE experiment on glucose- $^{13}\text{C}_6$ was attempted, and the total experimental time was 45 hours, or just under 2 days. Unfortunately, the resultant spectrum did not produce any correlation signals due to the loss of the FID resulting from an extremely short T_2 relaxation for the sample. Experimentation on this sample

was aborted, and the simpler two-spin glycine-1,2- $^{13}\text{C}_2$ was used as an alternative for experimental setup.

The glycine-1,2- $^{13}\text{C}_2$ sample was determined to have a recycle delay of 5 s, which was much more reasonable for such a time demanding experiment as the CP refocused INADEQUATE experiment. The total experimental time was 12 hours for the glycine-1,2- $^{13}\text{C}_2$ sample, and the Double Quantum-Single Quantum (DQ-SQ) crosspeaks between the two individual ^{13}C resonances in the spectrum are clearly visible in figure 5.7. Thus, the setup for the experiment was determined to be successful.

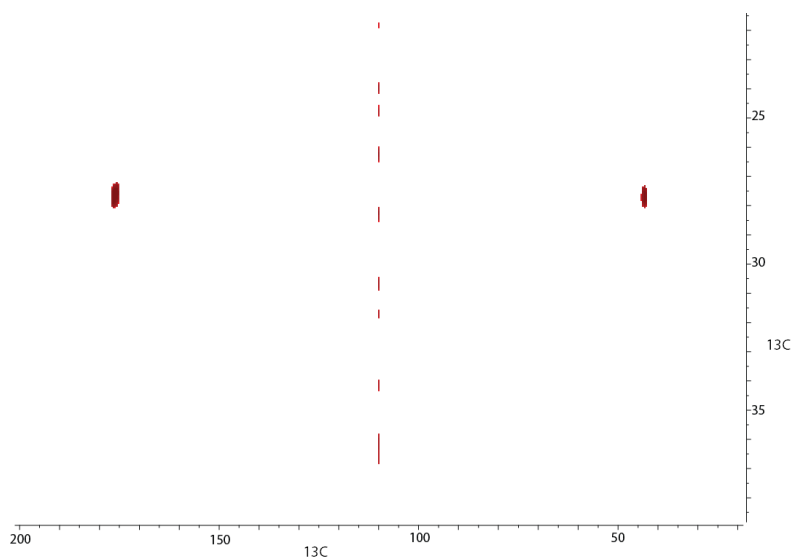


Figure 5. 7: The CP refocused INADEQUATE spectrum obtained for $^{13}\text{C}_2$ -Glycine

Since the INADEQUATE experiment performed on the $^{13}\text{C}_2$ -glycine sample was shown to be effective in the determination of the ^{13}C connectivities, it is likely that spin diffusion amongst the carbons in the fully labeled glucose sample was responsible for the loss of specific correlations between the carbons. Due to the short T_2 relaxation time, the signal was lost during the t_1 delay period required for the INADEQUATE experiment. Dilution of the fully labeled glucose sample with unlabeled glucose would likely yield better results.

Based on the experimental time required for the isotopically enriched $^{13}\text{C}_2$ -glycine sample, and the unusually long T_{1H} for T-2 toxin due to the high crystallinity of the sample, the experimental time required to complete the CP refocused INADEQUATE experiment on T-2 toxin was determined to be approximately 286 hours (or approximately 12 days) based on an acquisition time of 0.02 s, a recycle delay of 5.0 s, 1024 increments and 200 scans. Although it would be possible to reduce the number of increments in the second dimension from 1024 to 128, which reduces the experimental time to 36 hours, the signal-to-noise ratio is still unlikely to be sufficient to pull out the carbon-carbon connectivities at natural abundance. Recall that the natural abundance of the ^{13}C isotope is approximately 1.1%, which translates to the possibility that two ^{13}C atoms neighboring each other to be $(0.011) \times (0.011)$ or 0.01%. It is unreasonable to utilize twelve days of spectrometer time for a single experiment without sufficient evidence that good quality data would result. Thus, analysis of the carbon-carbon connectivities at natural abundance will not be practical in this case.

5.4.4. R-symmetry based CSA recoupling

The R-symmetry sequence, $R10_1^7$ (Figure 1. 12) was tested on the glucose- $^{13}\text{C}_6$ sample to determine if the parameters of the sequence were appropriately set. The resulting spectrum is depicted in figure 5.8. The first increment does not cycle through the back-to-back 180° R-pulses, and is thus representative of the ^{13}C CP spectrum for the isotopically-enriched glucose. Some phase modulation behavior is observed as the timescale of the experiment changes from 0.05 to 6.50 ms from which, in principle, the CSA parameters can be obtained for each carbon. However, as seen in the CP spectrum for the first increment, the carbon signals in the glucose spectrum are very broad and overlap significantly due to the presence of strong homonuclear coupling within the sample, that cannot be spun out with an MAS rate that can be used with the recoupling sequence. Deconvolution analysis of each signal would be required to map out the phase modulation behavior of the peaks in the second dimension. However, it is not necessary to put so much time into a setup sample when the purpose of the setup experiment is simply to determine whether phase modulations are observed in

the second dimension, and not just a simple decay of the signal over the timescale. In order to provide evidence that the experiment was successful, the intensity of one of the peaks in the glucose spectrum was plotted over the first 30 cycles of the R10 sequence for glucose, to show that phase modulation does occur in the second dimension the experiment (inset of figure 5.8). The intensity of the signals in the first dimension amount to points along the FID in the second dimension; thus, modulation in the intensity of the peaks indicates that information is contained in the FID in the second dimension pertaining to the chemical shielding tensors.

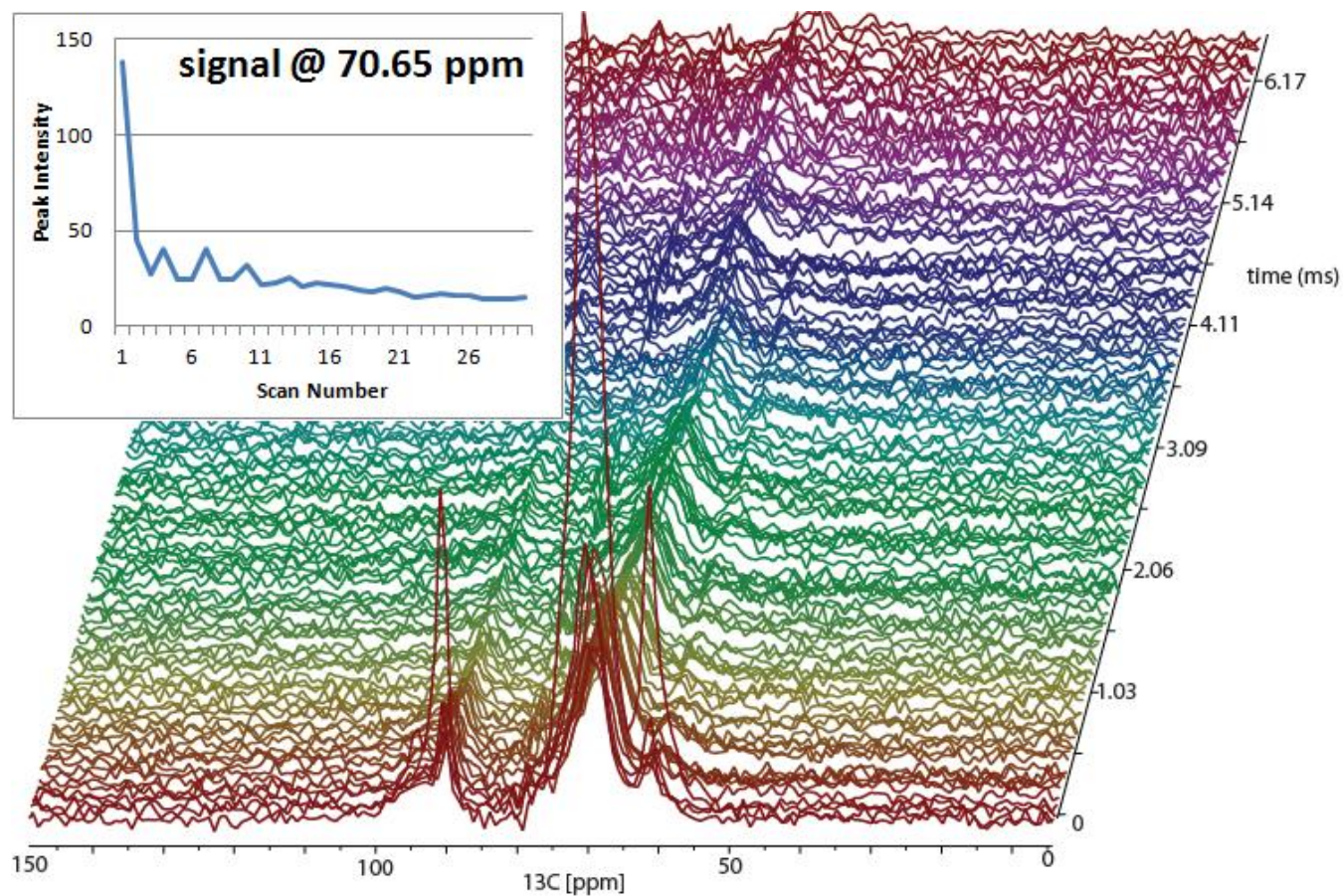


Figure 5. 8: Stacked plot of the spectra obtained for the $R10_1^7$ CSA recoupling sequence on the test sample for glucose- $^{13}\text{C}_6$. The scan at zero is the equivalent to a CP spectrum with polarization from ^1H to ^{13}C . The timescale of the experiments depict the modulation of the CSA interaction mediated through the number of cycles of the R10 pulses. The plot in the inset depicts the phase modulation of the peak measured at 70.65 pm in the glucose spectrum. The intensity of the peak was plotted over the first 30 scans, and depicts the generation of an FID in the second dimension.

As the T_{1H} for T-2 toxin is unusually long for carbon, the experimental parameters of the R-symmetry sequence, specifically the symmetry set, N , ν , and η and the phase φ , had to be adjusted in order to compensate for the increase in the recycle delay. The $R18_2^5$ version of the sequence was chosen to provide sufficient sampling of the signals for T-2 toxin, while maintaining the ability to select for the CSA interaction, as depicted in figure 5.8.

Thirty-three increments of sufficient signal-to-noise were acquired and are shown in the stacked plot in figure 5.9. The first increment is essentially the CP spectrum for T-2 toxin. Note that the sharpness of the peaks from the CP spectrum for T-2 toxin under the conditions used in the initial CP spectrum depicted in figure 5.1 is not present in this spectrum. The differences in decoupling methods and decoupling power result in significantly broader peaks in the $R18_2^5$ spectrum than in the original CP ^{13}C solid-state spectrum. In the original CP spectrum, the decoupling method used was the high power TPPM method; however, due to the complicated nature of the experimental setup, the simple continuous wave (CW) decoupling method was used in the $R18_2^5$ experiment instead.

The stacked plot in figure 5.10 appears at first glance to show little modulation in the signals along the timescale from 0 to 5.19 ms; however, when the intensities of individual signals are plotted over time, an FID results. The FID is then transformed using a cosine function, which results in a spectrum that is symmetric about the origin. The information regarding the CSA of the individual lines in the spectrum can be obtained by considering the spectrum along the positive frequency region. Figure 5.11(A) depicts the phase modulation behaviour of carbon C-2 of the C-ring, and 5.11(B) demonstrates the phase modulation in carbon C-8' on the isovalerate side chain. These frequency spectra in the positive region of the indirect dimension are powder patterns that depend on the CSA and asymmetry terms of the carbon of interest. The R-sequence removes the dependence on the isotropic term, so that the powder patterns all center at zero. The transformed signals for C-2, C-8' and C-9 are depicted in figure 5.11(C), (D) and (F), respectively.

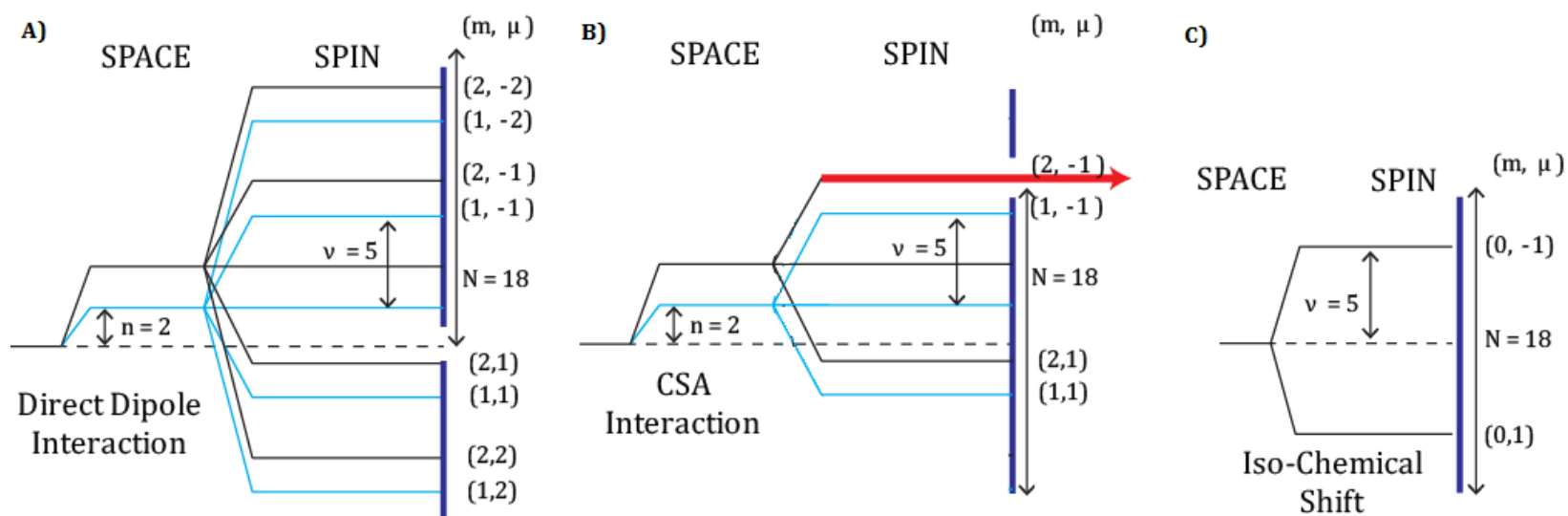


Figure 5. 9: Spin-Space Selection (SSS) diagrams for R-symmetry sequence $R18_2^5$. A) The SSS pathway for the dipole-dipole interaction. B) The SSS pathway for the CSA interaction. C) The SSS pathway for the isotropic chemical shift interaction. Only the CSA interaction is allowed under the conditions of the $R18_2^5$ symmetry-sequence.

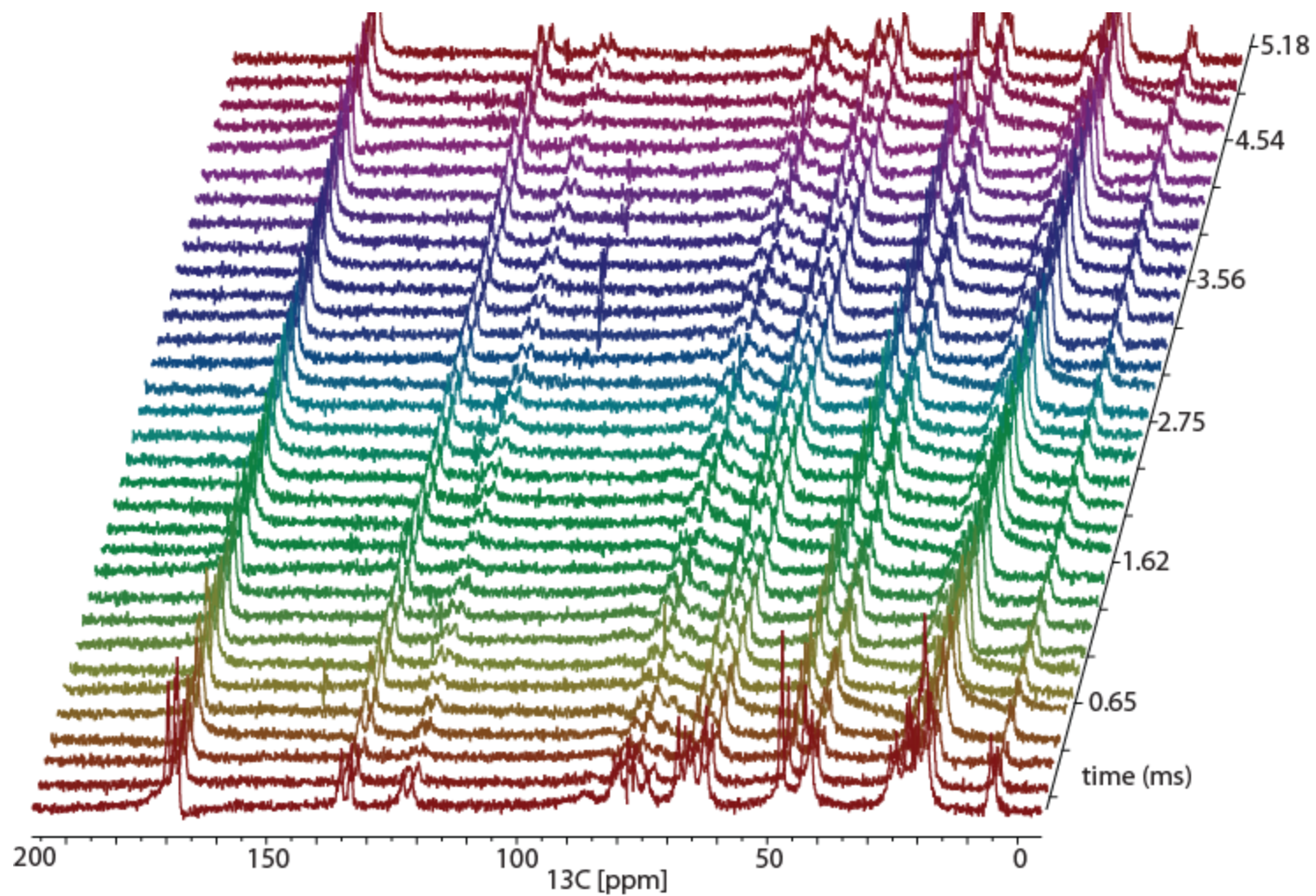
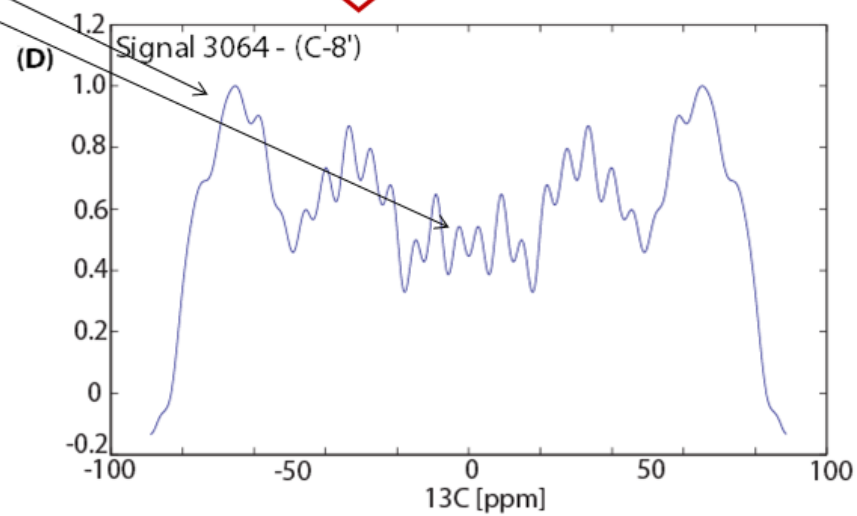
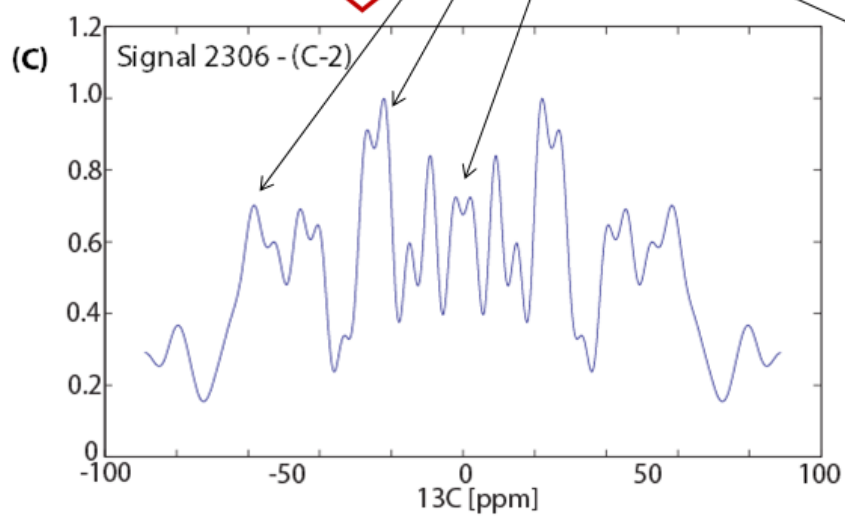
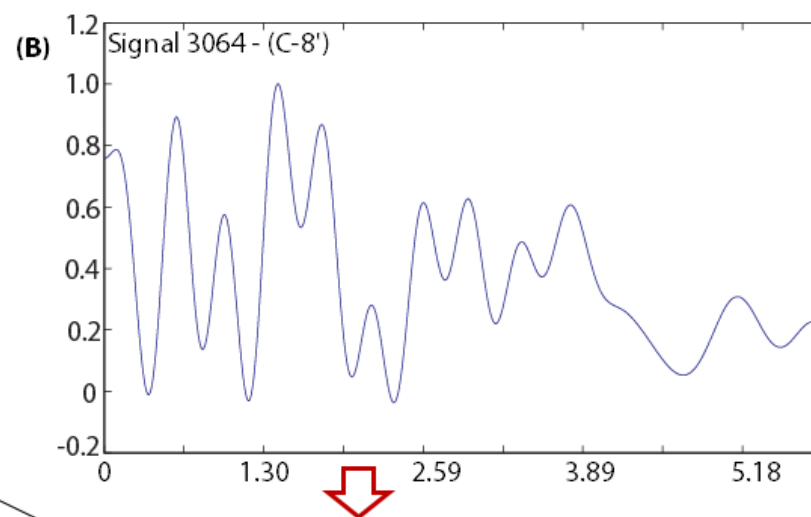
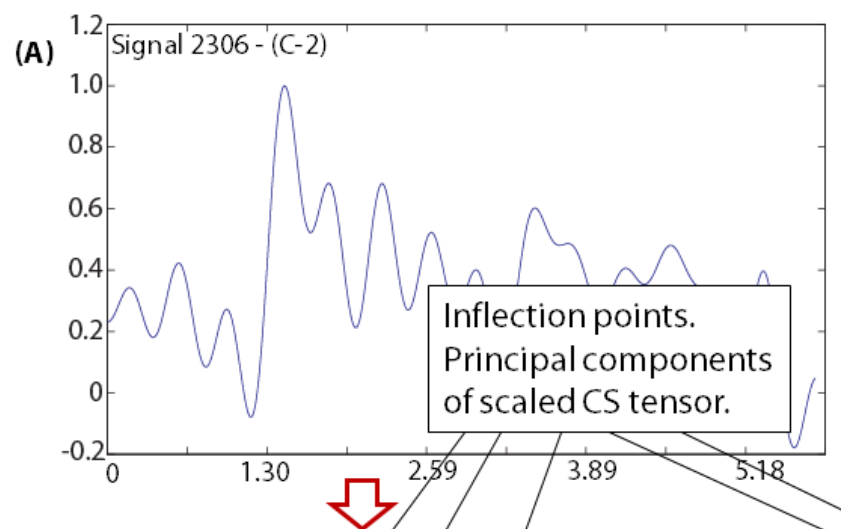


Figure 5. 10: Stacked plot of the resultant spectra obtained for the $R18_2^{55}$ CSA recoupling sequence for T-2 toxin. The scan at zero is the equivalent of a CP spectrum with polarization from ^1H to ^{13}C . The timescale of the experiments depicts the modulation of the CSA interaction mediated through the number of cycles of R18 pulses.



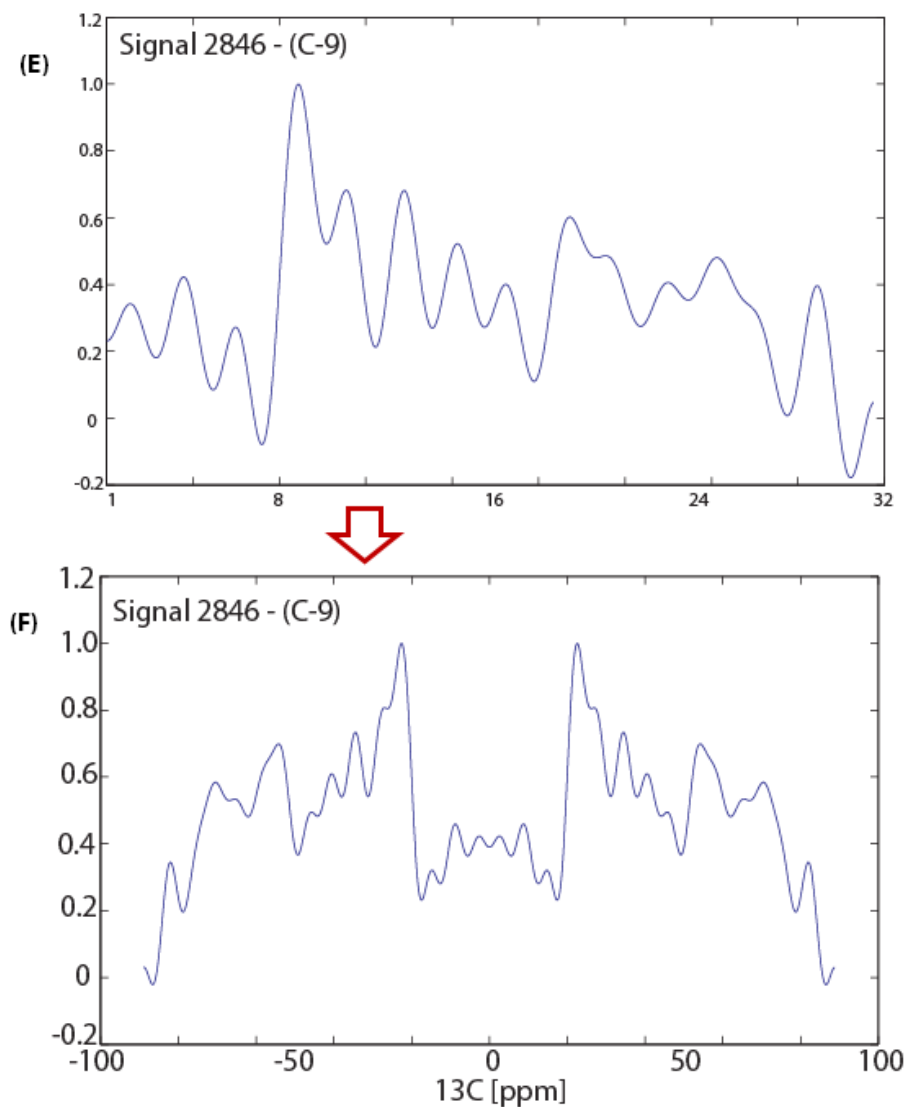


Figure 5. 11: Free Induction Decay (FID) signals arising from the phase modulation of individual spins in the $R18_2^5$ spectrum for T-2 toxin in the solid state. The powder pattern due to the chemical shielding interaction is obtained by cosine transformation of the FID signals. (A) FID of the signal for the C-2 resonance of the C-ring on the trichothecene core. (B) FID of the signal for the C-8' resonance of the isovalerate sidechain. (C) Symmetrical powder pattern for the C-2 resonance of the C-ring. (D) Symmetrical powder pattern for the C-8' resonance of the isovalerate side chain. The inflection points in the CSA powder pattern can be simulated by varying the CSA, asymmetry and isotropic shift parameters. (E) FID of the signal for the C-9 resonance on the A-ring. (F) Symmetrical powder pattern for the C-9 resonance on the A-ring.

Chemical shielding for carbon-13 nuclei generally spans from 20-200 ppm, but is motionally averaged to zero when MAS is much faster than the shielding parameters. The chemical shielding may be intentionally reintroduced into the spectrum through specialized techniques, such as a specific set of R-symmetry sequences. The phase modulations obtained in the direct dimension of the recoupled spectra depend on parameters from the shielding tensor and result in an FID in the indirect dimension which can be transformed to yield a powder pattern. The three principal values of the CSA interaction are directly obtained from the powder pattern in the recoupled spectra, as the shielding components are dependent on the scaling factors specific to the sequence [154]. The sequence of back-to-back π -pulses in the R-symmetry sequence establish a dependence on the center of gravity of the individual nuclei, and place them at the center of each of the powder patterns, which is not always true in the case of the static version of CSA experiment.

The inflection points for the powder patterns derived in the second dimension of the R-symmetry sequence can be utilized to map out the CSA and asymmetry values of the chemical shielding tensor via the inflection points of the scaled powder patterns, which are denoted by σ_{11} , σ_{22} , and σ_{33} . The interpretation of the static powder pattern for the carbon signals C-2, C-8' and C-9 are depicted in figure 5.12.

Recall that the CSA for a signal is equal to the largest deviation in chemical shift from the isotropic values, such that $\sigma_{\text{aniso}} = \sigma_{33} - \sigma_{\text{iso}}$, where σ_{iso} represents the isotropic shielding parameter, which is equal to the mean of the three principal values [91]. The asymmetry, η , is a representation of the difference between σ_{11} and σ_{22} divided by the anisotropy. From the inflection points only σ_{11} and σ_{22} can be measured; however, since σ_{iso} is equal to zero for the experiment, it is possible to extract the value for σ_{33} and σ_{aniso} , using the equation,

$$\begin{aligned}\sigma_{\text{iso}} &= (\sigma_{11} + \sigma_{22} + \sigma_{33})/3 \\ 0 &= \sigma_{11} + \sigma_{22} + \sigma_{33} \\ \sigma_{33} &= -(\sigma_{11} + \sigma_{22})\end{aligned}\tag{5.1}$$

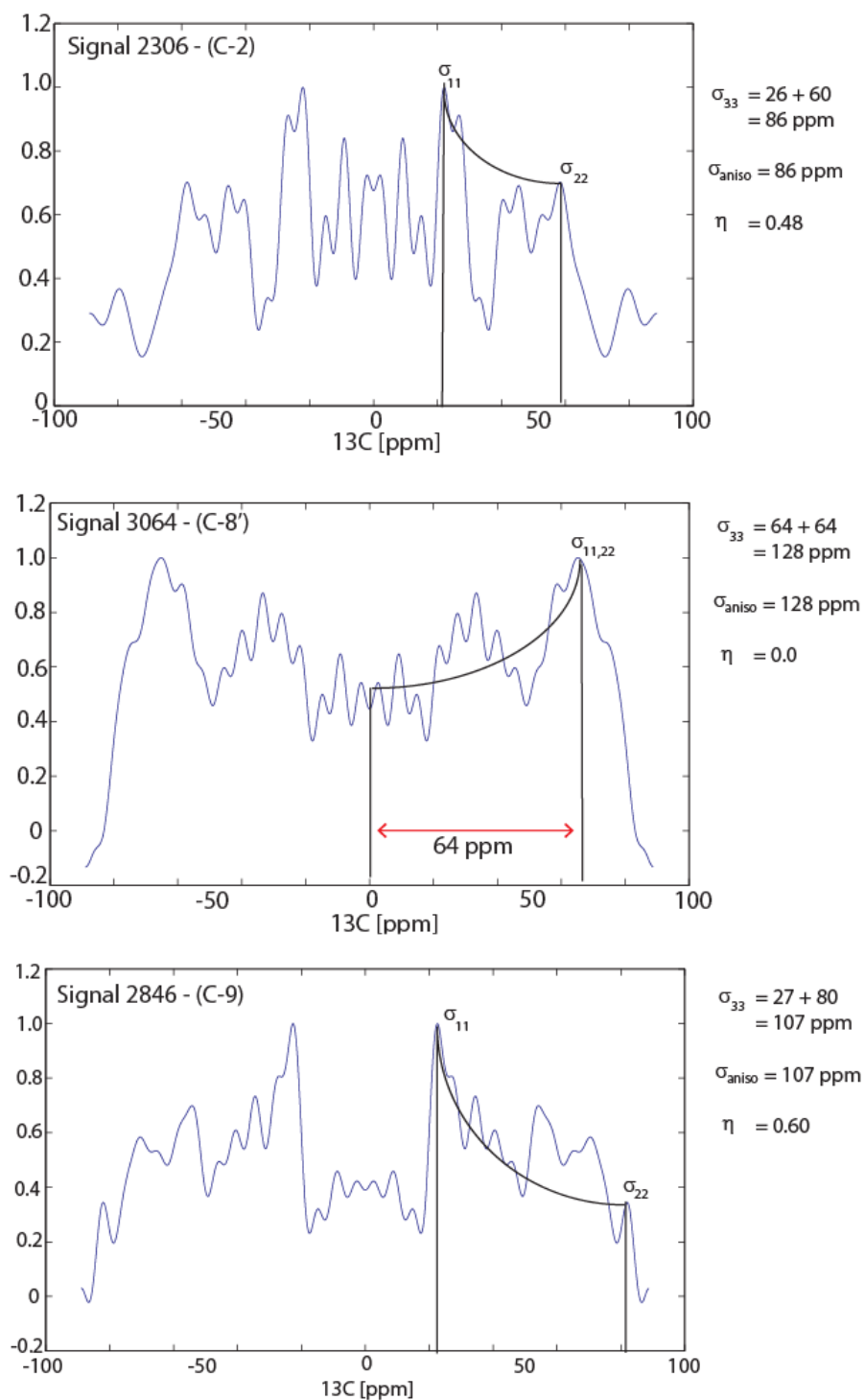


Figure 5. 12: Natural powder patterns for the individual signals pulled from the symmetrical powder patterns obtained for (A) The signal C-2 on the C-ring at 78.72 ppm depicting a CSA of approximately 86 ppm and an asymmetry of 0.48; (B) The signal C-8' on the isovalerate side chain at 172.70 ppm depicting a CSA of approximately 128 ppm, and an asymmetry of 0, and (C) The signal C-9 in the A-ring at 136.32 ppm, which is part of the conjugated double bond system, depicting a CSA of approximately 107 ppm and an asymmetry of 0.60.

For simplicity the principal values for the powder patterns observed for C-2, C-8' and C-9 were evaluated by eye. Carbon C-2 was determined to have a significant CSA of -90 ppm probably the result of the electron withdrawing effect of the neighboring oxygen, , and is very assymmetric, as indicated by an asymmetry parameter of -0.487, which is consistent with the lack of bonding symmetry around C₂ and its inability to undergo any form of bond rotation. The shielding tensor of C-8' is cylindrically symmetric, consistent with shape of the C=O bonding environment and rotation about the C-O and C-C bonds. Its significant size of the tensor is typical for carbonyl carbons which experience a large electron withdrawing effect from the bound oxygens and the planarity resulting from the delocalized π electrons. Furthermore C-9 has a very asymmetric shielding tensor, with an asymmetry parameter of -0.60, which is consistent with its planar binding environment, and its CSA is sizable at 100 ppm, which is in line with sp² carbons lacking nearby electron-withdrawing substituents.

Specialized programs for simulating the chemical shielding powder patterns and extracting the ¹³C tensor parameters for each of the lines in the T-2 toxin spectrum must be used for accurate analysis of these powder patterns. A suitable program for this type of analysis would be the SIMPSON or SPINEVOLUTION programs, which would require that the experimental spectrum be simulated by varying the CSA, asymmetry and isotropic shift parameters. Based on the symmetry numbers used in the R-sequence, along with the experimental parameters, it is possible to predict what the scaling factors may be [5,159]. The phase modulation of the signals in the data obtained is not long lived; thus, it is not necessary for many scans to be collected; 32 cycles appears to be sufficient. In order to obtain a spectrum that is well suited to the simulation analysis, it is recommended that the experiment be repeated with a larger number of transients, a larger sample volume, and more stable spinning in order to reduce the error in the scaling factor for the experiment.

5.5. Discussion

5.5.1. Conformations of T-2 Toxin²

²This section is reproduced in part from the manuscript: Chaudhary, P., Shank, R. A., Montina, T., Goettel, J. T., Foroud, N. A., Hazendonk, P., Eudes, F. (2011) Hydrogen-bonding interactions in T-2 toxin studied using solution and solid-state NMR. *Toxins*. **3**(10), 1310-1331. The section has been re written to reflect the contributions made by the author of the thesis.

The two contributors to the solid-state NMR spectrum were compared to the two molecules in the unit cell of the X-ray crystallography structure. Even though H-bonds cannot be observed directly by X-ray methods, close contacts between hydrogen bonding partners can be used to infer where they may occur, as is shown in the paper by Chaudhary *et al.* [27]. The methods used are beyond the scope of this work, and will not be further described herein. However, the information that was gathered is important, since it was vital to the interpretation of the solid-state conformations. The reader is referred to the paper by Chaudhary *et al.* for further proof of the solid-state conformations observed for T-2 toxin [27]. In this discussion, conformation 1 refers to the solid-state structure appearing in figure 5.13 C/D; whereas, conformation 2 refers to the solid-state structure appearing in figure 5.13 E/F.

It was determined that three structures exist in the data collected, one occurs in solution, and is depicted in figure 5.13 A/B and was described in detail in chapter 2; whereas the other two are present in the solid state.

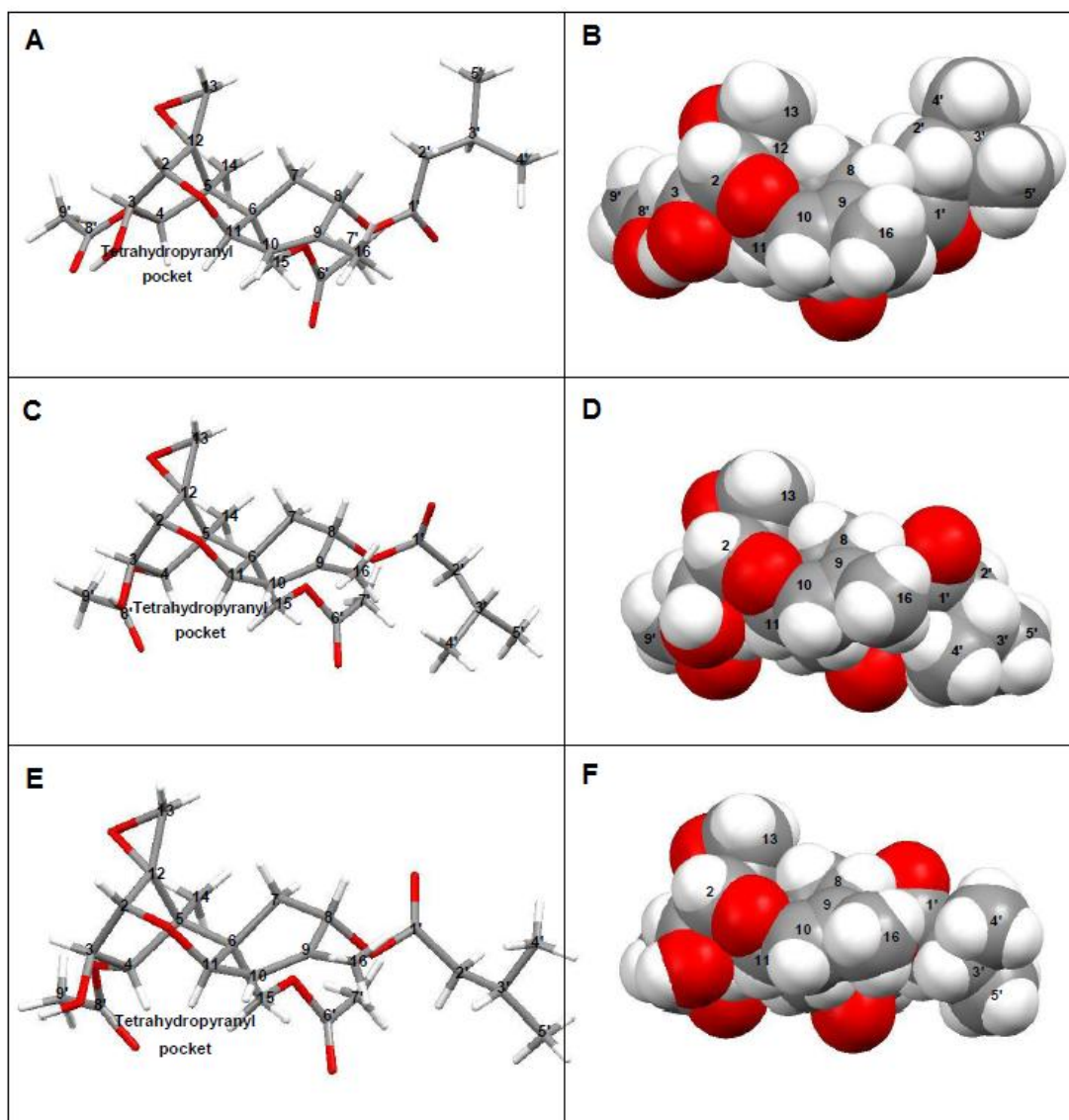


Figure 5.13: Comparison of solution and solid-state conformations of T-2 toxin. Models for the solution-state structure for T-2 toxin showing the lowest energy conformation appear in two different representations: A) stick model and B) van der Waals representation. However, it is important to note here that the side chains are flexible in the solution structure and are continuously moving, but the core ring structure is rigid. C) Stick and D) van der Waals representation for the solid-state conformation 1, respectively. E) Stick and F) van der Waals representation for solid-state conformation 2. Note that the solid-state structures differ only in the torsion angles of the side chains; whereas the solution state core structure differs substantially from the solid-state structures, particularly in the cyclohexene ring placement.

Water Binding

Extensive studies on the trichothecenes, such as the mutation studies described by Krska and Ueno, have revealed that the epoxide ring is required for toxicity and is believed to form the primary interaction in the PTC of the eukaryotic ribosome where it disrupts protein translation [81,156]. Opening of the epoxide ring leads to a complete loss of toxic activity [6,156]. However, the epoxide ring remains stable to nucleophilic attack in solution, due to the steric obstruction of carbons C-12 and C-13 on the side opposite from the epoxide oxygen [6,22,81,156]. The 3D solution-state structure, depicted in figure 5.14, demonstrates that the epoxide ring of T-2 toxin is obstructed on the side where the nucleophilic attack by an S_N2 like mechanism would have to occur [146]. This is further emphasized by the van der Waals representation of the molecule (Figure 5.14 B), where it becomes clear that a nucleophilic ion, or a bound water molecule in the top position (as seen in the solid-state structure), would be sterically hindered from attack. The rigidity conferred by the water bridge that occurs in the tetrahydropyranyl pocket of the toxin on the bottom side of the trichothecene core (shown in figure 5.14 A) may sterically lock the trichothecene core in this epoxide-protected position.

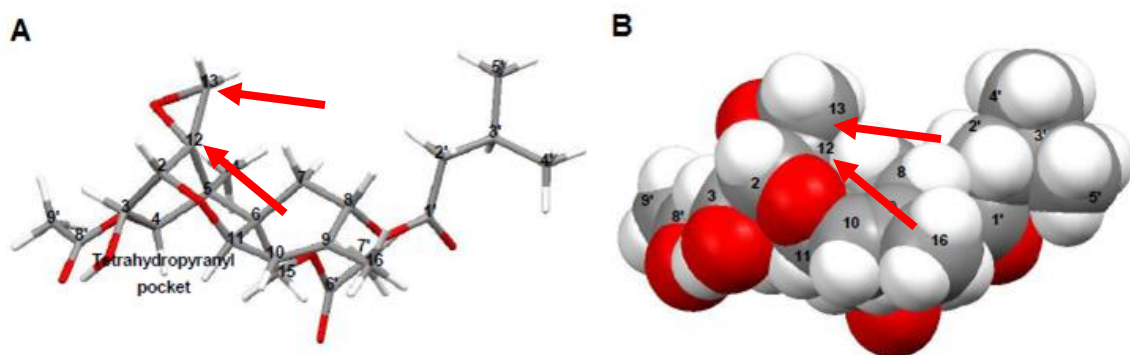


Figure 5. 14: S_N2 scheme. The angles from which water would have to attack from are shown for both C-12 and C-13.

The solid state conformation of T-2 toxin allows for the presence of a water molecule in close proximity to the epoxide, at the top of the molecule. An interaction from a water molecule at the top of the trichothecene core only appears to be present in the solid state. Since the sample is only in

a hydrated state in the solid state, the weaker interactions, such as dipole-induced dipole forces, between the water and the trichothecene molecule may be emphasized, influencing the conformation of the three-dimensional structure. Alternatively, addition of a weakly polar solvent, such as chloroform, may introduce forces that act to displace the bound water by the solvent, changing the three-dimensional geometry.

Close contacts described in the crystallographic data²

²The data provided for the analysis of the close contacts in the two conformations of T-2 toxin were derived from the X-ray crystallographic study performed by Gilardi *et al.* [52], and was evaluated by Praveen Chaudhary for the manuscript Chaudhary *et al.* [27]. Interpretation of the data is presented below and was performed by the author of this work.

The X-ray structure of T-2 toxin was used to infer the hydrogen bonding interactions occurring in the solid state, based on close contacts between potential hydrogen bonding pairs [27,52]. These interactions appear to have a profound impact on the chemical shifts of nearby carbons. All of the solid-state carbon chemical shifts given here were initially presented in the paper by Chaudhary *et al.* [27], and are consistent with the X-ray structural trends proposed by Gilardi *et al.* [52]. For example, the rotation of the acetyl side chain attached at C-4 has a rather large effect on the chemical shift of C-2, C-3 and C-4. In solution, the acetyl side chain should be relatively free to rotate; however, in the solid state the side chain becomes locked in one of two preferred positions. Using the first X-ray crystallographic structure for T-2, we can predict that C-2 will be slightly deshielded by the through-space interaction with O-7', and that C-4 will experience a slight shielding effect. This is reflected by the increase in chemical shift of C-2 and decrease in C-4, respectively. On the other hand, the second crystallographic structure suggests that O-8' has moved closer to C-2 and C-3 and that both of these nuclei should experience a slight deshielding, and this is confirmed by the increase in chemical shift of both of these signals in the solid-state spectrum. The isovalerate side chain arguably exhibits the largest structural changes between the three conformations of T-2 toxin. The preferential adoption of these conformations in the largely flexible isovalerate appear to support the evidence for a bound water molecule within the tetrahydropyranyl pocket on the bottom side of the molecule., as in all three cases, the double-bonded ester oxygen, which may act as a proton acceptor

for hydrogen bonding, is facing towards the interior of the tetrahydropyranyl pocket, and may form close contacts with 3-OH which likely participates in the interaction.

Another example of correspondence between the close contacts in the x-ray structure and the chemical shift deviations in the solid state is that of C-2' on the isovalerate side chain. In solution the isovalerate side chain is relatively free to rotate, and the chemical shifts represent the isotropic configurations for the individual peaks. In the solid state, two distinct conformations for the isovalerate exist; one where the isovalerate chain is primarily 'down' or on the same side of the trichothecene core, and one where the isovalerate chain is 'out', or facing away from the rest of the trichothecene molecule. C-2' is expected to experience the largest deviations in chemical shift, since the environment is vastly different in each case. In both cases large increases in chemical shift are noted. Solid-state conformation 1 displays a 5.42 ppm shift from that in the solution-state spectrum, while conformation 2 shifts by 8.72 ppm. In solution, no evidence for the top water binding position near the epoxide ring is available; however, in the solid state the top water binding position would sterically hinder some of the possible movements of the isovalerate side chain. Given the rather hydrophobic nature of the isovalerate group, one would expect that the preferred conformation would place the hydrophobic part of the isovalerate side chain towards the hydrophobic portion of the trichothecene core, which is present on the top side of the molecule; however, in the solid state the hydrophobic portion faces completely away from the top side of the molecule, and the hydrogen-bond acceptor, the double bonded oxygen (O-1') of the ester group, faces the top. This could serve to help bridge the water across the top of the molecule between O-1 and O-1', allowing it to be in close proximity to the epoxide ring, and on the opposite side of the epoxide oxygen, O-12.

The comparison of the chemical shifts in solution and solid state, as well as the lack of NOESY evidence for the top hydrogen bonding interaction in solution, indicate that the hydrogen bonding behavior of T-2 toxin in solution differs substantially from that in the solid state. The conformational differences observed in T-2 toxin in the solid state suggest that the epoxide ring is now available to hydrogen bond with another molecule, which would be consistent with the large increase in the chemical shift of C-12 as well as the simultaneous decrease in the chemical shift of the C-13

resonance. The carbon chemical shifts of C-12 in both conformations in the solid state, which is one of the proposed targets of nucleophilic attack (along with the C-13 carbon), are shifted significantly downfield, suggesting that these resonances are in close proximity to an electron-withdrawing group, lending support to the potential interaction with a water molecule.

The chemical shifts for the carbons C-2, C-6 and C-11 all experience rather large increases in chemical shift for both conformations of T-2 toxin in the solid state. An increase in chemical shift at these sites indicates that an electron withdrawing group is in close proximity. These resonances are all present on the top side of the trichothecene core. These changes in chemical shift, along with the large shifts in C-12 support the top water binding position in T-2 toxin.

5.5.2. Conformational Dynamics of Deoxynivalenol

Comparison of the Solid-State Spectra with the Solution-State Spectra for DON in CDCl₃ and DMSO-d₆

The chemical shifts of the ¹³C solid-state NMR spectrum of DON contains peaks that match those of the solution-state ¹³C spectrum; however, seven additional peaks were detected well above the noise level. Two of these signals very likely correspond to those reported in acetone-d₆ and DMSO-d₆ by Jarvis *et al.* [72]. The chemical shifts for DON in the solid state and in solution in CDCl₃ and DMSO-d₆ are listed in table 5.2, and the superimposition of the CDCl₃ and DMSO-d₆ spectra onto the solid state spectrum for DON is shown in figures 5.4 and 5.5, respectively. Jarvis observed additional peaks at 104 ppm and 121 ppm in solution, and attributed them to C-8 and C-10 respectively, for the hemiketal rearranged structure of DON.

In the solid state a few peaks stand out due to notable differences in the carbon chemical shift. C-6, a quaternary carbon that sits on one of the hinge points of the A- and B-rings, appears at 65.4 ppm for the major conformation of DON in the solid state, as opposed to the chemical shift of approximately 52 ppm for DON in solution. C-2, C-10 and C-13 also experience a slight 2 to 3 ppm increase in frequency. These carbons all appear on the top side of the trichothecene core. Recall that for T-2 toxin, a water molecule was determined to occupy the space on the top side of the core. These

same carbon resonances were affected; however, C-6 only increased by 3 ppm, while C-13 was shown to decrease by approximately 1 ppm. Furthermore, in T-2 toxin one of the conformations of the carbon C-12 experiences a chemical shift of 1.77 ppm and the other a shift of 7.37 ppm. In DON, the chemical shift in the solid state appears as a slight decrease in chemical shift of 1.45 ppm from that in CDCl_3 and 2.15 ppm in DMSO-d_6 . This difference may be due to a different orientation of the bound water in DON than observed in T-2 toxin. It appears as though in DON, the oxygen of the water molecule is in close proximity to C-6; whereas, in T-2 toxin, the oxygen is closer to C-12.

The shifts observed for DON support the existence of water binding in the top position in the type B trichothecenes in the solid state.

Few differences in chemical shift are observed between the CDCl_3 and DMSO-d_6 spectra. However, the carbons directly bound to hydroxyl resonances, C-3, C-7 and C-15, experience slight 1 to 3 ppm increases in chemical shift in the CDCl_3 spectrum as compared to the spectrum measured in DMSO-d_6 . Recall from chapter 4 that the vicinal couplings for the hydroxyl hydrogens were observed to change dramatically with the polarity of the solvent system. The change in coupling reflected a change to the pre-exponential term, A, in the Arrhenius equation $= Ae^{\frac{-\Delta E}{RT}}$, and a preference in the rotational isomer orientations. Carbon chemical shifts are particularly sensitive to changes in geometry and orientation; thus, these small differences in chemical shift for the hydroxyl substituted carbons are consistent with the change in the rotation about the C-O bond for the hydroxyls in the different solvent systems.

The carbon chemical shifts for C-3, C-7 and C-15 in the solid state more closely resemble the carbon chemical shifts observed for DON in DMSO-d_6 than in CDCl_3 . The close resemblance of these shifts appears to indicate that the orientation of the hydroxyl resonances in the solid state is similar to those in polar solvents. Since the polar solvents appear to support a rotation which is closer to an average than that observed for the CDCl_3 spectrum, the carbon chemical shifts may indicate that all possible rotational isomers are sampled equally in the solid state.

Comparison of the solid state structures for DON: Major structure versus the hemiketal structure

As with T-2 toxin, the ^{13}C MAS solid-state NMR spectrum observed for DON (figure 5.3) also contains other additional features attributed to a second structure of DON. In the carbon-13 experiment performed by Jarvis *et al.*, additional peaks at 104 ppm and 121 ppm in solution were observed, and attributed them to C-8 and C-10 respectively, for the hemiketal rearranged structure of DON[72].

The assignments for these two resonances, described by Jarvis *et al.* [72], as well as the three-dimensional structure determined for the minor hemiketal conformation of NIV in DMSO- d_6 , (figure 4.9 of chapter 4) were used to help determine the identity of the other six signals present in the solid-state spectrum. The six remaining peaks may be attributed to carbons belonging to the A- and B-rings, which experience a great deal of ring strain resulting from the formation of the hemiketal, and the consequent rearrangement of the B-ring from the chair to boat conformations. The electron withdrawing effects of the ketone functionality at C-8, as well as the hydroxyl at C-15 would have the potential for far-reaching influences on the diamagnetic shielding anisotropy; thus, the loss of these moieties during the formation of the hemiketal, may cause significant changes to the chemical shifts of nearby carbon nuclei [144]. Figure 5.6 describes the predicted 3D structure of the major conformation for DON in the solid state based on the 3D structure obtained for DON in chapter 4, and compares it to the overall 3D structure proposed for the hemiketal rearranged minor structure with emphasis placed on the changes expected within the electronic environment surrounding each of the carbon atoms in the trichothecene skeleton.

The change in electron density in the A-ring of the trichothecene core occurs as a result of the loss of conjugation between the carbonyl at C-8 and the C-9/10 ethene. Although the ethene bond remains, and does provide a significant amount of π -electron density, which serves to deshield the surrounding carbons, the loss of conjugation with the carbonyl results in a decrease in the chemical shift of C-10 from 141 ppm in the major trichothecene structure to 121 ppm in the hemiketal structure, as was predicted by Jarvis *et al.* [72]. C-9 on the other hand experiences an increase in ring strain due to the change in conformation about the A-ring, as well as the loss of conjugation from the adjacent carbonyl, and as a result experiences an increase in frequency from 136 ppm in the major

trichothecene structure to 146 ppm in the hemiketal structure. C-8 loses its double bond character and experiences a large decrease in frequency due to the change from a planar to a tetrahedral geometry; however, the overall chemical shift remains significantly deshielded due to the direct attachment of the oxygen. Thus, C-8 experiences a change in chemical shift from 202 ppm to 105 ppm for the hemiketal, as described by Jarvis *et al.* [72].

The other chemical shift deviations between the structures reflect the change in conformation about the B-ring, which experiences a rearrangement of the bonds from a chair conformation in the major conformation to a boat conformation in the minor conformation due to the increase in ring strain imposed on the carbon skeleton by the formation of the extra ring from C-8 to C-15. The B-ring of the trichothecene core is comprised of the oxygen of the tetrahydropyran ring, and carbons C-2, C-12, C-5, C-6 and C-11. In the major conformation, depicted in figure 5.6, the B-ring adopts a chair conformation, such that C-11 and C-6 point towards the bottom side of the core ring structure and C-12 points towards the top. In the minor conformation, C-11 and C-12 both point towards the top of the trichothecene molecule. C-11 and C-2 experience a change in geometry such that H-11 and H-2 move from equatorial positions on the ring to axial positions. C-14, which is attached to C-5, also moves from an equatorial position on the ring to an axial one, and a slight increase in chemical shift is observed due to the increased proximity to the epoxide oxygen. C-2 experiences a significant increase in chemical shift as it moves from 82 ppm to 93 ppm for the hemiketal conformation. C-6 is expected to exhibit large changes in chemical shift from the increase in ring strain, as C-6 now becomes an anchor point for 3 rings: the A-ring, B-ring and the hemiketal ring. This forces the movement of C-6 from the bottom side of the molecule in the major conformation, and is now in line with the plane of the central core in the minor conformation, and is shifted from 65 ppm in the original structure to 73 ppm in the hemiketal structure.

The change in C-15 from a hydroxyl substituent to an ether linkage is only expected to induce a small change in chemical shift for C-15, since the electron density is nearly equivalent for a hydroxyl carbon as that of an ether carbon; however, the added ring strain induced from the formation of the hemiketal ring from C-8 to C-6, may serve to deshield the C-15 resonance, resulting

in a much larger increase in the frequency for this signal, as it shifts from 61 ppm to 97 ppm in the hemiketal conformation.

The presence of a second signal for C-11 has been debated, a small shoulder does appear at 77.78 ppm; however, the validity of this peak has not been confirmed. Also, based on the differences in the bond geometry, C-5 would be expected to endure a significant amount of ring strain, which would likely result in a shift to a higher frequency; however, no additional observable signals are present in the spectrum. In order to confirm the identities of all extraneous peaks in the solid-state ^{13}C spectrum for DON, it is recommended that analysis of the carbon connectivities, through experiments such as INADEQUATE, be performed.

5.5.3. INADEQUATE

The experimental setup for the CP refocused INADEQUATE pulse sequence was successful for the $^{13}\text{C}_2$ -glycine sample, as crosspeaks due to the double quantum (DQ) coherence transfer were observed. Despite difficulties in obtaining a suitable spectrum for glucose- $^{13}\text{C}_6$ due to loss of signal from the extremely short T_2 relaxation for the sample, the experiment was determined to be of use for the determination of carbon-carbon correlations. The experimental setup for T-2 toxin was aborted as the experimental time required to perform the INADEQUATE experiment was determined to be unreasonable. The requirement to perform the experiment at natural abundance and the long relaxation delays in the T-2 toxin sample would have required nearly two weeks of spectrometer time to provide a single spectrum with sufficient signal-to-noise in order to be able to determine the carbon-carbon connectivities at natural abundance. Other experiments are being investigated to access the information contained in the solid-state ^{13}C data for T-2 toxin.

5.5.4. Chemical shielding tensors for T-2 toxin

The R-symmetry sequence produced a spectrum where the chemical shielding powder patterns of each of the carbon signals in the spectrum can be derived by extracting the intensity of

each of the scans and plotting over time, the resultant FID was then transformed in the t_2 time domain to access the powder pattern for the chemical shielding of each individual resonance. The setup of the R-symmetry sequence is specialized to only recouple the CSA interaction into the spectrum, and not the dipole-dipole, J-coupling, or isotropic interactions. The back-to-back π -pulses that are necessary to the recoupling behavior of the R-sequence average out the isotropic interactions, resulting in a symmetric powder pattern.

The CSA of a signal in essence represents the electronic environment surrounding that nucleus. An isotropic chemical shielding tensor will thus be represented by a spherical distribution of electrons about the nucleus, and a polarized nucleus will be represented by an ellipsoidal distribution.

The carbon C-2 is a tertiary carbon, which exists at the hinge point between the B- and C-rings and is directly bound to O-1; thus, it is expected to experience a strong polarization in the direction of the oxygen atom and exhibit a large CSA. C-2 was determined to experience a CSA of 86 ppm, as well as a slight asymmetry of approximately 0.48. The asymmetry in the CSA of C-2 may be due in part to the ring strain at the hinge point, as well as the proximity to the oxygen off of carbon C-3. The asymmetry in the pattern serves to reduce the CSA value, and suggests that the electron distribution surrounding C-2 is biaxial, as seen in figure 5.15

The CSA of C-8' was measured to be approximately 128 ppm with an asymmetry of zero. C-8' is a carbonyl carbon in the O-acetyl substituent group bound to C-3. Three of the four bonds to carbon C-8' are occupied by electron-withdrawing oxygen atoms, while the fourth is bound to a methyl carbon. The polarization in C-8' will be in the opposite direction of the methyl group, and distributed nearly equally between the bonds to oxygen. The electron distribution for C-8' will be slightly ellipsoidal and uniaxial, as seen in figure 5.15B.

The carbon C-9 forms part of the ethene bond in the trichothecene core and is directly bound to the C-14 methyl, as well as C-8 which is in turn bound to the isovalerate side chain. C-9 has a CSA of approximately 107 ppm, and an asymmetry of 0.60. Like C-2, C-9 exhibits an electron distribution

that is biaxial and ellipsoidal. The electron distribution will largely be along the double bond that C-9 shares with C-10, but a significant pull is also experienced in the direction of the C-8 oxygen.

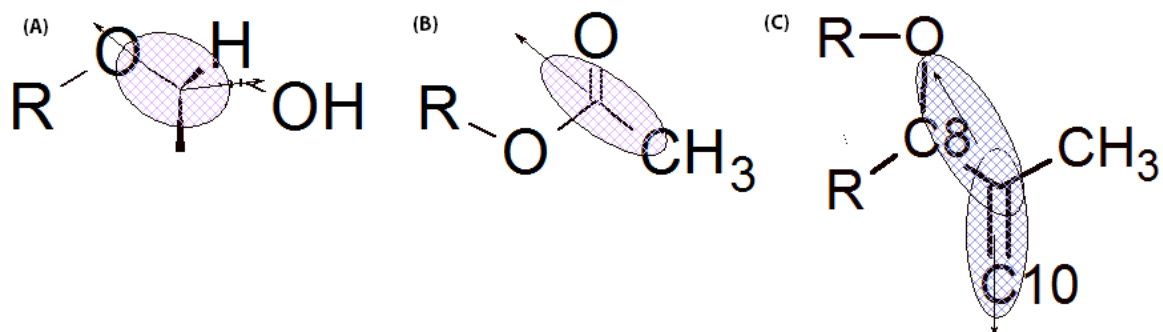


Figure 5. 15: Chemical shielding tensor representations for the carbons (A) C-2 representing a slight biaxiality in the tensor, the tensor is ellipsoid; (B) C-8' represents a chemical shielding tensor which is more cylindrical, and uniaxial, and (C) C-9 is largely biaxial.

Programs such as SIMPSON or SPINEVOLUTION, can be used to fit the parameters that determine the shape of the powder pattern, namely the CSA, asymmetry and isotropic shift. The symmetry numbers used in the R-sequence (N , ν , and η) can be used along with the experimental parameters to predict what the scaling factors for the experiment are. The scaling factor for experiments such as the R-symmetry sequence is a ratio that results in the reduction of intensity of the signals produced in the spectrum. As the number of cycles in the symmetry sequence increases, the scaling factor is multiplied; thus, the signals decay in the same way that an FID decays over time. The scaling factor is very sensitive, and is greatly affected by even small errors in the speed of sample rotation, setting of the magic angle, and inhomogeneities in the magnetic field. The inflection points of the powder patterns resulting after Fourier transformation of the FID obtained from the signal decay over the number of cycles gives rise to the three principal components of the chemical shielding tensors: the CSA, the asymmetry and the isotropic chemical shift values. Thus, it is possible to convert the true values using the scaling factors, where minimal error exists due to variables in the experiment [5,159].

For the chosen examples, the tensor properties support the assignment of the carbons. With better signal-to-noise and rotor stability, the CSA recoupled separated local field experiment can go a long way to validating the assignment and help differentiate between the carbons in conformations 1 and 2 in the solid state.

5.6. Conclusions

A solid-state NMR analysis of the T-2 toxin structure was performed, which not only confirms the presence of two distinct structural contributions to T-2 toxin in the solid state, as originally observed in the X-ray crystallographic analysis performed by Gilardi *et al.* [52]; but also indicates that an interaction with a water molecule may also occur in the solid state. Both of the solid-state conformations of T-2 toxin differ from that of the solution-state structure, as interpreted from the differences in the chemical shift of the ^{13}C resonances.

The solid-state NMR spectrum for DON indicates that DON also exists in two distinct conformations in the solid state. The major conformation for DON is hypothesized to resemble that of the solution-state structure described in chloroform [135], and presented in chapter 3; however, the second conformation seems to suggest that the hemiketal rearranged structure observed in DMSO- d_6 , which was presented in chapter 4, may also exist in the solid state. These hypotheses are based on the close agreement of the solid-state carbon chemical shifts to those in solution for the solvents CDCl_3 and DMSO- d_6 , as well as the electron density profiles presented for DON in figures 5.7 (A) and (B) which are based on the major and minor conformations observed for DON in DMSO- d_6 in chapter 4.

The R18 symmetry sequence was attempted on T-2 toxin, to help provide information regarding the chemical shielding on the individual signals in the spectrum. It was shown to provide individual FIDs for each signal, which could be Fourier transformed into chemical shielding powder patterns. The scaling factor for the R-symmetry based experiments is highly sensitive to errors in the spinning speed, and a unit that provides greater stability in the spinning speed of the sample would provide greater confidence in the results of the spectrum. The chemical shielding tensors may be pulled out from the individual powder patterns to provide information regarding the CSA and

asymmetry parameters of the signal. The powder patterns for C-2, C-8' and C-9 were analyzed and shown to reveal chemical shielding tensors and electron distribution patterns which are consistent with the rest of the data presented for the trichothecenes. A higher resolution data set is required for simulation in order to retrieve accurate CSA and asymmetry parameters for all signals in the T-2 toxin spectrum, with the potential to discern between the signals for each of the two individual structures depicted in the solid-state carbon-13 spectrum.

With these new insights into the three-dimensional solid-state structures of T-2 toxin and DON, it is possible to begin piecing together the mechanism for toxicity of trichothecenes, starting with the ribosome. As such, a novel mechanism for the interaction of the trichothecene toxins with the eukaryotic ribosome was proposed, which may be applicable to other toxins of this family[27]. Undoubtedly, this new information is a stepping stone towards the guided development of trichothecene resistance genes which can be developed for the introduction into transgenic plants, such as those previously discovered by groups such as Mitterbauer *et al.* for the engineering of Triticale cultivars [94,109]. The development of trichothecene resistance genes is essential to the prevention of crop loss due to Fusarium Head Blight and root rot, and will help to circumvent the occurrence of alimentary toxic aleukia, and other related ailments.

6. Conclusions and Future Directions

6.1 Conclusions

The structural analysis of trichothecene mycotoxins prior to this work has been primarily performed through solution-state nuclear magnetic resonance (NMR), with some additional work in the area of single crystal x-ray diffraction (SCXRD). Although much information had been gained in regards to determining the key features of trichothecene structure, little had been done in the way of structural dynamics of this class of toxins.

The first portion of this study focused primarily on the use of solution-state NMR analysis of selected type A and type B trichothecenes. Complete proton and carbon NMR analyses of the type A trichothecene T-2 toxin and the type B trichothecenes deoxynivalenol (DON), as well as a complete proton analysis for nivalenol (NIV), 3-O-acetyldeoxynivalenol (3-ADON), and 15-O-acetyldeoxynivalenol (15-ADON), and the incomplete carbon analyses for the acetylated DON derivatives, were performed in deuterated chloroform (CDCl_3) in order to verify the stereochemistry of the compounds in solution. These analyses served to confirm and refine the relative assignments of all protons within the spectra. In particular, for T-2 toxin, the refinement of the methylene protons, acetyl, methyl and carbonyl resonances was made. For the type B trichothecenes the methylene protons were also refined and in some cases corrected. For example, the assignment of the epoxide hydrogens, 13_{AB} , was reversed in the three-dimensional spectrum, and the assignment of the methylene protons $4_{\alpha\beta}$ for DON, 3-ADON and 15-ADON was reversed in the proton spectra. Furthermore, previously unreported proton chemical shifts and coupling constants were described for all of the type B trichothecenes, including those for the hydroxyl resonances and longer range couplings describing the rigidity of the fused ring system. The carbon chemical shifts for 3-ADON and 15-ADON in CDCl_3 were also missing from the literature, and are presented here.

In the second part of this study, the ability of the type A and type B trichothecenes to undergo both intra- and inter-molecular hydrogen bonding was investigated. The lowest energy conformation of DON was described in a Density Functional Theory (DFT study) by Nagy *et al.* to

involve an internal hydrogen bonded network from H-15_{OH} to H-7_{OH} and finally to the carbonyl at C-8. This internal hydrogen bonded network is confirmed in the proton spectra for DON in CDCl₃ based on the high resolution observed in the exchangeable protons H-7_{OH} and H-15_{OH} even upon the introduction of D₂O to the sample, which is expected to induce chemical exchange within these protons. The lack of exchange observed at these sites within the structure indicates that tight intramolecular hydrogen bonding must be present.

In terms of inter-molecular interactions for these toxins, water plays a large role, due to the knowledge that despite the lack of solubility of these toxins in aqueous systems, water is required for them to go into solution at all. In fact, a certain amount of water is present in the sample regardless of removal of adsorbed water from a powdered sample of DON under the influence of vacuum-pumping in a nitrogen atmosphere; and the removal of water from the solvent through the use of molecular sieves. This residual water, which is present in all of the spectra collected is attributed to at least one bound water molecule per molecule of toxin. The water is believed to bind within the tetrahydropyranyl pocket of T-2 toxin and the type B trichothecenes in the solvent deuterated chloroform to help stabilize the trichothecene core. The exchange between water and deuterated water was shown to be very slow, and occurs over several hours, indicating that the water molecule is tightly bound to the trichothecene core, and likely exists as a water-bridge within the trichothecene molecule. The addition of more water to the DON sample in CDCl₃ is believed to trigger a degradation mechanism, which results in a series of ring opening events, likely triggered by an interaction of water with the epoxide ring.

The structural dynamics within the type B trichothecenes were also investigated. Structural dynamics can offer a great deal of insight into the flexibility of a compound, as well as its ability to undergo structural rearrangements. The ability of the trichothecene class of compounds to undergo structural rearrangements has been well documented for the macrocyclic trichothecenes by the Jarvis group [67,69,79]; however, little evidence existed regarding the ability of the smaller type A and B trichothecenes to undergo rearrangement [72].

. Various solvent systems were used to determine the effect that polarity and solvent structure have on the compounds. A secondary, minor conformation was investigated and evidence for a structural rearrangement in the type B trichothecenes was provided in polar solvents, such as deuterated dimethyl sulfoxide (DMSO- d_6). The complete proton and carbon analyses for the major conformation of the type B trichothecenes DON and NIV and the complete proton and partial carbon analyses for the major conformation of the type B trichothecenes 3-ADON and 15-ADON are presented for the solvent DMSO- d_6 at 300 MHz for proton and 75 MHz for carbon. The complete proton analyses for the minor conformation for the type B trichothecenes DON, NIV and 3-ADON are also presented here, along with a partial analysis of the carbon resonances belonging to the minor conformations for DON and NIV in DMSO- d_6 .

The minor conformation was determined to be a structural rearrangement of the type B trichothecenes where a hydroxyl group is present at C-15. The rearrangement is mediated through the formation of a hemiketal from C-8 to C-15. This structure was previously proposed by Jarvis *et al.* [72], and is confirmed here for the type B trichothecenes DON, NIV and 3-ADON. The 15-ADON sample in DMSO- d_6 is also shown to have at least one minor conformation in the spectrum; however, it is believed that these may be degradation products, or different rotational isomers of the compound, as the hemiketal from C-8 to C-15 is not likely to occur due to the acetylation of 15-ADON at carbon 15.

The first step in the mechanism for hemiketal formation is also described, as it involves a change in the rotational isomers that are preferentially sampled in solution. In a non-polar solvent environment, such as that observed for $CDCl_3$, the vicinal couplings belonging to the hydroxyl resonances for the type B trichothecenes are small, suggesting that they sample primarily *gauche*, *gauche'* rotational isomers in solution; however, in polar solvent environments, the couplings increase which indicate that the rotational isomers are sampled more evenly. In the case of the hydroxyl resonance at C-15, the *trans* isomer is sampled to a much larger extent in polar environments, which places it in close proximity to the carbonyl at C-8. The change in the rotational

sampling of H-15_{OH} provides the opportunity for the hemiketal to form, and reduces the pre-exponential factor for the reaction in the process.

The complete proton and carbon analysis was also performed for the type B trichothecene DON in acetone-d₆ for the major conformation, as well as the complete proton analysis for the minor conformation of DON in acetone-d₆. DON was also studied in methanol-d₄ and THF-d₈ and a partial proton analysis of the major and minor conformations is presented. The hemiketal conformation was determined to exist for DON in all of the solvents studied, with the exception of CDCl₃.

Water binding also appears to occur for the hemiketal rearranged form of DON; however, the water-binding site appears to have moved away from the tetrahydropyranyl pocket, and the water molecule is now present in the newly formed hemiketal pocket, and evidence for a top water binding position exists based on the data observed for the carbon-13 spectrum in DMSO-d₆ and acetone-d₆. Further investigation into this water-binding arrangement is required for confirmation.

In the next part of the study, the solid-state ¹³C NMR spectra for T-2 toxin and DON were collected and analysed. The solid-state NMR analysis confirmed the presence of two molecules in the crystallographic unit cell for T-2 toxin. These each differ slightly in structure from each other, as well as from the solution-state NMR structure obtained in deuterated chloroform. Analysis of deoxynivalenol (DON) in the solid-state also provided evidence for a second structure, which is believed to be that of the hemiketal rearranged form observed for DON in the solution-state NMR spectrum obtained in polar solvent environments.

Inter-molecular interactions with water were also observed in the solid state for T-2 toxin. Evidence for the tetrahydropyranyl pocket, as well as a top water binding site is available in both conformations of T-2 toxin. Both of these water binding sites are confirmed in the major conformation for DON observed in the solid state.

NMR crystallographic analysis was attempted in order to distinguish between the individual signals obtained in the solid-state NMR spectra for T-2 toxin. The INADEQUATE experiment was set up; however, it was later determined that the relaxation delay required for the T-2 toxin sample

would require an excessive amount of experimental time in order to obtain a suitable spectrum for the compound at natural abundance. Thus, another method to access the information in the solid-state T-2 toxin spectrum was attempted by introducing the R-symmetry sequence $R18_2^5$. The phase modulation in the R-symmetry sequence for T-2 toxin was plotted versus the number of scans and transformed with a cosine function to obtain the CSA powder patterns for individual signals in the spectrum. The inflection points in the powder patterns correspond to the principal values of the chemical shielding tensor and can be used to extract the data for the signal(s) of interest. The signals obtained for C-2, C-8' and C-9 were analyzed by eye and the anisotropy and asymmetry terms for the signals were calculated and determined to support the assignment for those peaks in the T-2 toxin spectrum. Simulation of the data to extract the principal values would provide reliable data. The collection of a data set with a more reliable spinning speed is desired in order to reduce the uncertainty in the scaling factor, and will be the subject of a future study.

6.2 Biological Implications

These findings are important when considering the mechanistic descriptions of the biological interaction of trichothecenes. In particular, hydrogen bonding interactions become important when considering binding affinities and bond geometries of protein-ligand complexes. The interaction of trichothecenes with the ribosome creates a particularly interesting scenario, as the different substituent groups off the core have been shown to inhibit the different stages of protein translation. It is believed that all trichothecenes interact with the ribosomal protein L3 (RPL3) [53]; however, the different mechanisms of ribosomal inhibition are most likely linked to the different types of hydrogen bonding interactions that the substituent groups are able to form with the other surrounding atoms in the active site.

The functionality of the ribosome, and the availability of water molecules throughout the different stages of protein synthesis are important factors which should also be considered when studying the trichothecenes in the solution and solid states. The ratcheting behavior of the ribosome during protein translation works to reorganize water within the PTC pocket, and protect peptide bond formation from bulk water [128]. Furthermore, the removal of water from the PTC raises the

entropy of the system, thus providing a dramatic decrease in the free energy required for the enthalpically disfavored peptide bond formation. It is also important to note that the change in hydration within the PTC pocket could also result in a change in the local pH of the environment within the pocket, resulting in a change to the ionization state of the exposed amino acids. With the added knowledge regarding the various conformations that T-2 toxin may adopt in both the solution and solid states, the state of hydration within the PTC at different stages of protein synthesis and its potential effect on the conformation of T-2 toxin should be considered when attempting to discern the mode of interaction of the trichothecenes with the ribosome.

The same consideration regarding the conformation of the type B trichothecenes in various solvent systems also applies when considering their interaction with the ribosome. The differences in polarity may serve to change the structure of these trichothecenes, giving rise to conformations similar to those observed in the solid state. The signals in the solid-state spectrum for DON, figure 5.3, suggest that the second conformation may be due to the hemiketal rearrangement of the molecule. This rearrangement changes the geometry of the core dramatically and may now sterically allow the epoxide to directly interact with water, promoting hydrogen bonding interactions. It is also quite interesting to note that the carbon chemical shifts observed for DON in the solid state more closely resemble those for DON measured in DMSO- d_6 in both the major and minor conformations observed, than those observed for DON measured in $CDCl_3$. It is safe to presume that the overall 3D structural conformation for the type B trichothecenes in the solid state resembles the overall 3D structural conformation of the trichothecenes in polar solvent environments. Investigation into whether this is true for the type A trichothecene T-2 toxin is an interesting prospect to contemplate.

To the best of our knowledge, no kinetic studies have been performed to investigate the potential hydrogen-bonding interactions that may occur between the trichothecenes and RPL3. It is well understood that the epoxide ring serves as the primary toxicological feature of trichothecenes, and that it is both heat- and pH-stable in solution [2]. Based on the results depicted for the solid-state analysis of T-2 toxin, it is highly likely that the interaction between the trichothecenes occurs between the epoxide ring and the tryptophan residue of the W-finger domain present on RPL3 of the

ribosome, and that the interaction may be mediated through a water bridge, such as that observed to bind in the top water binding position in both T-2 toxin and DON in the solid-state.

However, it is important to note that RPL3 is only one of the proteins in a very complex RNA and protein complex, and unfortunately is not stable in solution on its own. Thus, a study to determine whether the W-finger domain is stable in solution must first be conducted. It is possible that one of the solid-state trichothecene conformations is critical for the interaction with the ribosome to explain its toxic effects, which are likely mediated through the water sequestration. The proposed interaction of one of the solid-state conformations of T-2 toxin with the W-finger of RPL3 is depicted in figure 6.1.

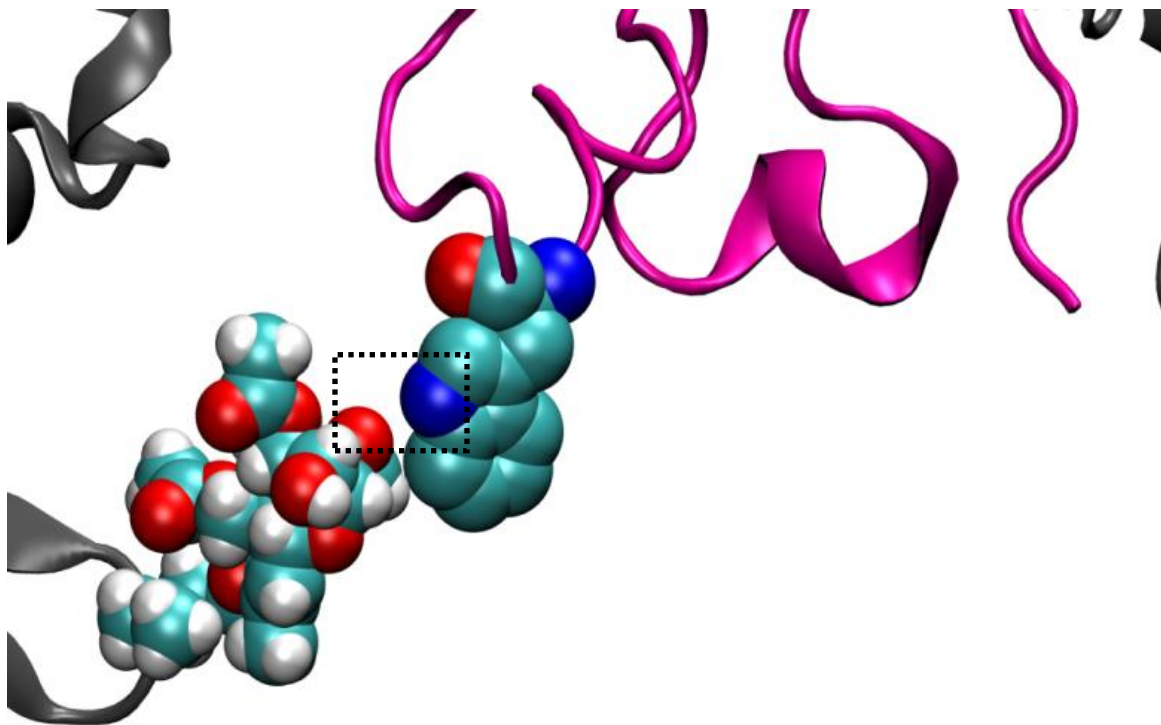


Figure 6. 1: Model representing the proposed transient interaction of the trichothecene T-2 toxin with W255 of the W-finger of ribosomal protein, RPL3. RPL3 is shown in magenta, with the tryptophan residue, W255, shown explicitly. Other nearby proteins of the PTC are depicted in grey. The van der Waals representation was used to demonstrate the close contacts of the epoxide with the nitrogen of the tryptophan.

The lack of the N-terminal extension in prokaryotic bacteria may also serve as a clue towards the lack of evidence of substantial toxicological effects of trichothecenes on bacterial protein translation. However, at this stage, too many variables in the toxicological behaviour of the trichothecenes exist to make any solid speculations on the subject.

6.3 Future Investigations

Future investigations regarding the NMR structural analysis of the trichothecene toxins involve the broadening of the database of toxins for the type A toxins, as well as structural investigations of the type C and type D trichothecenes in a variety of solvent systems. This will help to answer the questions raised regarding whether the hemiketal rearranged form is unique to type B trichothecenes due to the presence of the carbonyl at C-8, or whether similar structures may be formed in other types of trichothecenes. For example, does the presence of an O-acetyl group at C-8 and a hydroxyl at C-15 induce a similar rearrangement in trichothecene compounds?

A kinetic investigation into the rate of dissociation of the bound water in the tetrahydropyranyl water-binding pocket and other potential regions of the molecule where water binding may exist, such as the top water binding position and the hemiketal water-binding pocket, may provide further insight into the inter-molecular interactions of the trichothecenes.

Water-binding studies in the AAFC sample, as well as the other type B trichothecenes may prove to be a useful endeavor. Continuing the development of NMR crystallography at the University of Lethbridge solid-state NMR lab is also a priority for the group, and may require the development of new pulse sequences, as well as new equipment and probes for the current spectrometer. Furthermore, the development of an adequate processing and simulation platform for this type of work is required, and is currently in the process of being implemented in the lab.

Investigations into the mechanism of toxicity of the trichothecene mycotoxins is an on-going project at the Lethbridge research center of Agriculture and Agri-Food Canada, and ribosomal assays

have been put in place for the determination of toxicity towards individual cellular systems. Determining the mechanism of transport across the cellular membrane may be performed through specialized NMR techniques involving the orientation of cellular membranes within the magnetic field of the spectrometer.

Therefore, the information provided has advanced the knowledge of those involved in the study of the trichothecenes at both the University of Lethbridge, as well as the Lethbridge Research Center for Agriculture and Agri-Food Canada. Furthermore, it has provided information which has advanced the knowledge of the public, through publications in the online journal *Toxins*.

7. References

1. Alexander, N. J., McCormick, S. P., & Ziegenhorn, S. L. (1999). Phytotoxicity of selected trichothecenes using *Chlamydomonas reinhardtii* as a model system. *Nat. Toxins*, 7, 265-269.
2. Anderson, D. W., *et al.* (1989). Structure-activity studies of trichothecenes: cytotoxicity of analogs and reaction products derived from T-2 toxin and neosolaniol. *J. Med. Chem.*, 32, 555-562.
3. Andrew, E. R., Bradbury, A., & Eades, R. G. (1959). Removal of dipolar broadening of nuclear magnetic resonance spectra of solids by specimen rotation. *Nature*, 183, 1802-1803.
4. ApSimon, J. W., *et al.* (1991). The *Fusarium* genus: a versatile biosynthetic engine. In Atta-ur-Rahman (Ed.), *Studies in Natural Products Chemistry* (Vol. 9, pp. 201-218).
5. Bak, M. R., J. T.; Nielsen, N. C. (2000). SIMPSON: A General Simulation Program for Solid-State NMR Spectroscopy. *J. Mag. Res.*, 147(2), 296-330.
6. Bamburg, J. R. (1976). Chemical and biochemical studies of the trichothecene mycotoxins *Mycotoxins and other fungal related food problems* (Vol. 149, pp. 144-162): American Chemical Society.
7. Barich, D. H. D., J. M.; Schieber, L. J.; Zell, M. T.; Munson, E. J. (2006). Investigation of solid-state NMR line widths of ibuprofen in drug formulations. *J. Pharm. Sci.*, 95(7), 1586-1594.
8. Bennett, A. E., Rienstra, A. E., Auger, M. I., Lakshmi, K. V., & Griffin, R. G. (1995). Heteronuclear decoupling in rotating solids. *J. Chem. Phys.*, 103, 6951-6958.
9. Bennett, J. W., & Klich, M. (2003). Mycotoxins. *Clinical Microbiology Reviews*, 16(3), 497-+.
10. Beyer, M., Ferse, I., Mulac, D., Wurthwein, E. U., & Humpf, H. U. (2009). Structural Elucidation of T-2 Toxin Thermal Degradation Products and Investigations toward Their Occurrence in Retail Food. *Journal of Agricultural and Food Chemistry*, 57(5), 1867-1875.
11. Biselli, S., & Hummert, C. (2005). Development of a multicomponent method for *Fusarium* toxins using LC-MS/MS and its application during a survey for the content of T-2 toxin and deoxynivalenol in various feed and food samples. *Food. Addit. Contam.*, 22, 752-760.
12. Blackwell, B. A., Greenhalgh, R., & Bain, A. D. (1984). C-13 AND PROTON NUCLEAR MAGNETIC-RESONANCE SPECTRAL ASSIGNMENTS OF DEOXYNIVALENOL AND OTHER MYCOTOXINS FROM FUSARIUM-GRAMINEARUM. *Journal of Agricultural and Food Chemistry*, 32(5), 1078-1083.
13. Blackwell, B. A., Miller, J. D., & Greenhalgh, R. (1985). C-13 NMR-STUDY OF THE BIOSYNTHESIS OF TOXINS BY FUSARIUM-GRAMINEARUM. *Journal of Biological Chemistry*, 260(7), 4243-4247.
14. Bloch, F. (1946). Nuclear Induction. *Physical Review*, 70, 460-473.

15. Bordwell, F. G. M., R. J.; Olmstead, W. N. (1984). Acidities and hydrogen bonding of phenols in dimethyl sulfoxide. *J. O. C.*, 49(8), 1424-1427.
16. Boutigny, A. L., Richard, F. F., & Barreau, C. (2008). Natural mechanisms for cereal resistance to the accumulation of *Fusarium* trichothecenes. *Eur. J. Plant Pathol.*, 121, 411-423.
17. Bretz, M., Knecht, A., Gockler, S., & Humpf, H. U. (2005). Structural elucidation and analysis of thermal degradation products of the *Fusarium* mycotoxin nivalenol. *Molecular Nutrition & Food Research*, 49(4), 309-316.
18. Brian, P. W., Dawkins, A. W., Grove, J. F., Hemming, H. G., Lowe, D., & Norris, G. L. F. (1961). Phytotoxic compounds produced by *Fusarium equiseti*. *J. Exp. Bot.*, 12, 1-12.
19. Brouwer, D. H. R., J.A. (2007). Symmetry-based recoupling of proton chemical shift anisotropies in ultrahigh-field solid-state NMR. *Journal of Magnetic Resonance*, 185(2007), 173-178.
20. Bruins, M. B. M., Karsai, I., Schepers, J., & Snijders, C. H. A. (1993). Phytotoxicity of deoxynivalenol to wheat tissue with regard to in vitro selection for *Fusarium* Head Blight resistance. *Plant Science*, 94, 195-206.
21. Bunner, D. L., & Morris, E. R. (1988). Alteration of multiple cell membrane functions in L-6 myoblasts by T-2 toxin: an important mechanism of action. *Toxicol. Appl. Pharmacol.*, 92, 113-121.
22. Burrows, E. P., & Szafraniec, L. L. (1986). Hypochlorite-promoted transformations of trichothecenes. *Verrucarol. J. Org. Chem.*, 51, 1494-1497.
23. Campbell, H. C., T.M.; Vigier, B.; Underhill, L. (2002). Comparison of mycotoxin profiles among cereal samples from eastern Canada. *Canadian Journal of Botany*, 80(5), 526.
24. Carter, C. J., & Cannon, M. (1977). Structural requirements for the inhibitory action of 12,13-epoxytrichothecenes on protein synthesis in eukaryotes. *Biochem. J.*, 166, 399-409.
25. Carter, C. J., Cannon, M., & Smith, K. E. (1976). Inhibition of protein synthesis in reticulocyte lysates by trichodermin. *Biochem. J.*, 154, 171-178.
26. Cavanaugh, J., Fairbrother, W. J., Palmer, A. G., & Skelton, N. J. (1996). Relaxation and dynamic processes *Protein NMR spectroscopy: principles and practice* (pp. 243-300). San Diego, CA, USA: Academic Press.
27. Chaudhary, P. S., R.A.; Montana, T.; Goettel, J.T.; Foroud, N.A.; Hazendonk, P.; Eudes, F. (2011). Hydrogen-bonding interactions in T-2 toxin studied using solution and solid-state NMR. *Toxins*, 3(11), 1310-1331.

28. Cheng, B., *et al.* (2010). Detoxification of deoxynivalenol by *Bacillus* strains. *Journal of Food Safety*, 30, 599-614.
29. Cole, R. J., & Cox, R. H. (1981). The Trichothecenes *Handbook of toxic fungal metabolites* (pp. 152-263). Toronto, Ontario, Canada: Academic Press.
30. Cundliffe, E., & Davies, J. E. (1977). Inhibition of initiation, elongation, and termination of eukaryotic protein synthesis by trichothecene fungal toxins. *Antimicrobi. Agents*, 11, 491-499.
31. Dang, J., Bergdahl, B. M., Separovic, F., Brownlee, R. T. C., & Metzger, R. P. (2004). Difference in conformation of virginiamycin M1 in chloroform and bound form in the 50S ribosome or streptogramin acetyltransferase. *Aust. J. Chem*, 57, 415-418.
32. Dang, J., Separovic, F., Bergdahl, B. M., Brownlee, R. T. C., & Metzger, R. P. (2004). Solvent affects the conformation of virginiamycin M1 (Pristinamycin IIA, Streptogramin A). *Org. Biomol. Chem.*, 2, 2919-2924.
33. Desjardins, A. E. (2009). From Yellow Rain to Green Wheat: 25 Years of Trichothecene Biosynthesis Research. *Journal of Agricultural and Food Chemistry*, 57(11), 4478-4484.
34. Desjardins, A. E., Hohn, T. M., & McCormick, S. P. (1993). Trichothecene biosynthesis in *Fusarium* species: chemistry, genetics, and significance. *Microbiol. Rev.*, 57, 595-604.
35. Desjardins, A. E., McCormick, S. P., & Appell, M. (2007). Structure-activity relationships of trichothecene toxins in an Arabidopsis thaliana leaf assay. *Journal of Agricultural and Food Chemistry*, 55(16), 6487-6492.
36. Dohnal, V., Jezkova, A., Jun, D., & Kuca, K. (2008). Metabolic pathways of T-2 toxin. *Current Drug Metabolism*, 9(1), 77-82.
37. Dowd, P. F., Miller, J. D., & Greenhalgh, R. (1989). TOXICITY AND INTERACTIONS OF SOME FUSARIUM-GRAMINEARUM METABOLITES TO CATERPILLARS. *Mycologia*, 81(4), 646-650.
38. Duffy, M. J., & Reid, R. S. (1993). Measurement of the stability of T-2 toxin in aqueous solution. *Chem. Res. Toxicol.*, 6, 524-529.
39. Edwards, S. G., Barrier-Guillot, B., Clasen, P.-E., Hietaniemi, V., & Petterson, H. (2009). Emerging issues of HT-2 and T-2 toxins in European cereal production. *World Mycotoxin Journal*, 2, 173-179.
40. Ernst, M. (2003). Heteronuclear spin decoupling in solid-state NMR under magic-angle sample spinning. *J. Mag. Res.*, 162, 1-34.

41. Esmond, R., Fraserreid, B., & Jarvis, B. B. (1982). SYNTHESIS OF TRICHOVERRIN-B AND ITS CONVERSION TO VERRUCARIN-J. *Journal of Organic Chemistry*, 47(17), 3358-3360.
42. Eudes, F., Comeau, A., Rioux, S., & Collin, J. (2000). Phytotoxicite de huit mycotoxines associees a la fusariose de l'epi chez le ble. *Canadian Journal of Plant Pathology*, 22, 286-292.
43. Eudes, F., Comeau, A., Rioux, S., & Collin, J. (2001). Impact of trichothecenes on Fusarium head blight (*Fusarium graminearum*) development in spring wheat (*Triticum aestivum*). *Canadian Journal of Plant Pathology*, 23, 318-322.
44. Foroud, N. A., & Eudes, F. (2009). Trichothecenes in Cereal Grains. *International Journal of Molecular Sciences*, 10(1), 147-173.
45. Fragaki, G., Stefanaki, I., Dais, P., & Mikros, E. (2008). Conformational properties of the macrocyclic trichothecene mycotoxin verrucarin A in solution. *Magnetic Resonance in Chemistry*, 46(12), 1102-1111.
46. Fraser, R. R. K., M.; Morand, P.; Govil, G. (1968). Stereochemical dependence of vicinal H-C-O-H coupling constants. *Can. J. Chem.*, 47, 403-409.
47. Freeman, G. G., Gill, J. E., & Waring, W. S. (1959). The structure of trichothecin and its hydrolysis products. *J. Chem. Soc.*, 1105-1132.
48. Freeman, G. G., & Morrison, R. I. (1948). Trichothecin: an antifungal metabolic product of *Trichothecium roseum*. *Nature*, 162, 30.
49. Fried, H. M., & Warner, J. R. (1981). Cloning of yeast gene for trichodermin resistance and ribosomal and ribosomal protein L3. *Proceedings of National Academy of Science USA*, 78, 238-242.
50. Garvey, G. S., McCormick, S. P., Alexander, N. J., & Rayment, I. (2009). Structural and functional characterization of TRI3 trichothecene 15-O-acetyltransferase from *Fusarium sporotrichioides*. *Protein Science*, 18(4), 747-761.
51. Garvey, G. S., McCormick, S. P., & Rayment, I. (2008). Structural and functional characterization of the TRI101 trichothecene 3-O-acetyltransferase from *Fusarium sporotrichioides* and *Fusarium graminearum* - Kinetic insights to combating fusarium head blight. *Journal of Biological Chemistry*, 283(3), 1660-1669.
52. Gilardi, R., George, C., & Flippen-Anderson, J. L. (1990). The structure of T-2 toxin. *Acta Crystallogr. Sect. C.*, 46, 645-648.
53. Gilly, M., Benson, N. R., & Pellegrini, M. (1985). Affinity labeling the ribosome with eukaryotic-specific antibiotics: (bromoacetyl)trichodermin. *Biochemistry*, 24, 5787-5792.

54. Grant, P. G., Schindler, D., & Davies, J. E. (1976). Mapping of trichodermin resistance in *Saccharomyces cerevisiae*: a genetic locus for a component of the 60S ribosomal subunit. *Genetics*, 83, 667-673.
55. Greenhalgh, R., Blackwell, B. A., Savard, M., Miller, J. D., & Taylor, A. (1988). SECONDARY METABOLITES PRODUCED BY FUSARIUM-SPOROTRICHIOIDES DAOM-165006 IN LIQUID CULTURE. *Journal of Agricultural and Food Chemistry*, 36(1), 216-219.
56. Greenhalgh, R., Blackwell, B. A., & Savard, M. E. (1989). THE NMR-SPECTRA OF TRICOTHECENES AND RELATED FUNGAL METABOLITES. *Tetrahedron*, 45(8), 2373-2383.
57. Greenhalgh, R., Fielder, D. A., Blackwell, B. A., Miller, J. D., Charland, J. P., & Apsimon, J. W. (1990). SOME MINOR SECONDARY METABOLITES OF FUSARIUM-SPOROTRICHIOIDES DAOM 165006. *Journal of Agricultural and Food Chemistry*, 38(10), 1978-1984.
58. Greenhalgh, R., *et al.* (1989). APOTRICHOTHECENES - MINOR METABOLITES OF THE FUSARIUM SPECIES. In S. Natori, K. Hashimoto & Y. Ueno (Eds.), *Mycotoxins and Phycotoxins 88* (Vol. 10, pp. 223-232).
59. Greenhalgh, R., Hanson, A. W., Miller, J. D., & Taylor, A. (1984). Production and x-ray crystal structure of 3-acetoxy-7,15-dihydroxy-12,13-epoxytrichothec-9-en-8-one. *J. Agric. Food. Chem.*, 34, 98-102.
60. Greenhalgh, R., *et al.* (1986). PRODUCTION AND CHARACTERIZATION OF DEOXYNIVALENOL AND OTHER SECONDARY METABOLITES OF FUSARIUM-CULMORUM (CMI-14764, HLX-1503). *Journal of Agricultural and Food Chemistry*, 34(1), 98-102.
61. Grove, J. F., & Mortimer, P. H. (1969). The cytotoxicity of some transformation products of diacetoxyscirpenol. *Biochem. Pharmacol.*, 18, 1473-1478.
62. Harris, L. J., & Gleddie, S. C. (2001). A modified RPL3 gene from rice confers tolerance of the *Fusarium graminearum* mycotoxin deoxynivalenol to transgenic tobacco. *Physiol. Mol. Plant Path.*, 58, 173-181.
63. Harris, R. K., Washylshen, R. E., & Duer, M. J. (2009). *NMR Crystallography*. Chinchester, UK: John Wiley & Sons, Ltd.
64. Haubl, G., *et al.* (2007). Characterization of (C-13(24)) T-2 toxin and its use as an internal standard for the quantification of T-2 toxin in cereals with HPLC-MS/MS. *Analytical and Bioanalytical Chemistry*, 389(3), 931-940.
65. Ishii, K., & Ueno, Y. (1981). Isolation and characterization of two new trichothecenes from *Fusarium sporotrichiodes* strain M-1-1. *Applied Environmental Microbiology*, 42, 541-543.

66. Jarvis, B. B. (2003). Analysis for mycotoxins: The chemist's perspective. *Archives of Environmental Health*, 58(8), 479-483.
67. Jarvis, B. B., Alvarez, E. E., Mazzocchi, D. B., & Comezoglu, F. T. (1987). MECHANISMS FOR THE REARRANGEMENTS OF THE TRICHOTHECENES. *Abstracts of Papers of the American Chemical Society*, 194, 269-ORGN.
68. Jarvis, B. B., *et al.* (1987). ISOLATION OF MACROCYCLIC TRICHOTHECENES FROM A LARGE-SCALE EXTRACT OF BACCHARIS-MEGAPOTAMICA. *Journal of Organic Chemistry*, 52(1), 45-56.
69. Jarvis, B. B., Comezoglu, T. F., & Comezoglu, N. S. (1984). OXIDATION AND REARRANGEMENTS OF MACROCYCLIC TRICHOTHECENES. *Abstracts of Papers of the American Chemical Society*, 188(AUG), 201-ORGN.
70. Jarvis, B. B., Desilva, T., McAlpine, J. B., Swanson, S. J., & Whittern, D. N. (1992). NEW TRICHOVERROIDS FROM MYROTHECIUM-VERrucARIA ISOLATED BY HIGH-SPEED COUNTERCURRENT CHROMATOGRAPHY. *Journal of Natural Products*, 55(10), 1441-1446.
71. Jarvis, B. B., Lee, Y. W., Comezoglu, S. N., & Yatawara, C. S. (1986). TRICHOTHECENES PRODUCED BY STACHYBOTRYS-ATRA FROM EASTERN-EUROPE. *Applied and Environmental Microbiology*, 51(5), 915-918.
72. Jarvis, B. B., *et al.* (1990). Conformational effects in trichothecenes - structures of 15-hydroxy C4 and C8 ketones. *Journal of Organic Chemistry*, 55(11), 3660-3662.
73. Jarvis, B. B., & Mazzola, E. P. (1982). MACROCYCLIC AND OTHER NOVEL TRICHOTHECENES - THEIR STRUCTURE, SYNTHESIS, AND BIOLOGICAL SIGNIFICANCE. *Accounts of Chemical Research*, 15(12), 388-395.
74. Jarvis, B. B., Midiwo, J. O., Flippenanderson, J. L., & Mazzola, E. P. (1982). STEREOCHEMISTRY OF THE RORIDINS. *Journal of Natural Products*, 45(4), 440-448.
75. Jarvis, B. B., Midiwo, J. O., & Mazzola, E. P. (1984). ANTILEUKEMIC COMPOUNDS DERIVED BY CHEMICAL MODIFICATION OF MACROCYCLIC TRICHOTHECENES .2. DERIVATIVES OF RORIDIN-A AND RORIDIN-H AND VERRUCARIN-A AND VERRUCARIN-J. *Journal of Medicinal Chemistry*, 27(2), 239-244.
76. Jarvis, B. B., Stahly, G. P., Pavanadasivam, G., & Mazzola, E. P. (1980). ANTI-LEUKEMIC COMPOUNDS DERIVED FROM THE CHEMICAL MODIFICATION OF MACROCYCLIC TRICHOTHECENES .1. DERIVATIVES OF VERRUCARIN-A. *Journal of Medicinal Chemistry*, 23(9), 1054-1058.
77. Jarvis, B. B., & Wang, S. J. (1999). Stereochemistry of the roridins. Diastereomers of roridin E. *Journal of Natural Products*, 62(9), 1284-1289.

78. Jarvis, B. B., Yatawara, C. S., Greene, S. L., & Vrudhula, V. M. (1984). PRODUCTION OF VERRUCAROL. *Applied and Environmental Microbiology*, 48(3), 673-674.
79. Jarvis, B. B., Zeng, M., & Mazzola, E. P. (1990). NOVEL REARRANGEMENTS OF MACROCYCLIC TRICHOTHECENES. *Tetrahedron Letters*, 31(31), 4401-4404.
80. Khachatourians, G. G. (1990). Metabolic effects of trichothecene T-2 toxin. *Can. J. Physiol. Pharmacol.*, 68, 1004-1008.
81. Krska, R., Baumgartner, S., & Josephs, R. (2001). The state-of-the-art in the analysis of type-A and -B trichothecene mycotoxins in cereals. *Fresen. J. Anal. Chem.*, 371, 288-295.
82. Krska, R., *et al.* (2005). Processing and purity assessment of standards for the analysis of type-B trichothecene mycotoxins. *Analytical and Bioanalytical Chemistry*, 382(8), 1848-1858.
83. Kupce, E., & Freeman, R. (1995). Stretched adiabatic pulses for broadband spin inversion. *J. Mag. Res. Ser. A*, 115, 273-276.
84. Kupchan, S. M., Jarvis, B. B., Streelman, D. R., & Dailey, R. G. (1977). ISOLATION OF POTENT NEW ANTILEUKEMIC TRICHOTHECENES FROM B-MEGAPOTAMICA. *Abstracts of Papers of the American Chemical Society*, 173(MAR20), 61-61.
85. Langseth, W., & Rundberget, T. (1999). The occurrence of HT-2 toxin and other trichothecene in Norwegian cereals. *Mycopathologia*, 147, 157-165.
86. Lauren, D. R., Ashley, A., Blackwell, B. A., Greenhalgh, R., Miller, J. D., & Neish, G. A. (1987). TRICHOTHECENES PRODUCED BY FUSARIUM-CROOKWELLENSIS DAOM 193611. *Journal of Agricultural and Food Chemistry*, 35(6), 884-889.
87. Lee, D.-K. W., Y.; Ramamoorthy, A. (2001). A Two-Dimensional Magic-Angle Decoupling and Magic-Angle Turning Solid-State NMR Method: An Application to Study Chemical Shift Tensors from Peptides That Are Nonselectively Labeled with ¹⁵N Isotope. *J. Phys. Chem. B*, 105(20), 4752-4762.
88. Lee, Y. K. K., N.D.; Helmle, M.; Johannessen, O.G.; Nielsen, N.C.; Levitt, M.H. (1995). Efficient dipolar recoupling in the NMR of rotating solids. A sevenfold symmetric radiofrequency pulse sequence. *Chem. Phys. Letters*, 242, 304-309.
89. Lesage, A., Auger, C., Caldarelli, S., & Emsley, L. (1997). Determination of through-bond carbon-carbon connectivities in solid-state NMR using the INADEQUATE experiment. *J. Am. Chem. Soc.*, 119, 7867-7868.
90. Lesage, A., Bardet, M., & Emsley, L. (1999). Through-bond carbon-carbon connectivities in disordered solids by NMR. *J. Am. Chem. Soc.*, 121, 10993-10997.

91. Levitt, M. A. (2008). *Spin Dynamics; Basics of Nuclear Magnetic Resonance* (2nd Edition ed.). Chichester, UK: John Wiley & Sons Ltd.
92. Levitt, M. H. (2009). Symmetry-Based Pulse Sequences in Magic-Angle Spinning Solid-State NMR. *Encyclopedia of NMR*, 7704-7734.
93. Lowe, I. J. (1959). Free induction decays of rotating solids. *Phys. Rev. Lett.*, 2, 285-287.
94. Lucyshyn, D., *et al.* (2007). Cloning and characterization of the ribosomal protein L3 (RPL3) gene family for *Triticum aestivum*. *Mol. Genet. Genomics*, 277, 507-517.
95. Luzar, A. C., D. (1993). Structure and hydrogen bond dynamics of water-dimethyl sulfoxide mixtures by computer simulations. *J. Chem. Phys.*, 98(10), 8160-8173.
96. Madhyastha, M. S., Marquardt, R. R., & Abramson, D. (1994). STRUCTURE-ACTIVITY-RELATIONSHIPS AND INTERACTIONS AMONG TRICHOTHECENE MYCOTOXINS AS ASSESSED BY YEAST BIOASSAY. *Toxicon*, 32(9), 1147-1152.
97. Marat, K. (Producer). (2009) SpinWorks 3.1.6.
98. Masuda, E. T., T.; Tatsuno, T.; Obara, T. (1982). Immunosuppressive effect of a trichothecene mycotoxin, Fusarenon-X in mice. *Immunology*, 45(4), 743-749.
99. Matsumoto, M., Minato, H., Uotani, N., Matsumoto, K., & Kondo, E. (1977). New antibiotics from *Cylindrocarpon sp.* *J. Antibiot.*, 30, 681-682.
100. McLaughlin, C. S., Vaughn, M. H., Campbell, J. M., Wei, C. M., & Stafford, M. E. (1977). Inhibition of protein synthesis by trichothecenes. In J. V. Rodricks, C. W. Hesseltine & M. A. Mehlman (Eds.), *Mycotoxins in Human and Health* (pp. 263-275). Park Forest South, Illinois, USA: Pathotox Publishers.
101. McLean, M. (1996). The phytotoxicity of *Fusarium* metabolites: An update since 1989. *Mycopathologia*, 133, 163-179.
102. McPhail, A. T., & Sim, G. A. (1966). Fungal metabolites. Part VI. The structure of verrucarins A: X-ray analysis of verrucarins A p-iodobenzenesulphonate. *J. Chem. Soc. C Organic*, 1394-1406.
103. McRee, D. E., & David, P. R. (1999). *Practical Protein Crystallography* (2nd ed.). San Diego, California, USA: Academic Press.
104. Meskaukas, A., & Dinman, J. D. (2008). Ribosomal protein L3 functions as a 'rocker switch' to aid in coordinating of large subunit-associated functions in eukaryotes and archaea. *Nucleic Acids Research*, 36, 6175-6186.

105. Meskaukas, A., Petrov, A. N., & Dinman, J. D. (2005). Identification of functionally important amino acids of ribosomal protein L3 by saturation mutagenesis. *Molecular Cell Biology*, 25, 10863-10874.
106. Miller, J. D., ApSimon, J. W., Blackwell, B. A., Greenhalgh, R., & Taylor, A. (2001). Deoxynivalenol: a 25 year perspective on a trichothecene of agricultural importance. In L. Summerall, Backhouse, Bryden & Burgess (Eds.), *Fusarium, Paul E. Nelson memorial symposium* (pp. 310-320). St. Paul, Minnesota, USA: APS Press.
107. Miller, J. D., Greenhalgh, R., Wang, Y. Z., & Lu, M. (1991). TRICHOTHECENE CHEMOTYPES OF 3 FUSARIUM SPECIES. *Mycologia*, 83(2), 121-130.
108. Minervini, F., Fornelli, F., & Flynn, K. M. (2004). Toxicity and apoptosis induced by the mycotoxins nivalenol, deoxynivalenol and fumonisin B1 in a human erythroleukemia cell line. *Toxicol. In Vitro*, 18, 21-28.
109. Mitterbauer, R., *et al.* (2004). Toxin-dependent utilization of engineered ribosomal protein L3 limits trichothecene resistance in transgenic plants. *Plant Biotechnology Journal*, 2, 329-340.
110. Muhitch, M. J., McCormick, S. P., Alexander, N. J., & Hohn, T. M. (2000). Transgenic expression of the TRI101 or PDR5 gene increases resistance of tobacco to the phytotoxic effects of the trichothecene 4,15-diacetoxyscirpenol. *Plant Science*, 157, 201-207.
111. Nagy, C. M., Fejer, S. N., Berek, L., Molnar, J., & Viskolcz, B. (2005). Hydrogen bondings in deoxynivalenol (DON) conformations - A density functional study. *Journal of Molecular Structure-Theochem*, 726(1-3), 55-59.
112. Neuhaus, D. (2009). Nuclear Overhauser Effect. In D. M. Grant & R. K. Harris (Eds.), *Encyclopedia of Magnetic Resonance* (Vol. 9, pp. 4530-4541). Chichester, UK: John Wiley & Sons, Ltd.
113. Nielsen, C., Casteel, M., Didier, A., Dietrich, R., & Martlbauer, E. (2009). Trichothecene-induced cytotoxicity on human cell lines. *Mycotoxin Research*, 25, 77-84.
114. Ohsato, S., *et al.* (2007). Transgenic rice plants expressing trichothecene 3-O-acetyltransferase show resistance to the *Fusarium* phytotoxin deoxynivalenol. *Plant Cell Rep.*, 26, 531-538.
115. Okoye, Z. S. C. (1992). *Fusarium* mycotoxins nivalenol and 4-acetyl-nivalenol (fusarenon-x) in mouldy maize harvested from farms in Jos district, Nigeria. *Food. Addit. Contam.*, 10(4), 375-379.
116. Ouyang, S.-L. W., N-N.; Liu, J.-Y.; Sun, C.-L.; Li, Z.-W.; Gao, S.-Q. (2010). Investigation of hydrogen bonding in neat dimethyl sulfoxide and binary mixture (dimethyl sulfoxide + water) by concentration-dependent Raman study and *ab initio* calculation. *Chinese Phys. B*, 19(12).

117. Pace, J. G. (1983). Effect of T-2 mycotoxin on rat liver mitochondria electron transport system. *Toxicon*, 21, 675-680.
118. Pace, J. G., & Matson, C. F. (1988). Stability of T-2, HT-2, and T-2 tetraol in biological fluids. *J. Anal. Toxicol.*, 12, 48-50.
119. Pace, J. G., Watts, M. R., & Canterbury, W. J. (1988). T-2 mycotoxin inhibits mitochondrial protein synthesis. *Toxicon*, 26, 77-85.
120. Packa, D. (1991). Cytogenic changes in plant cells as influenced by mycotoxins. *Mycotoxins Research*, 7, 150-155.
121. Pestka, J. (2010). Toxicological mechanisms and potential health effects of deoxynivalenol and nivalenol. *World Mycotoxin Journal*, 3, 323-347.
122. Pestka, J. J. (2007). Deoxynivalenol: Toxicity, mechanisms and animal health risks. *Animal Feed Science and Technology*, 137(3-4), 283-298.
123. Poapolathep, A. S.-K., Y.; Doi, K.; Kumagai, S. (2003). The fates of trichothecene mycotoxins, nivalenol and fusarenon-X, in mice. *Toxicon.*, 41(8), 1047-1054.
124. Poppenberger, B., *et al.* (2003). Detoxification of the *Fusarium* mycotoxin deoxynivalenol by a UDP-glucosyltransferase from *Arabidopsis thaliana*. *Journal of Biological Chemistry*, 278, 47905-47914.
125. Purcell, E. T., H.; Pound, R. (1946). Resonance Absorption by Nuclear Magnetic Moments in a Solid. *Physical Review*, 69(1), 37-38.
126. Rhodes, G. (2006). *Crystallography made crystal clear: a guide for users of macromolecular model* (3rd ed.): Academic Press.
127. Rocha, O., Ansari, K., & Doohan, F. M. (2005). Effects of trichothecene mycotoxins on eukaryotic cells: a review. *Food. Addit. Contam.*, 22, 369-378.
128. Rodnina, M. V., Beringer, M., & Wintermeyer, W. (2007). How ribosomes make peptide bonds. *TRENDS Biochem. Sci.*, 32, 20-26.
129. Rotter, R. G., Thompson, B. K., Trenholm, H. L., Prelusky, D. B., Hartin, K. E., & Miller, J. D. (1992). A preliminary examination of potential interactions between deoxynivalenol (DON) and other selected *Fusarium* metabolites in growing pigs. *Can. J. Anim. Sci.*, 72, 107-116.
130. Roush, W. R., Marletta, M. A., Russorodriguez, S., & Recchia, J. (1985). TRICHOTHECENE METABOLISM STUDIES - ISOLATION AND STRUCTURE DETERMINATION OF 15-ACETYL-3-

- ALPHA-(1'-BETA-D-GLUCOPYRANOSIDURONYL)-SCIRPEN-3,4-BETA,15-T RIOL. *Journal of the American Chemical Society*, 107(11), 3354-3355.
131. Roush, W. R., Marletta, M. A., Russorodriguez, S., & Recchia, J. (1985). TRICHOTHECENE METABOLISM STUDIES - ISOLATION AND STRUCTURE DETERMINATION OF 15-ACETYL-3-ALPHA-(1'-BETA-D-GLUCOPYRANOSIDURONYL)SCIRPEN-3,4-BETA,15-TR IOL. *Abstracts of Papers of the American Chemical Society*, 189(APR-), 41-ORGN.
 132. Roush, W. R., Marletta, M. A., Russorodriguez, S., & Recchia, J. (1985). TRICHOTHECENE METABOLISM STUDIES .2. STRUCTURE OF 3-ALPHA-(1''BETA-D-GLUCOPYRANOSIDURONYL)-8-ALPHA-ISOVALERYLOXY-SCIRPEN-3 ,4-BETA, 15-TRIOLE 15-ACETATE PRODUCED FROM T-2 TOXIN INVITRO. *Tetrahedron Letters*, 26(43), 5231-5234.
 133. Roush, W. R., & Russorodriguez, S. (1985). TRICHOTHECENE DEGRADATION STUDIES - SYNTHESIS OF 12,13-DEOXYANGUIDINE AND 12,13-DEOXYVERRUCAROL. *Journal of Organic Chemistry*, 50(26), 5465-5468.
 134. Savard, M. E., & Blackwell, B. A. (1994). Spectral characteristics of secondary metabolites from *Fusarium* fungi. In J. D. Miller & H. L. Trenholm (Eds.), *Mycotoxins in Grains* (pp. 59-228). St. Paul, Minnesota, USA: Eagen Press.
 135. Savard, M. E., Blackwell, B. A., & Greenhalgh, R. (1987). An H-1 Nuclear-Magnetic-Resonance study of derivatives of 3-hydroxy-12,13-epoxytrichothec-9-enes. *Canadian Journal of Chemistry- Revue Canadienne De Chimie*, 65(9), 2254-2262.
 136. Schindler, D., Grant, P., & Davies, J. (1974). Trichodermin resistance-mutation affecting eukaryotic ribosomes. *Nature*, 248, 535-536.
 137. Schollenberger, M., Drochner, W., & Muller, H. M. (2007). Fusarium toxins of the scirpentriol subgroup: a review. *Mycopathologia*, 164(3), 101-118.
 138. Scott, P. M. (1989). The natural occurrence of trichothecenes. In V. R. Beasley (Ed.), *Trichothecene mycotoxins: pathophysiological effects* (Vol. 1, pp. 37-62). Boca Raton, Florida, USA: CRC Press.
 139. Scudamore, K. A., Patel, S., & Edwards, S. G. (2009). HT-2 toxin and T-2 toxin in commercial cereal processing in the United Kingdom, 2004-2007. *World Mycotoxin Journal*, 2, 357-365.
 140. Shank, R. A. F., N.A.; Hazendonk, P.; Eudes, F.; Blackwell, B.A.;. (2011). Current and Future Experimental Strategies for Structural Analysis of Trichothecene Mycotoxins - A Prospectus. *Toxins*, 3, 1518-1553.
 141. Shen, L., et al. (2006). Absolute configuration of new cytotoxic and other bioactive trichothecene macrolides. *Chemistry-a European Journal*, 12(21), 5596-5602.

142. Shifrin, V. I., & Anderson, P. (1999). Trichothecene mycotoxins trigger a ribotoxic stress response that activates c-Jun N-terminal kinase and p38 mitogen-activated protein kinase and induces apoptosis. *J. Biol. Chem.*, 274, 13985-13992.
143. Shimada, T., & Otani, M. (1990). Effects of *Fusarium* mycotoxins on the growth of shoots and roots at germination in some Japanese wheat cultivars. *Cereal Research Communications*, 18, 229-232.
144. Silverstein, R. M. B., G. C.; Morrill, T. C. (1974). *Spectrometric Identification of Organic Compounds* (Third ed.). Toronto: John Wiley & Sons.
145. Smith, S. A. P., W. E.; Gerig, J. T. (1992). The Hamiltonians of NMR; Part I. *Concepts in Magnetic Resonance*, 4, 107-144.
146. Sorrell, T. N. (2006). *Organic Chemistry* (Second ed.). Sausalito, CA: University Science Books.
147. Steinmetz, W. E., Robustelli, P., Edens, E., & Heineman, D. (2008). Structure and conformational dynamics of trichothecene mycotoxins. *Journal of Natural Products*, 71(4), 589-594.
148. Steinmetz, W. E., Rodarte, C. B., & Lin, A. (2009). 3D QSAR study of the toxicity of trichothecene mycotoxins. *Eur. J. Med. Chem.*, 44, 4485-4489.
149. Sudakin, D. L. (2003). Trichothecenes in the environment: Relevance to human health. *Toxicology Letters*, 143, 97-107.
150. Tatsuno, T. M., Saito, M., Enomoto, M., & Tasumodo, H. (1968). Nivalenol, a toxic principle of *Fusarium nivale*. *Chem. Pharm. Bull.*, 16, 2519-2520.
151. Tokuhiro, T. T. M., L.; Szmant, H. (1974). Contribution of relaxation and chemical shift results to the elucidation of the structure of the water-DMSO liquid system. *J. Chem. Phys.*, 61.
152. Trenholm, H. L., *et al.* (1983). Survey of vomitoxin contamination of 1980 Ontario white winter wheat crop: results of survey and feeding trials. *J. Assoc. Off. Anal. Chem.*, 66, 92-97.
153. Trusal, L. R., & O'Brien, J. C. (1986). Ultrastructural effects of T-2 mycotoxin on rat hepatocytes in vitro. *Toxicon*, 24, 481-488.
154. Tycko, R. D., G.; Mirau, P.A. (1989). Determination of Chemical-Shift-Anisotropy Lineshapes in a Two-Dimensional Magic-Angle-Spinning NMR Experiment. *Journal of Magnetic Resonance*, 85, 265-274.
155. Ueno, Y. (1983). *Trichothecenes: chemical, biological and toxicological aspects*. Amsterdam, Netherlands: Elsevier Scientific Publishers.

156. Ueno, Y. (1984). Toxicological features of T-2 toxin and related trichothecenes. *Toxicol. Sci.*, *4*, 124-132.
157. Ueno, Y. (1985). The toxicology of mycotoxins. *Critical Reviews in Toxicology*, *14*, 99-133.
158. Ueno, Y., & Ishii, K. (1985). Chemical and biological properties of trichothecenes from *Fusarium sporotrichioides*. In J. Lacey (Ed.), *Trichothecenes and other mycotoxins: proceedings of the international mycotoxin symposium of Sydney, Australia, 1984* (pp. 307-316). New York: John Wiley & Sons.
159. Veshtort, M. G., R. G. (2006). SPINEVOLUTION: A Powerful Tool For The Simulation of Solid and Liquid State NMR Experiments. *J. Mag. Res.*, *178*(2), 248-282.
160. Vesonder, R. F., & Hesseltine, C. W. (1980). Vomitoxin: natural occurrence on cereal grains and significance as a refusal and emetic factor to swine. *Process Biochem*, *44*(12), 12-14.
161. Voigt, C. A., Schafer, W., & Salomon, S. (2005). A secreted lipase of *Fusarium graminearum* is a virulence factor required for infection of cereals. *Plant Journal*, *42*, 364-375.
162. Wei, R. D., & Chu, F. S. (1985). Modification of in vitro metabolism of T-2 toxin by esterase inhibitors. *Applied Environmental Microbiology*, *50*, 115-119.
163. Williamson, K. L. (1963). Substituent Effects on Nuclear Magnetic Resonance Coupling Constants and Chemical Shifts in a Saturated System: Hexachlorobicyclo [2.2.1]heptenes. *J. Am. Chem. Soc.*, *85*(5), 516-519.
164. Wu, W. B., M.; Bursian, S.J.; Link, J.E.; Flannery, B.M.; Sugita-Konishi, Y.; Wantanabe, M.; Zhang, H.; Pestka, J.J. (2012). Comparison of Emetic Potencies of the 8-Ketotrichothecenes Deoxynivalenol, 15-Acetyldeoxynivalenol, 3-Acetyldeoxynivalenol, Fusarenol X and Nivalenol. *Toxicol. Sci.*
165. Yagen, B., & Jarvis, B. B. (1989). SYNTHESIS OF TRITIUM LABELED VERRUCAROL AND VERRUCARIN-A. *Journal of Labelled Compounds & Radiopharmaceuticals*, *27*(6), 675-681.
166. Yang, G.-H., Jarvis, B. B., Chung, Y.-J., & Pestka, J. J. (2000). Apoptosis induction by the satratoxins and other trichothecene mycotoxins: relationship to ERK, p38 MAPK, and SAPK/JNK activation. *Toxicol. Appl. Pharmacol.*, *164*, 149-160.
167. Yoshizawa, T., Sakamoto, T., & Okamoto, K. (1984). In vitro formation of 3'-hydroxy T-2 and 3'-hydroxy HT-2 toxins from T-2 toxin by liver homogenates from mice and monkeys. *Applied Environmental Microbiology*, *47*, 130-134.

168. Zamir, L. O., Devor, K. A., & Sauriol, F. (1991). BIOSYNTHESIS OF THE TRICHOTHECENE 3-ACETYLDEOXYNIVALENOL - IDENTIFICATION OF THE OXYGENATION STEPS AFTER ISOTRICHODERMIN. *Journal of Biological Chemistry*, 266(23), 14992-15000.
169. Zamir, L. O., Gauthier, M. J., Devor, K. A., Nadeau, Y., & Sauriol, F. (1989). TRICHODIENE IS A PRECURSOR TO TRICHOTHECENES. *Journal of the Chemical Society-Chemical Communications*(9), 598-600.
170. Zamir, L. O., Nikolakakis, A., Devor, K. A., & Sauriol, F. (1996). Biosynthesis of the trichothecene 3-acetyldeoxynivalenol - Is isotrichodermin a biosynthetic precursor? *Journal of Biological Chemistry*, 271(44), 27353-27359.
171. Zamir, L. O., *et al.* (1999). Biosynthesis of 3-acetyldeoxynivalenol and sambucinol - Identification of the two oxygenation steps after trichodiene. *Journal of Biological Chemistry*, 274(18), 12269-12277.
172. Zamir, L. O., Nikolakakis, A., Sauriol, F., & Mamer, O. (1999). Biosynthesis of trichothecenes and apotrichothecenes. *Journal of Agricultural and Food Chemistry*, 47(5), 1823-1835.
173. Zhou, H.-R., Lau, A. S., & Pestka, J. J. (2003). Role of double-stranded RNA-activated protein kinase R (PKR) in deoxynivalenol-induced ribotoxic stress response. *Toxicol. Sci.*, 74, 335-344.